

# Quantification of Aviation's Impact on Air Quality near Schiphol Airport using Low-Cost Gas Sensors



**J. Maes**

**MSc Thesis**

Section Aircraft Noise and Climate Effects

Faculty of Aerospace Engineering





# Quantification of Aviation's Impact on Air Quality near Schiphol Airport using Low-Cost Gas Sensors

by

J. Maes

to obtain the degree of Master of Science  
at the Delft University of Technology,  
to be defended publicly on Friday June 18, 2021 at 1:30 PM.

Student number: 4453468  
Project duration: April 23, 2020 – June 18, 2021  
Thesis committee: Dr. I. C. Dedoussi, TU Delft, supervisor  
Prof. D. G. Simons, TU Delft, chairman  
Dr. G. Biskos, TU Delft  
Dr. M. A. Mitici, TU Delft

*This thesis is not confidential.*

An electronic version of this thesis is available at <http://repository.tudelft.nl/>.

*Cover picture: Amsterdam Schiphol airport, Polderbaan arrival, own work.*

# Preface

Dear reader,

Thank you for showing interest in my MSc thesis report. This project was executed with the help of many people and would not have been such a success without them.

First of all, I would like to express my gratitude for Ing. Danny de Gans and Ing. Lars Leenheer from TU Delft's DEMO, who were fully responsible for manufacturing the sensor box. Without them, the sensor box in its current form would not exist.

Secondly, I would like to thank Dr. Dave de Jonge and his team from the GGD of Amsterdam, who have helped me in setting up the extremely valuable calibration experiment at Wijk aan Zee.

Next, I would like to acknowledge my roommates Jan, Benjamin, Margo, Christina and Fabien, with whom I spent multiple years living together. Thank you for being part of my life.

Hereafter, my thesis supervisor, Dr. I. C. Dedoussi should be recognised. She provided this thesis topic and project funding. Thank you Irene for the countless hours of listening and providing feedback. I sincerely hope that the project continues.

Finally, my utmost gratitude goes out to my grandparents, parents, Ann and Steven, and girlfriend, Lisa, who have done a marvellous job in supporting my dream to become an Aerospace Engineer.

*J. Maes  
Delft, May 2021*



# Contents

<b>List of Symbols and Acronyms</b>	<b>ix</b>
<b>List of Figures</b>	<b>xiii</b>
<b>List of Tables</b>	<b>xvii</b>
<b>1 Introduction</b>	<b>3</b>
1.1 Thesis Objective . . . . .	4
1.2 Outline of this Report . . . . .	4
<b>2 Background</b>	<b>5</b>
2.1 Introduction to Air Quality . . . . .	5
2.1.1 Air Quality and Emissions . . . . .	5
2.1.2 Primary and Secondary Air Pollutants . . . . .	5
2.1.3 Notation and Units . . . . .	5
2.2 Regulatory Air Quality Monitoring . . . . .	7
2.3 Low-Cost Monitoring . . . . .	8
2.3.1 Working Principle . . . . .	9
2.3.2 Performance Indicators . . . . .	10
2.3.3 Calibration Methods . . . . .	11
2.4 Air Quality Impacts from Aviation Activities . . . . .	12
2.4.1 Emission Index . . . . .	12
2.4.2 Landing and Take-off Operations versus Cruise Flight . . . . .	13
2.4.3 Exhaust Emissions . . . . .	14
2.4.4 Non-Exhaust Emissions . . . . .	17
2.4.5 Airport Related Emissions . . . . .	18
2.4.6 Final Selection of Chemical Species to be Measured . . . . .	18
2.5 Aircraft Activity Data . . . . .	18
2.5.1 Sound Measurements . . . . .	19
2.5.2 ADS-B Data . . . . .	19
<b>3 Sensor Box Design, Development and Integration</b>	<b>21</b>
3.1 Sensor Box Design . . . . .	21
3.1.1 Design Criteria . . . . .	21
3.1.2 Sensor Selection . . . . .	22
3.1.3 Conceptual Design . . . . .	23
3.2 Sensor Box Development . . . . .	24
3.2.1 Components . . . . .	24
3.2.2 Version 1: Sensor Box without Casing . . . . .	26
3.2.3 Iteration 1: Sensor Box with Open Casing . . . . .	27
3.2.4 Iteration 2: Sensor Box with Waterproof Casing . . . . .	28
3.2.5 Operating Procedures and Code . . . . .	29
3.3 Preliminary Experiments . . . . .	29
3.3.1 Indoor Measurements at the Aerospace Faculty . . . . .	29
3.3.2 Response to Car Exhaust . . . . .	31
3.4 Battery Performance . . . . .	34

<b>4</b>	<b>Sensor Box Calibration</b>	<b>37</b>
4.1	Terminology . . . . .	37
4.2	Calibration Data Collection . . . . .	38
4.2.1	Collocation for One Day - The Hague . . . . .	38
4.2.2	Collocation for Multiple Days at a Distance - The Hague . . . . .	39
4.2.3	Collocation for Multiple Days - Beverwijk . . . . .	40
4.2.4	Data Structure . . . . .	41
4.3	Calibration Data Exploration and Visualisation . . . . .	41
4.3.1	Collocation for One Day - The Hague . . . . .	41
4.3.2	Collocation for Multiple Days at a Distance - The Hague . . . . .	43
4.3.3	Collocation for Multiple Days - Beverwijk . . . . .	44
4.4	Preparing Data for Calibration Model . . . . .	46
4.4.1	Data Cleaning . . . . .	46
4.4.2	Creating a Train and Test Set . . . . .	48
4.4.3	Feature Scaling . . . . .	48
4.5	Calibration Model Selection and Development . . . . .	48
4.5.1	Multivariate Linear Regression . . . . .	49
4.5.2	Random Forest . . . . .	49
4.5.3	Feature Selection . . . . .	50
4.5.4	Training and Evaluating . . . . .	51
4.5.5	Evaluation using Cross-Validation . . . . .	54
4.6	Calibration Model Fine-Tuning . . . . .	55
4.6.1	Multivariate Linear Regression Model . . . . .	55
4.6.2	Random Forest Model . . . . .	55
4.7	Final Calibration Model Selection . . . . .	57
4.8	Calibration Model Integration . . . . .	60
<b>5</b>	<b>Extracting Aviation-Attributable Air Quality Impacts</b>	<b>61</b>
5.1	Aircraft Activity Data . . . . .	61
5.1.1	Sound Intensity Measurements . . . . .	61
5.1.2	ADS-B Data . . . . .	61
5.2	Weather Data . . . . .	63
5.3	Air Pollution Signals . . . . .	64
5.3.1	Extracting the Background Pollution Signal . . . . .	64
5.3.2	Extracting the Local Pollution Signal . . . . .	64
5.4	Linking Local Pollution Signal to Aircraft Activity . . . . .	65
5.5	Validation Methodology . . . . .	66
<b>6</b>	<b>Experimental Set-up</b>	<b>69</b>
6.1	Overview . . . . .	69
6.2	Experiment 1: Arrivals on the Polderbaan . . . . .	70
6.3	Experiment 2: Departures on the Aalsmeerbaan and Kaagbaan . . . . .	71
6.4	Experiment 3: Departures on the Aalsmeerbaan and Kaagbaan . . . . .	73
6.5	Experiment 4: Taxi Measurements on Airport Apron . . . . .	74
<b>7</b>	<b>Results</b>	<b>77</b>
7.1	Experiment 1: Arrivals on the Polderbaan . . . . .	77
7.1.1	Time-Series Measurements . . . . .	77
7.1.2	Analysis using Flight Activity Coupled to Local Signal . . . . .	79
7.1.3	Validation Results . . . . .	82
7.1.4	Discussion . . . . .	83
7.2	Experiment 2 and 3: Departures on the Aalsmeerbaan and Kaagbaan . . . . .	84
7.2.1	Time-Series Measurements . . . . .	84
7.2.2	Analysis using Flight Activity Coupled to Local Signal . . . . .	87
7.2.3	Validation Results . . . . .	89
7.2.4	Discussion . . . . .	90

7.3	Experiment 4: Taxi Measurements on Airport Apron . . . . .	92
7.3.1	Time-Series Measurements . . . . .	92
7.3.2	Analysis using Flight Activity Coupled to Local Signal . . . . .	93
7.3.3	Validation Results . . . . .	96
7.3.4	Discussion . . . . .	96
7.4	Discussion of Measurement Results from All Experiments. . . . .	97
<b>8</b>	<b>Conclusion and Recommendations</b>	<b>99</b>
	<b>Appendices</b>	<b>101</b>
<b>A</b>	<b>WHO and EU Emission Guidelines</b>	<b>103</b>
<b>B</b>	<b>Sensor Box Design</b>	<b>105</b>
<b>C</b>	<b>Flight Schedule via ADS-B Data</b>	<b>107</b>
C.1	Experiment 1: Arrivals on the Polderbaan . . . . .	107
C.2	Experiment 2: Departures on the Aalsmeerbaan . . . . .	108
C.3	Experiment 3: Departures on the Aalsmeerbaan . . . . .	109
C.4	Experiment 4: Taxi Measurements on Airport Apron . . . . .	110
<b>D</b>	<b>Baseline Concentrations</b>	<b>111</b>
D.1	Experiment 1: Arrivals on the Polderbaan . . . . .	111
D.2	Experiment 2: Departures on the Aalsmeerbaan and Kaagbaan . . . . .	112
D.3	Experiment 3: Departures on the Aalsmeerbaan and Kaagbaan . . . . .	113
D.4	Experiment 4: Taxi Measurements on Airport Apron . . . . .	114
<b>E</b>	<b>Local Air Quality Impacts per Aircraft Type and per Engine Configuration</b>	<b>115</b>
E.1	Experiment 1: Arrivals on the Polderbaan . . . . .	115
E.2	Experiment 2 and 3: Departures on the Aalsmeerbaan . . . . .	117
E.3	Experiment 4: Taxi Measurements on Airport Apron . . . . .	117
<b>F</b>	<b>Flight Schedule via Visual Inspection</b>	<b>119</b>
F.1	Experiment 1: Arrivals on the Polderbaan . . . . .	119
F.2	Experiment 2: Departures on the Aalsmeerbaan and Kaagbaan . . . . .	120
F.3	Experiment 3: Departures on the Aalsmeerbaan . . . . .	121
<b>G</b>	<b>Mixed Flight Activity</b>	<b>123</b>
G.1	Experiment 1: Arrivals on the Polderbaan . . . . .	123
G.2	Experiment 2: Departures on the Aalsmeerbaan . . . . .	124
G.3	Experiment 3: Departures on the Aalsmeerbaan . . . . .	124
G.4	Experiment 4: Taxi Measurements on Airport Apron . . . . .	125
<b>H</b>	<b>Sensor Box Operating Procedures</b>	<b>127</b>
H.1	Operating Procedures . . . . .	127
H.1.1	Air Quality Sampling . . . . .	127
H.1.2	Calibrating the Real-Time Clock . . . . .	128
H.2	Code . . . . .	129
<b>I</b>	<b>METAR Data</b>	<b>131</b>
<b>J</b>	<b>Final Calibration Equations</b>	<b>133</b>
	<b>Bibliography</b>	<b>135</b>



# List of Symbols and Acronyms

## List of Acronyms

ADC	Analog-to-Digital Converter
ADS-B	Automatic Dependent Surveillance-Broadcast
AE	Aerospace Engineering
AE	Auxiliary Electrode
ANN	Artificial Neural Network
API	Application Programming Interface
APU	Auxiliary Power Units
ATM	Air Traffic Management
BAD	Brake Abrasion Dust
BC	Black Carbon
BIC	Bayesian Information Criterion
CAA	Clean Air Act
CI	Confidence Interval
DEP	Diesel Exhaust Particles
EC	Electrochemical Cell
EC	Elemental Carbon
EI	Emission Index
EPA	Environmental Protection Agency
FAR	Fuel-to-air ratio
FB	Fractional Bias
FFT	Fast Fourier Transform
FSC	Fuel Sulphur Content
GGD	Gemeentelijke of Gemeenschappelijke Gezondheidsdienst
GPU	Ground Power Units
IATA	International Air Transport Association
IC	Internal combustion
ICAO	International Civil Aviation Organization
ISB	Individual Sensor Board
IUPAC	International Union of Pure and Applied Chemistry

LTO	Landing and Take-off Operations
MAE	Mean Absolute Error
MBE	Mean Bias Error
MLR	Multivariate Linear Regression
NAAQS	National Ambient Air Quality Standards
NaN	Not a Number
NRMSE	Normalised Root-Mean-Square Error
OC	Organic Carbon
OPC	Optical Particulate Counter
PCB	Printed Circuit Board
PM	Particulate Matter
POA	Primary Organic Aerosol
RF	Random Forest
RIVM	Rijksinstituut voor Volksgezondheid en Milieu
RMSE	Root-Mean-Square Error
RTC	Real-Time Clock
SOA	Secondary Organic Aerosol
UFP	Ultra Fine Particles
UHC	Unburned Hydrocarbons
VOC	Volatile Organic Compounds
WE	Working Electrode
WHO	World Health Organization

#### List of Greek Symbols

$\alpha$	Entrainment coefficient	
$\Phi$	Equivalence ratio	
$\rho_i$	Mass concentration	kg m <sup>-3</sup>
$\sigma_i$	Volume concentration	m <sup>3</sup> m <sup>-3</sup>
$\zeta_i$	Mass ratio	kg kg <sup>-1</sup>

#### List of Latin Symbols

$C_i$	Number concentration	m <sup>-3</sup>
$c_i$	Molar concentration	mol m <sup>-3</sup>
$x_i$	Mole fraction	mol mol <sup>-1</sup>
AE <sub>0</sub>	Auxiliary electrode sensor output in zero air	V
AE <sub>e</sub>	Auxiliary electrode electronic offset	V

$AE_u$	Uncorrected raw auxiliary electrode output	V
E	Emission rate	kg/s
k	Number of folds during cross-validation	
M	Molar mass	kg/mol
$M_i$	Sensor air quality concentration at time i	kg m <sup>-3</sup>
N	Amount of a substance	mol
n	Number of observations	
$N_a$	Avogadro's number	$6.022 \cdot 10^{23} \text{mol}^{-1}$
p	Pressure	Pa
R	Coefficient of determination	
R	Ideal gas constant	$8.314 \cdot \text{JK}^{-1} \text{mol}^{-1}$
R	Plume radius	m
$R^2$	Coefficient of correlation	
$RM_i$	Reference air quality concentration at time i	kg m <sup>-3</sup>
S	Plume length along wind streamline towards receptor	m
T	Temperature	K
T	Thrust force	N
u	Fluid velocity	m/s
V	Volume	m <sup>3</sup>
$WE_0$	Working electrode sensor output in zero air	V
$WE_c$	Corrected working electrode output	V
$WE_e$	Working electrode electronic offset	V
$WE_u$	Uncorrected raw working electrode output	V

### Other Symbols

$C_2H_2$	Acetylene
$C_2H_4$	Ethylene
$C_3H_6$	Propylene
$CH_x$	Hydrocarbons
$CH_2O$	Formaldehyde
$CH_3CO$	Acetaldehyde
$CH_4$	Methane
$CO_2$	Carbon Dioxide
CO	Carbon Monoxide
C	Carbon

Fe	Iron
H <sub>2</sub> CO <sub>3</sub>	Carbonic Acid
H <sub>2</sub> O	Water
H <sub>2</sub> SO <sub>4</sub>	Sulphuric Acid
H <sub>2</sub> S	Hydrogen Sulphide
H	Hydrogen
Mg	Magnesium
Mn	Manganese
N <sub>2</sub> O	Nitrous Oxide
N <sub>2</sub>	Dinitrogen
NO <sub>x</sub>	Oxides of Nitrogen
NO <sub>2</sub>	Nitrogen Dioxide
NO	Nitric Oxide
N	Nitrogen
O <sub>2</sub>	Dioxygen
O <sub>3</sub>	Ozone
O	Oxygen
Pb	Lead
SO <sub>x</sub>	Oxides of Sulphur
SO <sub>2</sub>	Sulphur Dioxide
SO <sub>3</sub>	Sulphur Trioxide
S	Sulphur
C <sub>soot</sub>	Carbon soot
PM <sub>10</sub>	Particulate Matter less than 10 microns in diameter
PM <sub>2.5</sub>	Particulate Matter less than 2.5 microns in diameter

# List of Figures

2.1	Regulatory air quality monitor of the Dutch air quality network in Ypenburg. . . . .	7
2.2	Time-series visualisation of regulatory measurements close to Schiphol during December 2020 for NO <sub>2</sub> , NO and CO (hourly averaged). . . . .	8
2.3	Low-cost air quality monitoring device [13]. . . . .	9
2.4	Low-cost air quality monitoring sensor [3]. . . . .	9
2.5	Cross section of a three-electrode electrochemical gas sensor [2]. . . . .	10
2.6	Current-voltage curve of an electrochemical gas sensor [2]. . . . .	10
2.7	Ideal EC gas sensor behaviour. . . . .	11
2.8	Actual EC gas sensor behaviour. . . . .	11
2.9	CO EI for common engines. . . . .	13
2.10	NO <sub>x</sub> EI for common engines. . . . .	13
2.11	Hydrocarbons EI for common engines. . . . .	13
2.12	Non-volatile PM EI for common engines. . . . .	13
2.13	Illustration of aircraft activities in the LTO phase [14]. . . . .	14
2.14	Fuel in LTO cycle for common engines. . . . .	14
2.15	Fuel flow for common engines. . . . .	14
2.16	Emissions discharge versus combustion regime [39]. . . . .	15
2.17	Ideal and real jet engine combustion. . . . .	16
2.18	Thrust reversal use during landing [18]. . . . .	17
2.19	Thrust reversal use during power-backing [18]. . . . .	17
2.20	Schematic representation of ADS-B working principle [4]. . . . .	19
3.1	Barometer sensor [19]. . . . .	23
3.2	Light sensor [10]. . . . .	23
3.3	Sound intensity sensor [11]. . . . .	23
3.4	Conceptual sensor box design. . . . .	24
3.5	Adafruit data logging shield [38]. . . . .	25
3.6	RTC mounted on Adafruit data logging shield. . . . .	25
3.7	SD card reader mounted on Adafruit data logging shield. . . . .	25
3.8	MCP3423 ADC as a component [16]. . . . .	26
3.9	ISB as a component [1]. . . . .	26
3.10	ISB in sensor box assembly. . . . .	26
3.11	LCD with text printed on the display. . . . .	27
3.12	Sensor box without casing. . . . .	27
3.13	Sensor box with open casing. . . . .	28
3.14	Sensor box with waterproof casing. . . . .	28
3.15	Internal lay-out of the final sensor box. . . . .	29
3.16	Experimental set-up of sensor box office measurements. . . . .	30
3.17	CO electrical response in office. . . . .	30
3.18	NO electrical response in office. . . . .	30
3.19	NO <sub>2</sub> electrical response in office. . . . .	31
3.20	O <sub>x</sub> electrical response in office. . . . .	31
3.21	Experimental set-up during first car exhaust experiment. . . . .	31
3.22	CO electrical response during first car exhaust experiment. . . . .	32
3.23	NO electrical response during first car exhaust experiment. . . . .	32
3.24	NO <sub>2</sub> electrical response during first car exhaust experiment. . . . .	32
3.25	O <sub>x</sub> electrical response during first car exhaust experiment. . . . .	32
3.26	Experimental set-up during second car exhaust experiment. . . . .	33
3.27	Sensor box rain protection open vs close. . . . .	33

3.28	Car exhaust experiment 2 flow. . . . .	33
3.29	CO electrical response during second car exhaust experiment. . . . .	34
3.30	NO electrical response during second car exhaust experiment. . . . .	34
3.31	NO <sub>2</sub> electrical response during second car exhaust experiment. . . . .	34
3.32	O <sub>x</sub> electrical response during second car exhaust experiment. . . . .	34
4.1	General machine learning terminology. . . . .	38
4.2	Experimental set-up of collocation with the "Den Haag - Bleriotlaan" air quality station. . . . .	39
4.3	Sensor box location at the AE Faculty. . . . .	40
4.4	Close-up of sensor box during faculty collocation. . . . .	40
4.5	Sensor box collocation with Wijk aan Zee station. . . . .	40
4.6	Close-up of sensor box during collocation with Wijk aan Zee station. . . . .	40
4.7	Normalised sensor box output with normalised temperature and light gradients for the first collocation experiment at the "Den Haag - Bleriotlaan" station. . . . .	41
4.8	Correlation between sensor box measurements at 1-min resampling for the first collocation experiment at the "Den Haag - Bleriotlaan" station. . . . .	42
4.9	Electrical signals for the working electrodes during AE faculty-The Hague collocation. . . . .	43
4.10	Meteorological signals during AE faculty-The Hague collocation. . . . .	43
4.11	Correlation between sensor box measurements at 60-min resampling during AE faculty-Ypenburg collocation. . . . .	44
4.12	Electrical signals for the working electrodes during collocation in Wijk aan Zee. . . . .	45
4.13	Meteorological signals during collocation in Wijk aan Zee. . . . .	45
4.14	Correlation at 1-hour resolution during collocation in Wijk aan Zee. . . . .	45
4.15	Correlation at 10-second resolution during collocation in Wijk aan Zee. . . . .	45
4.16	Time-series subset of the CO sensor during Wijk aan Zee calibration. . . . .	47
4.17	FFT for CO working electrode during Wijk aan Zee calibration. . . . .	47
4.18	FFT for CO auxiliary electrode during Wijk aan Zee calibration. . . . .	47
4.19	Time-series of original and filtered CO WE signal. . . . .	48
4.20	Time-series of original and filtered CO AUX signal. . . . .	48
4.21	Example of a voting scheme in ensemble predictions. . . . .	49
4.22	Example of random sampling in ensemble learning. . . . .	49
4.23	BIC score for MLR model for NO at 60 min resolution. . . . .	51
4.24	BIC score for RF model for NO at 60 min resolution. . . . .	51
4.25	1-to-1 plots for MLR calibration at Wijk aan Zee for CO. . . . .	51
4.26	1-to-1 plots for MLR calibration at Wijk aan Zee for NO. . . . .	52
4.27	1-to-1 plots for MLR calibration at Wijk aan Zee for NO <sub>2</sub> . . . . .	52
4.28	1-to-1 plots for RF calibration at Wijk aan Zee for CO. . . . .	53
4.29	1-to-1 plots for RF calibration at Wijk aan Zee for NO. . . . .	53
4.30	1-to-1 plots for RF calibration at Wijk aan Zee for NO <sub>2</sub> . . . . .	53
4.31	10-fold cross-validation illustration [9]. . . . .	54
4.32	1-to-1 plots for RF tuned calibration at Wijk aan Zee for CO. . . . .	57
4.33	1-to-1 plots for RF tuned calibration at Wijk aan Zee for NO. . . . .	57
4.34	1-to-1 plots for RF tuned calibration at Wijk aan Zee for NO <sub>2</sub> . . . . .	57
4.35	RMSE for different models applied to the Wijk aan Zee test data set. . . . .	58
4.36	Correlation coefficients for different models applied to the Wijk aan Zee test data set. . . . .	58
4.37	Prediction error in $\mu\text{gm}^{-3}$ for concentrations lower than the 50% quantile for different models. . . . .	59
4.38	Prediction error in $\mu\text{gm}^{-3}$ for concentrations higher than the 90% quantile for different models. . . . .	59
4.39	Block diagram of sensor box calibration model integration. . . . .	60
5.1	Schematic representation of ADS-B data querying. . . . .	62
5.2	ADS-B track classification algorithm. . . . .	63
5.3	Schematic representation of METAR data querying. . . . .	64
5.4	Local CO signal for window size variations between 1 and 24 during the first experiment at Schiphol airport. . . . .	65

5.5	Local CO signal for window size variations between 1 and 500 during the first experiment at Schiphol airport. . . . .	65
5.6	Graphical representation of coupling local pollution signal to aircraft activity. . . . .	66
5.7	Flow diagram of how the local signal coupling integrates in the code. . . . .	66
6.1	Overview of sensor box locations for the four measurement experiments at Amsterdam Schiphol airport. . . . .	69
6.2	Sensor box location during first experiment. . . . .	70
6.3	Wind rose during first experiment. . . . .	70
6.4	Trackpoints of all landings during first experiment at Schiphol airport. . . . .	71
6.5	Sensor box locations during second experiment. . . . .	72
6.6	Wind rose during second experiment. . . . .	72
6.7	Trackpoints of all departures during the second experiment at Schiphol airport. . . . .	72
6.8	Sensor box location during third experiment. . . . .	73
6.9	Wind rose during third experiment. . . . .	73
6.10	Trackpoints of all departures during the third experiment at Schiphol airport. . . . .	74
6.11	Sensor box locations during fourth experiment. . . . .	74
6.12	Wind rose during fourth experiment. . . . .	74
6.13	Detailed measurement locations for fourth experiment at Schiphol. . . . .	75
6.14	Trackpoints during the fourth experiment at Schiphol airport via ground radar data. . . . .	76
6.15	Trackpoints during the fourth experiment at Schiphol airport via ADS-B data. . . . .	76
7.1	Time-series visualisation of total air quality measurements for first experiment with aircraft types of landing aircraft on the Polderbaan. . . . .	78
7.2	Time-series visualisation of decomposed local air quality signal for first experiment. . . . .	79
7.3	Local CO impact per aircraft type for landings during the first experiment. . . . .	80
7.4	Local CO impact per aircraft engine configuration for landings during the first experiment. . . . .	80
7.5	Local NO <sub>2</sub> impact per aircraft type for landings during the first experiment. . . . .	80
7.6	Local NO <sub>2</sub> impact per aircraft engine configuration for landings during the first experiment. . . . .	80
7.7	Local signals for CO for different aircraft during first experiment. . . . .	81
7.8	Local signals for NO for different aircraft during first experiment. . . . .	81
7.9	Local signals for NO <sub>2</sub> for different aircraft during first experiment. . . . .	82
7.10	Validation results for CO for first measurement experiment. . . . .	82
7.11	Validation results for NO <sub>x</sub> for first measurement experiment. . . . .	82
7.12	Time-series visualisation of total air quality measurements for second experiment with aircraft types of departing aircraft on the Kaagbaan and Aalsmeerbaan in red and blue, respectively. . . . .	84
7.13	Time-series visualisation of total air quality measurements for third experiment with aircraft types of departing aircraft on the Aalsmeerbaan. . . . .	85
7.14	Time-series visualisation of decomposed local air quality signal for second experiment. . . . .	86
7.15	Time-series visualisation of decomposed local air quality signal for third experiment. . . . .	87
7.16	Local CO impact per aircraft type for departures during the second and third experiment. . . . .	88
7.17	Local CO impact per aircraft engine configuration for departures during the second and third experiment. . . . .	88
7.18	Local signals for CO for different aircraft during second and third experiment. . . . .	88
7.19	Local signals for NO for different aircraft during second and third experiment. . . . .	89
7.20	Local signals for NO <sub>2</sub> for different aircraft during second and third experiment. . . . .	89
7.21	Validation results for CO for second and third measurement experiment. . . . .	90
7.22	Validation results for NO <sub>x</sub> for second and third measurement experiment. . . . .	90
7.23	B789 hold and line-up with runway during second experiment. . . . .	91
7.24	A332 hold and line-up with runway during second experiment. . . . .	91
7.25	Time-series visualisation of total air quality measurements for fourth experiment with aircraft types of nearby aircraft categorised by distance (black: <100 m, red: 100-250 m, green: >250 m). . . . .	92
7.26	Time-series visualisation of decomposed local air quality signal for fourth experiment. . . . .	93
7.27	Local CO impact per aircraft type for activity during the fourth experiment. . . . .	94

7.28	Local CO impact per aircraft engine configuration for activity during the fourth experiment.	94
7.29	Local NO impact per aircraft type for activity during the fourth experiment.	94
7.30	Local NO impact per aircraft engine configuration for activity during the fourth experiment.	94
7.31	Local signals for CO for different aircraft during fourth experiment.	95
7.32	Local signals for NO for different aircraft during fourth experiment.	95
7.33	Local signals for NO <sub>2</sub> for different aircraft during fourth experiment.	96
7.34	Validation results for CO for fourth measurement experiment.	96
7.35	Validation results for NO <sub>x</sub> for fourth measurement experiment.	96
7.36	Local concentration per aircraft activity type.	98
B.1	Customised PCB to host ISBs.	105
C.1	Timeline of arrivals on the Polderbaan based on OpenSky ADS-B for first experiment.	107
C.2	Timeline of departures on the Aalsmeerbaan based on OpenSky ADS-B for second experiment.	108
C.3	Timeline of departures on the Aalsmeerbaan based on OpenSky ADS-B for third experiment.	109
C.4	Timeline of nearby aircraft activity (<50 m) based on ground radar data for fourth experiment.	110
D.1	Time-series visualisation of decomposed baseline air quality signal for first experiment.	111
D.2	Time-series visualisation of decomposed baseline air quality signal for second experiment.	112
D.3	Time-series visualisation of decomposed baseline air quality signal for third experiment.	113
D.4	Time-series visualisation of decomposed baseline air quality signal for fourth experiment.	114
E.1	Local CO impact per aircraft type for landings during the first experiment.	115
E.2	Local CO impact per aircraft engine configuration for landings during the first experiment.	115
E.3	Local NO impact per aircraft type for landings during the first experiment.	116
E.4	Local NO impact per aircraft engine configuration for landings during the first experiment.	116
E.5	Local NO <sub>2</sub> impact per aircraft type for landings during the first experiment.	116
E.6	Local NO <sub>2</sub> impact per aircraft engine configuration for landings during the first experiment.	116
E.7	Local CO impact per aircraft type for departures during the second and third experiment.	117
E.8	Local CO impact per aircraft engine configuration for departures during the second and third experiment.	117
E.9	Local CO impact per aircraft type for activity during the fourth experiment.	117
E.10	Local CO impact per aircraft engine configuration for activity during the fourth experiment.	117
E.11	Local NO impact per aircraft type for activity during the fourth experiment.	118
E.12	Local NO impact per aircraft engine configuration for activity during the fourth experiment.	118
E.13	Local NO <sub>2</sub> impact per aircraft type for activity during the fourth experiment.	118
E.14	Local NO <sub>2</sub> impact per aircraft engine configuration for activity during the fourth experiment.	118
G.1	Mixed flight activity based on ADS-B signal pass-by and normalised sound intensity for first experiment.	123
G.2	Mixed flight activity based on ADS-B signal pass-by and normalised sound intensity for second experiment.	124
G.3	Mixed flight activity based on ADS-B signal pass-by and normalised sound intensity for third experiment.	124
G.4	Mixed flight activity based on ADS-B signal pass-by and normalised sound intensity for subset of fourth experiment.	125
H.1	Sensor box operating procedures for <code>x_sensorBox_V2.ino</code> .	127
H.2	Sensor box operating procedures for <code>set_time_on_rtc.ino</code> .	128
H.3	Graphical internal lay-out of the final sensor box.	129

# List of Tables

1.1	Overview of previous near-airport air quality monitoring studies. . . . .	4
2.1	Molar mass of common air pollutants. . . . .	6
2.2	Monitoring equipment of the GGD Amsterdam [29]. . . . .	7
2.3	Key parameters of the consulted regulatory air quality analysers [15]. . . . .	8
2.4	Performance tier classification based on determination coefficient [55]. . . . .	10
2.5	Emission indices during different aircraft operating modes as defined by ICAO [14]. . . . .	14
2.6	Key air pollutants that are directly released or secondary formed from commercial jet aircraft emissions. . . . .	16
2.7	Final chemical species selection. . . . .	18
3.1	Low-cost gas sensor selection and specifications. . . . .	22
3.2	Barometer sensor specifications [19]. . . . .	23
3.3	Light sensor specifications [10]. . . . .	23
3.4	Sound sensor specifications [11]. . . . .	23
3.5	Battery performance statistics. . . . .	35
4.1	Regulatory air quality analysers consulted for calibration as defined by the Dutch air quality network. . . . .	38
4.2	Summary of the first collocation experiment with the "Den Haag - Bleriotlaan" air quality station. . . . .	39
4.3	Summary of the second collocation experiment with the "Den Haag - Bleriotlaan" air quality station. . . . .	40
4.4	Summary of the collocation experiment with the "Wijk aan Zee - De Banjaert" air quality station. . . . .	40
4.5	Parameters obtained by sensor box measurements. . . . .	50
4.6	Feature selection using BIC for MLR models at different temporal resolutions. . . . .	50
4.7	Feature selection using BIC for RF models at different temporal resolutions. . . . .	50
4.8	RMSE in $\mu\text{gm}^{-3}$ for different species at different temporal scales using the MLR model. . . . .	52
4.9	Evaluation on the test set for the MLR models at different temporal scales. . . . .	52
4.10	RMSE in $\mu\text{gm}^{-3}$ for different species at different temporal scales using the RF model. . . . .	54
4.11	Evaluation on the test set for the non-tuned RF models at different temporal scales. . . . .	54
4.12	10-fold cross-validation RMSE (in $\mu\text{gm}^{-3}$ ) statistics for different species at different temporal scales using the MLR model. . . . .	55
4.13	10-fold cross-validation RMSE (in $\mu\text{gm}^{-3}$ ) statistics for different species at different temporal scales using the RF model. . . . .	55
4.14	Considered hyperparameters during RF model tuning. . . . .	56
4.15	RF hyperparameters for best estimators at different temporal scales. . . . .	56
4.16	RMSE in $\mu\text{gm}^{-3}$ for different species at different temporal scales using the hyperparameter-tuned RF model. . . . .	56
4.17	10-fold cross-validation RMSE (in $\mu\text{gm}^{-3}$ ) statistics for different species at different temporal scales using the hyperparameter-tuned RF model. . . . .	56
4.18	Evaluation on the test set for the best estimators obtained during hyperparameter optimisation at different temporal scales. . . . .	56
4.19	Absolute prediction errors (difference) at concentrations lower than the 50% quantile of Wijk aan Zee test set for both models. . . . .	59
4.20	Absolute prediction errors (difference) at concentrations higher than the 90% quantile of Wijk aan Zee test set for both models. . . . .	59

---

5.1	Parameters and units for ADS-B database [17]. . . . .	62
5.2	Parameters and units for local weather (METAR) database. . . . .	64
5.3	Measured jet engine exhaust velocities at the horizontal stabiliser of a B787 [24]. . . . .	67
6.1	Specifications of the first measurement experiment at Schiphol airport. . . . .	70
6.2	Specifications of the second measurement experiment at Schiphol airport. . . . .	72
6.3	Specifications of the third measurement experiment at Schiphol airport. . . . .	73
6.4	Specifications of the fourth measurement experiment at Schiphol airport. . . . .	75
6.5	Sensor box coordinates over time during fourth measurement experiment at Schiphol airport. . . . .	75
A.1	WHO guidelines [22, 52]. . . . .	103
A.2	European Union guidelines [20]. . . . .	104
B.1	Comparison between Arduino and Raspberry Pi. . . . .	105
F.1	Visually observed landings on the Polderbaan 22-01-2021. . . . .	119
F.2	Visually observed departures on the Aalsmeerbaan and Kaagbaan 17-02-2021. . . . .	120
F.3	Visually observed departures on the Aalsmeerbaan 19-02-2021. . . . .	121
I.1	METAR data for first experiment at Schiphol airport. . . . .	131

# Summary

A low-cost multi-pollutant sensor box is developed, calibrated and deployed to quantify aviation-attributable air quality impacts at Amsterdam Schiphol airport.

The sensor box contains four low-cost electrochemical gas sensors that respond to CO, NO, NO<sub>2</sub> and O<sub>3</sub> concentrations in ambient air. Additional sensors in the sensor box allow the determination of pressure, temperature, relative humidity, sound intensity, UV-light, visible light and IR-light. The pressure, temperature and relative humidity sensors assist in calibrating the gas measurements obtained by the gas sensors. Sound intensity measurements and ADS-B data assist in the detection of nearby aircraft activity.

Calibration of the sensor box was done by collocating it for ~74 hours with an air quality monitor of the Dutch air quality network in Wijk aan Zee, the Netherlands. Regulatory air quality data could be obtained at 10 s resolution for CO, NO and NO<sub>2</sub>. The absence of regulatory O<sub>3</sub> measurements results in discarding the corresponding low-cost sensor in further analysis. Next, multivariate linear regression and random forest models were constructed to transform the raw sensor box measurements into meaningful concentrations. The random forest model has a strong tendency to overfit, even though it performs better in absolute numbers. The final calibration models for each species are multivariate linear regression models with an RMSE for CO, NO and NO<sub>2</sub> of 118.13 µg m<sup>-3</sup>, 2.38 µg m<sup>-3</sup> and 3.96 µg m<sup>-3</sup>, respectively. Corresponding correlation coefficients are 0.94, 0.99 and 0.98.

Three different types of aircraft activity have been evaluated by deploying the sensor box at Amsterdam Schiphol airport. On 22 January 2021, the air quality impacts from landings on the Polderbaan were investigated by deploying the sensor box ~200 m from the runway. On both 17 and 19 February 2021, the impact of aircraft departures on the Aalsmeerbaan and Kaagbaan were investigated by measuring ~300 m from the runway. Finally, on 30 March 2021, air quality impacts from taxiing aircraft were obtained by taking measurements on the airport apron with aircraft coming as close as 43 m to the sensor box.

The obtained sensor box measurements represent total air quality concentrations, which contain impacts from multiple sources. Quantifying the proportion of aviation-attributable concentrations is achieved via a data-driven approach in which a baseline signal helps to extract the local aviation-attributable signal. It was found that this strategy results in local signals that can be linked to activity from aircraft.

Maximum aviation-attributable concentrations for CO, NO and NO<sub>2</sub> are ~3500 µg m<sup>-3</sup>, ~175 µg m<sup>-3</sup> and ~70 µg m<sup>-3</sup>, respectively. First, for CO, this maximum concentration of ~3500 µg m<sup>-3</sup> was recorded during the taxi measurements and could be linked to the B777 freighter. Next, the NO maximum concentration of ~175 µg m<sup>-3</sup> was recorded during two different experiments. First peak stems from measurements obtained during the arrivals experiment, linked to the B777-300ER. Second peak was linked to the A330-200 during the second departure experiment. Finally, the NO<sub>2</sub> maximum concentration of ~70 µg m<sup>-3</sup> was recorded during the arriving traffic measurements, linked to the B777-300ER.

Interestingly, these observations do not fully match with the expectations. In fact, a lower thrust setting should result in less NO<sub>x</sub> and more CO formation and vice versa. That means that the maximum peaks for NO and NO<sub>2</sub> obtained during the arrivals experiments are unexpected. A first reason for this behaviour is the fact that arriving aircraft have the ability to apply reverse thrust to slow down the aircraft. Video recordings show that thrust reversal was used during some of the arrivals, however uncertainty remains over the applied thrust setting during thrust reversal. A second explanation for this unexpected result is the reduced distance (~100 m) between the aircraft and the sensor box during the arrivals experiment, resulting in higher concentrations, theoretically.

This study shows that it is possible to quantify individual aviation-attributable air quality impacts at Amsterdam Schiphol airport using low-cost electrochemical gas sensors, but that large discrepancies remain in measured and calculated NO<sub>x</sub> concentrations. Future sensor box developments could have multiple sensors per chemical species to improve confidence in the results. In addition, the simultaneous deployment of multiple low-cost sensor boxes near the airport can improve accountability for individual plumes during peak traffic hours.



# 1

## Introduction

*"To measure is to know. If you cannot measure it, you cannot improve it"*

---

Lord Kelvin

Poor air quality was responsible for 4.9 million deaths in 2017 [59]. To put this in perspective, the exposure to PM<sub>2.5</sub> and ozone formed via aircraft emissions results in an estimated 16,000 deaths (90% CI: 8,300–24,000) per year, which is a fraction smaller than 0.33% of the total deaths attributed to air pollution, but still 200 times larger than the amount of fatalities attributed to air traffic in 2017 [23, 74]. There are various reasons why aviation's impacts should not be neglected. First of all, fuel burn is directly related to the released emissions, which used to be in a rising trend in the pre-COVID 19 era, but is already forecasted to be in a rising trend again in the post-COVID 19 era [8]. Secondly, landing and take-off operations (LTO) in Europe and North America are responsible for ~50% of the mortalities attributable to aviation even though only ~25% of the emissions are released in these phases, underlining a more negative impact on near-airport communities. Finally, it has been estimated that the health costs associated with air quality impacts from aviation exceed fatal accident and noise costs, being of the same order as aviation's climate costs [74].

The development of mitigation strategies can assist in reducing aviation's local air quality footprint and thus the attributed mortalities, however accurate quantification of aviation's air quality footprint is necessary. Aviation's air quality impacts have been quantified in the past using both modelling and monitoring, both having advantages and disadvantages. Modelling requires accurate input data such as emission rates and meteorology. More specifically, accurate wind data is a necessity as it plays a major role in emissions dispersion [65]. Chati and Balakrishnan [28] find that the thrust setting guidelines provided by ICAO have deviations as high as ~40% from the actual thrust settings, introducing additional inaccuracies in the model. On the other hand, air quality monitoring is cumbersome to execute. Many countries have implemented a network of air quality monitors. Unfortunately, the high costs of such air quality monitors results in networks that are extremely sparse, which makes it impossible to fully understand the air quality impacts of highly variable emission sources [46].

As a supplement to regulatory air quality monitoring, low-cost air quality sensors are being developed. Parts-per-billion level quantification of gaseous species can be achieved using low-cost electrochemical gas sensors, and similarly optical particle counters are a promising low-cost technology to monitor particulates [55]. Borrego et al. [27] have assessed low-cost air quality sensors at an unseen scale. They deploy hundreds of low-cost sensors collocated with reference air quality analysers for a two-week period in the city of Aveiro, Portugal. They conclude that such sensors can provide useful information if they are supported by the correct post-processing tools. Near-airport air quality monitoring studies have been performed in the past. The obtained studies in literature are summarised in Table 1.1. The first and only study using low-cost gas sensors has been performed by Popoola et al. [56] at London Heathrow airport, but they do not quantify contributions of individual aircraft. Quantifying ultrafine particles (UFPs) contributions from individual aircraft is done however by Lopes et al. [42], but only making a distinction between long-haul and short/medium-haul aircraft.

Table 1.1: Overview of previous near-airport air quality monitoring studies.

Year	Species	Airport	Duration	Temporal resolution	Authors
2009	BC	Warwick T.F. Green Int. (PVD), US	July 2005 - August 2006	1 minute	Dodson et al. [30]
2012	UFPs	Warwick T.F. Green Int. (PVD), US	3x 1 week	1 minute	Hsu et al. [35]
2014	UFPs	Warwick T.F. Green Int. (PVD), US	2x 1 week	1 minute	Hsu et al. [36]
2015	BC, NO <sub>x</sub>	Los Angeles Int. (LAX), US	42 days	1 minute	Penn et al. [54]
2015	NO <sub>x</sub> , O <sub>3</sub> , CO, PM <sub>10</sub> , PM <sub>25</sub>	London Heathrow Int. (LHR), UK	8 years	1 hour	Masiol and Harrison [44]
2015	UFPs	Schiphol (AMS), the Netherlands	March 2014 - May 2014	1 hour	Keuken et al. [40]
2016	BC	Venice Marco Polo (VCE), Italy	April 2014 - June 2014	1 hour	Masiol et al. [45]
2017	PM	Mytilene Int. (MJT), Greece	Unknown	3 minutes	Psanis et al. [57]
2018	CO, NO, NO <sub>2</sub> , CO <sub>2</sub> , VOCs	London Heathrow Int. (LHR), UK	5 weeks	20 seconds	Popoola et al. [56]
2018	VOCs	Beijing Int. (PEK), China	2015, all seasons	NA	Yang et al. [73]
2019	UFPs	Lisbon (LIS), Portugal	75 hours	Unknown	Lopes et al. [42]
2019	VOCs	Beirut Int. (BEY), Lebanon	5x 1 week	NA	Mokalled et al. [49]

## 1.1. Thesis Objective

From Table 1.1 it can be concluded that near-airport pollution monitoring studies are scarce. Moreover, the majority of the previous studies focus on black carbon (BC), UFPs and volatile organic compounds (VOCs). In addition, the utilised monitoring technique varies across studies. Most notably, Yang et al. [73] deploy summa canisters and Mokalled et al. [49] use multi-bed stainless steel thermal desorption tubes, which are both considered passive sampling techniques. Given the limitations and suggestions of previous studies, the goal of this thesis has been formulated as follows:

*The objective of the thesis is to contribute to the development of a low-cost multi-pollutant sensor device optimised for near-airport use that can extract aviation's pollution signature near Schiphol airport.*

Along with the research objective, four research questions are defined:

1. What are the expected pollutant species to be found at/near Schiphol airport and what are the estimated concentrations?
2. How can a low-cost air quality sensor box be calibrated?
3. Which additional insights are found by combining air quality measurement data with aircraft activity data and noise measurement data at/near Schiphol airport?
4. What are the measured air pollution levels attributed to aviation activities at/near Schiphol airport?

## 1.2. Outline of this Report

This report, together with the earlier carried out literature study serve as a summary of the work performed during the thesis. First, chapter 2 presents the necessary background. Next, chapter 3 presents the proposed low-cost sensor box design, as well as several preliminary experiments. Hereafter, the sensor box calibration procedure is presented in chapter 4. Then, chapter 5 presents how the aircraft-attributable component is extracted from the total measured air quality signals, including a methodology for validating these results. The experimental set-up for the experiments executed at Amsterdam Schiphol Airport is presented in chapter 6, with the corresponding results in chapter 7. Finally, chapter 8 presents the conclusions drawn in this thesis, including suggestions for further improvements.

# 2

## Background

This chapter provides the background necessary to support the proposed methodology. First, the concept of air quality is introduced in section 2.1. Hereafter, regulatory air quality monitoring is presented in section 2.2, followed by low-cost air quality monitoring in section 2.3. The air quality impacts per type of aircraft activity are presented in section 2.4. Finally, section 2.5 presents two forms of aircraft activity data that are implemented.

### 2.1. Introduction to Air Quality

Air quality has many definitions but in essence it relates to the quality of both indoor and outdoor air. Both natural occurring and anthropogenic processes impact the quality of the air due to the emission of air pollutants. The US EPA defines six criteria air pollutants, which are O<sub>3</sub>, particulate matter (PM), CO, Pb, SO<sub>2</sub> and NO<sub>2</sub> [68]. A formal definition of air quality reads as follows [21]:

”Air pollution can be defined as the presence of toxic chemicals or compounds in the air, at levels that pose a health risk. In an even broader sense, air pollution means the presence of chemicals or compounds in the air which are usually not present and which lower the quality of the air or cause detrimental changes to the quality of life.”

The health risk is confirmed by looking at the numbers. In 2017, air pollution was responsible for 4.9 million deaths worldwide, which is 9% of all deaths [59]. As an air quality control measure, the US EPA has implemented National Ambient Air Quality Standards (NAAQS). Similarly, the World Health Organization (WHO) and European Union (EU) have implemented such standards. An overview of these standards is given in Appendix A.

#### 2.1.1. Air Quality and Emissions

The scope of this thesis is to quantify the impact of aviation emissions on local air quality. Emissions are directly discharged via a combustion process and have the ability to be transformed over time into another species due to chemical reactions, affecting air quality.

#### 2.1.2. Primary and Secondary Air Pollutants

A distinction should be made between primary and secondary air pollutants. Primary air pollutants are directly emitted into the atmosphere from a source, and can thus immediately impact air quality. On the other hand, secondary pollutants emerge after the reaction between primary pollutants and readily present pollutants.

#### 2.1.3. Notation and Units

A framework for notation and units is necessary to have consistency. First, four definitions of concentrations are given, which are obtained from the Compendium of Chemical Terminology [51]. Hereafter, conversion between  $\mu\text{g m}^{-3}$  and parts-per notation is presented.

### Mass Concentration

The mass concentration  $\rho_i$  is defined as the mass of constituent  $m_i$  divided by the mixture volume  $V$  and can be calculated using Equation 2.1. The SI unit is  $\text{kg/m}^3$ .

$$\rho_i = \frac{m_i}{V} \quad (2.1)$$

### Volume Concentration

The volume concentration  $\sigma_i$  is defined as the volume of constituent  $V_i$  divided by the mixture volume  $V$  and can be calculated using Equation 2.2. As readily deduced from Equation 2.2, the SI unit is dimensionless.

$$\sigma_i = \frac{V_i}{V} \quad (2.2)$$

### Mole Fraction

The mole fraction  $x_i$  is defined as the amount of constituent  $n_i$  divided by the total amount of all constituents in the mixture  $n$  and can be calculated using Equation 2.3. The SI unit is in fact dimensionless but mol/mol is often used, as well as parts-per notation.

$$x_i = \frac{n_i}{n} \quad (2.3)$$

### Mass Ratio

The mass ratio  $\zeta_i$  is defined as the mass of constituent  $m_i$  divided by the total mass of all other constituents in the mixture. The SI unit is again dimensionless, but kg/kg is used as well as parts-per notation.

$$\zeta_i = \frac{m_i}{m_{\text{tot}} - m_i} \quad (2.4)$$

### Converting between Parts-per Notation and Mass Concentrations

Frequently, concentrations are expressed in  $\mu\text{g/m}^3$  as opposed to parts-per notation. Conversion between the two can be achieved via Equation 2.5. The molecular mass  $M$  can be obtained via the atomic mass parameter in the periodic table of elements<sup>1</sup>. The molar volume  $V$  is species independent in the case of an ideal gas and can be calculated via modification of the ideal gas law presented in Equation 2.6, resulting in Equation 2.7. Assuming a standard temperature  $T$  of 298.15 K, a standard pressure  $p$  of 101325 Pa and the gas constant  $R$  equal to  $8.3144 \text{ J mol}^{-1} \text{ K}^{-1}$ , the molar volume of an ideal gas equals  $0.02445 \text{ m}^3$ , or 24.45 l. The molecular mass for different species as well as the division by the molar volume gas is presented in Table 2.1. Conversion from ppb to ppm is a matter of dividing by factor 1000. The amount of a substance is indicated with  $n$ , the mass of a substance is indicated with  $m$ .

$$\text{Concentration } (\mu\text{g/m}^3) = \text{Concentration } (\text{ppb}) \cdot \frac{\text{Molecular mass } (\text{g/mol})}{\text{Molar volume } (\text{L})} \quad (2.5)$$

$$pV = nRT, \quad \text{where } n = \frac{m}{M} \quad (2.6)$$

$$V = \frac{nRT}{p} \quad (2.7)$$

Table 2.1: Molar mass of common air pollutants.

Species	Molar mass (g/mol)
NO	30.00615
NO <sub>2</sub>	46.00555
CO	28.01010
O <sub>3</sub>	47.99820

<sup>1</sup>Periodic table of elements: <https://pubchem.ncbi.nlm.nih.gov/ptable/>

## 2.2. Regulatory Air Quality Monitoring

The Netherlands has implemented an air quality network of 95 regulatory air quality monitors, the so-called "luchtmeetnet" [15]. Live and historical data can be accessed and downloaded manually, or accessed via an API (<https://api-docs.luchtmeetnet.nl>). The luchtmeetnet publishes air quality concentrations every hour of the day, 24/7, expressed in  $\mu\text{g m}^{-3}$  or number of particles per  $\text{m}^3$  in the case of ultrafine particles. A 2019 study concerning the air quality monitors surrounding Amsterdam confirms that there is no station with more than 4% data loss due to maintenance or faults [29]. It should be noted that the data for the current year is not validated and will only be validated in the next year, and thus values of the current year are subject to change.

An example of a luchtmeetnet station is visualised in Figure 2.1. In terms of cost, these air quality monitors are expensive, with prices around 20,000 euros for a single station and 5,000 to 10,000 euros for maintenance per year, per station [64].

Globally, air quality data from both regulatory analysers and low-cost equipment is uploaded to <https://aqicn.org/here/>. The European Union (EU Air Quality Directive 2008/50/EC) determines standards for measurement equipment, however this does not mean that regulatory air quality stations are the same across country borders.



Figure 2.1: Regulatory air quality monitor of the Dutch air quality network in Ypenburg.

For the monitoring stations nearby Amsterdam, the measurement equipment is summarised in Table 2.2. It can be seen from the accuracy column that 95% of the measurements are within a 16.3% deviation.

Table 2.2: Monitoring equipment of the GGD Amsterdam [29].

Species	Device	Sample rate	Accuracy at yearly limit (95% CI)
PM <sub>2.5</sub>	Met One, BAM 1020	Hourly	$\pm 16.3\%$
PM <sub>10</sub>	Met One, BAM 1020	Hourly	$\pm 8.2\%$
CO	API T300	10 seconds	$\pm 12.2\%$
NO/NO <sub>2</sub>	Thermo/API	10 seconds	$<\pm 12.9\%$

The regulatory air quality analysers of Badhoevedorp, Hoofddorp and Oude Meer are in close proximity to Schiphol airport. A time-series visualisation of these stations for the month December is presented in Figure 2.2. It can be seen that the maximum concentrations for NO<sub>2</sub>, NO and CO are  $\sim 80 \mu\text{g m}^{-3}$ ,  $\sim 125 \mu\text{g m}^{-3}$  and  $\sim 800 \mu\text{g m}^{-3}$ , respectively. Detailed information about the consulted regulatory analysers is presented in Table 2.3.

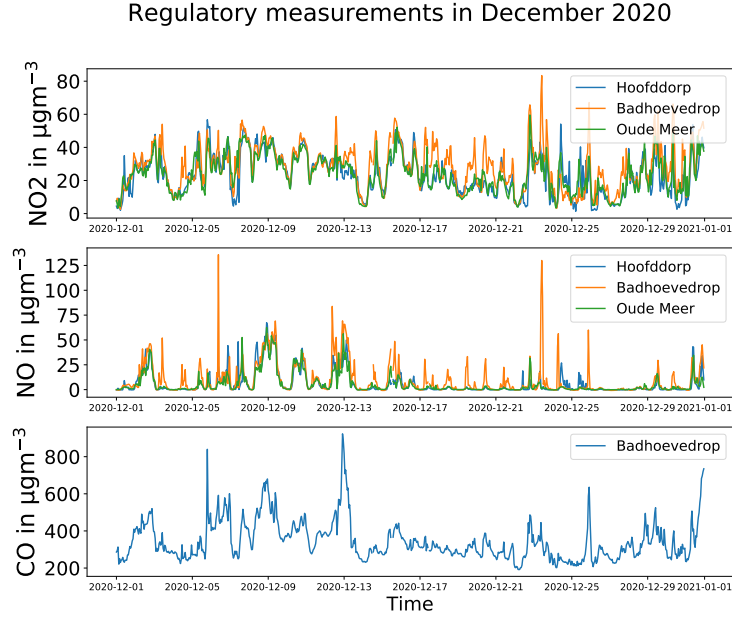


Figure 2.2: Time-series visualisation of regulatory measurements close to Schiphol during December 2020 for NO<sub>2</sub>, NO and CO (hourly averaged).

Table 2.3: Key parameters of the consulted regulatory air quality analysers [15].

Official station name	Station ID	Species	Latitude	Longitude
Hoofddorp-Hoofdweg	NL49564	NO <sub>2</sub> , NO, PM <sub>10</sub>	52°19'38.95"N	4°42'53.90"E
Badhoevedorp-Sloterweg	NL49561	NO <sub>2</sub> , NO, PM <sub>10</sub> , PM <sub>25</sub> , CO	52°20'2.35"N	4°46'26.42"E
Oude Meer-Aalsmeerderdijk	NL49565	NO <sub>2</sub> , NO, PM <sub>10</sub>	52°16'47.84"N	4°46'14.43"E

### Time Notation

The obtained measurements are hourly averages and saved in coordinated universal time format (UTC). Mathematically, this process can be described using Equation 2.8, where  $N_t$  represents the number of samples in the interval  $t - 1$  to  $t$ .

$$X_t = \frac{\sum X_i}{N_t}, \forall i \in [t - 1, t] \quad (2.8)$$

## 2.3. Low-Cost Monitoring

Low-cost air quality monitoring is becoming more and more popular due to the development of novel sensing technologies and improved accuracy. A distinction should be made between commercially available low-cost devices as visualised in Figure 2.3, and low-cost air quality sensors as presented in Figure 2.4. Due to the need for customisation and traceability, a sensor box will be developed from scratch in this thesis. Therefore, only component-level air quality sensors are selected, like the one presented in Figure 2.4.



Figure 2.3: Low-cost air quality monitoring device [13].

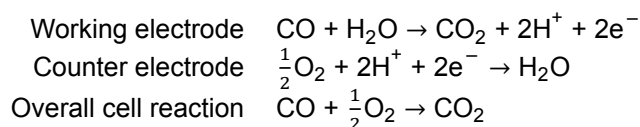


Figure 2.4: Low-cost air quality monitoring sensor [3].

Different types of low-cost air quality sensors exist, based on the used technology. Readily in the literature study these different technologies have been investigated and it could be concluded that electrochemical cell (EC) sensor technology is best-suited for the particular application in this thesis. The main advantages of the EC sensor technology are high sensitivity, improved stability and a ppb-level limit of detection [55]. Based on this information, subsection 2.3.1 presents the working principle of such sensors. Hereafter, subsection 2.3.2 presents performance indicators that can be used to assess sensor performance. Finally, subsection 2.3.3 presents methods for calibrating low-cost EC sensors.

### 2.3.1. Working Principle

Electrochemical gas sensors induce a current that is linearly dependent on the gas concentration. Both three- and four-electrode gas sensors have been developed, which work very similarly. As can be seen in Figure 2.5, a three-electrode gas sensor consists of three electrodes, a gas diffusion barrier, wetting filters and an electrolyte reservoir. The working electrode, kept at a constant potential, is in contact with both the electrolyte and the catalyst, and is the electrode where the electrochemical oxidation or reduction occurs. The electrolyte provides ionic electrical contact between electrodes. The other two electrodes are not exposed to the gas as they are nested deeply into the sensor. The counter electrode balances the working electrode reaction by generating an equivalent current in opposite direction. In the case of carbon monoxide oxidation at the working electrode, the reactions at the two electrodes can be described as follows:



Finally, the reference electrode has been implemented to ensure that the working electrode is kept at the correct potential. The correct potential is that at the diffusion limited plateau of the current voltage curve, as visualised in Figure 2.6. At this plateau, the current is controlled completely by the diffusional flux of the target gas to the working electrode. Newer electrochemical sensor models contain a fourth electrode, the auxiliary electrode (AE). This electrode is exposed to the same ambient conditions as the working electrode, but is not exposed to the gas concentration.

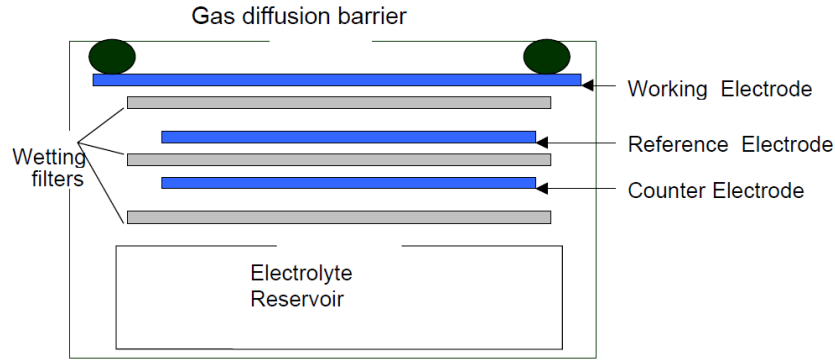


Figure 2.5: Cross section of a three-electrode electrochemical gas sensor [2].

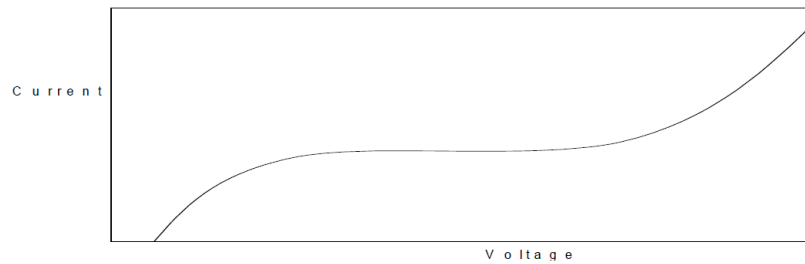


Figure 2.6: Current-voltage curve of an electrochemical gas sensor [2].

Unfortunately, but not surprising, these sensors underperform compared to regulatory monitoring equipment. There are three main issues with this type of technology [72]. First, these sensors do not only respond to the target gas, but also to other gasses. Fortunately, the manufacturer specifies the sensor's sensitivity to other gasses. Secondly, the sensor is sensitive to varying ambient conditions of temperature, pressure and relative humidity. Finally, the sensor response degrades in magnitude over time, implying recalibration is necessary. Not accounting for the aforementioned problems results in an air quality signal that substantially differs from the truth.

### 2.3.2. Performance Indicators

Performance indicators are a necessity to compare the low-cost sensor results with regulatory measurement equipment. Penza [55] presents different key performance indicators. In addition, a performance tier classification is presented in Table 2.4 based on the determination coefficient  $R^2$ .

Table 2.4: Performance tier classification based on determination coefficient [55].

Tier	Description	$R^2$
0	Just don't use it	$0.00 < R^2 < 0.25$
1	Qualitative	$0.25 < R^2 < 0.50$
2	Semi-quantitative	$0.50 < R^2 < 0.75$
3	Reasonably quantitative	$0.75 < R^2 < 0.90$
4	Almost regulatory quality	$0.90 < R^2 < 1.00$

### Mean Bias Error

The mean bias error (MBE) quantifies the average difference between the low-cost sensor measurements  $M_i$  and the reference measurements  $RM_i$  and can be calculated using Equation 2.9 [55]. The number of observations is represented by  $n$ .

$$\text{MBE} = \frac{1}{n} \sum_{i=1}^n M_i - RM_i \quad (2.9)$$

### Mean Absolute Error

The mean absolute error (MAE) quantifies the average absolute difference between the low-cost sensor measurements and the reference measurements and can be calculated using Equation 2.10 [55]. Opposed to the mean bias error, it does not indicate the direction of the error.

$$\text{MAE} = \frac{1}{n} \sum_{i=1}^n |M_i - RM_i| \quad (2.10)$$

### Correlation Coefficient

The correlation coefficient  $R$  quantifies the strength of a linear relationship between two variables [55]. It has a value between -1 and 1, with -1 implying perfect inverse correlation and 1 indicating perfect linear correlation, 0 implies no correlation between the two variables.

$$R = \frac{\frac{1}{n} \sum_{i=1}^n (M_i - \bar{M})(RM_i - \overline{RM})}{\sqrt{\frac{1}{n} \sum_{i=1}^n (M_i - \bar{M})^2 \frac{1}{n} \sum_{i=1}^n (RM_i - \overline{RM})^2}} \quad (2.11)$$

In addition to the correlation coefficient  $R$ , the coefficient of determination  $R^2$  is also frequently used. This metric is the square of the correlation coefficient and ranges between 0 and 1.

### Root-Mean-Square-Error

The root-mean-square-error (RMSE) quantifies the square root of the average squared error, as described by Equation 2.12. Due to the square of the error, it is more sensitive to large errors.

$$\text{RMSE} = \sqrt{\frac{1}{n} \sum_{i=1}^n (M_i - RM_i)^2} \quad (2.12)$$

### Fractional Bias

The fractional bias (FB) quantifies the agreement between low-cost and reference measurements. It can be calculated using Equation 2.13, where a perfect agreement would mean a fractional bias of zero. The mean sensor and reference measurements are indicated by  $\mu_M$ ,  $\mu_{RM}$ , respectively.

$$\text{FB} = \frac{\mu_M^2 - \mu_{RM}^2}{\frac{1}{2}(\mu_M^2 + \mu_{RM}^2)} \quad (2.13)$$

### 2.3.3. Calibration Methods

Ideally, an electrochemical gas sensor takes as input the target gas and returns an output that is linearly dependent on the target gas concentration, as visualised in Figure 2.7. What in reality occurs is that the sensor does not only take the target gas as input, but also its environment including other gasses. The output is then a complex transformation of the different inputs, as visualised in Figure 2.8. In newer electrochemical sensor models, a fourth electrode (auxiliary electrode) has been implemented. This electrode has been nested deeply into the sensor such that it is not exposed to the target gas, resulting in this electrode capturing the effects of varying environmental conditions. In theory, it is then possible to correct the working electrode using the auxiliary electrode by simple subtraction.

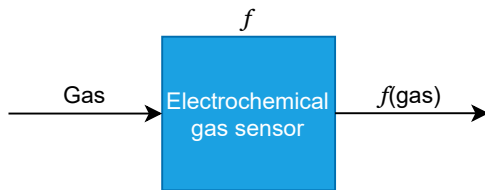


Figure 2.7: Ideal EC gas sensor behaviour.

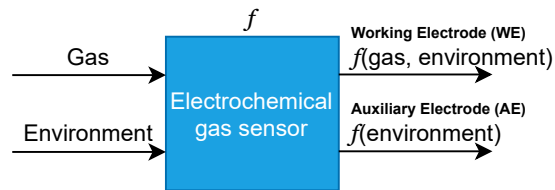


Figure 2.8: Actual EC gas sensor behaviour.

Readily in the literature study, three calibration methodologies are presented of which one is considered to be better than the others. These three different methods each have advantages and disadvantages:

### 1. Correction equations provided by sensor manufacturer

- **PRO:** Simple to implement, implement 4 equations in software;
- **CON:** Based on empirical correction factors only;

### 2. Expose sensor to a calibration gas

- **PRO:** Good calibration if sensor would be used in clean conditions at constant environment;
- **CON:** Not guaranteed to work well when used in varying environment, expensive, cumbersome;

### 3. Collocation with a regulatory monitor & regression

- **PRO:** Good calibration, simple conceptually;
- **CON:** Necessary to have true data, collocation for several days/weeks, more difficult to implement;

The literature study concluded to do a collocated calibration strategy. This decision was based on earlier research in the field of calibration. However, there was no final decision made on which regression methodology to use. The goal is not to select a model upfront. Instead, the goal is to pick several models based on what earlier research has indicated and then implement and evaluate each method.

Mijling et al. [48] use a multilinear regression approach in which they collocate low-cost NO<sub>2</sub> sensors with a reference station for 8 consecutive days. The typical standard deviation was found to be 7 µgm<sup>-3</sup>. Topalović et al. [66] implement and test simple linear regression, multivariate linear regression (MLR) and artificial neural networks (ANN) to calibrate low-cost O<sub>3</sub> and CO sensors. They conclude that even simple MLR models are able to provide good accuracy, as also concluded by Mijling et al. [48], but that the ANN models are better. More specifically, ANNs improved the median of the correlation coefficient and reduced the interquartile distance of the NRMSE (Normalised Root-Mean-Square Error).

Random forest (RF) regression has been applied by Wang et al. [70] on a low-cost indoor PM<sub>2.5</sub> monitor. They test this RF model against a linear regression model and conclude that RF calibration results in a higher correlation with regulatory measurements. The features apart from the measurements are temperature and relative humidity.

Wesseling et al. [71] collocate eight NO<sub>2</sub> sensors for several weeks with official equipment. They use a multivariate linear regression approach that results in correlation coefficients above 0.95 for each sensor. Moreover, they highlight the need for frequent recalibration as some sensors suffer from drift and sensitivity changes.

## 2.4. Air Quality Impacts from Aviation Activities

In this section, the air quality impacts from aviation activities are discussed. First, subsection 2.4.1 presents the use of emission indices for pollution quantification. Hereafter, subsection 2.4.2 makes the distinction between landing and take-off operations (LTO) and cruise flight. Next, aircraft exhaust emissions are explained in subsection 2.4.3, followed by aircraft non-exhaust emission in subsection 2.4.4. Hereafter, subsection 2.4.5 discusses emissions related to airport activities. Finally, subsection 2.4.6 presents the final chemical species selection based on the different emission classes.

### 2.4.1. Emission Index

The emission index (EI) represents the mass of a species produced per kilogram of fuel used. The emission index varies per engine regime, i.e. take-off, climb, approach and taxi. The emission indices of three commonly used jet engine models at Schiphol airport are presented in Figure 2.9, Figure 2.10, Figure 2.11 and Figure 2.12.

From these figures, it can be concluded that at lower thrust settings, i.e. idle and approach, elevated hydrocarbon, non-volatile PM and CO concentrations are expected. At high thrust settings such as take-off and climb-out, higher NO<sub>x</sub> concentrations should be observed. The time-in-modes and thrust settings for different aircraft operating modes are reported in Table 2.5.

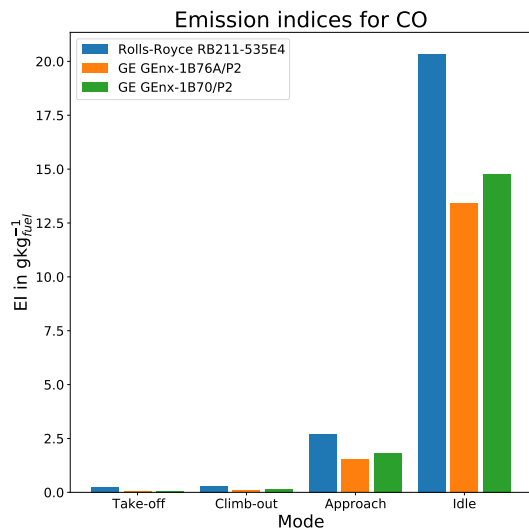


Figure 2.9: CO EI for common engines.

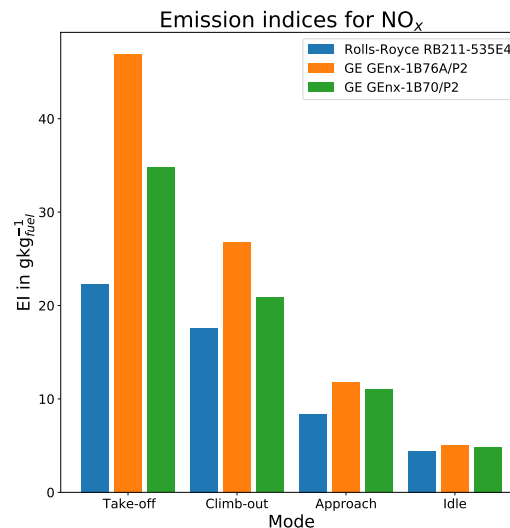
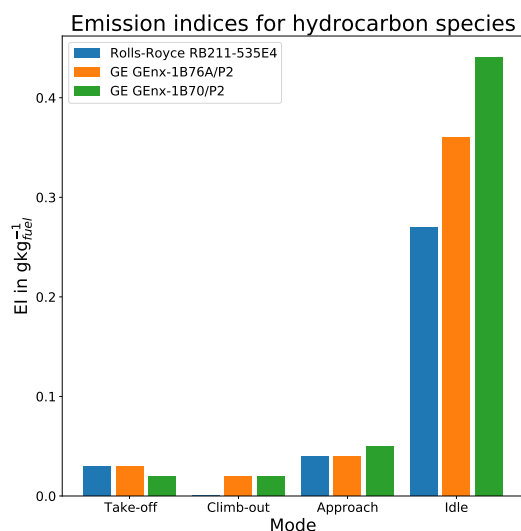
Figure 2.10: NO<sub>x</sub> EI for common engines.

Figure 2.11: Hydrocarbons EI for common engines.

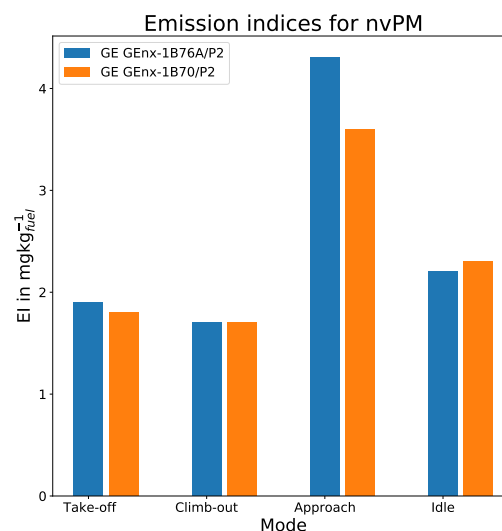


Figure 2.12: Non-volatile PM EI for common engines.

### 2.4.2. Landing and Take-off Operations versus Cruise Flight

The research scope is limited to emissions during landing and take-off operations, which are all flight activities below 3,000 feet. The LTO cycle contains four operating modes, taxi, approach, take-off and climb. Each operating mode has received a time-in-mode and thrust setting, which should be a good representation of the actual thrust settings and time-in modes. Schematically, the LTO cycle is visualised in Figure 2.13 along with the reported time-in-modes and thrust settings in Table 2.5. As readily mentioned in the introduction, Chati and Balakrishnan [28] report deviations as high as ~40% from the actual thrust settings. Moreover, emission indices for thrust reversal are not included in airport emission inventories but are estimated to account for 15% or more of the on-airport NO<sub>x</sub> [18].

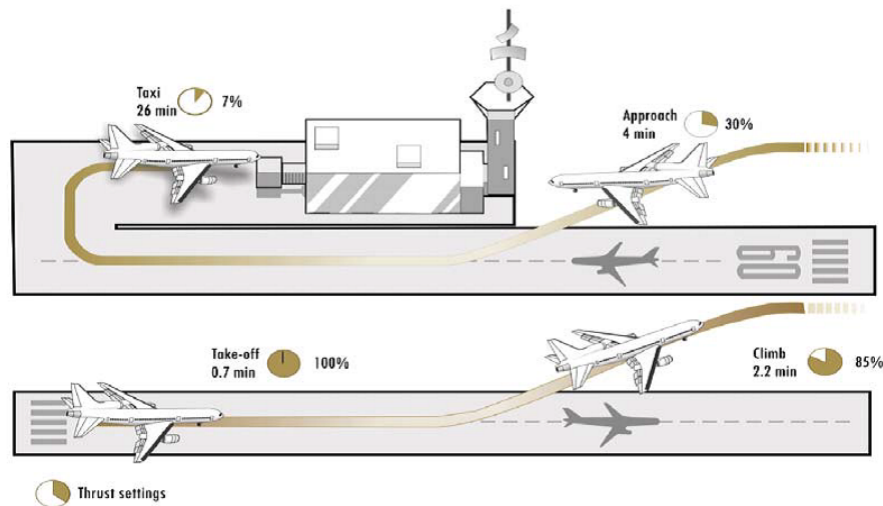


Figure 2.13: Illustration of aircraft activities in the LTO phase [14].

Similarly to the emission indices, the fuel used during combustion can be obtained for most jet engines using ICAO's aircraft engine emissions data bank [12]. In Figure 2.14, the LTO fuel use of three common engine models is presented. Dependent on the aircraft operating mode, different values for the fuel flow are observed, as can be seen in Figure 2.15.

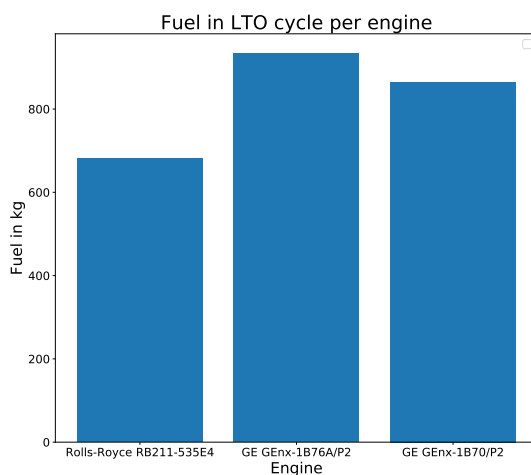


Figure 2.14: Fuel in LTO cycle for common engines.

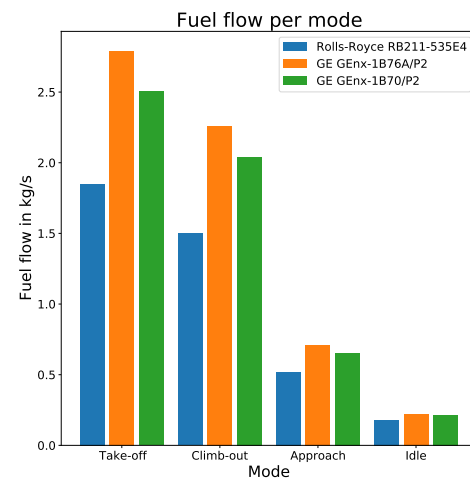


Figure 2.15: Fuel flow for common engines.

Table 2.5: Emission indices during different aircraft operating modes as defined by ICAO [14].

Mode	Thrust setting (%)	Time-in-mode (min)
Taxi	7	26
Approach	30	4
Climb	85	2.2
Take-off	100	0.7

### 2.4.3. Exhaust Emissions

The combustion of a hydrocarbon fuel requires oxygen. When there is precisely enough oxygen to fully burn the fuel, the quantities are stoichiometric. If there is more fuel in the mixture than oxygen neces-

sary, the mixture is called rich. In contrary, when there is more oxygen than fuel, the mixture is called lean. The ratio of fuel and air at stoichiometric proportions is called the fuel-to-air ratio ( $FAR_{stoich}$ ). To express whether a mixture is rich, lean or stoichiometric, the equivalence ratio  $\Phi$  has been defined. It is defined as the ratio of the fuel-to-oxidiser ratio to the stoichiometric fuel-to-oxidiser ratio, as presented in Equation 2.14.

In the case of jet engine operations, the jet engine combustion equation described by Equation 2.15 leads to the discharged emissions. This is visually presented in Figure 2.17. The emissions discharge for different species for different combustion regimes is presented in Figure 2.16.

$$\Phi = \frac{\dot{m}_f}{\dot{m}_{air}} \frac{1}{FAR_{stoich}} \quad (2.14)$$

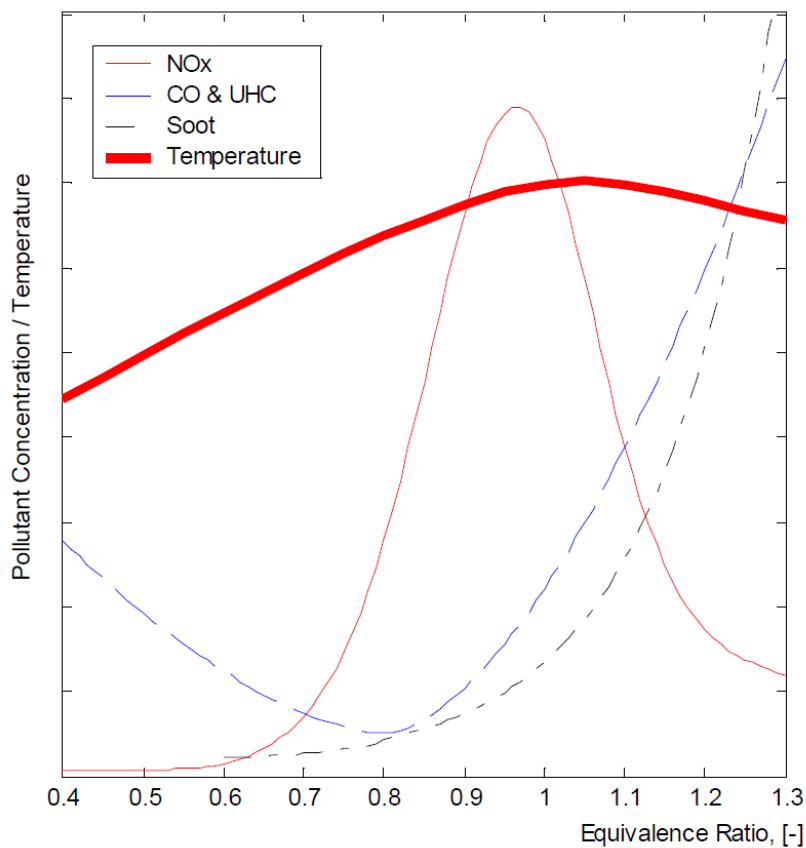
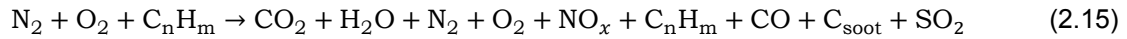


Figure 2.16: Emissions discharge versus combustion regime [39].

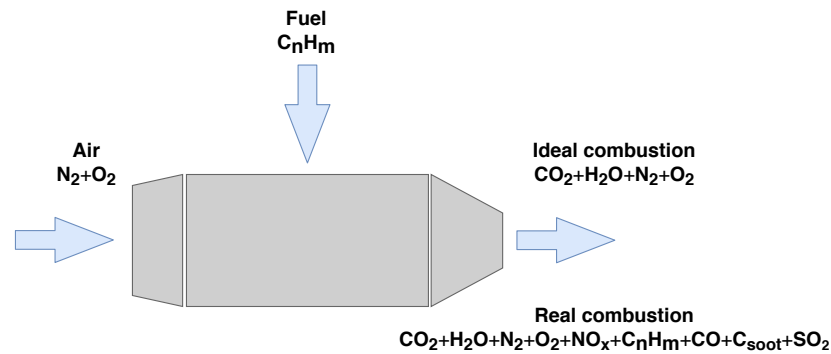


Figure 2.17: Ideal and real jet engine combustion.

Water vapour ( $H_2O$ ), carbon dioxide ( $CO_2$ ), dinitrogen ( $N_2$ ) and dioxygen ( $O_2$ ) are emitted in high quantities. They are however not considered air pollutants as they do not cause direct harm. The literature study addressed the different air pollutants in-depth. In Table 2.6, a summary is given of these air pollutants as well as their dependencies. The combustion equation presented in Equation 2.15 includes  $C_nH_m$  and  $C_{soot}$ .  $C_nH_m$  is included in the hydrocarbon species (HC),  $C_{soot}$  is part of particulate matter.

Table 2.6: Key air pollutants that are directly released or secondary formed from commercial jet aircraft emissions.

Species	Origin	Dependencies	Source
$O_3$	Reaction between $NO_x$ , VOCs and sunlight	VOCs, CO, sunlight	Finlayson-Pitts and Jr [32]
CO	Product of incomplete combustion	Inverse with T	Masiol and Harrison [43]
$NO_2$	Byproduct of combustion, fuel impurities	T, fuel nitrogen content	EPA [31]
NO	Byproduct of combustion, fuel impurities	T, fuel nitrogen content	EPA [31]
$SO_2$	Fuel impurities	Fuel sulphur content	Hunton et al. [37]
$SO_4$	Fuel impurities	Fuel sulphur content	Hunton et al. [37]
VOC	Product of incomplete combustion	-	Zhang et al. [76]
PM	Primary and secondary formation via combustion	T	Robinson et al. [60]
HC	Product of incomplete combustion	-	Masiol and Harrison [43]

Reverse thrust can be used as a braking aid during roll-out after touchdown or for taxiing the aircraft backwards i.e. powerbacking. An analysis spanning 655 landings at several US airports concluded that average thrust reversal use during landing equals approximately 16 seconds [18]. Classification of thrust reversal use by aircraft type is visualised in Figure 2.18. In addition, 79 power-back manoeuvres at Austin-Bergstrom International Airport were timed, leading to the distribution presented in Figure 2.19 [18]. The mean duration is 43.8 seconds with a standard deviation of 5.5 seconds.

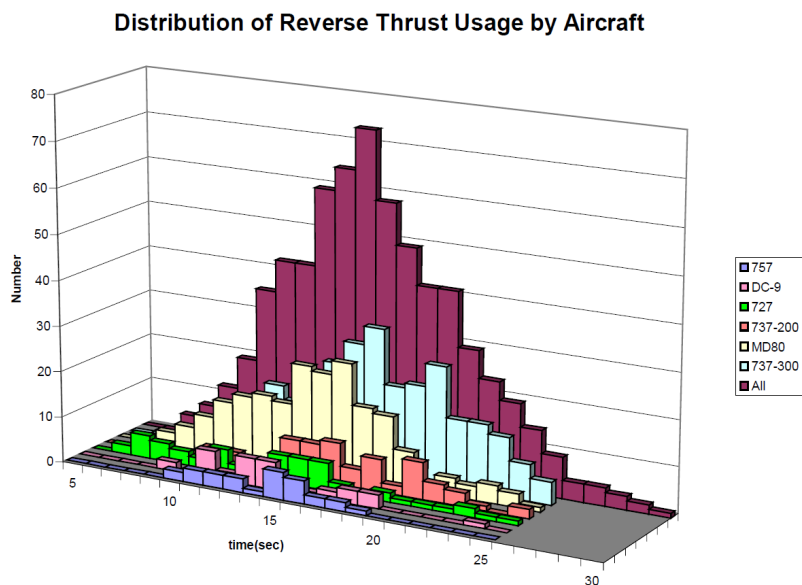


Figure 2.18: Thrust reversal use during landing [18].

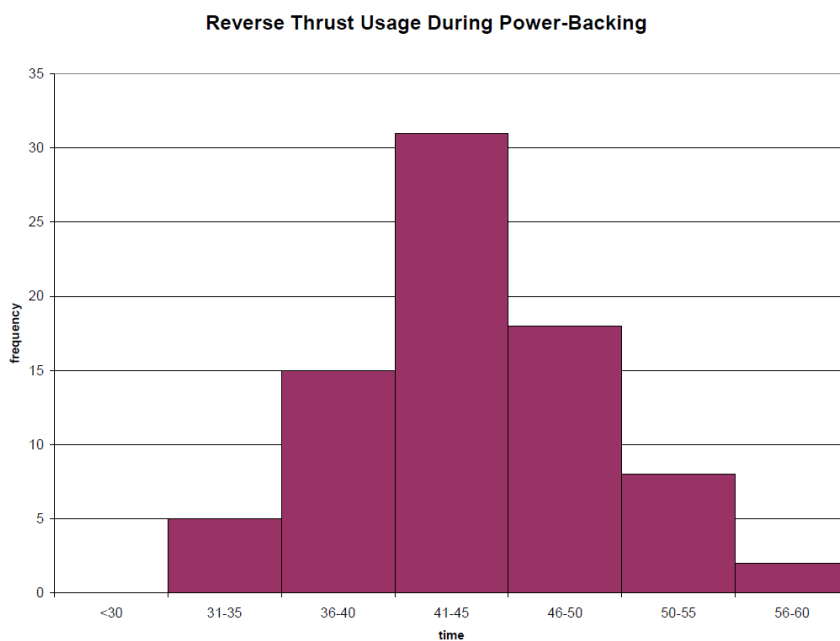


Figure 2.19: Thrust reversal use during power-backing [18].

### 2.4.4. Non-Exhaust Emissions

Non-exhaust emissions have been investigated by Masiol and Harrison [43]. These emissions are less abundant and have a different pollution signature, though these emissions impact local air quality. Sources of non-exhaust emissions include auxiliary power units (APUs), ground power units (GPUs), undercarriage erosion, oil leaks and airframe corrosion [43]. The emissions of APUs and GPUs are addressed in subsection 2.4.5 as they are more relevant to airport related emissions.

Aircraft tyre mass is lost every LTO cycle. The rotational inertia of the tyres causes friction between tyres and the runway leading to tyre particles being scraped off. These particles then either fall immediately to the ground or become airborne, dependent on their weight, constituting to particulate matter. A technical study conducted by British Airways has investigated the mass lost per flight for different aircraft types [6]. In the most extreme case, ~800 grams of total tyre mass is lost per landing of a

B747-400.

Brake wear due to stopping the aircraft on taxiways and during roll-out after landing impacts brake linking material of brake discs and pads. Garg et al. [33] have conducted a brake wear analysis and conclude that 35% of the suspended mass is in the form of airborne PM. Moreover, they find that 86% of the airborne PM is smaller in diameter than 10  $\mu\text{m}$  and 63% smaller than 2.5  $\mu\text{m}$ . Airframe corrosion has been observed by Amato et al. [25] at Barcelona El Prat airport, Spain. They deploy a laser-spectrometer at the airport and find a strong presence of 5-25  $\mu\text{m}$  thick micro-flakes of aluminium, presumable from the airframe.

Oil may vaporise or burn from lubricated aircraft parts. Yu et al. [75] investigate the contribution of oil leaks to PM concentrations. At idle, the emission index of lubrication oil is in the range 2-12 mg (kg Fuel)<sup>-1</sup>. Also, they find that engine thrust does not affect the composition of air-suspended oil droplets.

### 2.4.5. Airport Related Emissions

Finally, airport related emissions impact local air quality. This includes APU and GPU use as mentioned before, but also ground service equipment (GSE).

The emissions of APUs cannot be neglected due to the long run times [61]. More specifically, APUs are responsible for ~40-50% of total GSE emissions in terms of CO and NO<sub>x</sub>. Ratliff et al. [58] investigate emissions at 325 US airports using the Emission and Dispersion Modelling System (EDMS) provided by the FAA. They estimate that APU use is responsible for ~5-25% of CO, VOCs, NO<sub>x</sub>, SO<sub>x</sub> for emissions below 3,000 feet.

GSE are motorised vehicles in and around the airport which includes taxis, private cars, shuttle busses, trucks and towing vehicles. Specific emissions are hard to pinpoint to such vehicles as they are a large group of different vehicles. Moreover, type of motorisation and fuel used are important considerations. In the current situation, most GSE are equipped with diesel or gasoline engines, having similar characteristics as road-traffic emissions. SO<sub>2</sub> and SO<sub>4</sub> emissions from GSEs are negligible compared to aircraft emissions [63]. On the other hand, organic carbon (OC) emissions play a significant role, with contributions around ~66% from GSE. A study by Nambisan et al. [50] concerning McCarran airport, US, indicates that GSE emissions are accountable for ~60% of the total airport emissions. Both NO and NO<sub>2</sub> concentrations are found in GSE traffic paths, but CO emissions are dominated by aircraft movement on the tarmac [62]. A similar study carried out by Unal et al. [67] at Atlanta international airport, US, concludes that the calculated impact of O<sub>3</sub> and PM<sub>2.5</sub> are 2 ppb and 9  $\mu\text{g m}^{-3}$ , respectively.

### 2.4.6. Final Selection of Chemical Species to be Measured

Based on the exhaust, non-exhaust and airport related emissions, presented in subsection 2.4.3, subsection 2.4.4 and subsection 2.4.5, respectively, a final selection of chemical species to be measured is presented in Table 2.7. Along with this final selection, a concise argumentation is given on why these species are of interest.

Table 2.7: Final chemical species selection.

Abbreviation	Full name	Argumentation
O <sub>3</sub>	Ozone	Forms via the reaction of NO <sub>x</sub> , VOCs and sunlight
NO <sub>2</sub>	Nitrogen dioxide	Byproduct of combustion, product of fuel impurities
NO	Nitric oxide	Byproduct of combustion, product of fuel impurities
SO <sub>2</sub>	Sulphur dioxide	Product of fuel impurities
CO	Carbon monoxide	Product of incomplete combustion
VOC	Volatile organic compounds	Product of incomplete combustion, forcer of ozone
PM	Particulate matter 2.5 and 0.1 $\mu\text{m}$	Primary and secondary formation via combustion
HC	Hydrocarbons; formaldehyde	Product of incomplete combustion

## 2.5. Aircraft Activity Data

Keeping track of aircraft activity while simultaneously sampling air quality enhances the detection of aviation-attributable pollution. The temporal resolution of such aircraft activity data should be high enough to facilitate the detection of short-term impacts from aircraft. First, subsection 2.5.1 presents

how sound data can assist. Hereafter, subsection 2.5.2 discusses the potential of automatic dependent surveillance - broadcast (ADS-B) data.

### 2.5.1. Sound Measurements

Noise data can be used to link elevations in pollutant concentrations to aircraft activity. For example, sound intensity can be sampled while simultaneously monitoring air quality. Ideally, peaks in sound intensity correspond to nearby aircraft activity.

The type of aircraft activity, i.e. take-off, landing, approach or taxi determines the emission signature, as presented in subsection 2.4.3. Merino-Martinez et al. [47] propose a methodology to estimate the fan rotational speed N1%, which is linked to the thrust setting. They estimate the blade passing frequency by analysing the tonal peak. As experimental set-up, they use a NOMOS system that continuously measured the noise, using a set of microphones.

### 2.5.2. ADS-B Data

ADS-B data is a means of surveillance data in which aircraft determine their position via satellite navigation and periodically broadcast it [5]. A schematic representation of the working principle is provided in Figure 2.20. Automatic dependent surveillance - broadcast is based on the following principles:

- **Automatic:** no pilot or external input necessary;
- **Dependent:** data depends on aircraft navigational system;
- **Surveillance:** received by ATC but also by other aircraft to have situational awareness and self-separation;
- **Broadcast:** the data is broadcast periodically;

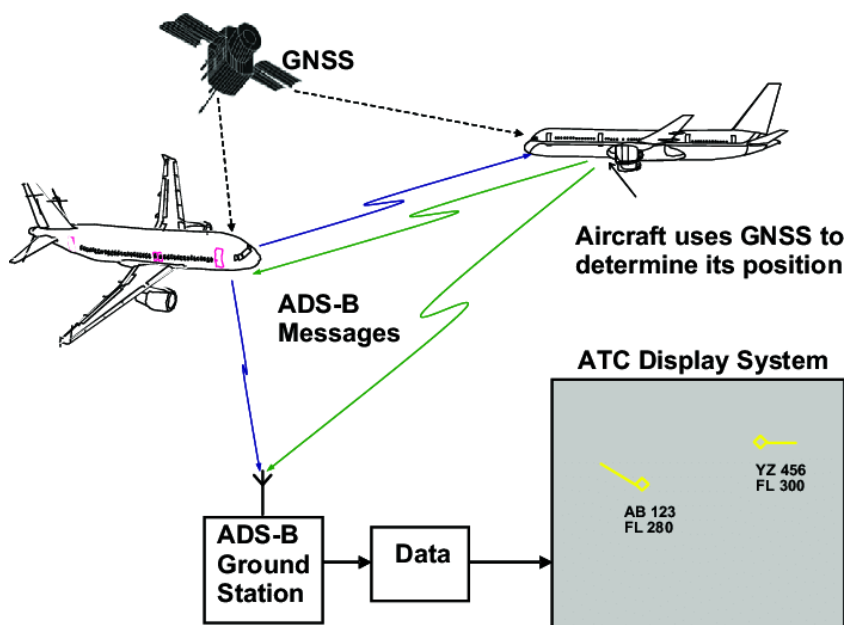


Figure 2.20: Schematic representation of ADS-B working principle [4].

The data derived from the ADS-B messages generally contain position, velocity and an identity, coupled to a timestamp. Each aircraft is associated with a unique 24-bit address, often referred to as the ICAO24 address, which is represented by a 6-character hex code [17]. The high-temporal resolution of ADS-B data makes it an excellent candidate to assist in the detection of aviation-attributable pollution signals. There are however two considerations. First, the received ADS-B data should be accurate. The accuracy depends on the aircraft navigation system as this is where the ADS-B information is taken from. Secondly, the ADS-B data should be complete. Not all aircraft are fitted with ADS-B transponders.

In addition, it can be that the signal is broadcast, but that the receiver does not pick up anything. In these cases, it becomes impossible to link aircraft activity to air quality impacts using ADS-B.

# 3

## Sensor Box Design, Development and Integration

The sensor box will be deployed near Amsterdam Schiphol airport with the aim to quantify air quality impacts from individual aircraft. Due to these very specific needs, the sensor box will be developed from scratch in order to maximise the chances of succeeding. Therefore, a large amount of time and effort has been spent on the design, development and integration of the sensor box.

First, section 3.1 presents the sensor box design methodology. Secondly, section 3.2 covers the development of both the hard- and software side. Next, two preliminary sensor box tests are presented in section 3.3. Finally, battery performance is evaluated in section 3.4.

### 3.1. Sensor Box Design

The sensor box design addresses all the necessary steps before the actual production process. First, subsection 3.1.1 presents the necessary criteria for design. Hereafter, the sensor selection process is described in subsection 3.1.2. Finally, a conceptual design is presented in subsection 3.1.3 based on the design criteria and the selected sensors.

#### 3.1.1. Design Criteria

No design criteria were specified at the start of this thesis. Instead, several design criteria could be derived from the research objective presented in chapter 1.

Based on the thesis objective, the following requirements are established:

1. **The utilised gas sensors shall be of the low-cost type;** No formal definition is given about what is considered low-cost and what is not. To avoid misinterpretation, only sensors are considered of the following type: electrochemical, spectroscopic, non-dispersive infrared, photoionization detector, optical particulate counters, metal oxides and pellistors, as these are generally low-cost sensing technologies [55].
2. **The utilised gas sensors shall resemble multiple air pollutants;** This requirement has been implemented as air pollution due to aviation activities can be linked to multiple chemical pollutant species.
3. **The utilised gas sensors shall focus on air pollution quantification from aviation activities;** This requirement mandates the use of sensors that are in line with the expected pollutant species from aviation activities.
4. **The sensor box shall be operable near Schiphol airport;** More specifically, this means that the operating limits of the sensor box, such as temperature, pressure and humidity, should be so that it can be operated near Schiphol airport. In addition, given that the sensor box will be operated near Schiphol airport, an alternative for grid power is required.

### 3.1.2. Sensor Selection

In this subsection, the selected sensors are presented and described.

#### Low-Cost Gas Sensors

Initially, four electrochemical sensors of the brand Alphasense are selected, capable of measuring NO, NO<sub>2</sub>, CO and O<sub>x</sub>. These sensors are chosen as they proved to be reliable in previous studies, as carried out by Borrego et al. [27] and Popoola et al. [56] for example. In addition, sticking to a single manufacturer reduces compatibility issues but potentially leads to the selection of sub-optimal sensors.

An in-depth search spanning 39 manufacturers towards the most optimal sensor configuration to monitor air quality near the airport has been performed in the literature study. Implementing sensors from this iterated sensor selection will be done only when deemed necessary. Key parameters of the currently implemented low-cost gas sensors are presented in Table 3.1.

Table 3.1: Low-cost gas sensor selection and specifications.

Species	NO	NO <sub>2</sub>	O <sub>x</sub>	CO
Sensor name	NO-B4	NO2-B43F	OX-B431	CO-B4
<b>Performance</b>				
Sensitivity (nA/ppm)	500/850	-200/-650	-225/-750	420/650
Response time t <sub>90</sub> (s)	<45	<80	<80	<30
Zero current (nA @ 20°C)	30/200	-80/80	-80/80	30/-250
Noise (ppb)	15	15	15	4
Range (ppm)	20	20	20	1000
Linearity (ppb at full scale)	<±1	<±0.5	<±0.5	20/35
Overgas limit (ppm)	50	50	50	2000
<b>Lifetime</b>				
Zero drift (ppb)	0/50	0/20	0/20	<±100
Sensitivity drift (%change/year)	0/-20	-20/-40	-20/-40	<10
Operating life (months to 50% signal)	>24	>24	>24	>36
<b>Environmental</b>				
Sensitivity @ -20 °C (% output @-20 °C/output @20 °C)	60/90	60/80	70/90	40/70
Sensitivity @ 50 °C (% output @50 °C/output @20 °C)	97/110	65/110	95/125	110/125
Zero @ -20 °C (nA)	0/30	0/25	0/25	-30/30
Zero @ 40 °C (nA)	100/200	-10/50	5/100	-50/-200
<b>Key Specifications</b>				
Temperature range (°C)	-30/40	-30/40	-30/40	-30/50
Pressure range (kPa)	80/120	80/120	80/120	80/120
Humidity range (% RH)	15/85	15/85	15/85	15/90
Storage period (months, sealed)	6	6	6	6

#### Other Sensors

Three additional sensors have been added to the sensor selection for multiple reasons.

First, a barometric sensor measuring temperature, pressure and humidity has been added to the configuration [19]. It allows correcting the sensor response for temperature, pressure and humidity variations, as readily investigated by Mead et al. [46], Penza [55] and Borrego et al. [27]. The barometric sensor and its specifications are presented in Figure 3.1 and Table 3.2 respectively.

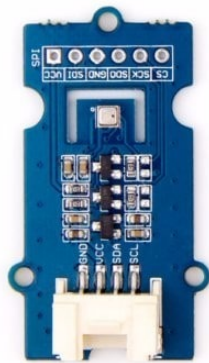


Figure 3.1: Barometer sensor [19].

In addition, a sensor measuring UV-light, visible light and infrared light has been added to the configuration as O<sub>3</sub> formation occurs via the reaction between NO<sub>x</sub>, VOCs and sunlight [10, 69]. Using the NO<sub>x</sub>, light and O<sub>3</sub> signals, it might be possible to observe delayed O<sub>3</sub> formation. The light sensor and its specifications are presented in Figure 3.2 and Table 3.3 respectively.

Table 3.2: Barometer sensor specifications [19].

Parameter	Value
Input voltage	3.3 V or 5 V
I/O voltage	3.3 V or 5 V
Operating current	0.4 mA
Operating temperature	-40 - 85°C
Pressure sensor range	300 - 1100 hPa
Pressure sensor accuracy	± 1.0 hPa
Temperature sensor range	-40 - 85°C
Temperature sensor accuracy	± 1.0°C
Humidity sensor measurements	0% - 100%
Humidity sensor accuracy	± 3.0%
Chip	BME 280
Dimensions	40 mm x 20 mm



Figure 3.2: Light sensor [10].

Table 3.3: Light sensor specifications [10].

Parameter	Value
Operating voltage	3 V - 5.5 V
Operating current	3.5 mA
Wave length	280-950 nm
Operating temperature	-45 - 85°C

Finally, a sound intensity sensor is added to the configuration [11]. The role of this sensor is to enhance the detection of aviation-attributable air quality impacts. The sound intensity sensor and its specifications are presented in Figure 3.3 and Table 3.4 respectively.



Figure 3.3: Sound intensity sensor [11].

Table 3.4: Sound sensor specifications [11].

Parameter	Value
Operating voltage	5 V
Operating current (@5V)	4.5 mA
Voltage gain (V=6V, f=1kHz)	26 dB
Microphone sensitivity (1kHz)	52-48 dB
Microphone impedance	2.2 kΩ
Microphone frequency	16-20 kHz
Microphone S/N Ratio	54 dB
Dimensions	24 mm x 20 mm x 9.8 mm

### 3.1.3. Conceptual Design

A conceptual design has been developed using the aforementioned sensor selection, visually presented in Figure 3.4. Several elements in Figure 3.4 have not yet been introduced. First, at the core of the sensor box is the microcontroller which connects with all sensors, provides power to the sensors and extracts their signals. The sensor box signals cannot be stored on the microcontroller so therefore an external memory is added. Finally, a PC datalink with the microcontroller is necessary to upload the sensor box operating code. The air quality sensor array consists of the four selected gas sensors. The weather sensor array contains the light and barometric sensor. Finally, the aircraft activity sensor array is simply the sound intensity sensor.

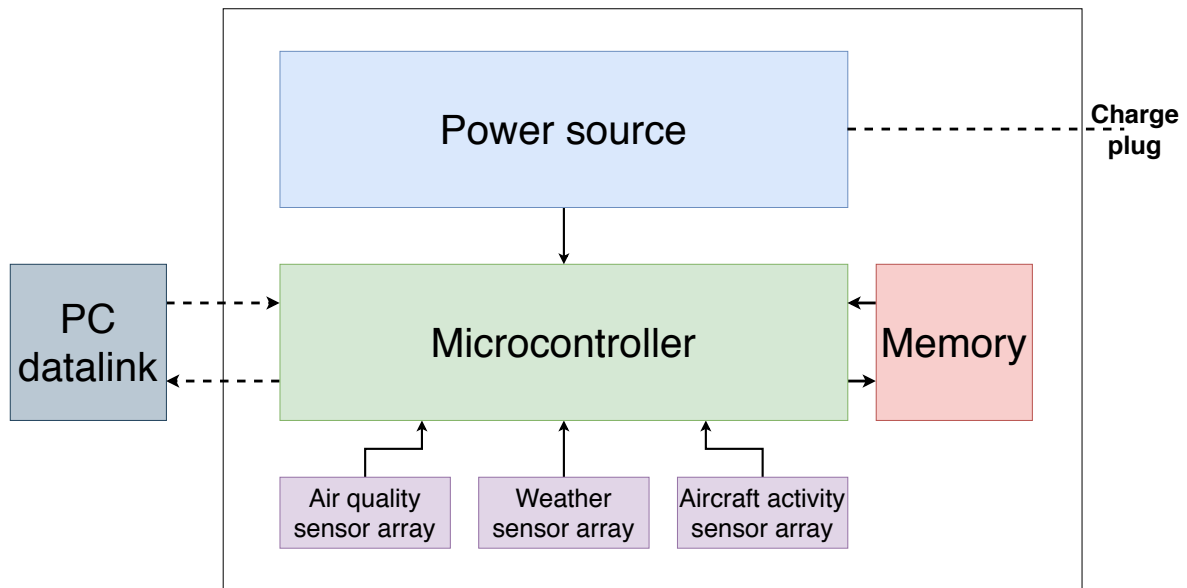


Figure 3.4: Conceptual sensor box design.

Both a Raspberry Pi and an Arduino have been considered as microcontrollers. The Raspberry Pi is more powerful in terms of memory and clock speed. The Arduino's simple structure however makes it harder to break. In addition, the analogue capability of the Arduino, which the Raspberry Pi lacks, is a strong advantage. For this reason, the Arduino Uno Rev 3 is selected as a suitable microcontroller. A full list with the differences between the Arduino and the Raspberry Pi is disclosed in Table B.1.

## 3.2. Sensor Box Development

The sensor box development process presents how the different components are combined in an iterative process to come up with the final design. Two major sensor box iterations have been performed leading to three different designs along the way. Additional components are presented in subsection 3.2.1. Hereafter, the first sensor box prototype is presented in subsection 3.2.2. A first iteration leads to the design presented in subsection 3.2.3. A second smaller iteration leads to the design presented in subsection 3.2.4. Finally, subsection 3.2.5 presents the operating procedures and the developed sensor box code.

### 3.2.1. Components

Several additional components have been suggested and added by TU Delft's DEMO (Dienst Elektronische en Mechanische Ontwikkeling) to ensure proper working of the sensor box. The real-time clock (RTC), secure digital (SD) card reader, analog-to-digital converters (ADCs) and individual sensor boards (ISBs) are crucial components.

#### Real-Time Clock

The Arduino is not able to measure time by itself, and thus the addition of a real-time clock (RTC) is necessary. The RTC is a PCF8523 and is powered by a GP-CR1220 3 V button cell battery. This RTC is included in the Adafruit Assembled Data Logging shield, visualised in Figure 3.5. The time indicated by the RTC drifts slowly over time and therefore frequent recalibration is necessary to avoid large time differences. Figure 3.6 displays how the RTC is integrated in the developed sensor box.

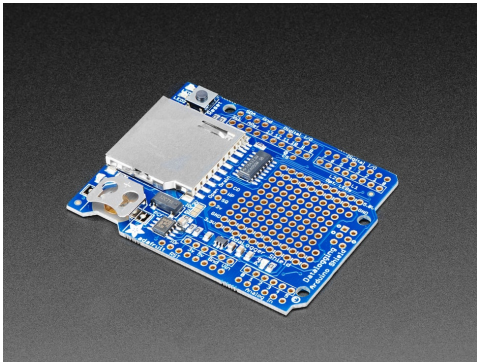


Figure 3.5: Adafruit data logging shield [38].

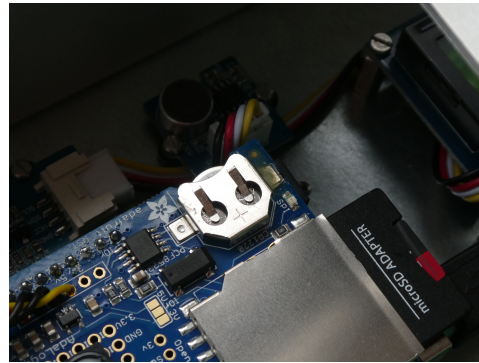


Figure 3.6: RTC mounted on Adafruit data logging shield.

### SD Card Reader

The SD card reader and writer is used to store the timestamped data returned by the Arduino. A more advanced option would be to transmit the data via a wireless connection, however for simplicity the SD card reader is chosen. Also this module is not bought separately but is included in the Adafruit Assembled Data Logging shield. The utilised microSD is a Transcend 16 GB Premium 400x Class 10 UHS-I.

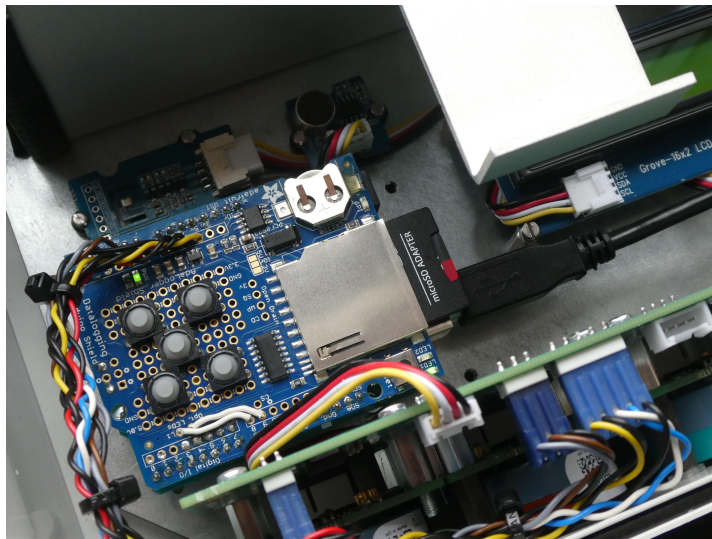


Figure 3.7: SD card reader mounted on Adafruit data logging shield.

### Analog-to-Digital Converters

Analog-to-digital converters (ADCs) have been implemented to convert the analog air quality signals - which are voltages - into a digital signal. These ADCs are of the type MCP3423, which are 18-bit delta-sigma signal converters, as can be seen in Figure 3.8. The full voltage range is 4.096 V at 18-bits resolution so that results in  $4.096/2^{18}$  volt per bit. Conversion from analog to digital can be performed continuously or one-shot, i.e. at the moment of request. One-shot conversion is implemented in the operating code as this results in a lower power consumption.

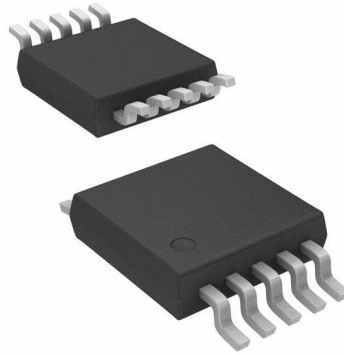


Figure 3.8: MCP3423 ADC as a component [16].

### Individual Sensors Boards

The individual sensor boards (ISBs) are designed by Alphasense and function as potentiostats. These boards maintain the potential of the working electrode at a constant level with respect to the reference electrode by altering the current of the counter electrode. The ISB configuration is dependent on the target gas species. Figure 3.9 visualises the ISB as a component, Figure 3.10 presents how the ISB is integrated with the PCB and gas sensors.



Figure 3.9: ISB as a component [1].



Figure 3.10: ISB in sensor box assembly.

### Push Buttons

Five programmable push buttons are added to the sensor box. These buttons are programmed to start and stop the measurements. Figure 3.7 presents these five buttons.

### Liquid Crystal Display (LCD)

A LCD has been added for visual inspection by the user. The screen is a 16x2 black on yellow LCD of the brand Grove, as can be seen in Figure 3.11. The backlight of the LCD has been disabled to minimise power consumption.

### Printed Circuit Board (PCB) to Dock ISBs

DEMO has developed their own PCB to host the different ISBs of the different air quality sensors. This leads to a significant reduction in necessary wire length, which reduces the electrical noise. A sketch of this PCB is presented in Figure B.1 in Appendix B.

### 3.2.2. Version 1: Sensor Box without Casing

The sensor box initially consists of a metal sheet with the individual components mounted on top, as presented in Figure 3.12. Unfortunately this had several drawbacks. First, there is no protection



Figure 3.11: LCD with text printed on the display.

against precipitation, which is unwanted as electronics and water do not mix well. Secondly and most importantly, it was observed that sudden temperature changes - as caused by a blowing wind or a sudden change in UV light - would induce unwanted transients in the sensor outputs. As presented in subsection 3.2.3, a casing solves this problem.

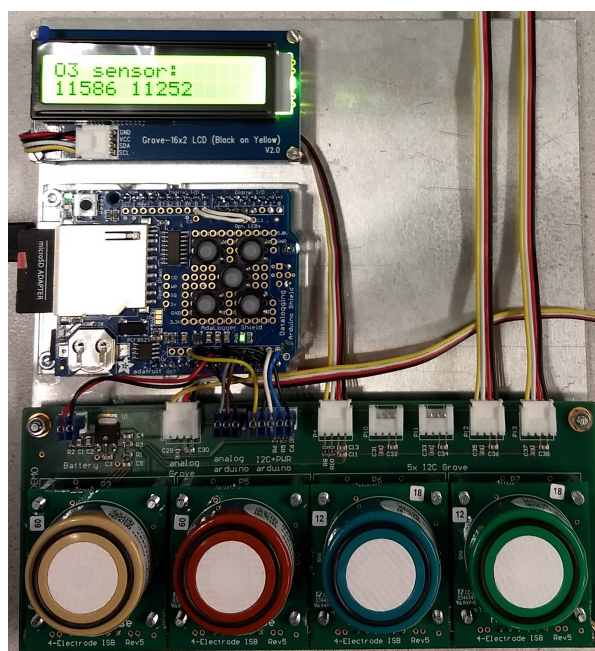


Figure 3.12: Sensor box without casing.

### 3.2.3. Iteration 1: Sensor Box with Open Casing

A first iteration results in the addition of a casing, as can be seen in Figure 3.13. The airflow can be controlled via a small plate in front of the gas sensors. This design results in less temperature variations as the sensors are now encapsulated by a waterproof box. Certainly, the airflow control plate influences the obtained results, but it is uncertain to which extent. Therefore, the plate is set to maximum opening in all the experiments unless stated otherwise.



Figure 3.13: Sensor box with open casing.

This design functions well when there is no precipitation. However, during calibration via collocation in which the sensor box is exposed to the outdoor environment for a prolonged period, water may enter the gas sensing holes, damaging the sensors.

#### 3.2.4. Iteration 2: Sensor Box with Waterproof Casing

Given that the first iteration is not sufficient to prevent water from entering the gas sensor holes, a second iteration is required. The second iteration only has minor impact on the sensor box design compared to the first iteration, as can be seen in Figure 3.14. A small encapsulation has been added to the readily existing airflow control plate to prevent water absorption. Moreover, several holes have been drilled in the outer shell of the casing to facilitate zip ties for easily mounting.



Figure 3.14: Sensor box with waterproof casing.

The internal lay-out of the sensor box is modified during the first iteration but is unaffected in the second iteration. A graphical representation of the sensor box internal lay-out is presented in Figure 3.15.

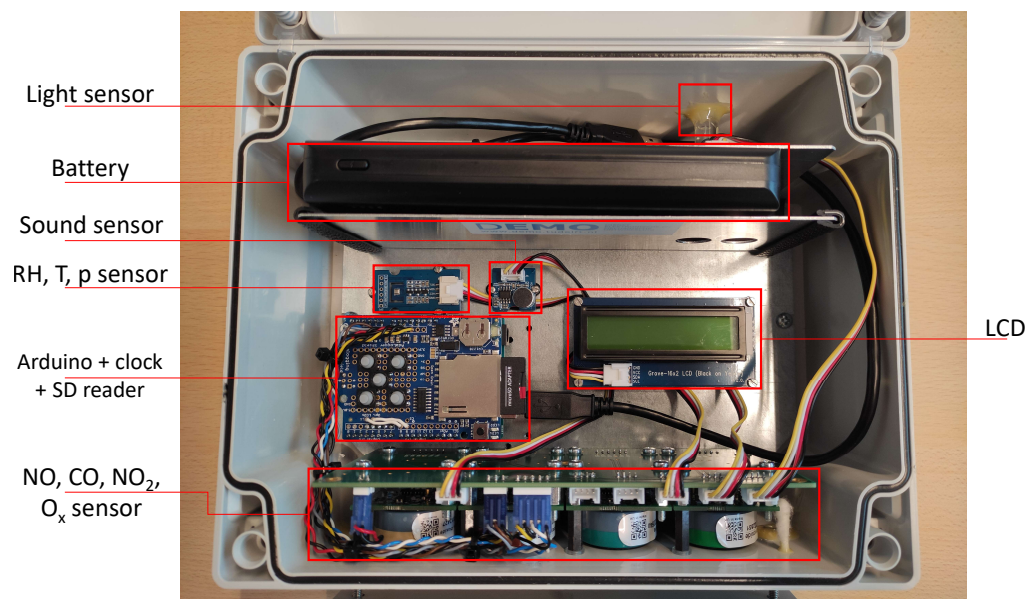


Figure 3.15: Internal lay-out of the final sensor box.

### 3.2.5. Operating Procedures and Code

Use has been made of the Arduino programming language to transform the connected hardware into a scientific instrument. It has been designed with the intent to be easy to use and fault tolerant. The sensor box operating procedures and code are presented in Appendix H.

## 3.3. Preliminary Experiments

Two experiments have been performed during the sensor box iteration process. First, subsection 3.3.1 presents the obtained measurements when left inside an office environment. Hereafter, a short experiment involving the exhaust of two different cars is presented in subsection 3.3.2. At this point, the importance is not to quantify pollutant concentrations but to observe sensor behaviour.

### 3.3.1. Indoor Measurements at the Aerospace Faculty

Multiple sets of indoor measurements have been taken within an office of TU Delft's Aerospace Engineering faculty. The reason for this is that such an office environment can be considered relatively clean and constant, especially when nobody is working there. The sensor box has been deployed for seven consecutive days in such an office. The electrical responses for CO, NO, NO<sub>2</sub> and O<sub>x</sub> are visualised in Figure 3.17, Figure 3.18, Figure 3.19 and Figure 3.20, respectively. The experimental set-up is presented in Figure 3.16.



Figure 3.16: Experimental set-up of sensor box office measurements.

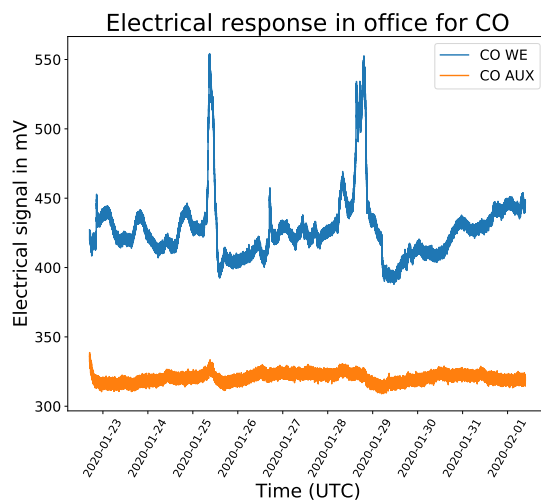


Figure 3.17: CO electrical response in office.

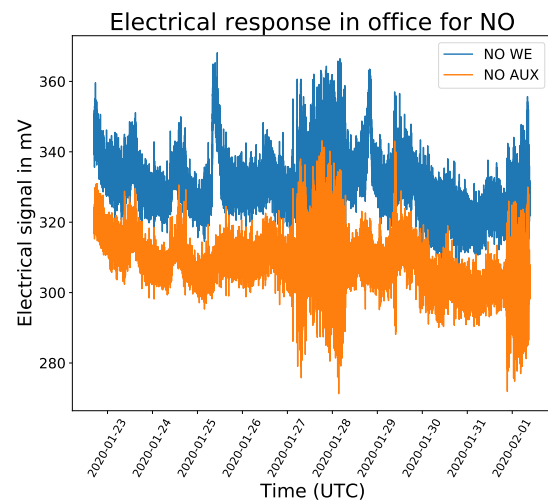


Figure 3.18: NO electrical response in office.



$O_x$  sensor ( $O_x = O_3 + NO_2$ ) as  $O_3$  is not a primary pollutant in combustion processes. The drop in CO and NO concentration around 200 seconds from the start is most likely due to the presence of strong wind gusts. In addition, it can be seen that the maximum electrical response (2.048 V) of the analog-to-digital converters is reached for CO and NO. This indicates that these sensors are not in the correct measurement range for this experiment as concentrations are likely even higher than what is indicated.

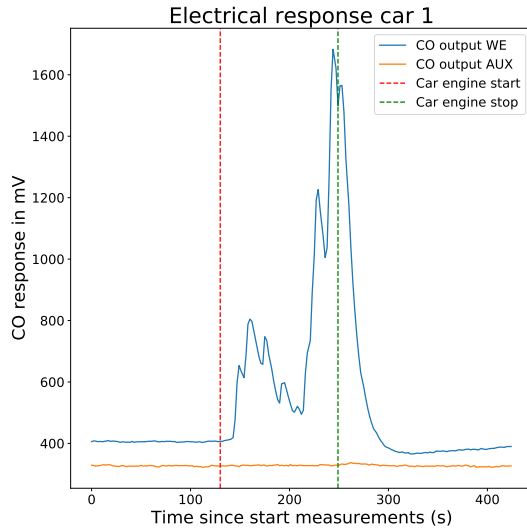


Figure 3.22: CO electrical response during first car exhaust experiment.

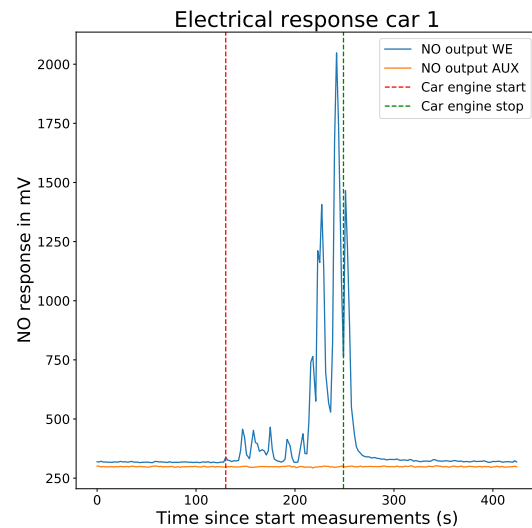


Figure 3.23: NO electrical response during first car exhaust experiment.

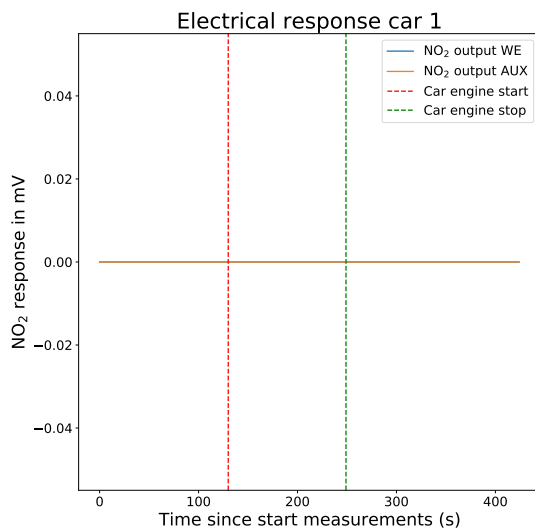


Figure 3.24:  $NO_2$  electrical response during first car exhaust experiment.

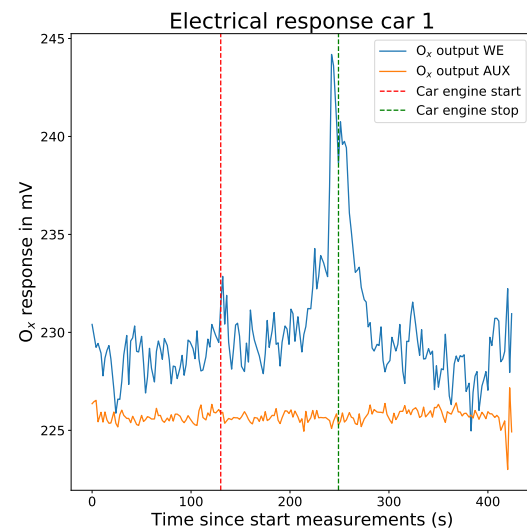


Figure 3.25:  $O_x$  electrical response during first car exhaust experiment.

### Response to Car 2

The second experiment was done 16 February 2021 using a diesel car manufactured between 2004 and 2007. The experimental set-up is presented in Figure 3.26. The electrical response is visualised for CO, NO,  $NO_2$  and  $O_x$  in Figure 3.29, Figure 3.30, Figure 3.31 and Figure 3.32, respectively. The

purpose of this experiment was to investigate the impact of the second sensor box iteration, which led to the addition of a small lid for rain protection. Consecutive measurements have been taken behind the exhaust with this rain protection lid maximally closed and maximally opened, respectively. For each species, two concentration peaks are present. Figure 3.28 schematically presents what happens in this experiment.



Figure 3.26: Experimental set-up during second car exhaust experiment.



Figure 3.27: Sensor box rain protection open vs close.

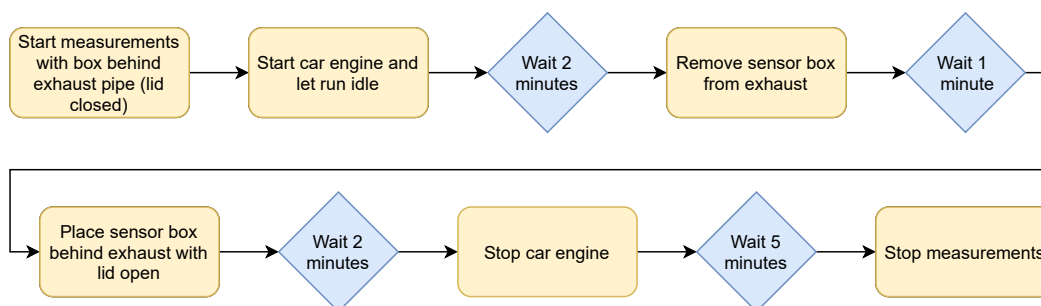


Figure 3.28: Car exhaust experiment 2 flow.

Differences in response between lid open or closed are minimal for CO, as can be seen in Figure 3.29. The deviations are larger for NO as less and lower concentration peaks are observed when the lid is closed, as presented in Figure 3.30. For NO<sub>2</sub> the difference is largest as no pollutant concentration peak is visible when the lid is closed. With the lid opened, a NO<sub>2</sub> can be detected. Similarly, the O<sub>x</sub> sensor does not pickup any pollutant concentration when the lid is closed, but does when the lid is open, as visualised in Figure 3.32.

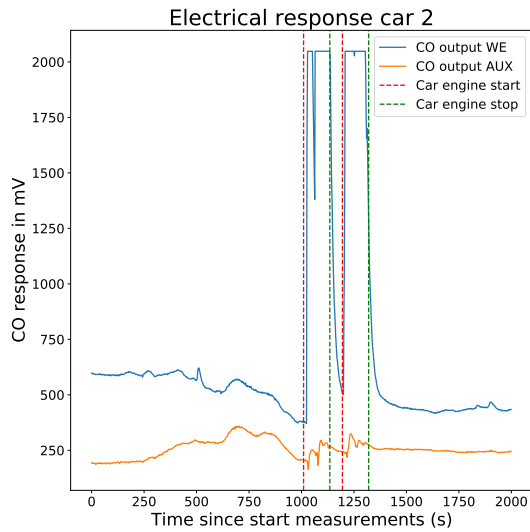


Figure 3.29: CO electrical response during second car exhaust experiment.

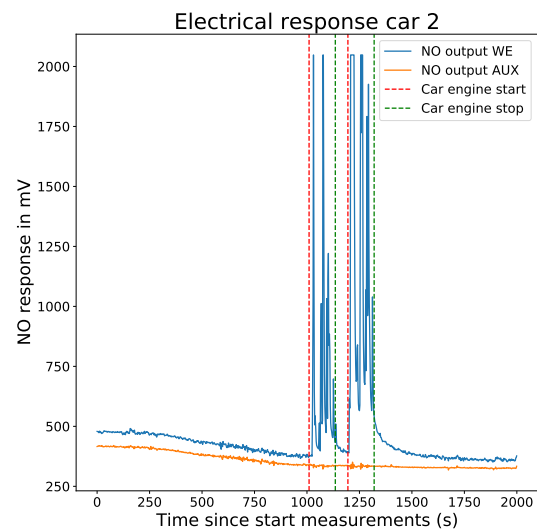


Figure 3.30: NO electrical response during second car exhaust experiment.

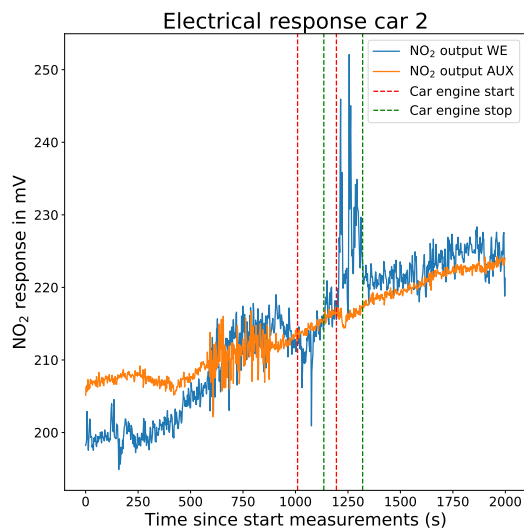


Figure 3.31: NO<sub>2</sub> electrical response during second car exhaust experiment.

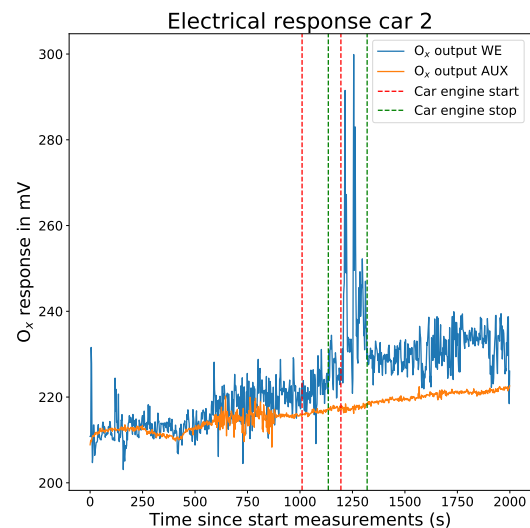


Figure 3.32: O<sub>x</sub> electrical response during second car exhaust experiment.

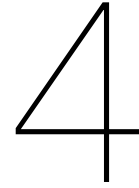
### 3.4. Battery Performance

Battery checks have been performed to get an estimate for the current consumption. In addition, TU Delft's DEMO has measured a ~50 mA current consumption for the sensor box in its final version. Recalculations from spontaneous battery checks shows variations between 181 and 321 mAh, as can be seen in Table 3.5. The tests presented in Table 3.5 were conducted outside. It is uncertain why the current consumption varies to this extent. During crucial measurement campaigns, it is advised to thoroughly test the batteries before deployment.

Table 3.5: Battery performance statistics.

Battery used	Current	Voltage	Duration	Indicator start	Indicator end	Consumed	Current drawn
20Ah ANSMANN	20000 mAh	5 V	103.655 h	100 %	0 %	20000 mAh	192.95 mA
24Ah XTPOWER	24000 mAh	9 V	46.25 h	100 %	65 %	8400 mAh	181.62 mA
24Ah XTPOWER	24000 mAh	9 V	67.59 h	100 %	47 %	12720 mAh	188.19 mA
24Ah XTPOWER	24000 mAh	9 V	74.82 h	100 %	0 %	24000 mAh	320.77 mA





# Sensor Box Calibration

Sensor box calibration is a cornerstone in this thesis. Without sufficient calibration, the sensor box might return measurements that deviate substantially from the truth. Different calibration strategies have been investigated in the literature study, concluding that a collocated calibration strategy together with a reference air quality monitor is best suited for the application envisioned in this thesis. Hereafter, the implementation of calibration models assists in transforming the raw measurements into concentrations.

First, section 4.1 presents the used terminology. Hereafter, section 4.2 presents how collocation data is gathered. Next, section 4.3 explores the different data sets and aspires to draw preliminary conclusions from the data. Then, section 4.4 presents the different processes involved in data preparation. Hereafter, subsection 4.5.3 presents the feature selection methodology. The model selection and development is presented in section 4.5, followed by section 4.6 which presents strategies to further optimise the developed methods. The final model selection is presented in section 4.7. Finally, section 4.8 presents how the calibration model integrates in the thesis as a whole.

## 4.1. Terminology

This chapter is terminology-heavy. In this section, the used terms are explained. The visual aid presented in Figure 4.1 assists in understanding the terminology.

- *Classification*: A supervised learning approach in which the machine learns from the data, distinguishing classes. For example categorising bananas and apples based on the fruit's weight;
- *Regression*: A supervised learning approach in which the machine learns from the data, predicting a numeric value. For example predicting the price of a piece of fruit, based on type, weight, colour and quality;
- *Attribute*: A data type, "length" or "temperature" for example;
- *Feature*: Attribute with its value, "length = 10" or "temperature = 290";
- *Instance*: A set of features with the corresponding label. A single element to "learn" from;
- *Label*: The target value. The numeric value or the class a model uses for training;
- *Training Set*: A subset of the full data set used for training the model;
- *Test Set*: A subset of the full data set used for testing the model;

	Features					Labels
	$X_1$	$X_2$	$X_3$	...	$X_M$	$Y$
Instance 1	25.1 °C	101325 Pa	34 %	...	1.013 V	30.1 $\mu\text{gm}^{-3}$
Instance 2	24.5 °C	101313 Pa	37 %	...	1.805 V	305.7 $\mu\text{gm}^{-3}$
Instance 3	22.3 °C	101121 Pa	39 %	...	1.050 V	28.6 $\mu\text{gm}^{-3}$
...	...	...	...	...	...	...
Instance N	32.1 °C	100128 Pa	64 %	...	1.323 V	43.8 $\mu\text{gm}^{-3}$

} Training set  
} Test set

Figure 4.1: General machine learning terminology.

## 4.2. Calibration Data Collection

The proposed calibration strategy consists of placing the developed sensor box next to a reference air quality analyser for several days or weeks. Even though there are many regulatory air quality analysers available for collocation, there are some concerns. First of all, there is the risk of theft. The sensor box only weighs  $\sim 1$  kg and has the size of a small shoe box, making it an easy target. Apart from the financial setback in case of theft, there is a serious setback in terms of time. The second concern is about the monitored species. Ideally, the reference air quality monitor samples at least the same species as the sensor box, but there are no such stations in the province of South-Holland. Only the stations "Amsterdam-Van Diemenstraat" and "Amsterdam-Vondelpark" in the province of North-Holland measure all four species ( $\text{NO}$ ,  $\text{NO}_2$ ,  $\text{CO}$  and  $\text{O}_x$ ). The final concern is over the ambient concentrations of the species. Knowing that the sensor box will be deployed near operating aircraft, where concentrations are both high and low, it is paramount that during calibration the sensor box is exposed to such variations as well.

Several calibration experiments have been performed. First, subsection 4.2.1 presents one day of collocation with a reference air quality analyser in The Hague, Ypenburg. Hereafter, subsection 4.2.2 presents collocation at the Aerospace Engineering faculty using reference data from that station again but now at a distance. Next, subsection 4.2.3 presents a multi-day calibration in Beverwijk, Wijk aan Zee. Finally, subsection 4.2.4 presents how the different packages of data are structured and processed. Table 4.1 summarises the used reference analysers from the Dutch air quality network to collocate the sensor box with.

Table 4.1: Regulatory air quality analysers consulted for calibration as defined by the Dutch air quality network.

Used in experiment	Station name	Station id	Species
Collocation for One Day - The Hague	Den Haag - Bleriotlaan	NL10446	$\text{NO}_2$ , $\text{NO}$ , $\text{O}_3$ , $\text{PM}_{10}$
Collocation for Multiple Days at a Distance - The Hague	Den Haag - Bleriotlaan	NL10446	$\text{NO}_2$ , $\text{NO}$ , $\text{O}_3$ , $\text{PM}_{10}$
Collocation for Multiple Days - Beverwijk	Wijk aan Zee - De Banjaert	NL49553	$\text{NO}_2$ , $\text{NO}$ , $\text{CO}$ , $\text{PM}_{10}$ , $\text{PM}_{25}$ , $\text{SO}_2$ , $\text{H}_2\text{S}$ , soot

### 4.2.1. Collocation for One Day - The Hague

On 11 November 2020, the sensor box was collocated with an air quality analyser of the Dutch air quality network in The Hague (id: NL10446) for eight consecutive hours. The experimental set-up consists of the sensor box in its primary form placed on the roof of the regulatory air quality station, as visualised in Figure 4.2. Table 4.2 presents the relevant information for this particular collocation experiment.



Figure 4.2: Experimental set-up of collocation with the "Den Haag - Bleriotlaan" air quality station.

Table 4.2: Summary of the first collocation experiment with the "Den Haag - Bleriotlaan" air quality station.

Start time	2020-11-11 07:59:43 (AMS time)
End time	2020-11-11 16:03:59 (AMS time)
Duration	8.07 hours
Set-up	Sensor box V1 with 24 Ah battery

#### 4.2.2. Collocation for Multiple Days at a Distance - The Hague

Due to the lack of regulatory stations where the sensor box can be left safely for a longer period of time, another approach was taken. The sensor box is generally stored at the Aerospace Engineering (AE) faculty, which is approximately 6 km away from the regulatory air quality analyser in The Hague (id: NL10446). By placing the sensor box safely outdoors at the faculty and using the "Den Haag - Bleriotlaan" station data for training, it might be possible to calibrate the sensor box. The sensor box is placed in an outdoor chemical storage shed, situated at the yellow pin in Figure 4.3. Inside this shed, the sensor box is placed on top of a cupboard at approximately 1.5 m above the ground, as can be seen in Figure 4.4. The drawback in this case is the ~6 km discrepancy between the two measurements locations, which makes it far from ideal, but nevertheless an interesting experiment. Table 4.3 presents the relevant information for this particular collocation at-a-distance experiment.



Figure 4.3: Sensor box location at the AE Faculty.

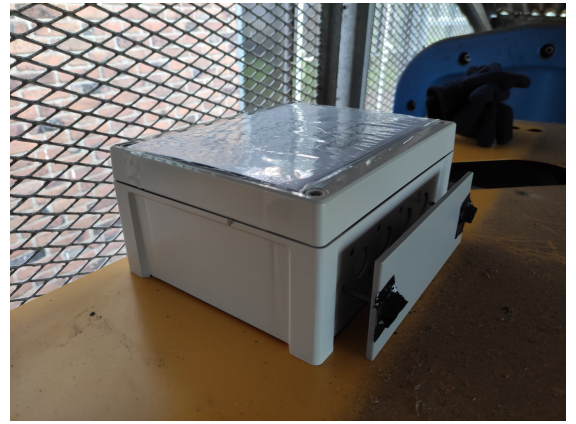


Figure 4.4: Close-up of sensor box during faculty collocation.

Table 4.3: Summary of the second collocation experiment with the "Den Haag - Bleriotlaan" air quality station.

Start time	2021-01-15 14:35:31 (UTC time)
End time	2021-01-22 08:09:00 (UTC time)
Duration	161.56 hours
Set-up	Sensor box V2 with 24 Ah and 20 Ah battery (swapped)

### 4.2.3. Collocation for Multiple Days - Beverwijk

Finally, an opportunity with the GGD was created to collocate the sensor box in Beverwijk, Wijk aan Zee with a regulatory air quality analyser of the Dutch air quality network (id: NL49553), as visualised in Figure 4.5. The sensor box was mounted to the station using zip ties with the sensors facing downward, as can be seen in Figure 4.6. Moreover, 10-second resolution data was obtained via the GGD for that reference analyser. Table 4.4 presents the relevant information for this particular collocation experiment.



Figure 4.5: Sensor box collocation with Wijk aan Zee station. Figure 4.6: Close-up of sensor box during collocation with Wijk aan Zee station.

Table 4.4: Summary of the collocation experiment with the "Wijk aan Zee - De Banjaert" air quality station.

Start time	2021-02-19 12:43:05 (UTC time)
End time	2021-02-22 15:31:47 (UTC time)
Duration	74.82 hours
Set-up	Sensor box V3 with 24 Ah battery

#### 4.2.4. Data Structure

The sensor box measurements are saved in the form of a .txt file on the SD card that is docked to the Arduino. The hourly air quality data obtained via the official air quality analysers from the Dutch air quality network are obtained via an API connection with a Python script. There is one data set obtained via the GGD containing official air quality measurements at a 10-second resolution. This data set is provided in the form of a .xlsx file. Data processing is done with Python 3.7.6, using the packages *pandas*, *numpy* and *sklearn*.

### 4.3. Calibration Data Exploration and Visualisation

The three aforementioned collocation experiments result in three different calibration data sets. Obtaining three different calibration data sets was not something that was planned at the start, but rather a necessity due to issues with the sensor box and the obtained data. In this section, all three data sets are explored and visualised.

First, subsection 4.3.1 presents the data for the one-day collocation with the The Hague station. Hereafter, subsection 4.3.2 presents the data for the multi-day collocation at-a-distance at the aerospace engineering faculty. Finally, subsection 4.3.3 presents the data for the multi-day collocation with the station in Beverwijk, Wijk aan Zee.

#### 4.3.1. Collocation for One Day - The Hague

This subsection presents the data for the one-day collocation with the The Hague station. In addition, concluding remarks are presented for this experiment.

##### Time-Series

Figure 4.7 presents the normalised sensor box output for each species. In addition, the light and temperature differences over time are visualised.

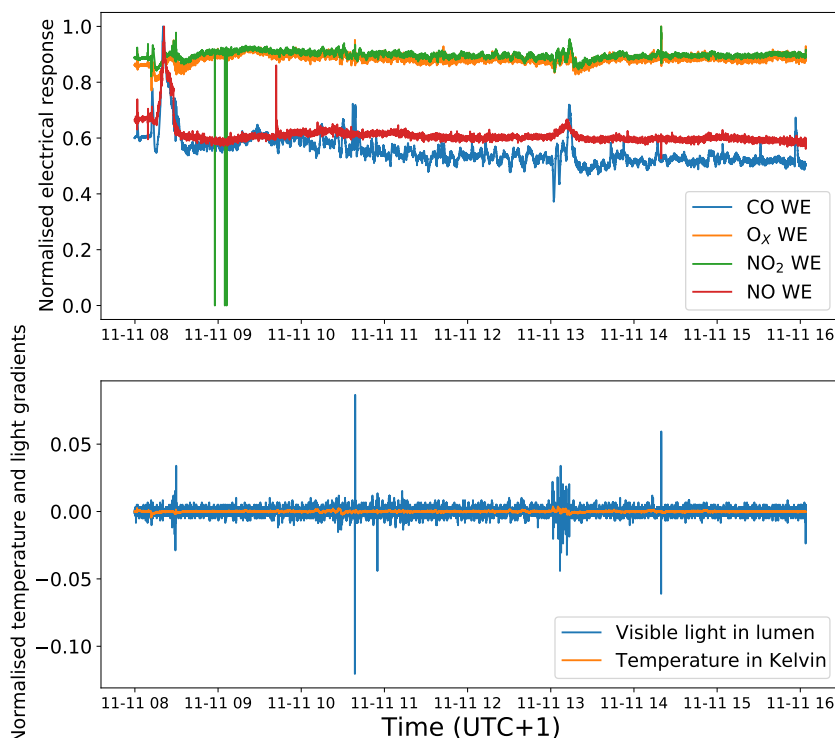


Figure 4.7: Normalised sensor box output with normalised temperature and light gradients for the first collocation experiment at the "Den Haag - Bleriotlaan" station.

### Correlations

The Pearson correlation coefficients,  $R$ , between the different variables are visualised by means of a matrix in Figure 4.8. Clearly, the light parameters (VisibleLight, IRLight and UVLight) are perfectly correlated, which makes sense as the only difference between the three is the wavelength. Strongest anti-correlations are observed between humidity and temperature, the light parameters and humidity and finally between the humidity and the auxiliary electrode of the NO sensor. Strongest correlations are observed - apart from the perfect correlations - between the NO<sub>2</sub>, NO and O<sub>x</sub> working- and auxiliary electrodes. In addition, a strong correlation is observed between the different electrodes of the O<sub>x</sub> and NO<sub>2</sub> sensors, which is expected as the O<sub>x</sub> sensor includes the measurement of NO<sub>2</sub>. Also, the auxiliary electrodes of each sensor are positively correlated with temperature but show no correlation with pressure. Relative humidity shows only little positive correlation with the NO<sub>2</sub> and O<sub>x</sub> working electrodes, but stronger anti-correlations with the auxiliary electrodes of the O<sub>x</sub>, NO, CO and NO<sub>2</sub> sensors.

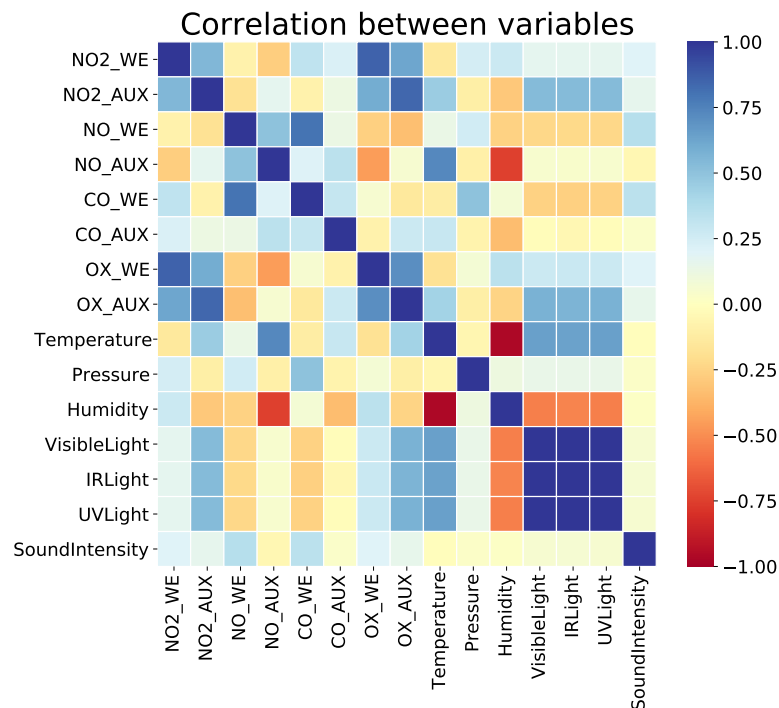


Figure 4.8: Correlation between sensor box measurements at 1-min resampling for the first collocation experiment at the "Den Haag - Bleriotlaan" station.

### Conclusions

The data was gathered successfully but is of poor quality for two reasons. First of all, the sensor box has been placed with the sensors facing upward, thus exposed to sunlight. As can be observed in Figure 4.7, changes in sunlight affect sensor temperature, which on its turn impacts the sensor response. Secondly, the data set is too short for calibration. The luchtmeetnet publishes air quality at an hourly resolution, so when measuring for eight hours there are only eight points for calibration.

Given these two problems, this data set will not be used in further analysis to calibrate the sensor box. Instead, longer term collocation experiments are a necessity, as readily indicated by literature. Topalović et al. [66] collocate their low-cost sensors with reference analysers up to 120 consecutive days. Wesseling et al. [71] mention a collocation period of several weeks to calibrate an Alphasense B43F NO<sub>2</sub> sensor. Mijling et al. [48] only report 8.5 collocation days to calibrate an Alphasense NO<sub>2</sub>-B4 sensor. Clearly, there are no one-day collocations in literature, which indicate that longer term measurements are necessary.

### 4.3.2. Collocation for Multiple Days at a Distance - The Hague

Longer term measurements were obtained by deploying the sensor box at the Aerospace Engineering faculty and using the data from the "Den Haag - Bleriotlaan" station as the labels. This subsection presents the data as well as concluding remarks for that experiment.

#### Time-Series

Figure 4.9 presents the electrical response obtained during the multi-day collocation experiment. Figure 4.10 visualises the meteorological signals. The NO<sub>2</sub> electrode response presented in Figure 4.9 jumps frequently to 0 mV around 2021-01-17. This error is present due to a bad connection in the designed PCB, which was repaired later on. The error only appeared below temperatures of ~5 °C due to thermal contraction.

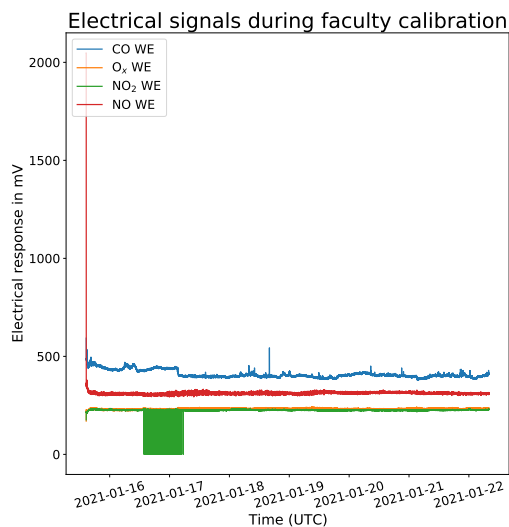


Figure 4.9: Electrical signals for the working electrodes during AE faculty-The Hague collocation.

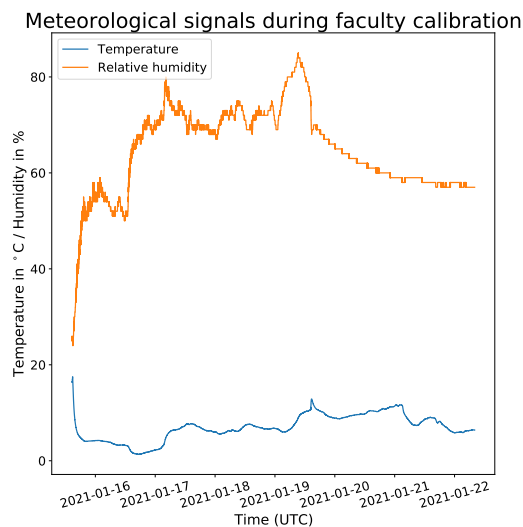


Figure 4.10: Meteorological signals during AE faculty-The Hague collocation.

#### Correlations

The Pearson correlation coefficients between the different variables are visualised by means of a matrix in Figure 4.11. Apart from the measurements obtained by the sensor box, now also the reference station measurements for NO, NO<sub>2</sub> and O<sub>3</sub> are included in the correlation matrix, designated by the variable names NO, NO<sub>2</sub> and O<sub>3</sub>. Including these hourly regulatory measurements required the sensor box measurements to be resampled to a 1-hour resolution. As presented in Table 4.3, 161.56 hours of data is accumulated. In total, 161 points are thus included to make the correlation matrix.

Strongest anti-correlations are observed between the O<sub>x</sub> and CO working electrodes, temperature and the CO working electrode, humidity and the auxiliary electrode of the CO auxiliary electrode. Strongest positive correlations are observed for both the NO electrodes and temperature, as well as between the NO and NO<sub>2</sub> sensors, but also between the NO and NO<sub>2</sub> sensor's electrodes. Temperature is positive correlated with all electrodes of the NO and NO<sub>2</sub> sensor, whereas pressure and humidity show little negative correlation with these electrodes.

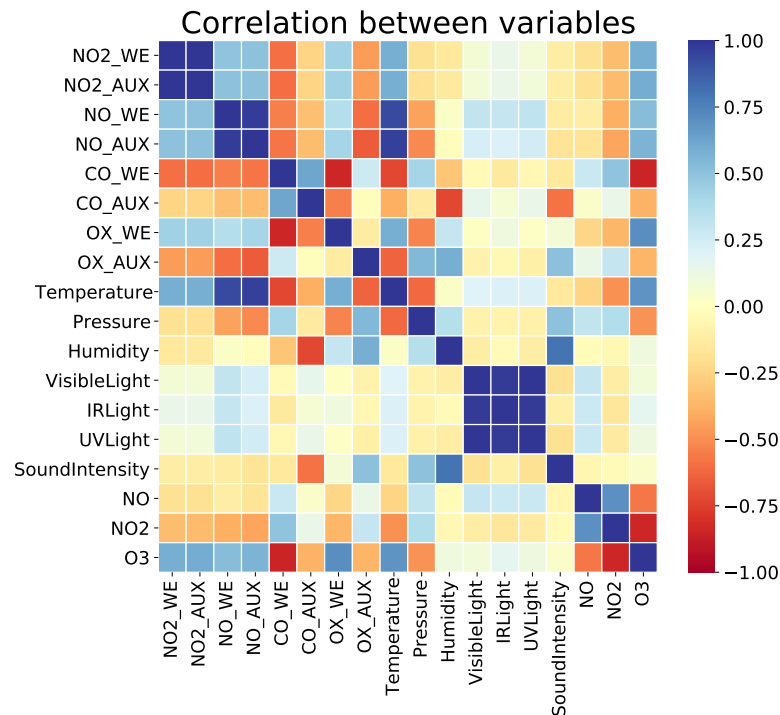


Figure 4.11: Correlation between sensor box measurements at 60-min resampling during AE faculty-Ypenburg collocation.

### Conclusions

The  $\text{NO}_2$  and  $\text{NO}$  sensors are surprisingly slightly negatively correlated with what the official measurements at the station in The Hague indicate. The working electrode of the  $\text{O}_x$  sensor however shows positive correlation with respect to the reference  $\text{O}_3$  measurements. These discrepancies can be caused by the  $\sim 6$  km spatial discrepancy between the two measurement locations. Given these observations, this data set will not be used in further analysis to calibrate the sensor box. Also, the inability to calibrate the  $\text{CO}$  sensor at this station only strengthens the decision to discard this approach.

### 4.3.3. Collocation for Multiple Days - Beverwijk

Multi-day measurements without a large spatial discrepancy between the sensor box and the reference analyser are obtained by collocating it with the reference analyser of "Wijk aan Zee - De Banjaert". This subsection presents the data as well as concluding remarks for this collocation experiment.

### Time-Series

Figure 4.12 presents the electrical response obtained during the multi-day collocation experiment. Figure 4.13 visualises the meteorological signals.

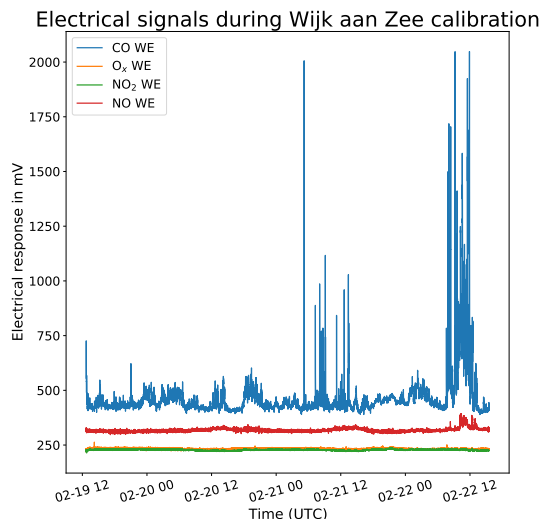


Figure 4.12: Electrical signals for the working electrodes during collocation in Wijk aan Zee.

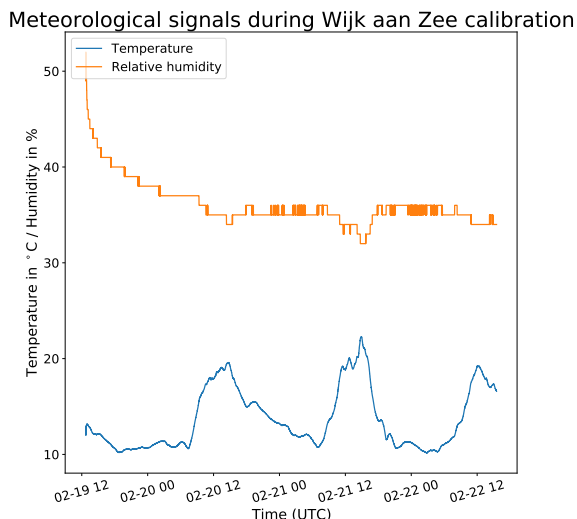


Figure 4.13: Meteorological signals during collocation in Wijk aan Zee.

**Correlations**

Again, the Pearson correlation coefficients are calculated and visualised, but now at two different temporal scales. Figure 4.14 and Figure 4.15 present these coefficients at a 1-hour and 10-second temporal resolution, respectively. Data from the reference station at Wijk aan Zee was obtained at a 10-second temporal resolution via the GGD. The reference measurements are indicated by the variable names NO, NO<sub>2</sub> and CO.

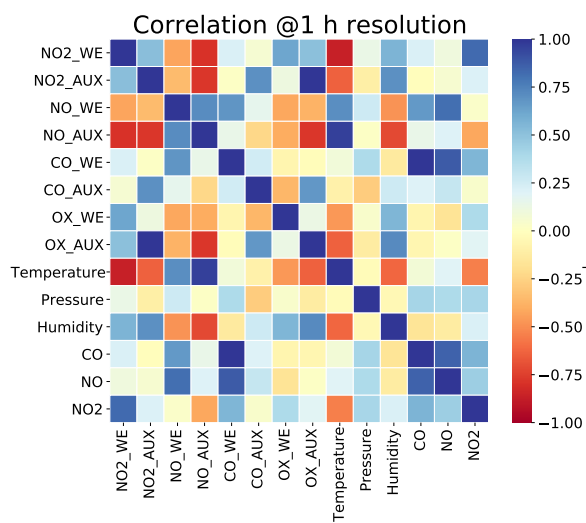


Figure 4.14: Correlation at 1-hour resolution during collocation in Wijk aan Zee.

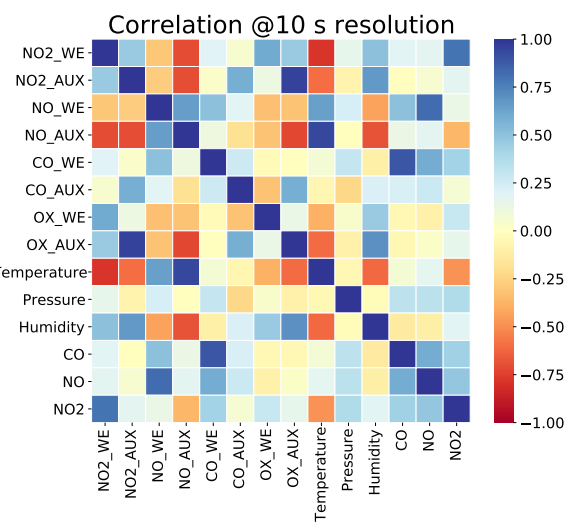


Figure 4.15: Correlation at 10-second resolution during collocation in Wijk aan Zee.

**Conclusions**

Strong positive correlations are observed between the CO working electrode and the regulatory CO measurements. In addition, the NO and NO<sub>2</sub> working electrodes correlate well with their regulatory counterparts. The CO working electrode also has a medium-strong positive correlation with the regulatory NO measurements. Similarly, the NO working electrode has a medium-strong positive correlation with the CO regulatory measurements. In addition, the CO working electrode also has a fair positive correlation with the NO<sub>2</sub> regulatory measurements. Temperature correlates strongly negative with regulatory and low-cost NO<sub>2</sub> measurements, but strongly positive with the working and auxiliary electrode

of the NO sensor. The pressure sensor indicates weak correlations in general. The humidity sensor indicates opposite correlation behaviour with respect to the temperature sensor, most likely due to the strong anti-correlation between temperature and humidity. Correlations do not vary much relative to each other when being resampled. In general, it can be observed that strongest correlations are obtained in the hourly resampled concentrations.

## 4.4. Preparing Data for Calibration Model

No matter which model will be used, the data requires preprocessing. First, subsection 4.4.1 presents how the data set is cleaned. Hereafter, subsection 4.4.2 describes how data is split in a train and test set. Finally, subsection 4.4.3 discusses the scaling of the features.

### 4.4.1. Data Cleaning

Three steps make-up the data cleaning process [34]. The concept is however the same, removing unwanted parts from the data.

#### Unstable Part Removal

The utilised gas sensors require stabilisation time after being connected to power. The stabilisation period is generally in the order of hours. The sensor box was powered already for ~4 hours before starting the calibration experiment at Wijk aan Zee, however a battery swap was done right before starting the collocation. As can be seen in Figure 4.12, the first two hours are discarded to allow further stabilisation.

#### Dealing with NaNs

Training or even testing models on NaNs (Not a Number) is not possible. In fact, NaNs are purposeless, but they slip into the data set for various reasons. The sensor box measurements do not contain NaNs. The data from the reference stations however contains NaNs. There are three things that can be done with NaNs [34]:

1. Remove of the attributes that contain a NaN;
2. Replace the NaNs by some value;
3. Remove of the instances that contain a NaN;

Given the limited amount of NaNs, it was decided to remove instances that contain a NaN. This leads to a 2.1% reduction in size of the data set, using the data at 10 s resolution, which is considered acceptable.

#### Removing Unwanted Spikes

Normally, the sensor box is powered using a 5 V battery output. Due to internal adjustments of the sensor box, the 5 V battery output was blocked and the 9 V output had to be used during the calibration experiment. Using the 9 V battery should not matter as the Arduino transforms any input voltage between 6-20 V to 5 V. Unfortunately, using the 9 V output resulted in unwanted repetitive spikes in the data, as can be observed in Figure 4.16. Filtering out these peaks is essential in preserving data quality.

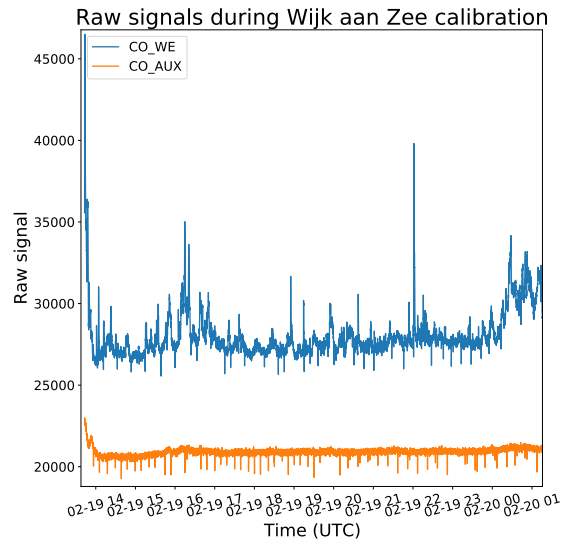


Figure 4.16: Time-series subset of the CO sensor during Wijk aan Zee calibration.

Due to the repetitive nature of the original signal, the fast Fourier transform (FFT) was applied to investigate the problem in more depth. Figure 4.17 and Figure 4.18 show the resulting signals for the CO working and auxiliary electrodes, respectively. As can be seen in these plots, multiple unwanted frequencies lay at the foundation of the problem.

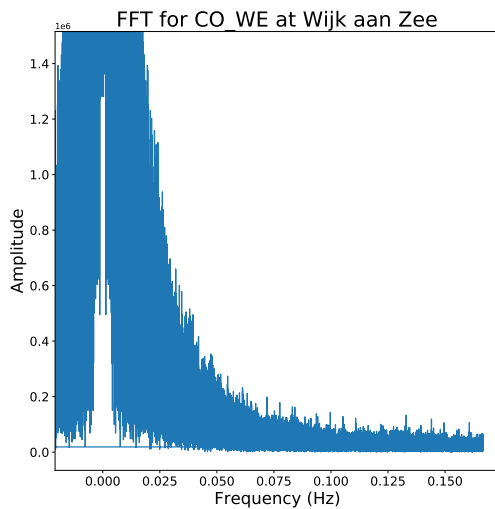


Figure 4.17: FFT for CO working electrode during Wijk aan Zee calibration.

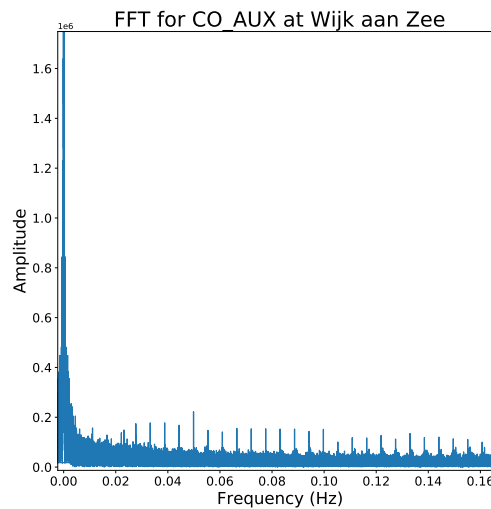


Figure 4.18: FFT for CO auxiliary electrode during Wijk aan Zee calibration.

From the time-series signals, it can be seen that these spikes are very temporary. By applying a 3-window rolling median filter on the data set, most of the spikes are removed while still preserving short-term fluctuations, as presented in Figure 4.19 and Figure 4.20.

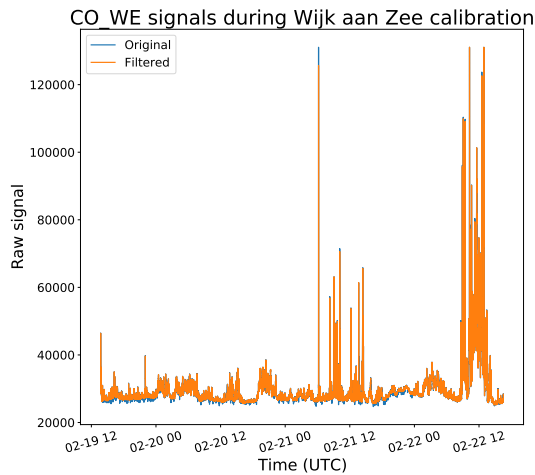


Figure 4.19: Time-series of original and filtered CO WE signal.

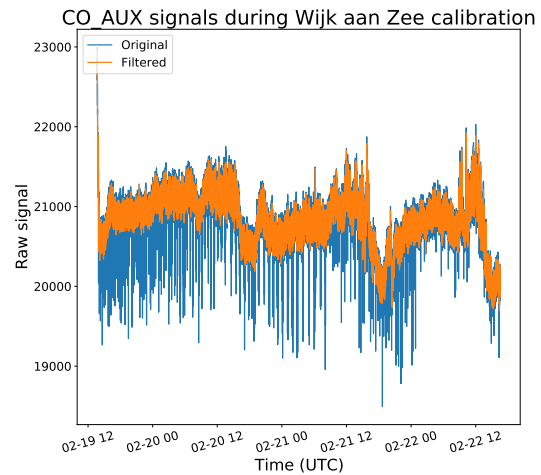


Figure 4.20: Time-series of original and filtered CO AUX signal.

#### 4.4.2. Creating a Train and Test Set

The full data set is split into a training and test set. The training data set is used to create the model. To evaluate model performance on unseen data - what it eventually will have to do - the test set is used. How much data should be allocated for training is free for interpretation. Generally, 10% to 30% is allocated for testing the model [34]. It was decided to allocate 20% of the full data set for testing the model.

#### 4.4.3. Feature Scaling

Feature scaling is an important transformation as most features have very different numeric ranges. For example, the temperature ranges from 10.14 °C to 22.27 °C while the pressure ranges from 100815 Pa to 101902 Pa. Feature scaling is the process of transforming the range of the variables of features of data. There are different feature scaling methods, however two very common methods are min-max scaling and standardisation [34].

Min-max scaling transforms the feature range from 0 to 1. This is achieved by subtracting the minimum value and dividing by the max minus the min. The function `MinMaxScaler` in the *sklearn* Python package can be used to do such scaling.

Standardisation on the other hand transforms the data such that it has zero mean and unit variance. The advantage of such scaling is that it is less affected by outliers, whereas in min-max scaling an extreme outlier can push all the non-outliers to zero. The function `StandardScaler` in the *sklearn* Python package allows the implementation of this scaling method. For now, it is decided to implement min-max scaling as standardisation causes problems in models like neural networks as it does not bound to a value range.

### 4.5. Calibration Model Selection and Development

Model selection and development is based on earlier research. Wesseling et al. [71], Mijling et al. [48] and Topalović et al. [66] use multivariate linear regression models to calibrate low-cost Alphasense sensors. Apart from linear models, Topalović et al. [66] also apply neural networks. Finally, Wang et al. [70] use a random forest model to calibrate a low-cost PM<sub>2.5</sub> sensor.

First, subsection 4.5.1 and subsection 4.5.2 present the development of a multivariate linear regression (MLR) model and random forest (RF) model, respectively. Hereafter, subsection 4.5.3 presents the feature selection. Next, in subsection 4.5.4 both models are trained and evaluated on the training set created earlier. Finally, evaluation using cross-validation is presented in subsection 4.5.5.

### 4.5.1. Multivariate Linear Regression

The multivariate linear regression model computes the weighted sum of the input features, plus an intercept term. Mathematically it can be described using Equation 4.1, where  $\hat{y}$  is the predicted value,  $n$  the number of features,  $x_i$  the  $i^{th}$  feature value and  $\theta_j$  the  $j^{th}$  model parameter [34]. The model is trained by exposing it to training set and calculating performance metrics on the test set for different model parameters,  $\theta$ . Performance metrics include the root mean square error (RMSE), defined in Equation 2.12.

$$\hat{y} = \theta_0 + \theta_1x_1 + \theta_2x_2 + \dots + \theta_nx_n \tag{4.1}$$

The model is implemented via the Python package `sklearn.linear_model` using the class `LinearRegression`.

### 4.5.2. Random Forest

An ensemble learning method, such as random forests benefit from the "wisdom of the crowd" effect. Getting a diverse set of classifiers can be achieved by using different training algorithms, and also by using the same training algorithm but on different random subsets of the training set. A random forest is an ensemble of decision trees that are trained on such random subsets of the training set. When the sampling of the random subsets is done with replacement, as presented in Figure 4.22, this is called *bagging*, short for *bootstrap aggregating*. Without replacement, this approach is called *pasting* [34]. The ensemble prediction can then be achieved by aggregating the predictions of all individual predictors. To better understand this visually, Figure 4.21 has been implemented.

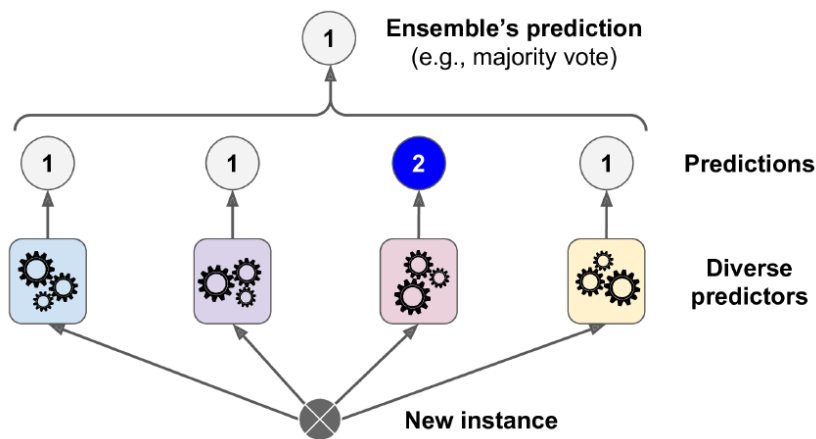


Figure 4.21: Example of a voting scheme in ensemble predictions.

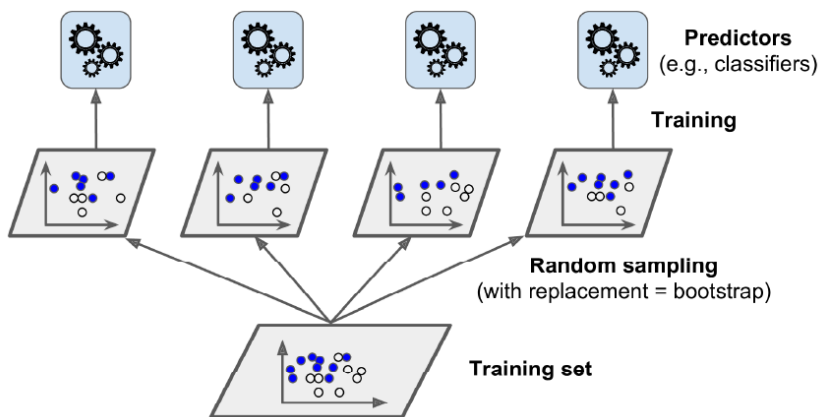


Figure 4.22: Example of random sampling in ensemble learning.

The model is implemented via the Python package *sklearn.ensemble* using the class `RandomForestRegressor`. A single model is created for each species that needs to be calibrated. Due to the absence of reference  $O_3$  measurements at Wijk aan Zee, this species is discarded.

### 4.5.3. Feature Selection

There are 15 signals obtained by the sensor box, as presented in Table 4.5. The sound intensity and light measurements are excluded from the feature candidate set due to their limited physical relation with air quality. In total, 11 features remain for developing the calibration models.

Table 4.5: Parameters obtained by sensor box measurements.

NO2_WE	NO_WE	CO_WE	OX_WE	Pressure
NO2_AUX	NO_AUX	CO_AUX	OX_AUX	Temperature
Sound intensity	UVLight	VisibleLight	IRLight	Humidity

There are various reasons to keep the number of features in the model to a minimum. First, there is computational complexity which increases with the number of features. Secondly, generalisation is improved when the ratio of the number of training patterns to the number of free classifier parameters is higher [41].

To make this simultaneous trade-off between model complexity and performance, the Bayesian Information Criterion (BIC) is used. It can be calculated using Equation 4.2, where  $L(\hat{\theta}_m)$  is the log-likelihood function calculated for the estimate  $\hat{\theta}_m$  in this case.  $K_m$  represents the number of free parameters [41]. The BIC score increases with the number of parameters and decreases with the log-likelihood for  $\hat{\theta}_m$ . Therefore, the feature set leading to lowest BIC score is preferred.

$$\text{BIC} = -2L(\hat{\theta}_m) + K_m \ln N \quad (4.2)$$

The BIC score is implemented via the Python package *RegscorePy* and calculated for both MLR and RF models and for all feature combinations that can be constructed using the 11 features, which are  $2^{11}-1$  non-empty combinations per model. As an example, the BIC score for different feature combinations for NO at 60 min resolution for the MLR and RF models are visualised in Figure 4.23 and Figure 4.24, respectively.

Table 4.6: Feature selection using BIC for MLR models at different temporal resolutions.

Species	Resolution	MSE	BIC	Attributes at minimum BIC
CO	10 s	17728.76	203506.39	Pressure, NO_AUX, CO_AUX, NO_WE, CO_WE, Temperature, Humidity, OX_WE, OX_AUX
CO	1 min	13865.65	33130.58	Pressure, NO_AUX, CO_AUX, NO_WE, CO_WE, Temperature, OX_AUX
CO	60 min	66.53	284.36	Pressure, NO2_WE, CO_AUX, NO_WE, CO_WE, OX_WE, OX_AUX, NO2_AUX
NO <sub>2</sub>	10 s	22.27	64629.5	Pressure, NO2_WE, NO_AUX, CO_AUX, NO_WE, Temperature, Humidity, OX_WE, OX_AUX, NO2_AUX
NO <sub>2</sub>	1 min	15.57	9615.5	Pressure, NO2_WE, NO_AUX, NO_WE, CO_AUX, CO_WE, Temperature, Humidity, OX_WE, OX_AUX, NO2_AUX
NO <sub>2</sub>	60 min	4.72	136.45	Pressure, NO2_WE, NO_AUX, NO_WE, CO_AUX, CO_WE, Temperature, OX_WE, OX_AUX, NO2_AUX
NO	10 s	13.93	54882.97	Pressure, NO2_WE, NO_AUX, NO_WE, CO_WE, Temperature, Humidity, OX_WE, OX_AUX, NO2_AUX
NO	1 min	5.64	6096.73	Pressure, NO2_WE, NO_AUX, NO_WE, CO_AUX, CO_WE, Temperature, Humidity, OX_WE, OX_AUX, NO2_AUX
NO	60 min	1.22	44.47	NO_AUX, NO_WE, CO_WE, Humidity, OX_WE, OX_AUX, NO2_AUX

Table 4.7: Feature selection using BIC for RF models at different temporal resolutions.

Species	Resolution	MSE	BIC	Attributes at minimum BIC
CO	10 s	324.83	120296.21	Humidity, NO_AUX, Temperature, OX_WE, Pressure
CO	1 min	1863.05	26163.46	CO_AUX, NO_AUX, NO_WE, CO_WE, NO2_WE, Temperature, OX_WE
CO	60 min	329.94	354.37	NO_AUX, CO_WE, Humidity
NO <sub>2</sub>	10 s	0.47	-15656.33	Humidity, CO_WE, Temperature, Pressure, NO2_AUX
NO <sub>2</sub>	1 min	0.75	-964.69	CO_AUX, Humidity, NO_WE, Temperature, Pressure, OX_AUX
NO <sub>2</sub>	60 min	2.7	74.86	CO_WE, NO2_WE, NO_WE, Pressure
NO	10 s	0.86	-3002.52	CO_AUX, Humidity, NO_WE, Temperature, NO2_WE, Pressure, NO2_AUX
NO	1 min	0.44	-2783.58	CO_AUX, Humidity, NO_AUX, NO_WE, NO2_WE, Temperature, OX_WE, Pressure, OX_AUX, NO2_AUX
NO	60 min	4.99	102.95	NO2_WE, NO_WE

BIC score for MLR model for NO @60Min resolution

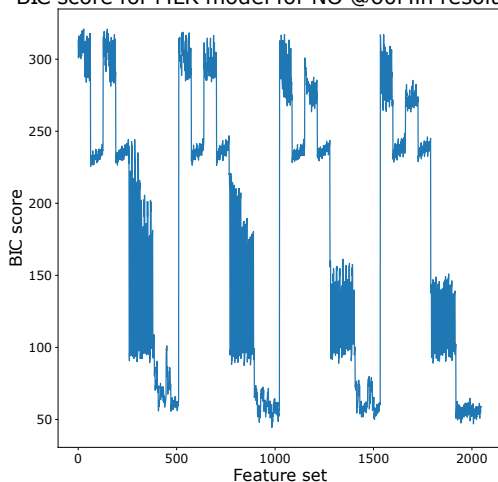


Figure 4.23: BIC score for MLR model for NO at 60 min resolution.

BIC score for RF model for NO @60Min resolution

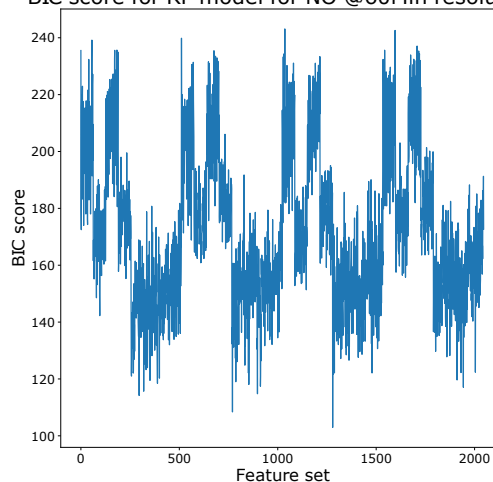


Figure 4.24: BIC score for RF model for NO at 60 min resolution.

#### 4.5.4. Training and Evaluating

The next step is to train the models and evaluate them on the previously defined training set and features. Data at three different temporal scales is used to create the calibration models, more specifically, 10 seconds, 1 minute and 60 minutes. These three temporal scales were selected to observe the effect of resampling on model performance.

##### Multivariate Linear Regression Model

The attributes for the MLR model are taken from the performance-complexity trade-off presented in Table 4.6. 1-to-1 plots are used to display the performance of the models. It compares the value returned by the model with that of a reference measurement. Ideally, all points are situated on the red dashed line, which indicates that the calibrated response matches the observations of the regulatory measurement instrument. Figure 4.25a, Figure 4.25b and Figure 4.25c present these plots for CO at 10 seconds, 1 minute and 60 minutes resolution, respectively. Figure 4.26a, Figure 4.26b and Figure 4.26c present these plots for NO at 10 seconds, 1 minute and 60 minutes resolution, respectively. Figure 4.27a, Figure 4.27b and Figure 4.27c present these plots for NO<sub>2</sub> at 10 seconds, 1 minute and 60 minutes resolution, respectively.

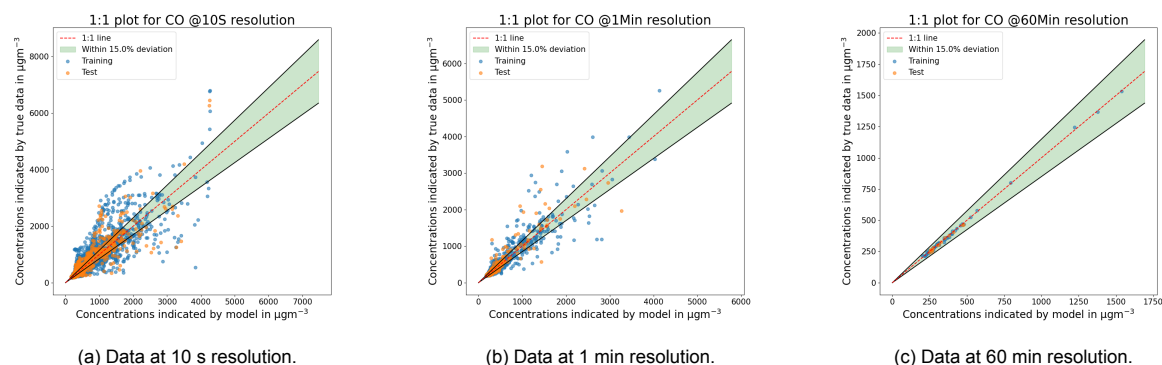


Figure 4.25: 1-to-1 plots for MLR calibration at Wijk aan Zee for CO.

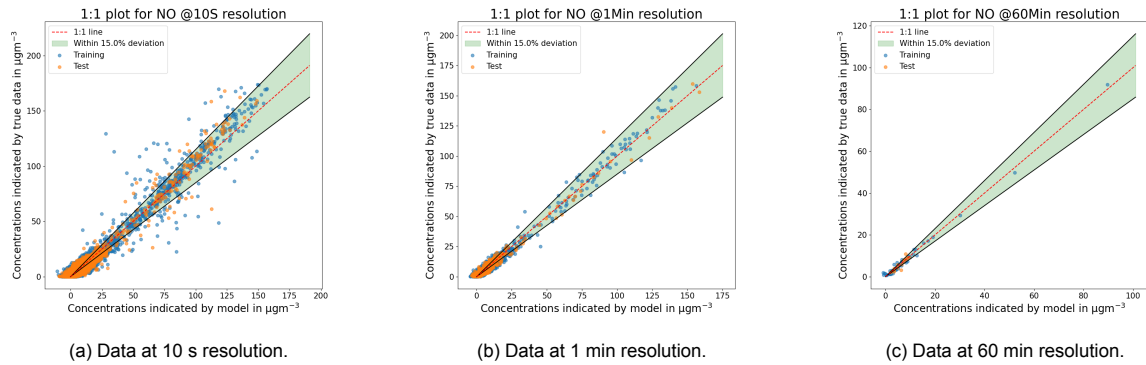


Figure 4.26: 1-to-1 plots for MLR calibration at Wijk aan Zee for NO.

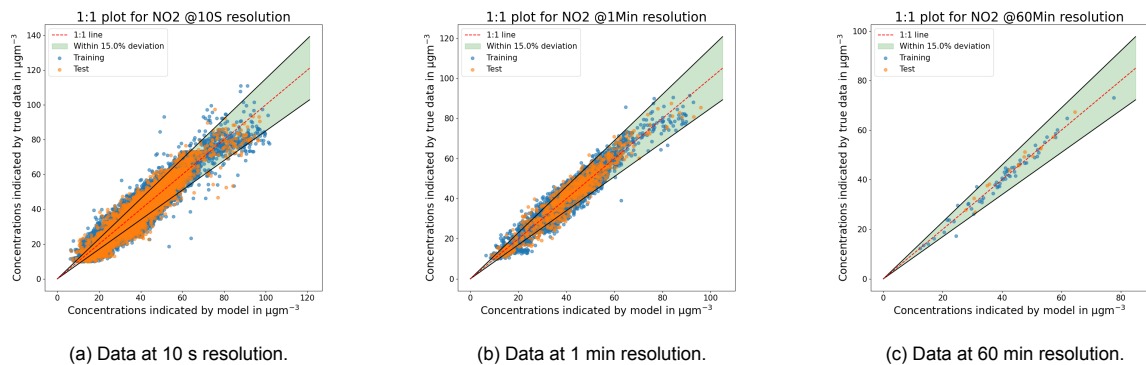
Figure 4.27: 1-to-1 plots for MLR calibration at Wijk aan Zee for NO<sub>2</sub>.

Table 4.8 presents the RMSE statistics on the training and test data sets using the MLR model. No large differences are observed between the RMSE on the train and test set, indicating no over- or underfitting. To potentially further reduce the RMSE, random forest models will be explored.

Table 4.8: RMSE in  $\mu\text{g}\text{m}^{-3}$  for different species at different temporal scales using the MLR model.

Temporal resolution	RMSE CO (test, train)	RMSE NO (test, train)	RMSE NO <sub>2</sub> (test, train)
60 min	7.21, 8.16	1.17, 1.11	2.01, 2.17
1 min	126.61, 117.75	2.32, 2.38	4.1, 3.95
10 s	130.16, 133.15	3.62, 3.73	4.82, 4.72

Finally, each MLR model is evaluated on the test set. Metrics include the RMSE, correlation and accuracy. Accuracy is defined as the percentage of predictions within a 15% deviation from the target value. A 15% deviation is selected as this is approximately the deviation reported for the used official reference air quality analyser [29]. The results are summarised in Table 4.9.

Table 4.9: Evaluation on the test set for the MLR models at different temporal scales.

	CO 10 s	CO 1 min	CO 60 min	NO 10 s	NO 1 min	NO 60 min	NO <sub>2</sub> 10 s	NO <sub>2</sub> 1 min	NO <sub>2</sub> 60 min
RMSE	130.16	126.61	7.21	3.62	2.32	1.17	4.82	4.10	2.01
Correlation	0.90	0.91	1.00	0.97	0.99	0.91	0.94	0.96	0.99
Accuracy	78.32%	83.62%	100.00%	22.41%	32.18%	80.00%	77.16%	82.81%	100.00%

### Random Forest Model

The attributes for the RF model are taken from the performance-complexity trade-off presented in Table 4.7. Again, 1-to-1 plots are used to visualise the performance of the random forest model at different temporal scales. Figure 4.28a, Figure 4.28b and Figure 4.28c present these plots for CO at 10 seconds,

1 minute and 60 minutes resolution, respectively. Figure 4.29a, Figure 4.29b and Figure 4.29c present these plots for NO at 10 seconds, 1 minute and 60 minutes resolution, respectively. Figure 4.30a, Figure 4.30b and Figure 4.30c present these plots for NO<sub>2</sub> at 10 seconds, 1 minute and 60 minutes resolution, respectively.

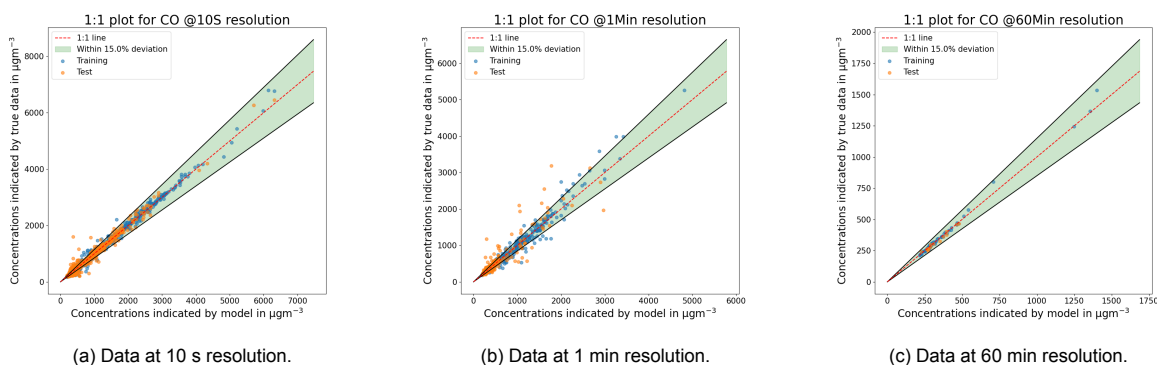


Figure 4.28: 1-to-1 plots for RF calibration at Wijk aan Zee for CO.

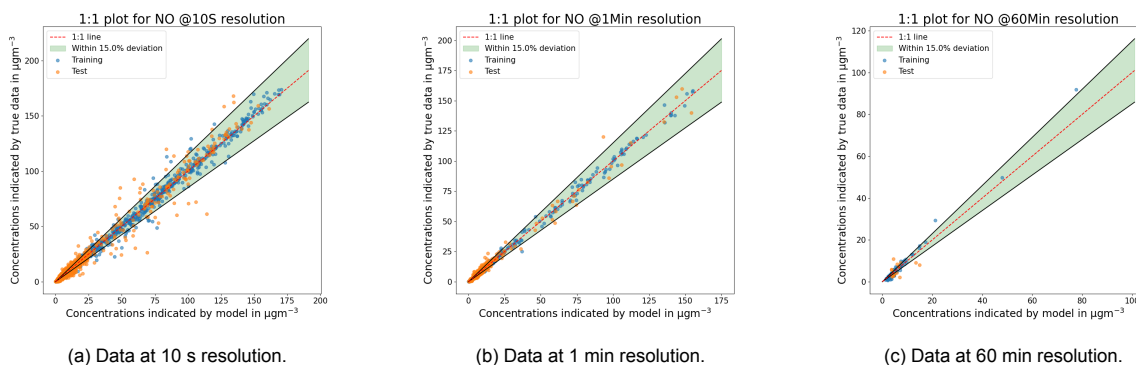


Figure 4.29: 1-to-1 plots for RF calibration at Wijk aan Zee for NO.

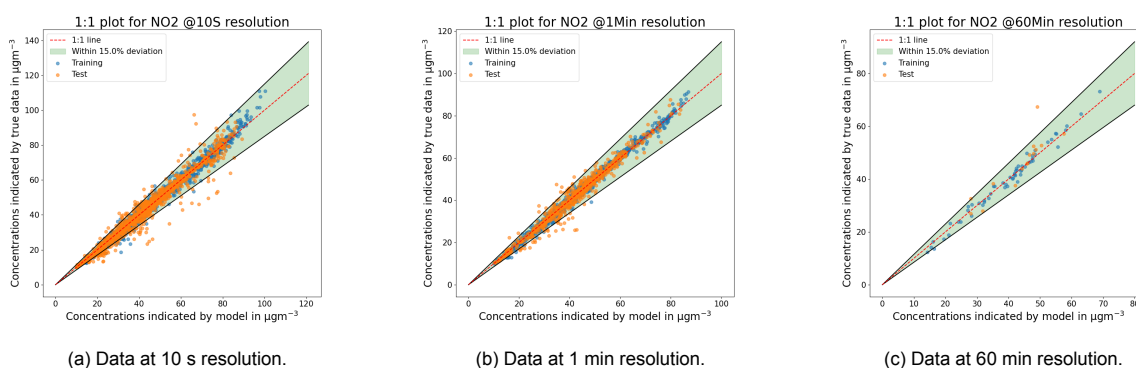


Figure 4.30: 1-to-1 plots for RF calibration at Wijk aan Zee for NO<sub>2</sub>.

Table 4.10 presents the RMSE statistics on the training and test data set using the RF model. Larger differences are observed between the RMSE on the train and test data compared with the MLR model results presented in Table 4.8.

At the finest temporal scale (10 s), the RF models outperform the MLR models. The opposite is true at the largest temporal scale (60 min). At the medium temporal scale (1 min), the models perform

comparably. For the RF models however, it can be seen that the RMSE is up to 3 times better on the training set than on the test set, which indicates overfitting.

Table 4.10: RMSE in  $\mu\text{g m}^{-3}$  for different species at different temporal scales using the RF model.

Temporal resolution	RMSE CO (test, train)	RMSE NO (test, train)	RMSE NO <sub>2</sub> (test, train)
60 min	13.71, 22.87	3.24, 2.41	5.43, 1.71
1 min	113.16, 46.22	1.85, 0.72	2.45, 0.88
10 s	44.04, 19.2	2.46, 0.93	1.93, 0.7

Finally, each RF model is evaluated on the test set. Metrics include the RMSE, correlation and accuracy. Accuracy is in this case again the percentage of predictions within a 15% deviation from the target value. The results are summarised in Table 4.11.

Table 4.11: Evaluation on the test set for the non-tuned RF models at different temporal scales.

	CO 10 s	CO 1 min	CO 60 min	NO 10 s	NO 1 min	NO 60 min	NO <sub>2</sub> 10 s	NO <sub>2</sub> 1 min	NO <sub>2</sub> 60 min
RMSE	63.53	105.15	13.49	2.30	2.04	3.40	1.90	2.57	5.28
Correlation	0.98	0.94	0.99	0.99	0.99	0.44	0.99	0.98	0.90
Accuracy	93%	88%	100%	80%	68%	7%	98%	95%	87%

#### 4.5.5. Evaluation using Cross-Validation

Instead of looking at the training data set as a single set, it is possible to split up the training set into  $k$  subsets. Using one subset as a test set and the other  $k - 1$  sets as the training set, it is possible to train and evaluate the model  $k$  times. Taking this approach allows to get an estimate of the model performance, by the RMSE for example, but also it quantifies how precise this estimate of the model performance is by calculating the standard deviation of the respective performance metric. This process is called  $k$ -fold cross-validation, which is illustrated in Figure 4.31 for 10 folds. Train folds are indicated in grey, the test fold is presented in blue. The availability of 10 folds allows to do 10 iterations. Typical values for  $k$  are 5 or 10 [34].

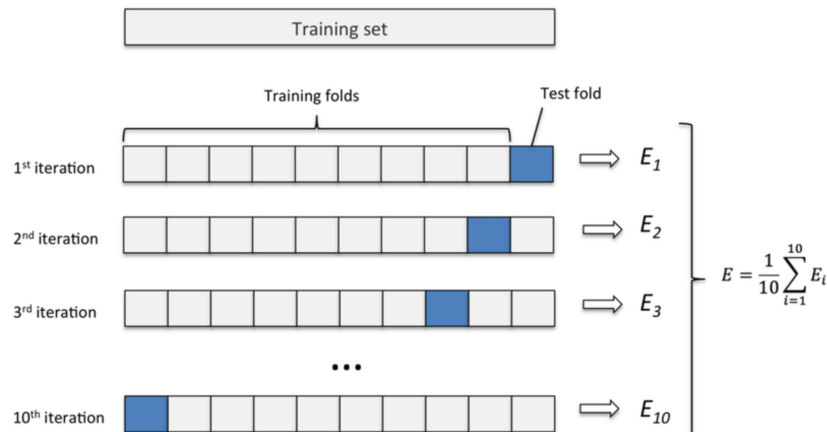


Figure 4.31: 10-fold cross-validation illustration [9].

#### Multivariate Linear Regression Model

Table 4.12 presents the RMSE statistics for a 10-fold cross-validation on the training data using the MLR model. It should be noted that the size of the training set varies with the temporal resolution used, so comparison between different temporal scales is difficult.

Table 4.12: 10-fold cross-validation RMSE (in  $\mu\text{gm}^{-3}$ ) statistics for different species at different temporal scales using the MLR model.

Temporal resolution	RMSE CO ( $\mu, \sigma$ )	RMSE NO ( $\mu, \sigma$ )	RMSE NO <sub>2</sub> ( $\mu, \sigma$ )
60 min	9.86, 3.62	1.44, 0.83	2.93, 1.58
1 min	118.13, 28.66	2.38, 0.16	3.96, 0.09
10 s	132.88, 13.86	3.73, 0.29	4.72, 0.11

### Random Forest Model

Table 4.13 presents the RMSE statistics for a 10-fold cross-validation on the training data using the RF model.

Table 4.13: 10-fold cross-validation RMSE (in  $\mu\text{gm}^{-3}$ ) statistics for different species at different temporal scales using the RF model.

Temporal resolution	RMSE CO ( $\mu, \sigma$ )	RMSE NO ( $\mu, \sigma$ )	RMSE NO <sub>2</sub> ( $\mu, \sigma$ )
60 min	46.46, 43.52	5.66, 5.38	4.6, 1.49
1 min	123.91, 23.92	1.85, 0.35	2.35, 0.17
10 s	52.79, 6.5	2.54, 0.39	1.87, 0.16

## 4.6. Calibration Model Fine-Tuning

The presented models are not optimised. Further optimisation may improve the model performance and reduce the overfit present in the random forest model. First, subsection 4.6.1 presents optimisation of the MLR model. Hereafter, subsection 4.6.2 presents the optimised random forest model.

### 4.6.1. Multivariate Linear Regression Model

The multivariate linear regression model does not contain tunable free parameters. Instead, optimisation of this model can only be achieved by altering the learning features or the data itself. The learning features are obtained by using the Bayesian Information Criterion, which already takes into account only the features that matter most in the complexity-performance trade-off. On the other hand, the data cannot be changed. It can be further smoothed but that will reduce the model's ability to detect short-term fluctuations in pollutant concentration, which is to be avoided. Given these observations, it was decided to not look for further improvements.

### 4.6.2. Random Forest Model

The random forest is initially trained using the default settings provided in the *sklearn.ensemble* package. The tuning of hyperparameters can improve the random forest's performance and reduce the overfit.

Hyperparameters can be tuned manually but that is a tedious process. The Python package *sklearn* includes a class `GridSearchCV` that automatically tries a set of hyperparameters and evaluates all possible combinations using cross-validation. The considered hyperparameters for optimisation, along with their default settings are the following:

- `n_estimators`: number of trees in the forest (default=10);
- `max_depth`: maximum depth of the tree (default=None, max expansion);
- `min_samples_leaf`: minimum number of samples required to be at a leaf node (default=1);
- `max_features`: number of features to consider when looking for the best split (default=`n_features`);

The hyperparameters considered during the random forest model optimisation are listed in Table 4.14, which make 144 ( $4 \times 3 \times 4 \times 3$ ) hyperparameter combinations in total. This means that the random forest model is trained and evaluated 144 times per species per temporal resolution, in total thus 1296 ( $144 \times 3 \times 3$ ) times.

The selected values for the hyperparameters are based on the current knowledge that the random forest overfits. For this reason, `n_estimators` was increased as this grows more trees. In addition,

`max_features` was kept small as it determines the number of features that are randomly assigned to a single tree. The lower this number of features, the less likely it is to overfit. Next, the `max_depth` was kept small as this reduces the longest path between the root node and the leaf node, which reduces complexity. Finally, `min_samples_leaf` was kept low as it behaves similar to the `max_depth` parameter, but determines when a branch stops splitting.

The final models are those that achieve best RMSE during cross validation. Table 4.15 presents the optimised hyperparameter settings. It should be noted that three models perform better using the default hyperparameter settings when comparing cross-validated RMSE metrics in Table 4.13 and Table 4.17. This is the case for the CO model at 10 s resolution, and for NO and 1 min and 60 min resolution.

Table 4.14: Considered hyperparameters during RF model tuning.

Parameter	Values considered during hyperparameter tuning
<code>n_estimators</code>	27, 54, 162, 324
<code>max_features</code>	1, 2, 3
<code>max_depth</code>	30, 40, 50, 60
<code>min_samples_leaf</code>	1, 2, 3

Table 4.15: RF hyperparameters for best estimators at different temporal scales.

	CO 10 s	CO 1 min	CO 60 min	NO 10 s	NO 1 min	NO 60 min	NO <sub>2</sub> 10 s	NO <sub>2</sub> 1 min	NO <sub>2</sub> 60 min
<code>n_estimators</code>	324	27	27	324	324	324	162	54	54
<code>max_depth</code>	30	40	3	50	60	60	40	60	40
<code>min_samples_leaf</code>	1	1	1	1	3	3	1	1	1
<code>max_features</code>	3	2	60	3	3	3	3	3	3

The RMSE scores for these optimised models are calculated by applying them to the train and test set. The results are presented in Table 4.16. To strengthen the analysis, a 10-fold cross-validation was carried out and is presented in Table 4.17.

Table 4.16: RMSE in  $\mu\text{g m}^{-3}$  for different species at different temporal scales using the hyperparameter-tuned RF model.

Temporal resolution	RMSE CO (test, train)	RMSE NO (test, train)	RMSE NO <sub>2</sub> (test, train)
60 min	15.55, 24.61	3.54, 2.76	5.56, 1.74
1 min	96.21, 42.64	2.06, 0.84	2.55, 0.89
10 s	61.52, 26.58	2.31, 0.9	1.9, 0.67

Table 4.17: 10-fold cross-validation RMSE (in  $\mu\text{g m}^{-3}$ ) statistics for different species at different temporal scales using the hyperparameter-tuned RF model.

Temporal resolution	RMSE CO ( $\mu, \sigma$ )	RMSE NO ( $\mu, \sigma$ )	RMSE NO <sub>2</sub> ( $\mu, \sigma$ )
60 min	42.82, 44.12	5.72, 5.33	4.6, 1.25
1 min	120.19, 29.29	2.17, 0.73	2.35, 0.1
10 s	73.43, 14.13	2.41, 0.43	1.84, 0.17

Finally, each optimised RF model is evaluated on the test set again. Metrics include the RMSE, correlation and accuracy. Accuracy is in this case again the percentage of predictions within a 15% deviation from the target value. The results are summarised in Table 4.18.

Table 4.18: Evaluation on the test set for the best estimators obtained during hyperparameter optimisation at different temporal scales.

	CO 10 s	CO 1 min	CO 60 min	NO 10 s	NO 1 min	CO 60 min	NO <sub>2</sub> 10 s	NO <sub>2</sub> 1 min	NO <sub>2</sub> 60 min
RMSE	61.52	96.21	15.55	2.31	2.06	3.54	1.90	2.55	5.56
Correlation	0.98	0.95	0.98	0.99	0.99	0.44	0.99	0.98	0.89
Accuracy	93.23%	88.00%	100.00%	80.45%	67.70%	6.67%	97.88%	94.93%	93.33%

Finally, 1-to-1 plots are used to visualise the performance of the tuned random forest model at different temporal scales. Figure 4.32a, Figure 4.32b and Figure 4.32c present these plots for CO at 10 seconds, 1 minute and 60 minutes resolution, respectively. Figure 4.33a, Figure 4.33b and Figure 4.33c present these plots for NO at 10 seconds, 1 minute and 60 minutes resolution, respectively. Figure 4.34a, Figure 4.34b and Figure 4.34c present these plots for NO<sub>2</sub> at 10 seconds, 1 minute and 60 minutes resolution, respectively.

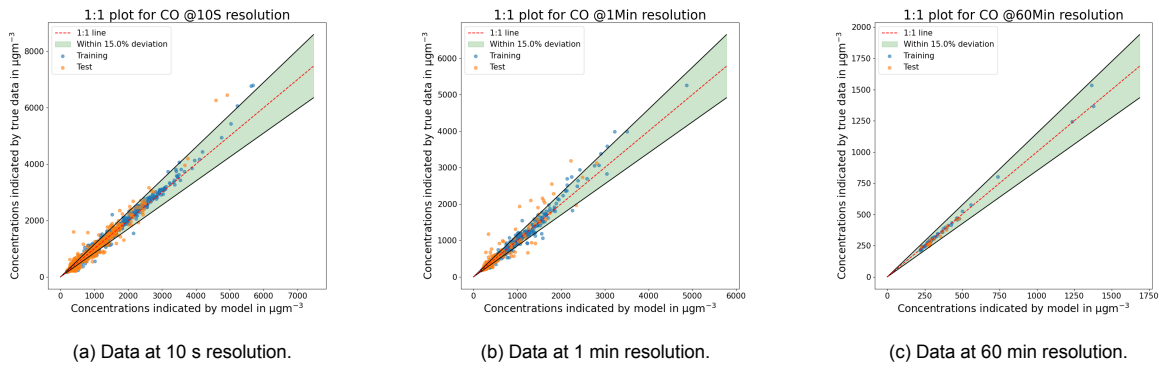


Figure 4.32: 1-to-1 plots for RF tuned calibration at Wijk aan Zee for CO.

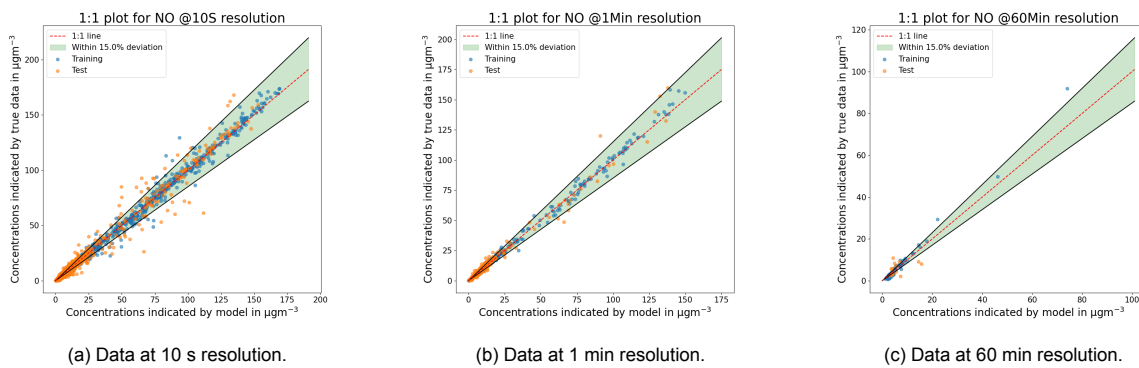


Figure 4.33: 1-to-1 plots for RF tuned calibration at Wijk aan Zee for NO.

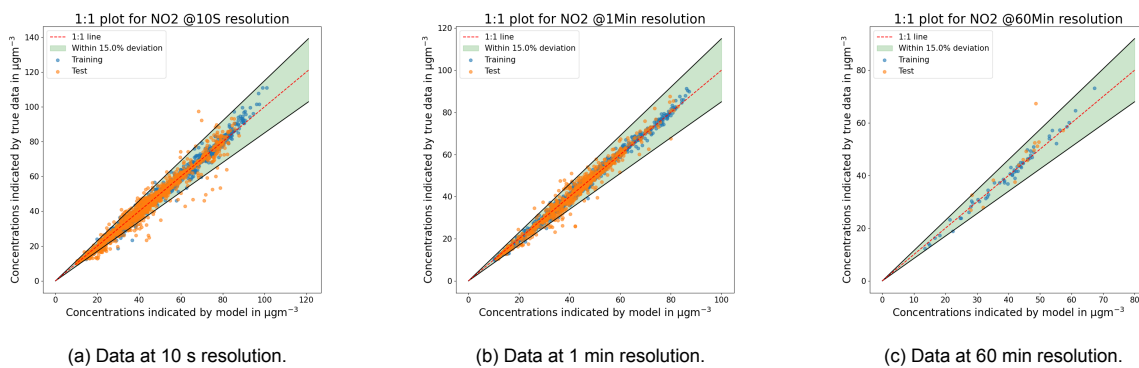


Figure 4.34: 1-to-1 plots for RF tuned calibration at Wijk aan Zee for NO<sub>2</sub>.

## 4.7. Final Calibration Model Selection

Both multivariate linear regression and random forest models have been constructed to convert the raw measurements into meaningful concentrations for CO, NO and NO<sub>2</sub>, at three temporal scales, 10

s, 1 min and 60 min. In total, there are thus six calibration models per species.

The RMSE performance of each model on the test set is visualised in Figure 4.35. Differences in RMSE are subtle for NO and NO<sub>2</sub>. It can be observed that at lowest temporal resolution (60 min), the RMSE is generally higher for the RF models. At finest temporal scale (10 s), the RF models outperform the MLR models. Larger discrepancies exist for CO, in which the RF performs better at 10 s and 1 min resolution.

Similarly, the correlation coefficients are visualised in Figure 4.36. Again, there are only subtle differences between most models, except for the NO calibration models at 60 min resolution, which is still unclear why this happens. RF model correlation is generally higher at higher temporal resolution, whereas the opposite is true for the MLR models.

Comparing the cross-validated RMSE metrics of the MLR models in Table 4.12 with the cross-validated RMSE metrics of the RF models presented in Table 4.17, it can be seen that the MLR models perform better at lowest temporal resolution (60 min). On the other hand, the RF models perform slightly better at medium temporal resolution (1 min), but perform up to two times better on the highest temporal resolution (10 s).

When looking at the test/train RMSE values of the random forest models presented in Table 4.16, it is clear that the performance on the train set is substantially better 8 out of 9 times, indicating overfitting. In some cases, the RMSE is up to 3 times higher on the test set compared to the training set.

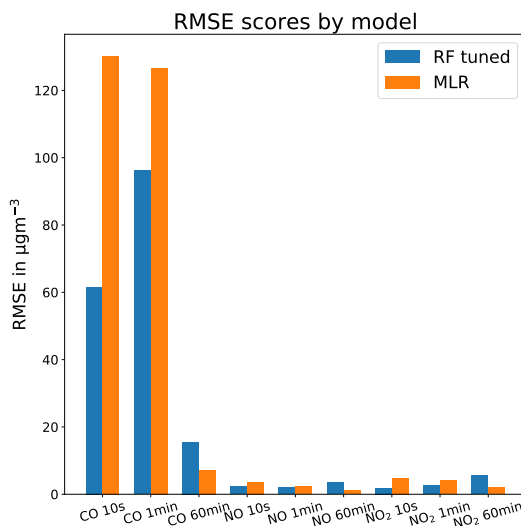


Figure 4.35: RMSE for different models applied to the Wijk aan Zee test data set.

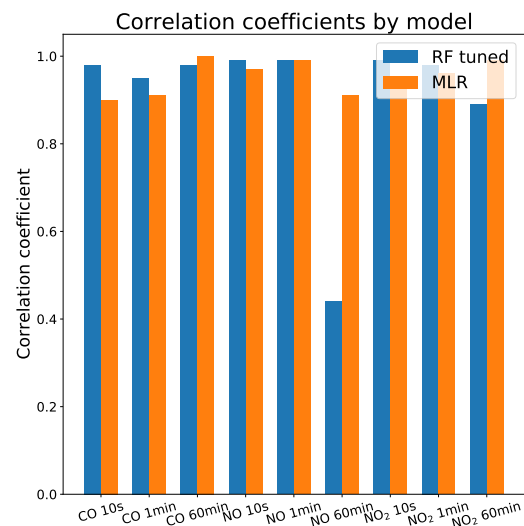


Figure 4.36: Correlation coefficients for different models applied to the Wijk aan Zee test data set.

Correctly quantifying both low and high concentrations of air pollutants is essential in further steps of the research. More specifically, it is expected that near Schiphol concentrations are generally low, but with high short-term peaks when aircraft operate nearby. Therefore, before making a final decision, the performance of correctly quantifying low and high concentrations is investigated. This is done by calculating the prediction error at times of low and high pollutant concentrations during the Wijk aan Zee experiment. To calculate the mean absolute prediction error at low concentrations, reference air quality measurements lower than the 50% quantile are included. The mean absolute prediction error at high concentrations is calculated with reference air quality measurements above the 90% quantile. Results of these calculations are summarised in Table 4.19 and Table 4.20. A visual representation of these results is presented in Figure 4.37 and Figure 4.38.

Table 4.19: Absolute prediction errors (difference) at concentrations lower than the 50% quantile of Wijk aan Zee test set for both models.

	CO 10 s		CO 1 min		CO 60 min		NO 10 s		NO 1 min		NO 60 min		NO <sub>2</sub> 10 s		NO <sub>2</sub> 1 min		NO <sub>2</sub> 60 min	
	MLR	RF	MLR	RF	MLR	RF	MLR	RF	MLR	RF	MLR	RF	MLR	RF	MLR	RF	MLR	RF
Mean error ( $\mu\text{g m}^{-3}$ )	24.64	11.70	19.37	14.45	6.70	11.30	1.99	0.24	1.28	0.34	0.78	2.31	3.84	0.73	3.30	1.55	1.86	2.76
Median error ( $\mu\text{g m}^{-3}$ )	19.47	6.23	15.51	10.15	6.65	9.15	1.65	0.10	1.01	0.23	0.48	2.24	3.11	0.24	2.57	0.81	2.01	2.42

Table 4.20: Absolute prediction errors (difference) at concentrations higher than the 90% quantile of Wijk aan Zee test set for both models.

	CO 10 s		CO 1 min		CO 60 min		NO 10 s		NO 1 min		NO 60 min		NO <sub>2</sub> 10 s		NO <sub>2</sub> 1 min		NO <sub>2</sub> 60 min	
	MLR	RF	MLR	RF	MLR	RF	MLR	RF	MLR	RF	MLR	RF	MLR	RF	MLR	RF	MLR	RF
Mean error ( $\mu\text{g m}^{-3}$ )	219.17	97.25	220.24	205.67	9.77	23.18	4.91	3.44	3.00	3.44	1.64	5.71	5.06	1.56	4.36	2.12	1.43	9.20
Median error ( $\mu\text{g m}^{-3}$ )	111.56	49.35	89.50	106.83	9.77	23.18	3.27	1.42	2.11	1.99	1.64	5.71	4.32	0.41	3.99	1.21	1.43	9.20

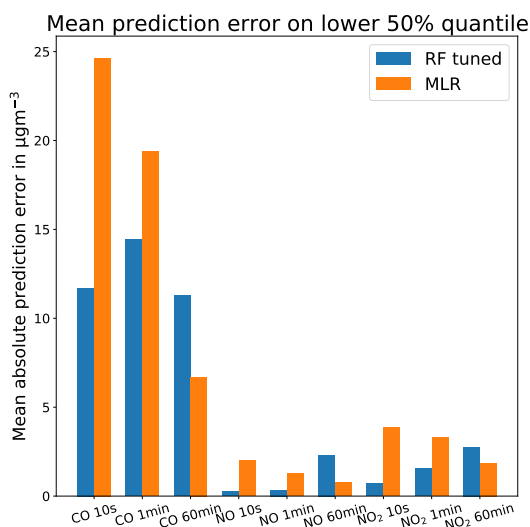


Figure 4.37: Prediction error in  $\mu\text{g m}^{-3}$  for concentrations lower than the 50% quantile for different models.

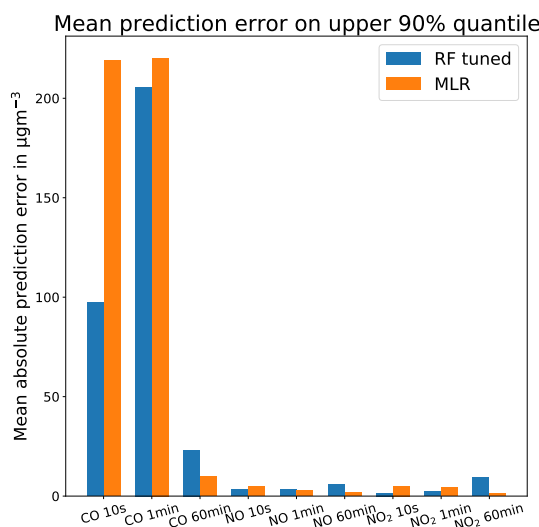


Figure 4.38: Prediction error in  $\mu\text{g m}^{-3}$  for concentrations higher than the 90% quantile for different models.

Given the fact that almost each random forest model has a strong overfitting tendency, which is confirmed by Table 4.16, it is discarded in the final model selection. In that case, three MLR models are left per species, which is a matter of selecting between three different temporal resolutions.

For the MLR models, the cross-validated RMSE values in Table 4.12, the peak quantification performance in Table 4.20 and baseline quantification performance in Table 4.19 indicate that the models at 60 min resolution perform best and the models at 10 s resolution worst. This makes sense, as during the construction of the 60 min models, the data is resampled from 3 s resolution to 60 min resolution, leading to a reduction in noise and errors and an increase in performance.

Selecting a suitable model also depends on the foreseen application, which is the quantification of short-term peak concentrations due aviation activities at Amsterdam Schiphol airport. Resampling the data to an hourly resolution is therefore not a preferred solution as this will reduce many of the short-term fluctuations which are critical for the assessment of individual aircraft operations. One could then argue to simply select the model with highest temporal resolution, but there is a concern over this signal. The real-time clock mounted on the sensor box's microcontroller slips over time in the order of seconds, every day. This possibly causes measurements to be impair with what the reference instrument indicates. Therefore, the best option is to take a step back in terms of temporal resolution and using the MLR model at 1 minute resolution. The final calibration equations for CO, NO and NO<sub>2</sub> are presented in Appendix J.

## 4.8. Calibration Model Integration

Each model is saved as a .pkl file using the *joblib* package in Python. The models can then be applied to unseen data, such as to the measurements at Schiphol airport. Figure 4.39 presents how the calibration model is integrated. Out of the data sets obtained during the three collocation experiments, only the data set obtained at Wijk aan Zee is actually used to develop the calibration models. One reason for this is that the sensor box was mounted closest to the reference analyser during this experiment, minimising delay and effects of local wind conditions. In addition, only during the Wijk aan Zee calibration experiment regulatory air quality data at 10 s resolution could be obtained.

Four data sets are obtained at Schiphol airport, which will be discussed in chapter 6. Each of these data sets is transformed using the Wijk aan Zee calibration models.

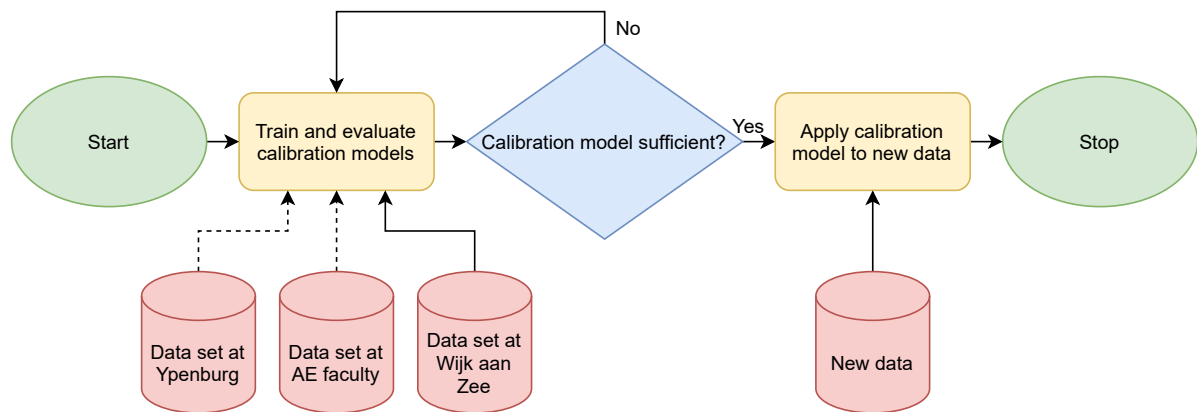


Figure 4.39: Block diagram of sensor box calibration model integration.

# 5

## Extracting Aviation-Attributable Air Quality Impacts

The goal of this thesis is to quantify short-term air quality impacts from aviation activities at Amsterdam Schiphol airport using the developed sensor box in this thesis. The sensor box measures total air quality concentrations, which is a build-up of multiple individual contributors. To correctly investigate the aviation-attributable impacts, it is thus desired to separate the aviation-attributable pollution signal from the rest. A data-driven approach is selected to do such separation. Aircraft activity data is then used to link the aviation-attributable impacts to certain activities. In addition, validating the extracted impacts is necessary to confirm the highly-experimental approach proposed in this thesis.

First, section 5.1 presents practical implementations for two types of aircraft activity data. Next, section 5.2 shows how weather information is obtained in the form of METAR messages for Schiphol airport, as wind speed and direction have a direct influence on pollution dispersion. Hereafter, section 5.3 presents the methodology to extract a baseline and local pollution signal. Hereafter, section 5.4 presents the methodology of linking the local pollution signals to aircraft activity. Finally, section 5.5 presents a validation methodology for the extracted impacts.

### 5.1. Aircraft Activity Data

Where section 2.5 presents a more general approach towards the use of aircraft activity data in pollution signal linking, this section presents a practical approach. First, subsection 5.1.1 presents the use of the implemented sound intensity sensor. Hereafter, subsection 5.1.2 presents in-depth how ADS-B data has been gathered and processed.

#### 5.1.1. Sound Intensity Measurements

A sound intensity sensor was added to the sensor box with the intention to detect nearby aircraft activity. An initial test at Schiphol airport indicated that the sensor was not accurate enough to quantify peaks from aviation. The problem was that the sensor's maximum response was already reached due to a strong blowing wind. DEMO has improved the sensor such that peaks only arise when the sound is loud enough. The sound intensity sensor can help in verifying the ADS-B data, whether indeed aircraft are passing by at certain times.

#### 5.1.2. ADS-B Data

The use of ADS-B data in this thesis is manifold. This subsection presents which ADS-B data sources are considered, how highly temporal ADS-B data is gathered and classified and finally the observed loss of data and inaccuracies.

#### The OpenSky Network

An ADS-B database has been constructed that takes flight information directly from the OpenSky live traffic API. More specifically, a script was written that accumulates the aircraft state vectors in real-time

from the OpenSky network and saves them to an SQL database. The OpenSky network receives ADS-B messages from all over the world, eventually leading to a very large database within minutes after deployment. Therefore, a filter was implemented to only keep flights that are in a square box of 30 km by 30 km centred around the Schiphol ATC tower. Each experiment carried out at Schiphol airport has a separate ADS-B database. A flow chart demonstrating how the ADS-B data has been gathered is presented in Figure 5.1. It works by first creating the database if it does not yet exist, else it simply opens the database. Then, a timer of three seconds is added to prevent sending too many requests to the OpenSky API. Hereafter, the returned message is checked for updates. If updates are present, these are written to the ADS-B database, else the program loops the query. The parameters obtained via the OpenSky API contain all variables presented in Table 5.1.

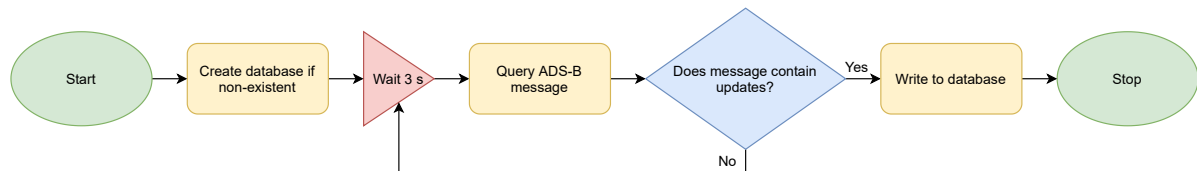


Figure 5.1: Schematic representation of ADS-B data querying.

Table 5.1: Parameters and units for ADS-B database [17].

Variable name	Refers to
baro_altitude	Barometric altitude in meters. Can be null.
callsign	Callsign of the vehicle (8 chars). Can be null if no callsign has been received.
geo_altitude	Geometric altitude in meters. Can be null.
heading	Track heading in decimal degrees clockwise from north (north=0°). Can be null.
icao24	Unique ICAO 24-bit address of the transponder in hex string representation.
last_contact	Unix timestamp (s) for the last update in general. This field is updated for any new, valid message received from transponder.
latitude	WGS-84 latitude in decimal degrees. Can be null.
longitude	WGS-84 longitude in decimal degrees. Can be null.
on_ground	Boolean value which indicates if the position was retrieved from a surface position report.
origin_country	Country name inferred from the ICAO 24-bit address.
position_source	Origin of this state's position: 0 = ADS-B, 1 = ASTERIX, 2 = MLAT
sensors	IDs of the receivers which contributed to this state vector. Is null if no filtering for sensor was used in the request.
spi	Whether flight status indicates special purpose indicator.
squawk	The transponder code aka Squawk. Can be null.
time_position	Unix timestamp (seconds) for the last position update. Can be null if no position report received by OpenSky within the past 15s.
velocity	Velocity over ground in m/s. Can be null.
vertical_rate	Vertical rate in m/s. A positive value indicates that the airplane is climbing. Can be null.

### Aircraft Activity Classification

To make use of the accumulated ADS-B data, classification of track activity is necessary. The ADS-B data contains tracks from ground support vehicles, which need to be separated from aircraft. In addition, there is a difference in pollution signature between take-off, landing and taxi. Therefore, also flights need to be classified according to their activity.

Tracks are classified according to six categories:

1. Take-off
2. Landing
3. On ground/taxi
4. Overflight
5. Surface vehicle

6. Unknown

A simple track classification algorithm has been developed and which is visualised in Figure 5.2. The script takes a unique track, belonging to an unique icao24 code and an unique callsign. This set is sorted ascending by time, and when referring to the "first trackpoint" in Figure 5.2, this means the first trackpoint in time of that track data set. Similarly, the "last trackpoint" is the last available trackpoint in time for a particular track. To preserve the quality of the classification, a threshold has been set to the minimum number of trackpoints in order to be classified. This threshold has been set equal to six, so in other words, a track will be classified if the track data set contains six or more trackpoints.

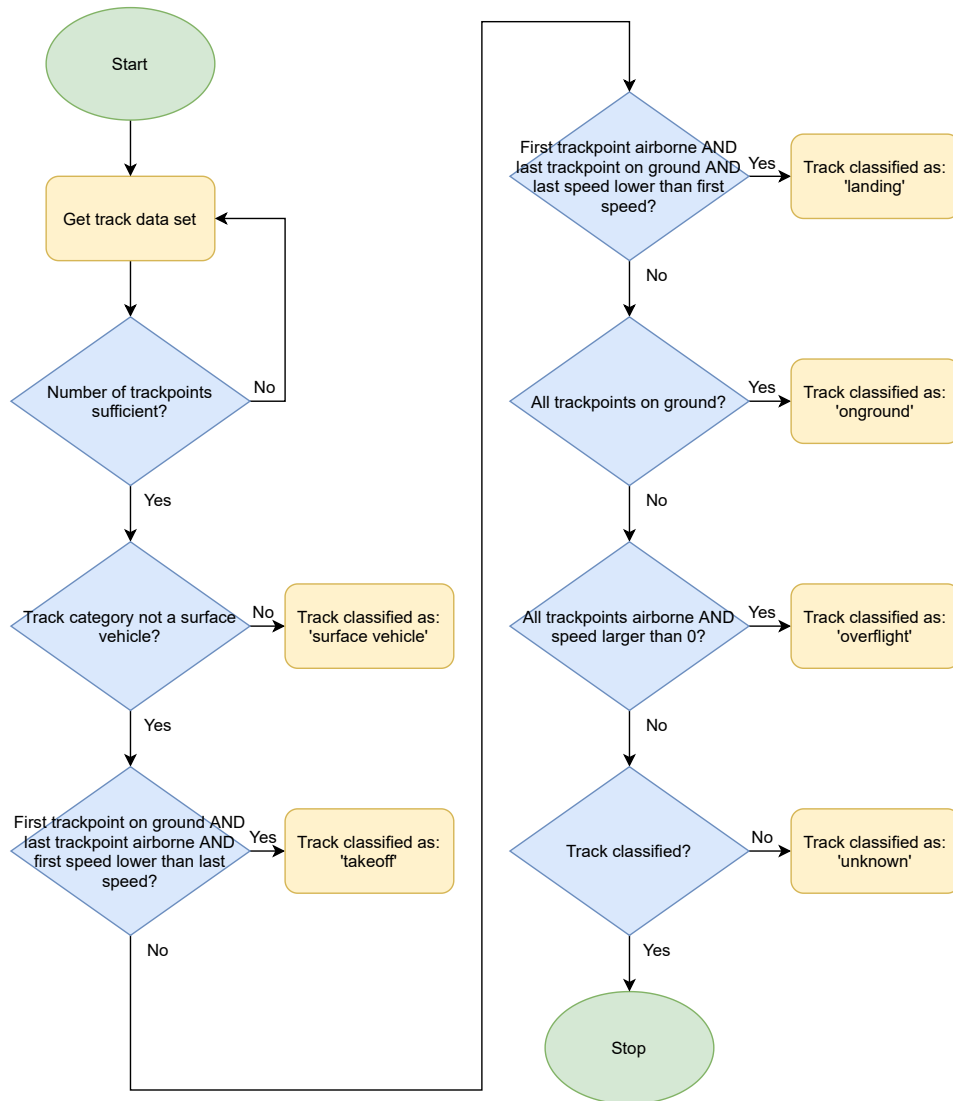


Figure 5.2: ADS-B track classification algorithm.

Aircraft specifications were obtained using the icao24 and the aircraft registration codes. Both the OpenSky metadata set (<https://opensky-network.org/datasets/metadata/aircraftDatabase.csv>) and the Dutch aircraft registry (<https://www.ilent.nl/onderwerpen/luchtvaartuigregister>) have been used to obtain the necessary aircraft information.

## 5.2. Weather Data

Weather data is a necessity as ambient conditions influence sensor box performance. Local weather data in the form of a METAR (Meteorological Terminal Aviation Routine Weather Report) is obtained in a similar manner as the ADS-B data. In real-time, updates from <https://www.checkwx.com/>

`weather/EHAM/metar` are requested and saved in a database. The received parameters with their units are summarised in Table 5.2. A METAR update is received generally every 30 minutes. An API key is necessary to receive messages, which can be obtained after registration on the website. A flow chart demonstrating how the METAR data has been gathered is presented in Figure 5.3.

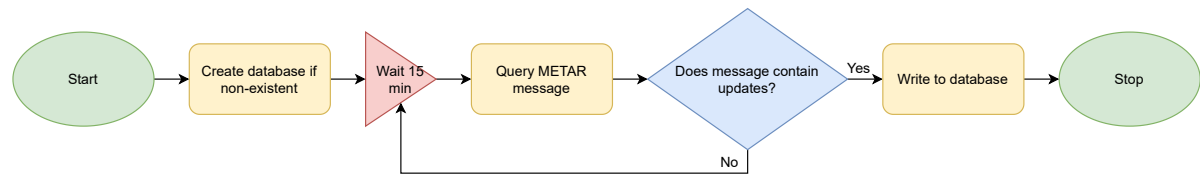


Figure 5.3: Schematic representation of METAR data querying.

Table 5.2: Parameters and units for local weather (METAR) database.

Variable name	Refers to
pressure	Atmospheric pressure in millibar.
dewpoint	Temperature at dew formation ° Celsius.
elevation	Airport elevation in meters.
flight_category	Flight category, VFR vs IFR.
humidity	Relative humidity in %
icao	ICAO airport code.
observed	Timestamp of update.
temperature	Temperature in ° Celsius.
visibility	Visibility in meters.
wind_speed	Wind speed in knots.
wind_direction	Wind direction in degrees.

### 5.3. Air Pollution Signals

The measured air quality concentration levels by the sensor box are total air pollution levels. These are a mixture of all the different contributing sources. In order to estimate the impact of aircraft, it is necessary to establish a baseline (or background) pollution signal. The methodology to establish the baseline pollution signal for the different species is presented in subsection 5.3.1. The methodology of establishing the local pollution signal, due to aviation activities only, is presented in subsection 5.3.2.

#### 5.3.1. Extracting the Background Pollution Signal

The developed methodology is inspired by Popoola et al. [56], who deploy 17 low-cost sensor boxes for a five-week period at London Heathrow airport, taking samples every 20 seconds. The baseline pollution signal in their case is the minimum concentration across the sensor box network. Mathematically, this approach can be described by Equation 5.1. The subscripts  $j$  and  $i$  represent the station number and point in time, respectively.

$$y_{baseline_i} = \min(y_{measured_{ij}}), \quad \forall i, j \in \mathbb{N} \quad (5.1)$$

In this thesis, only use of one sensor box is proposed. Therefore, the methodology proposed by Popoola et al. [56] is adjusted such that it can be used with a single sensor box. This is achieved by applying a rolling window of size  $t$  that extracts the minimum concentration within this window and equates it to the baseline.

$$y_{baseline_i} = \min(y_{measured_i}) , \quad \forall i \geq i - t \quad (5.2)$$

#### 5.3.2. Extracting the Local Pollution Signal

Apart from the baseline extraction methodology proposed by Popoola et al. [56], they also extract local pollution signals. In their case, the local signal is simply the total measured concentration minus the established baseline.

$$y_{local_i_j} = y_{measured_{i_j}} - y_{baseline_{i_j}}, \quad \forall i, j \in \mathbb{N} \quad (5.3)$$

In the case of a single sensor box, Equation 5.3 is adjusted to Equation 5.4. The local signal is then simply the measured total signal minus the baseline.

$$y_{local_i} = y_{measured_i} - y_{baseline_i}, \quad \forall i \in \mathbb{N} \quad (5.4)$$

Figure 5.4 displays the effect of applying such a minimum-extracting rolling window on the total measured concentrations for CO during the first experiment at Schiphol airport for a window size variation between 1 and 24. Similarly, Figure 5.5 shows such a signal for a window size variation between 1 and 500.

In general, it can be observed that the smaller the window size, the smaller the local pollution signal. This makes sense as the difference between the minimum and maximum within a small window of values is smaller. For larger window sizes, the difference between the minimum and maximum is generally larger, hence resulting in larger local pollution signals. At the point that the global minimum is reached, the local pollution signal becomes saturated. In that case, the baseline concentration is thus equal to simply the global minimum.

Since the goal is to extract aviation-attributable pollution signals only, it is decided to make the window size  $t$  such that it matches with the largest plume duration. In that case, only the aviation-attributable peaks are extracted from the total signal. The maximum plume duration is approximately equal to 2 minutes, but to avoid not fully capturing the peaks, maximum plume duration is assumed to be 2 minutes and 30 seconds. Using the sensor box measurements at 3 s resolution, this results in a window size  $t$  of 50 (150 s/3 s resolution).

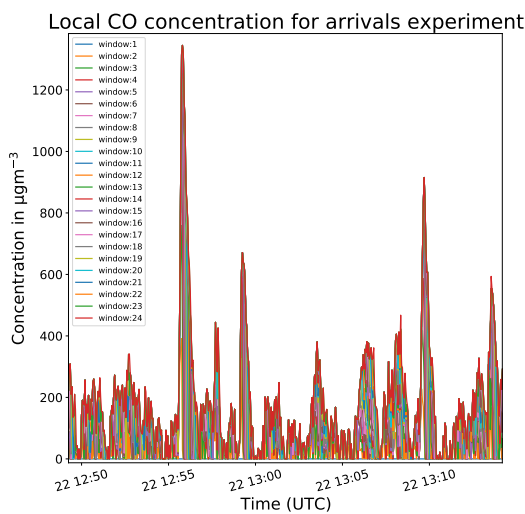


Figure 5.4: Local CO signal for window size variations between 1 and 24 during the first experiment at Schiphol airport.

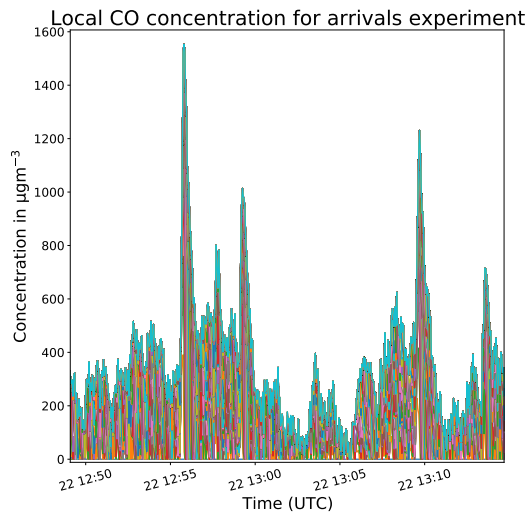


Figure 5.5: Local CO signal for window size variations between 1 and 500 during the first experiment at Schiphol airport.

## 5.4. Linking Local Pollution Signal to Aircraft Activity

The local pollution signal is based on the measured air quality levels only. The magnitude of this local pollution signal is most likely linked to the different types of aircraft activity near the sensor box, as well as the aircraft configuration. To confirm this hypothesis, the local pollution signal is linked to the aircraft activity database constructed in subsection 5.1.2.

The flight activity data set obtained via the aircraft activity classification algorithm presented in Figure 5.2 includes the time at which the trackpoint of each flight is closest to the sensor box. A subset is created around this time point, containing the sensor box measurements. This subset start 20 seconds

before the closest trackpoint and ends 20 seconds before the closest trackpoint of the next aircraft activity. A visual representation of this strategy is presented in Figure 5.6. Adding the 20 seconds delay to the front of the subset accounts for the low temporal resolution of the ADS-B data.

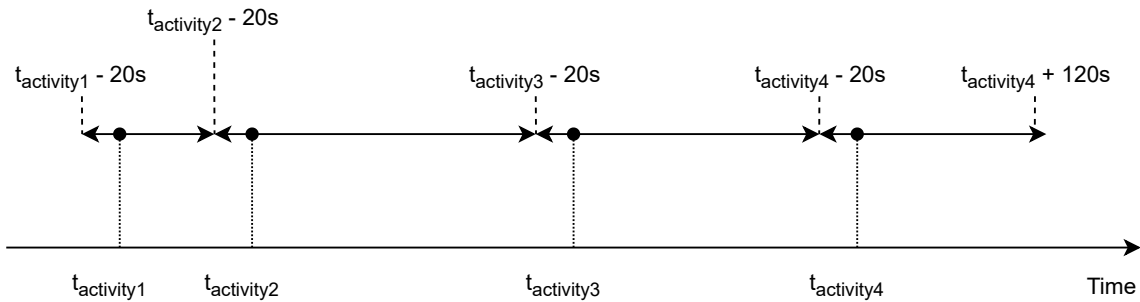


Figure 5.6: Graphical representation of coupling local pollution signal to aircraft activity.

Linking local pollution signals to aircraft activity is integrated in the Python code as presented in Figure 5.7.



Figure 5.7: Flow diagram of how the local signal coupling integrates in the code.

## 5.5. Validation Methodology

Validation is crucial to determine whether the air quality concentrations returned by the sensor box are of an acceptable level. The literature study proposed the use of an air quality box model to validate the measurements. On further consideration, this box model is too coarse to quantify pollutant concentrations on the required spatiotemporal scale and is therefore discarded.

Barrett et al. [26] investigate the impacts of single aircraft plume dynamics on local air quality. They formulate a three-dimensional integral plume model to model aircraft exhaust plumes at airports. Apart from formulating the plume dynamics, they assume a top-hat pollution concentration profile with the concentration described by Equation 5.5, where  $E$  is the emission rate,  $u$  the fluid velocity and  $R$  the plume radius.

$$\chi = \begin{cases} \frac{E}{\pi u R^2} & \text{within the plume,} \\ 0, & \text{otherwise} \end{cases} \quad (5.5)$$

Relationships for  $u$  and  $R$  are derived using the conservation of mass and momentum, leading to the final implementable plume equation given in Equation 5.6. The entrainment coefficient  $\alpha$  is an experimentally obtained factor to parameterise the mixing of the plume with the ambient fluid.  $S$  is the distance along the wind streamline to the receptor.

$$\chi = \begin{cases} \frac{E}{\pi R_0 u_0 (2\alpha S + R_0)} & \text{within the plume,} \\ 0, & \text{otherwise} \end{cases} \quad (5.6)$$

The emission rate  $E$  of a particular species in a certain aircraft operating mode can be obtained by multiplying the fuel flow with the corresponding emission index. The initial plume radius  $R_0$  is set equal to the engine fan diameter, obtained via an online jet engine database [7]. The flow is assumed to be pure momentum jet and thus  $\alpha$  is set equal to 0.057 [53]. Due to the large discrepancy between the effective and actual exhaust velocities, the actual jet engine exhaust velocity  $u_0$  is obtained via experiments on a B787 [24]. The measured exhaust velocities for the B787 in different operating modes are then generalised to other aircraft engines. These velocities are summarised in Table 5.3.

Table 5.3: Measured jet engine exhaust velocities at the horizontal stabiliser of a B787 [24].

Mode	Measured exhaust velocity in m/s
Idle	15.56
Breakaway	22.22
Takeoff	44.72

It should be mentioned that this model is rather a simple calculation. First of all, the calculation assumes that the pollutant species is spread homogeneously across the plume area. In addition, exceeding the plume boundaries results in the concentration being zero. Secondly, this calculation does not incorporate the effects of chemical transformations.



# 6

## Experimental Set-up

The purpose of this chapter is to explain how the different monitoring experiments at Schiphol airport are set-up. Four separate experiments have been executed at Schiphol airport, each serving a different purpose. First, an overview is given in section 6.1. Hereafter, the first experimental set-up is presented in section 6.2. The second experimental set-up is given in section 6.3. The third experimental set-up is presented in section older 6.4. Finally, the fourth experimental set-up is presented in section 6.5.

These experiments at Schiphol airport have been executed without causing any inconvenience to aircraft, radar systems and airport in general.

### 6.1. Overview

An overview with the sensor box locations, air traffic and local wind conditions in a single visualisation is presented in Figure 6.1.

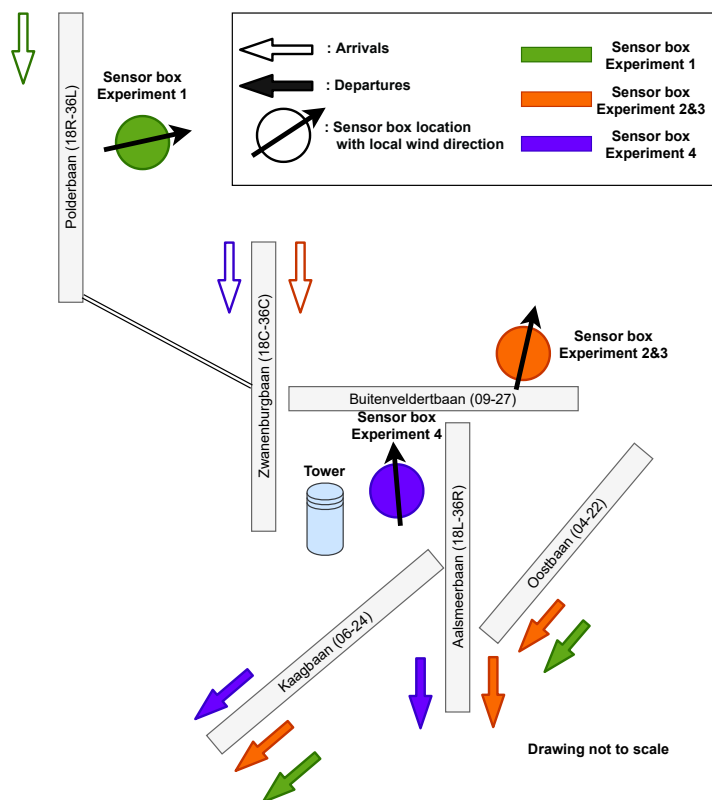


Figure 6.1: Overview of sensor box locations for the four measurement experiments at Amsterdam Schiphol airport.

## 6.2. Experiment 1: Arrivals on the Polderbaan

The first experiment at Schiphol airport was carried out Friday 22 January 2021, near the Polderbaan runway. The Polderbaan was selected as an initial experiment location due to its planned closure from 25 January to 26 April. The sensor box was configured according to the first iteration, presented in subsection 3.2.3. An indication for its location near the runway is visualised Figure 6.2. A summary of the experiment details is given in Table 6.1. A wind rose was constructed using wind data for the measurement period, visualised in Figure 6.3. The purpose of this experiment is twofold. First of all, it serves as a proof that the sensor box can pickup aviation-attributable pollution signals. Secondly, to quantify the impacts of aircraft landings.

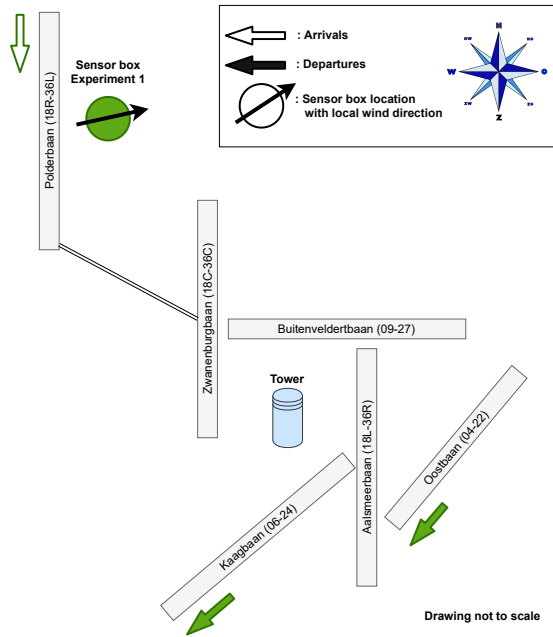


Figure 6.2: Sensor box location during first experiment.

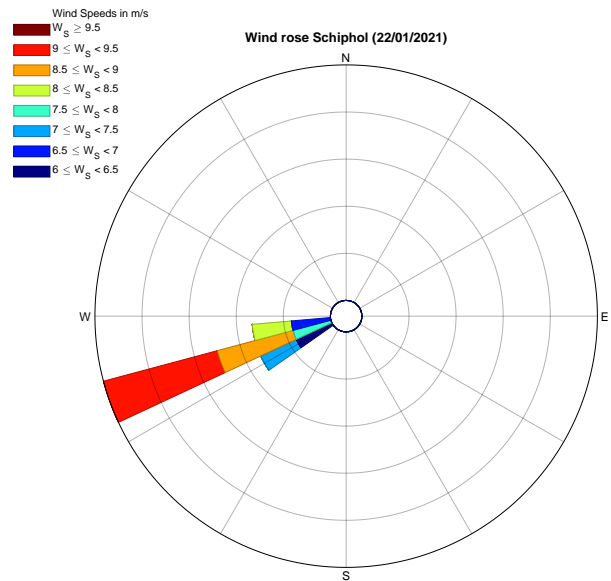


Figure 6.3: Wind rose during first experiment.

Table 6.1: Specifications of the first measurement experiment at Schiphol airport.

Parameter	
Date	22 January 2021
Start measurements	2021-01-22 08:47:31 UTC
End measurements	2021-01-22 15:00:56 UTC
Sensor box latitude	52°20'53.08"N
Sensor box longitude	4°42'48.21"E
Sensor box configuration	Iteration 1, wind/rain protection maximally opened.
Closest distance to runway	200 meters
Sample rate	1 reading for all sensors every 2-3 seconds

In addition, aircraft activity data was gathered in the form of ADS-B data. A reconstruction of all recorded landings is presented in Figure 6.4, along with the sensor box location for that measurement experiment.

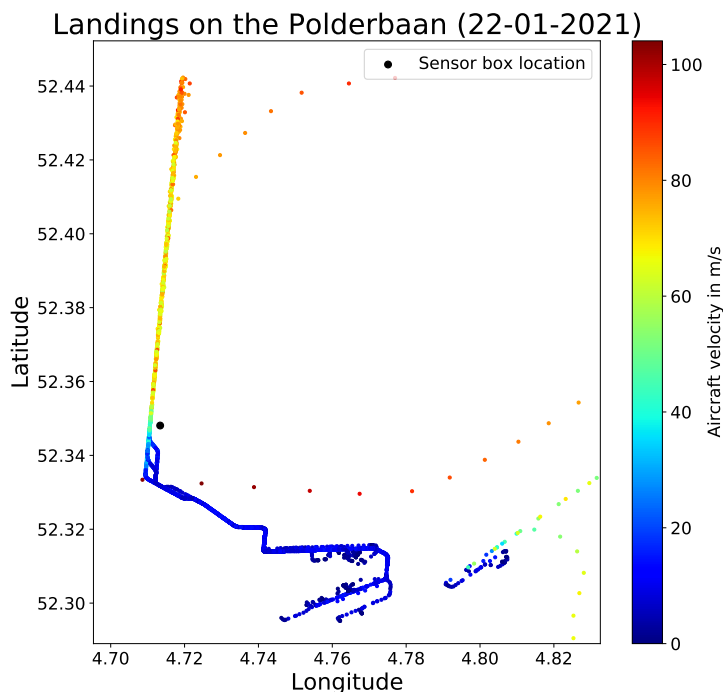


Figure 6.4: Trackpoints of all landings during first experiment at Schiphol airport.

### 6.3. Experiment 2: Departures on the Aalsmeerbaan and Kaagbaan

The second experiment at Schiphol airport was carried out Wednesday 17 February 2021, near the crossing of the Aalsmeerbaan and Buitenveldertbaan runways. Due to persistent southwesterly winds, this location has been selected to monitor takeoffs. The sensor box was configured according to the second iteration, presented in subsection 3.2.4. An indication for its location near the runway is visualised Figure 6.5. A summary of the experiment details is given in Table 6.2. A wind rose was constructed using wind data for the measurement period, visualised in Figure 6.6. The purpose of this experiment is to quantify aviation-attributable impacts from take-off and taxi activities on both the Aalsmeerbaan and Kaagbaan runways. No measurements were taken within the airport's fence line.

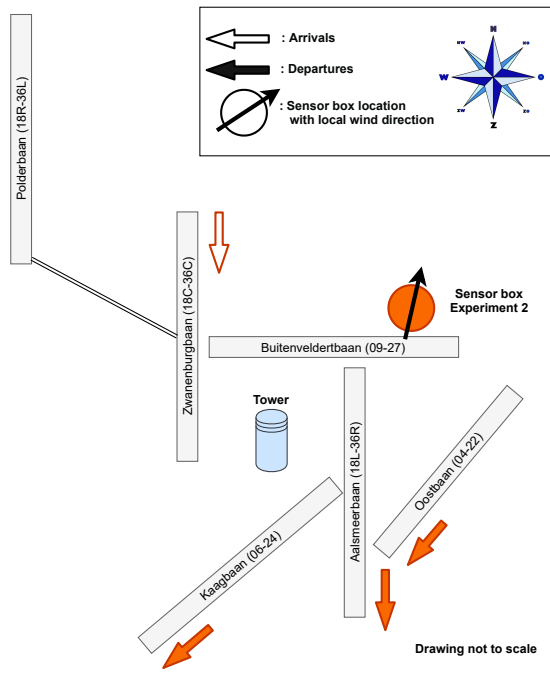


Figure 6.5: Sensor box locations during second experiment.

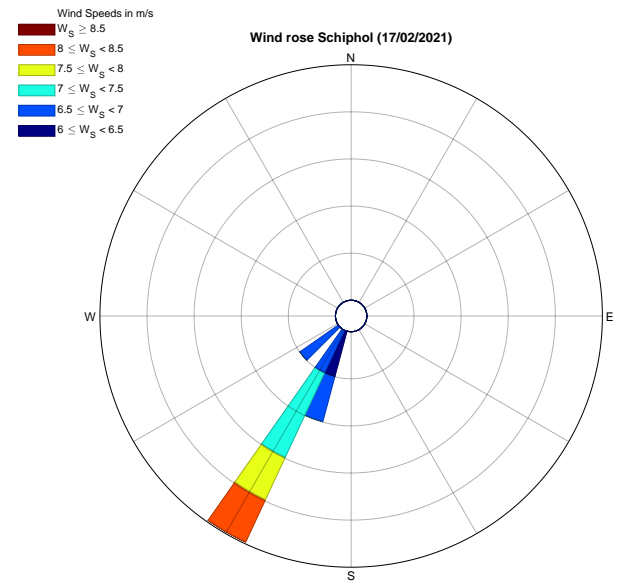


Figure 6.6: Wind rose during second experiment.

Table 6.2: Specifications of the second measurement experiment at Schiphol airport.

Parameter	
Date	17 February 2021
Start measurements	2021-02-17 07:16:17 UTC
End measurements	2021-02-17 09:48:33 UTC
Sensor box latitude	52°19'21.18"N
Sensor box longitude	4°47'2.61"E
Sensor box configuration	Iteration 2, wind/rain protection maximally opened.
Closest distance to runway	300 meters
Sample rate	1 reading for all sensors every 2-3 seconds

Again, aircraft activity data was gathered in the form of ADS-B data. A reconstruction of all recorded departures is presented in Figure 6.7, along with the sensor box location.

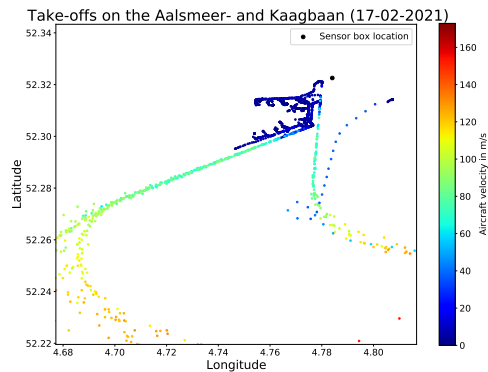


Figure 6.7: Trackpoints of all departures during the second experiment at Schiphol airport.

### 6.4. Experiment 3: Departures on the Aalsmeerbaan and Kaagbaan

The third experiment at Schiphol airport was carried out Friday 19 February 2021. The sensor box location is very similar to that of the second experiment. However, a small shift towards the left was necessary to stay downwind the aircraft exhaust. The sensor box was configured according to the second iteration, presented in subsection 3.2.4. An indication for its location near the runway is visualised Figure 6.8. A summary of the experiment details is given in Table 6.3. A wind rose was constructed using wind data for the measurement period, visualised in Figure 6.9. The purpose of this experiment is to quantify aviation-attributable impacts from take-off and taxi activities on both the Aalsmeerbaan and Kaagbaan runways, but now for a longer period of time compared to the second experiment. Again, no measurements were taken within the airport’s fence line.

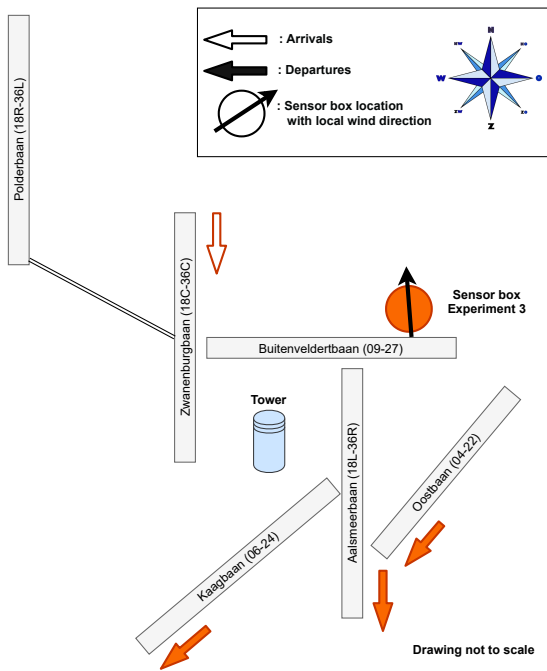


Figure 6.8: Sensor box location during third experiment.

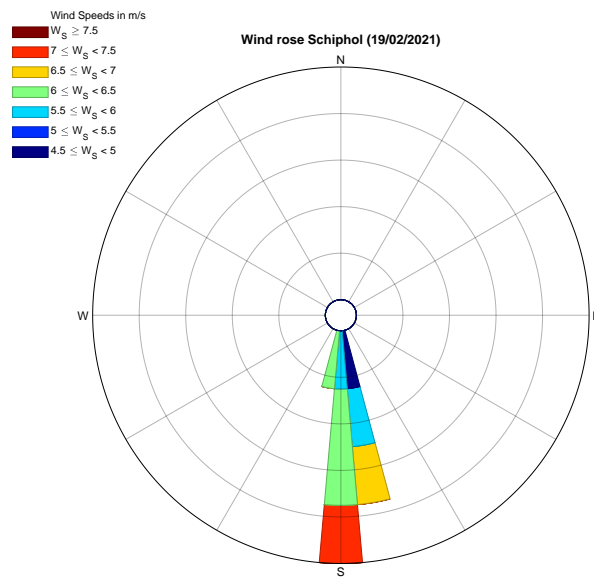


Figure 6.9: Wind rose during third experiment.

Table 6.3: Specifications of the third measurement experiment at Schiphol airport.

Parameter	
Date	19 February 2021
Start measurements	2021-02-19 07:34:14 UTC
End measurements	2021-02-19 10:55:51 UTC
Sensor box latitude	52°19'27.13"N
Sensor box longitude	4°46'51.29"E
Sensor box configuration	Iteration 2, wind/rain protection maximally opened.
Closest distance to runway	320 meters
Sample rate	1 reading for all sensors every 2-3 seconds

Very similar to the second experiment, reconstructions of the departures during the third experiment are presented in Figure 6.10. Due to the similarities between measurement experiment two and three, their results will be presented and discussed together.

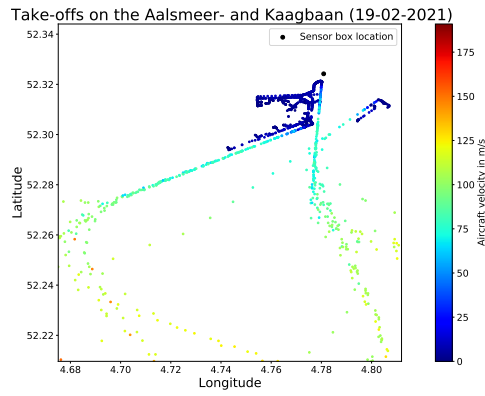


Figure 6.10: Trackpoints of all departures during the third experiment at Schiphol airport.

### 6.5. Experiment 4: Taxi Measurements on Airport Apron

The fourth and final experiment at Schiphol airport was carried out Friday 30 March 2021. The sensor box was taken within the airport fencing and configured according to the second iteration, presented in subsection 3.2.4. An indication for its location near the runway is visualised in Figure 6.11. Four measurement locations were selected in the end, which are visualised in more detail in Figure 6.13. A summary of the experiment details is given in Table 6.4. The sensor box coordinates over time are presented in Table 6.5. A wind rose was constructed using wind data for the measurement period, visualised in Figure 6.12. The purpose of this experiment is to quantify aviation-attributable impacts from nearby taxi activities at the intersection of the Aalsmeerbaan and Buitenveldertbaan runways.

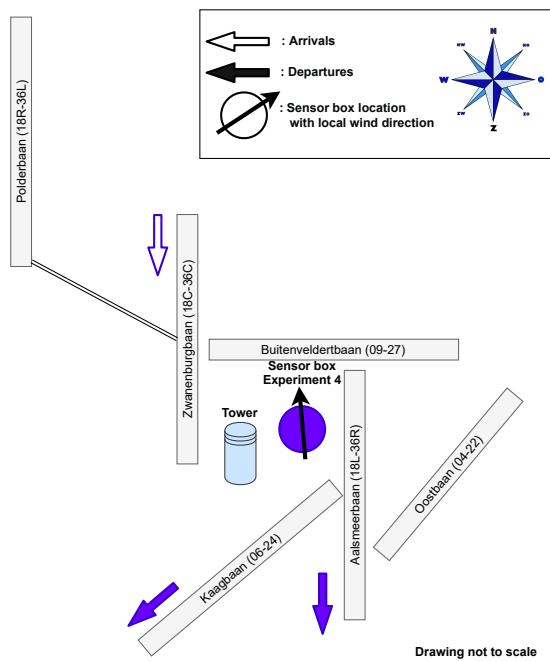


Figure 6.11: Sensor box locations during fourth experiment.

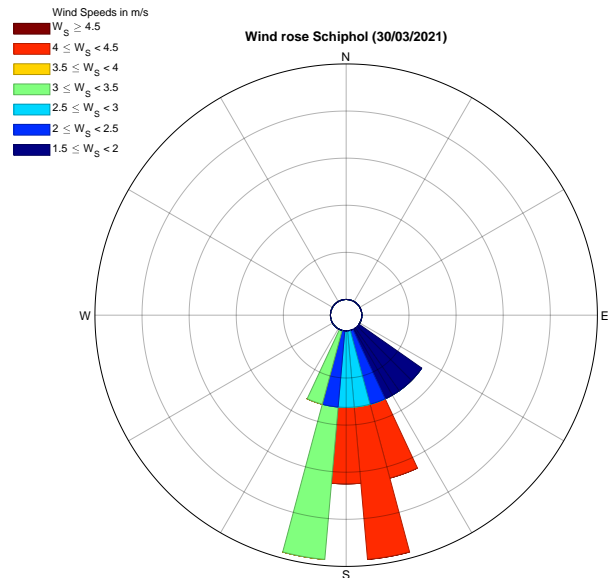


Figure 6.12: Wind rose during fourth experiment.



Figure 6.13: Detailed measurement locations for fourth experiment at Schiphol.

Table 6.4: Specifications of the fourth measurement experiment at Schiphol airport.

Parameter	
Date	30 March 2021
Start measurements	2021-03-30 07:46:00 UTC
End measurements	2021-03-30 13:41:00 UTC
Sensor box latitude	see Table 6.5
Sensor box longitude	see Table 6.5
Sensor box configuration	Iteration 2, wind/rain protection maximally opened.
Closest distance to runway	270 meters
Sample rate	1 reading for all sensors every 2-3 seconds

Table 6.5: Sensor box coordinates over time during fourth measurement experiment at Schiphol airport.

From (UTC)	To (UTC)	Latitude	Longitude
2021-03-30 07:45:00	2021-03-30 08:30:00	52.311846	4.774311
2021-03-30 08:50:00	2021-03-30 10:30:00	52.314401	4.769451
2021-03-30T10:50:00	2021-03-30T11:29:00	52.314921	4.772720
2021-03-30T11:30:00	2021-03-30T13:40:00	52.313486	4.775148

During the fourth experiment, aircraft activity data was gathered in the form of ADS-B and ground radar data. Figure 6.14 presents a reconstruction of tracks nearby the sensor box from the ground radar. Figure 6.15 presents these tracks via the OpenSky ADS-B data.

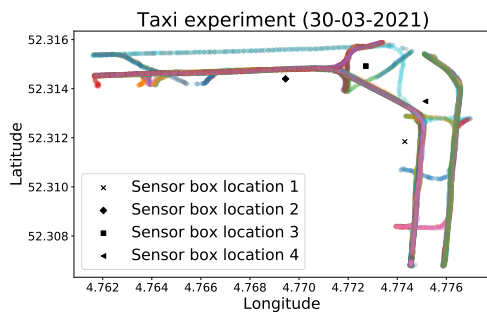


Figure 6.14: Trackpoints during the fourth experiment at Schiphol airport via ground radar data.

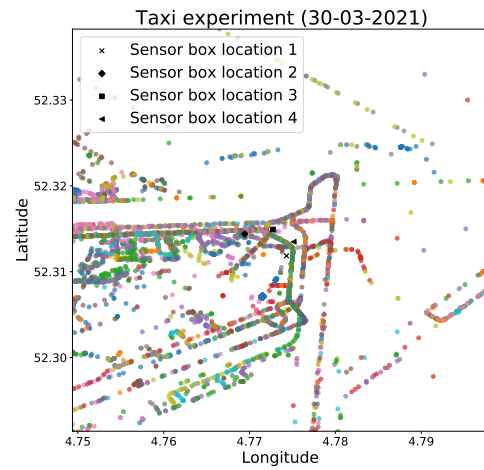


Figure 6.15: Trackpoints during the fourth experiment at Schiphol airport via ADS-B data.

# 7

## Results

In this chapter, the results of the four Schiphol monitoring experiments are disclosed, immediately followed by discussion. The results of experiment two and three are combined due to their similar objective and set-up. The results are limited to aircraft that come within a 1100 m radius from the sensor box as this allows including departures on the Aalsmeerbaan further away from the sensor box during the second and third experiment. In addition, a threshold was set before linking aircraft to a local signal as many times the local signal is simply equal to more or less the background concentration. For CO this threshold is  $150 \mu\text{g m}^{-3}$ , for NO and NO<sub>2</sub> the threshold is set to  $25 \mu\text{g m}^{-3}$ .

First, section 7.1 presents the results of the first experiment at Schiphol airport, which concerns arrivals on the Polderbaan. Hereafter, results of the second and third experiment, which are departures on the Aalsmeerbaan and Kaagbaan are presented in section 7.2. Next, the results of the taxi experiment on the apron are presented in section 7.3. Finally, section 7.4 presents a global discussion concerning the obtained results.

### 7.1. Experiment 1: Arrivals on the Polderbaan

The results of the first experiment are presented in this section. First, time-series measurements for the total signal are presented along with the decomposed local signal in subsection 7.1.1. Next, subsection 7.1.2 presents the results using the local air quality signal coupled to the flight activity data. Hereafter, the validation results are presented in subsection 7.1.3. Finally, the discussion of these results is presented in subsection 7.1.4.

The decomposed baseline pollution signals as well as a timeline of aircraft activity are presented in Figure D.1 and Figure C.1 in Appendix D and Appendix C, respectively. The sound intensity measurements combined with flight activity from the ADS-B data are presented in Figure G.1 in Appendix G.

#### 7.1.1. Time-Series Measurements

Time-series data of the sensor box measurements are presented in the form of total and local pollution signals, visualised in Figure 7.1 and Figure 7.2, respectively. The total signal is obtained by applying the calibration model to the raw sensor box data and reflects the calibrated ambient concentrations. The local signal is the total signal minus the extracted baseline signal and reflects the contributions of individual aircraft activity. The aircraft types visualised in Figure 7.1 are the flights that were visually spotted at the airport.

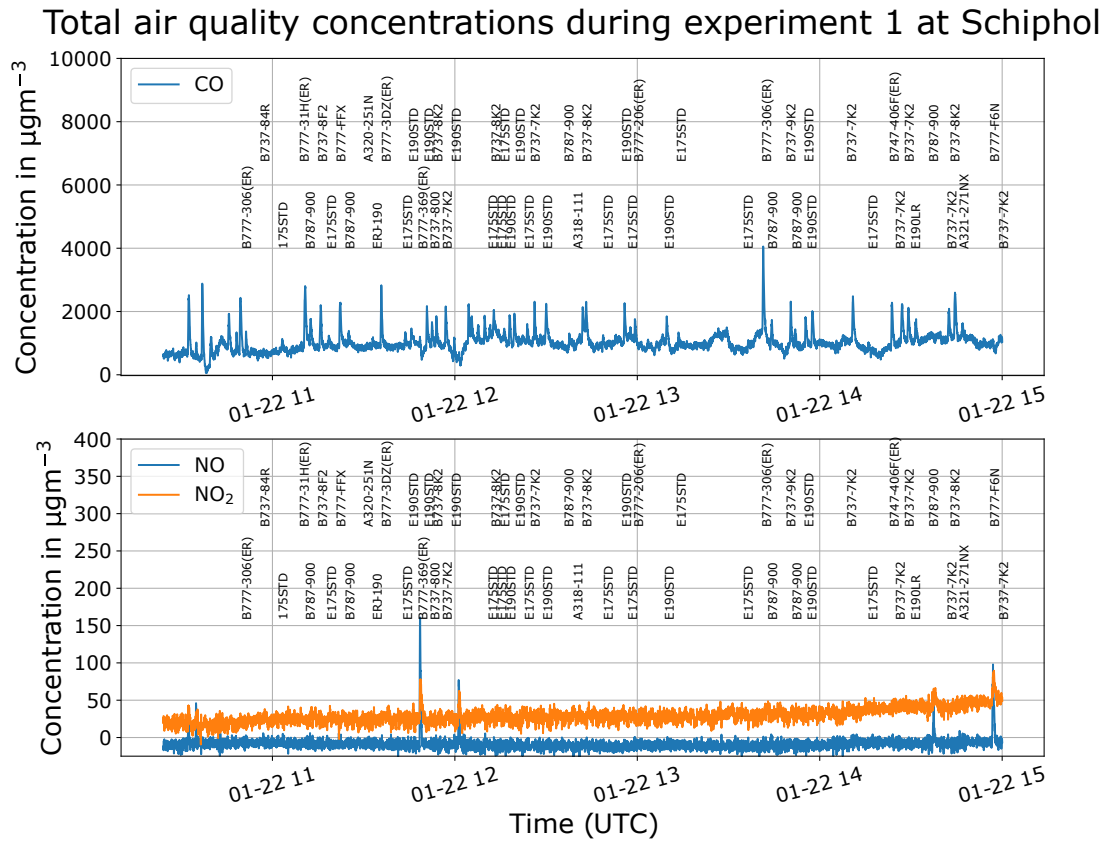


Figure 7.1: Time-series visualisation of total air quality measurements for first experiment with aircraft types of landing aircraft on the Polderbaan.

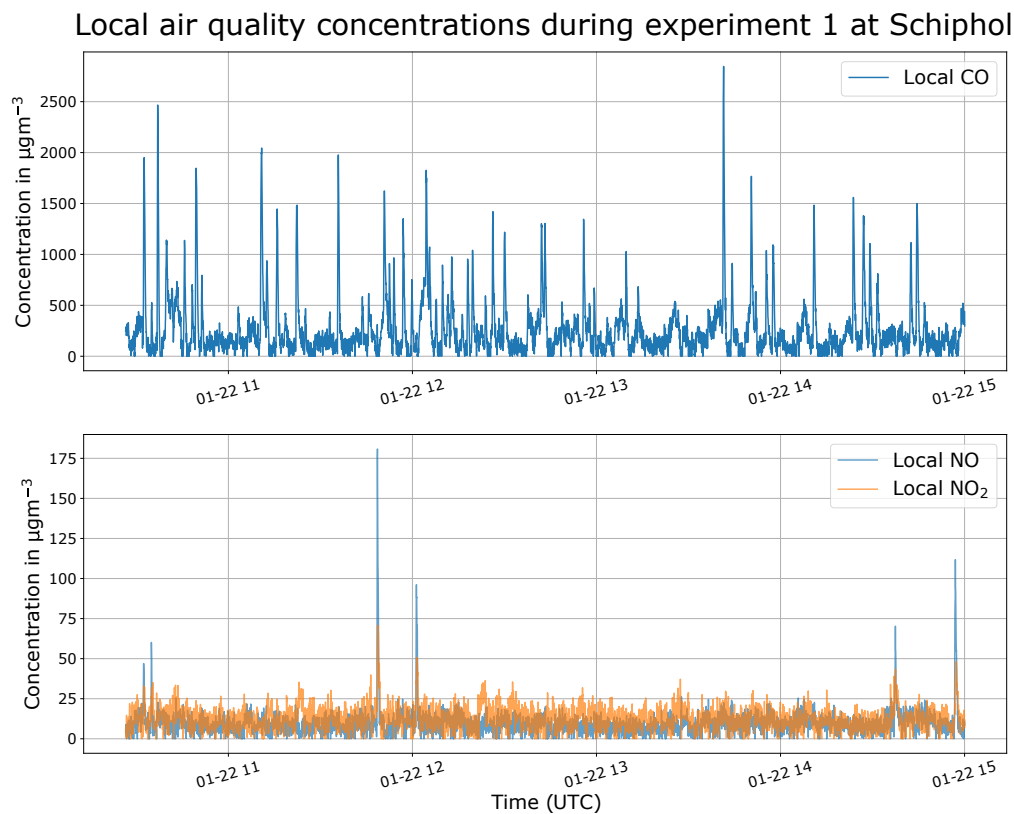


Figure 7.2: Time-series visualisation of decomposed local air quality signal for first experiment.

### 7.1.2. Analysis using Flight Activity Coupled to Local Signal

Using the pollutant concentration coupled to each flight, it is possible to analyse specific aircraft and engine configurations in more depth. In addition, it is possible to investigate the pollution signal of specific aircraft.

The local air quality impacts per aircraft type and per engine configuration are visualised via box plots. These box plots are constructed per aircraft type and per engine configuration only if three or more data points are available. Swarm plots for the full data set, including the sets where less than three data points are available for a certain aircraft type or engine configuration are presented in Appendix E. For the first experiment, these box plots are presented for CO and NO<sub>2</sub> in Figure 7.3, Figure 7.4, Figure 7.5 and Figure 7.6.

Individual pollution signals for CO, NO and NO<sub>2</sub> are visualised in Figure 7.7, Figure 7.8 and Figure 7.9. The horizontal axis in these plots is the time in seconds since the aircraft was closest to the sensor box. It starts at -20 s to account for inaccuracies in the determination of the closest point to the sensor box.

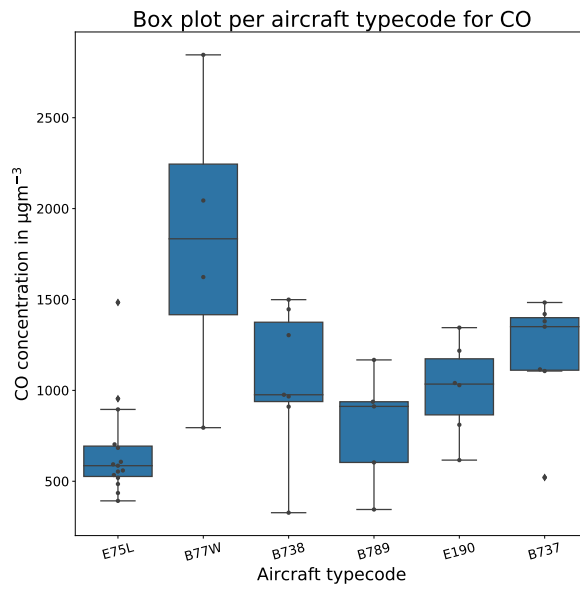


Figure 7.3: Local CO impact per aircraft type for landings during the first experiment.

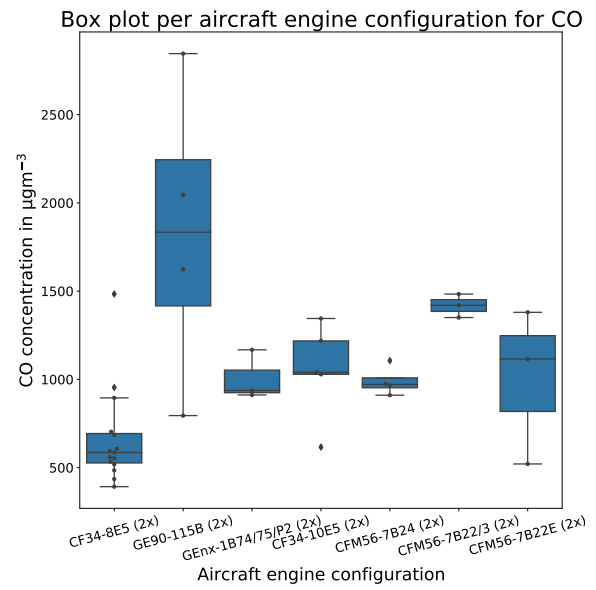


Figure 7.4: Local CO impact per aircraft engine configuration for landings during the first experiment.

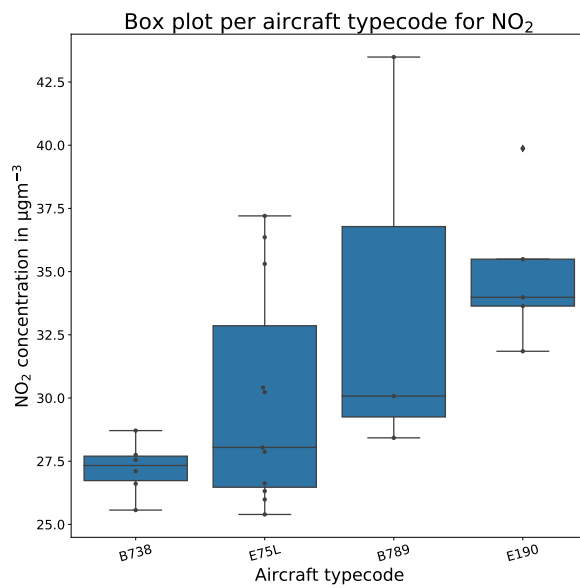


Figure 7.5: Local NO<sub>2</sub> impact per aircraft type for landings during the first experiment.

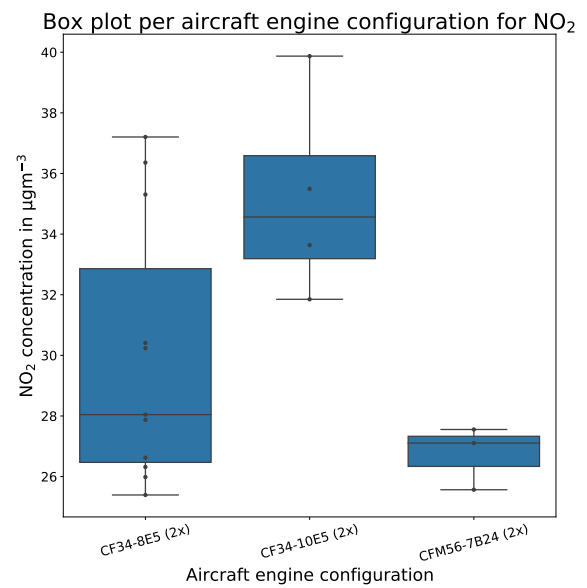


Figure 7.6: Local NO<sub>2</sub> impact per aircraft engine configuration for landings during the first experiment.

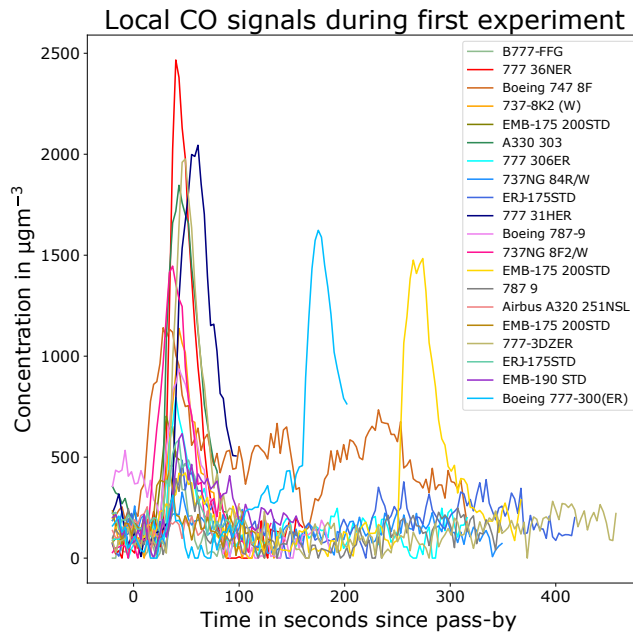


Figure 7.7: Local signals for CO for different aircraft during first experiment.

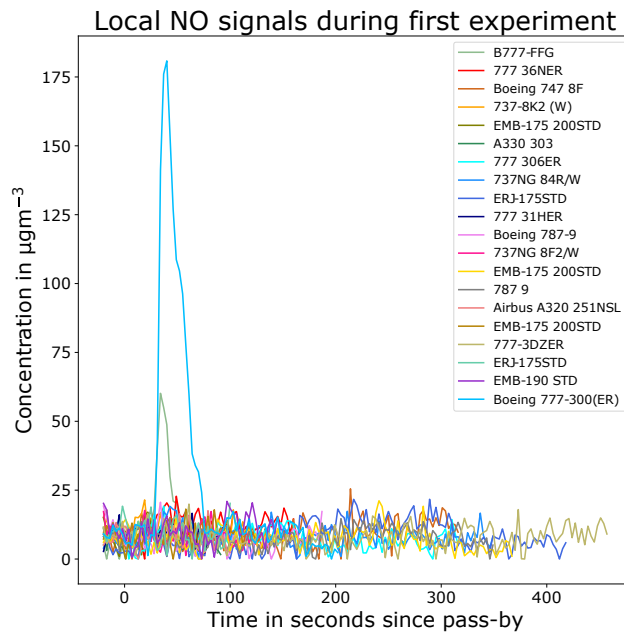


Figure 7.8: Local signals for NO for different aircraft during first experiment.

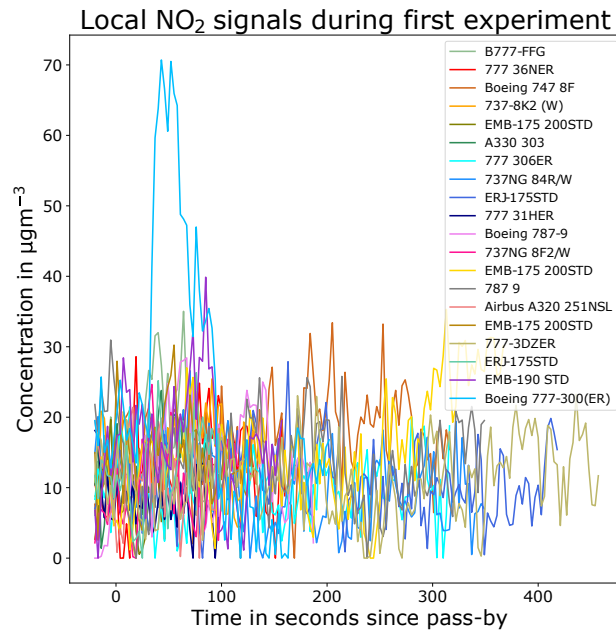


Figure 7.9: Local signals for NO<sub>2</sub> for different aircraft during first experiment.

### 7.1.3. Validation Results

Based on the validation method presented in section 5.5, a value is calculated for individual CO and NO<sub>x</sub> impacts of aircraft activity. These values are then compared with the measured local impact. Not for every aircraft a value could be calculated due to missing engine information. Figure 7.10 and Figure 7.11 present these comparisons for CO and NO<sub>x</sub> respectively.

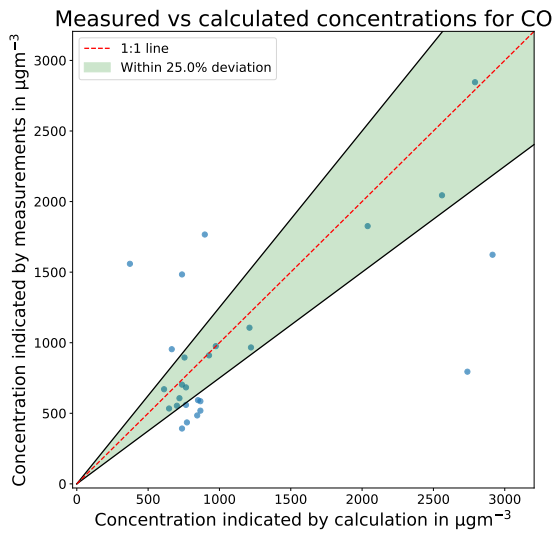


Figure 7.10: Validation results for CO for first measurement experiment.

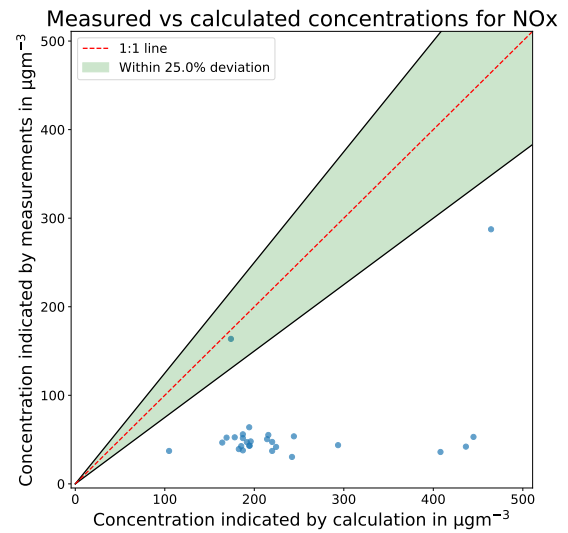


Figure 7.11: Validation results for NO<sub>x</sub> for first measurement experiment.

The average wind speed during the measurement period is 15.1 knots, which corresponds to 7.8 m/s. The shortest distance between the sensor box and the runway is 200 meters during this experiment, as presented in Table 6.1. A simple estimate for the plume to reach the sensor box is then simply

distance divided by velocity, resulting in a plume travel time of 25.6 seconds. In Figure 7.7, it can be seen that the CO concentration has a sharp increase after ~25-30 seconds, which is in line with the earlier calculation. For completeness, the METAR data is provided in Table I.1 in Appendix I.

#### 7.1.4. Discussion

The track points in Figure 6.4 are oriented west of the sensor box location. Looking at the wind rose presented in Figure 6.3, it can be seen that the wind is dominantly coming from the west with speeds below 10 m/s. The combination of these two circumstances results in the total measured concentrations visualised in Figure 7.1 and the locally decomposed signals in Figure 7.2. In Figure 7.1, it can be observed that many of the CO peaks are lined-up with landings on the Polderbaan. The orientation of the Polderbaan with respect to the airport combined with the wind conditions for that day have largely contributed to this. It should also be said that the presence of peaks reduces drastically for the NO and NO<sub>2</sub> measurements. In Figure 7.1, it is clear that only the larger aircraft such as B77W, B744, B789 and B77L can be linked to peaks. In addition, it can be seen that at times when there are no landings, the NO and NO<sub>2</sub> signals look very similar to times when there is aircraft activity of smaller to medium size aircraft, in some cases even large size aircraft.

It is still unknown why only some of the NO and NO<sub>2</sub> peaks are picked up. One of the reasons can be the use of thrust reversers. As indicated in subsection 2.4.3, a previous study found that the average thrust reversal use is 16 seconds. During thrust reversal, the thrust is increased from idle to a certain setting, which results in more NO<sub>x</sub> and less CO emissions. The NO and NO<sub>2</sub> peaks in that case would be explained by aircraft having thrust reversal active by the time they pass by the sensor box. Thrust reversal is generally deactivated after touch-down as thrust reversal at lower aircraft roll speeds increases the risk of the engines blowing debris in the air [18]. All observed aircraft had already touched-down when passing by the sensor box.

During this experiment, several times the same aircraft type has landed or different aircraft but with the same engine configuration. This allows investigating the coherence between the individual aircraft and engines. As can be seen in Figure 7.3, the impacts for CO can be as high as ~3000 µgm<sup>-3</sup> in the case of the B77W. Most data is available for the E75L with a median impact of ~550 µgm<sup>-3</sup>. Figure 7.4 presents these results per engine. Variations are largest for the GE90-115B where impacts can be as low as ~800 µgm<sup>-3</sup> and as high as ~3000 µgm<sup>-3</sup>. Impacts for NO<sub>2</sub> are smaller, with variations between the threshold value (25 µgm<sup>-3</sup>) and values up to ~40 µgm<sup>-3</sup>.

The individual pollution signals for CO, NO and NO<sub>2</sub> indicate that most of the peaks are present for CO. In addition, it can be seen that the majority of peaks group together around approximately 50 s after being closest to the sensor box. There are however still peaks around ~200 s and ~300 s, which can be caused due to the nature of the extraction algorithm. To be more specific, not all flights are recorded by the ADS-B, so these peaks at ~200 s and ~300 s are most likely due to an undetected flight arriving after a detected flight. Another reason could be that the closest distance between the aircraft and the sensor box was detected earlier than should have happened in theory. In that case, some delay in the pollution signal would be expected, as is the case for the signals with peaks at ~200 s and ~300 s.

The validation results for CO in Figure 7.10 show that there is some coherence between the measurements and calculations. There are 14 points that fall within the 25% deviation area, but still 12 that fall outside. For NO<sub>x</sub>, larger discrepancies are observed as only one point falls within 25% deviation, as can be observed in Figure 7.11. The calculated concentrations are higher than the observed ones. This can indicate that the sensor box simply fails to pick up the NO<sub>x</sub> concentrations. It can also indicate that the aircraft are operated in thrust settings different than reported by the ICAO data bank, however in that case also the CO measurements are expected to be different. The calculated plume travel time based on distance and velocity shows that peaks should arrive after 25.6 s, which is in line with the ~25-30 s indicated by the sensor box measurements.

Finally, Figure G.1 in Appendix G shows that sound intensity peaks do not align well with activity of aircraft. Many times there are peaks when there is no aircraft activity. Also, there are many more sound intensity peaks than there is aircraft activity. TU Delft's DEMO adjusted the sound intensity sensor after this experiment with the goal to only have it indicating peaks when there is nearby activity.

## 7.2. Experiment 2 and 3: Departures on the Aalsmeerbaan and Kaagbaan

The results of the second and third experiment are presented in this section. First, time-series measurements for the total signal are presented along with the decomposed local signal in subsection 7.2.1. Next, subsection 7.2.2 presents the results using the local air quality signal coupled to the flight activity data. Hereafter, the validation results are presented in subsection 7.2.3. Finally, the discussion of these results is presented in subsection 7.2.4. The decomposed baseline pollution signals as well as a timeline of aircraft activity are presented in Figure D.2 and Figure D.3, Figure C.2 and Figure C.3 in Appendix D and Appendix C, respectively. The sound intensity measurements combined with flight activity from the ADS-B data are presented in Figure G.2 and Figure G.3 in Appendix G.

### 7.2.1. Time-Series Measurements

The total and local pollution signals for the second experiment are visualised in Figure 7.12 and Figure 7.14, respectively. For the third experiment, these signals are visualised in Figure 7.13 and Figure 7.15. The aircraft types visualised in Figure 7.12 and Figure 7.13 are the flights that were visually spotted at the airport. It should be noted that the axis scales are different per experiment due to variations in the length of the measurement experiments.

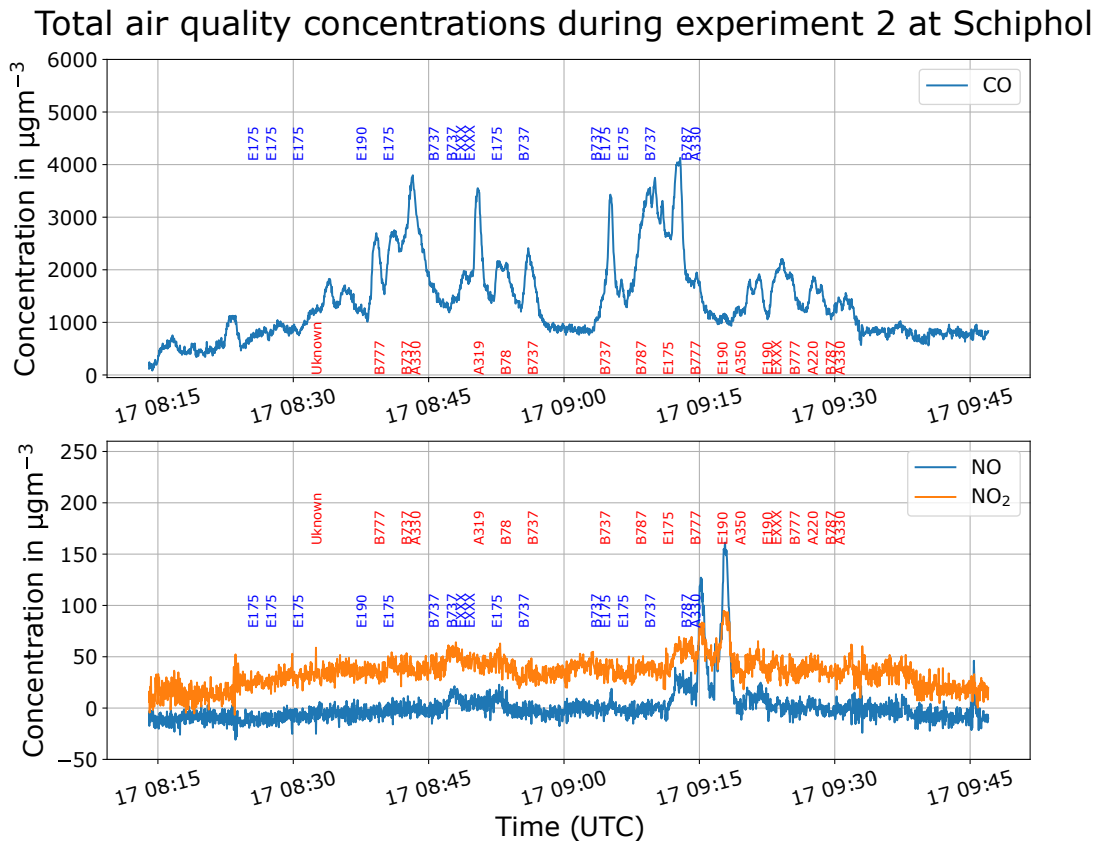


Figure 7.12: Time-series visualisation of total air quality measurements for second experiment with aircraft types of departing aircraft on the Kaagbaan and Aalsmeerbaan in red and blue, respectively.

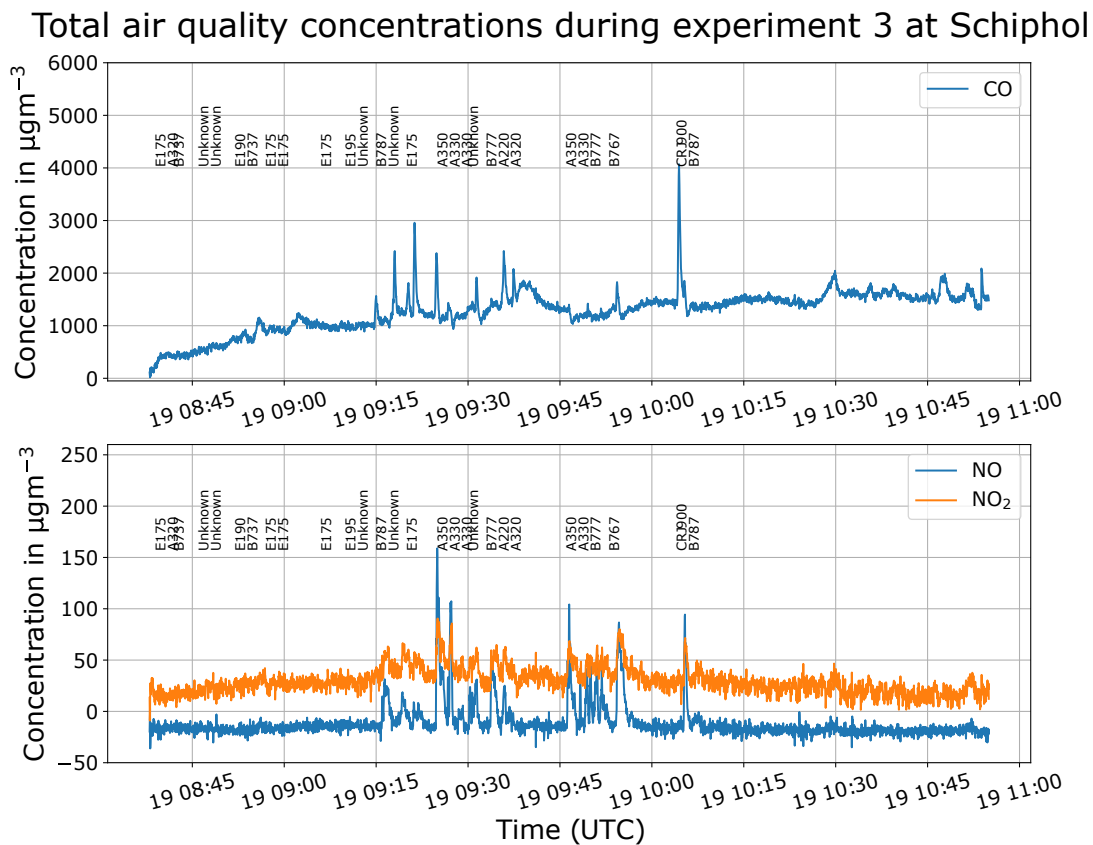


Figure 7.13: Time-series visualisation of total air quality measurements for third experiment with aircraft types of departing aircraft on the Aalsmeerbaan.

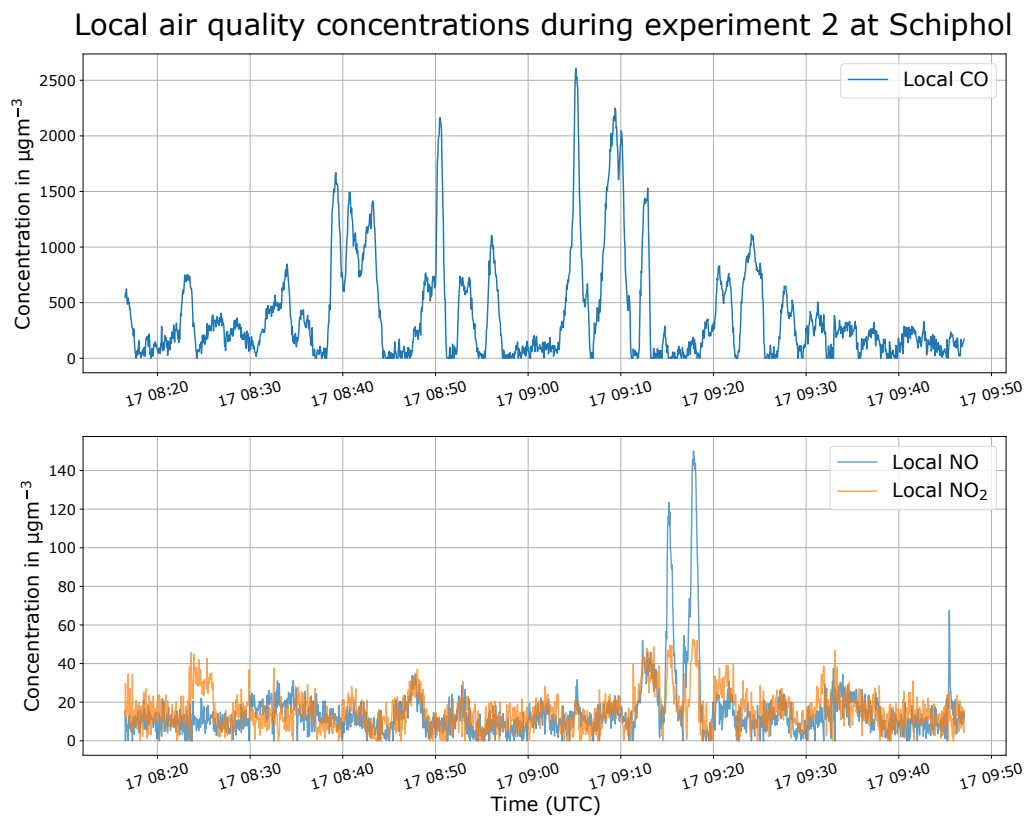


Figure 7.14: Time-series visualisation of decomposed local air quality signal for second experiment.

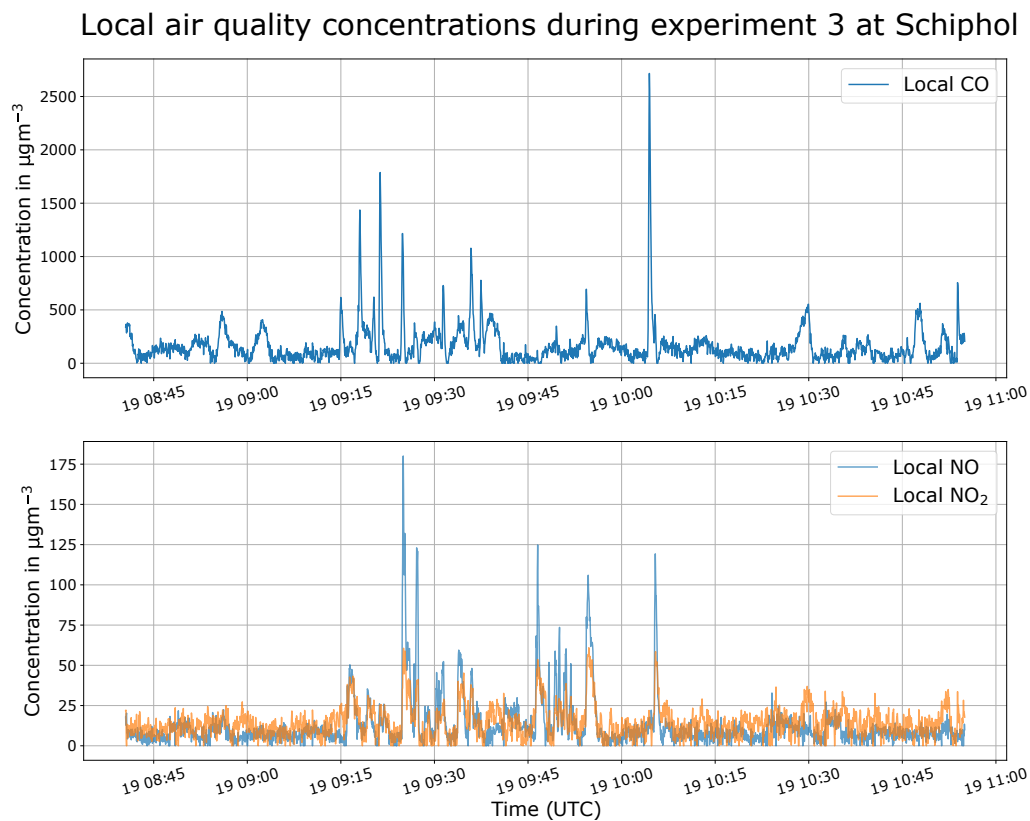


Figure 7.15: Time-series visualisation of decomposed local air quality signal for third experiment.

### 7.2.2. Analysis using Flight Activity Coupled to Local Signal

Again, the local air quality impacts per aircraft type and per engine configuration are visualised via local signals and box plots. Individual pollution signals for CO, NO and NO<sub>2</sub> are visualised in Figure 7.18, Figure 7.19 and Figure 7.20. Box plots per aircraft type and engine configuration are presented for CO in Figure 7.16 and Figure 7.17 for both experiment two and three. Swarm plots for the full data set, including the sets where less than three data points are available for a certain aircraft type or engine configuration are presented in Appendix E.

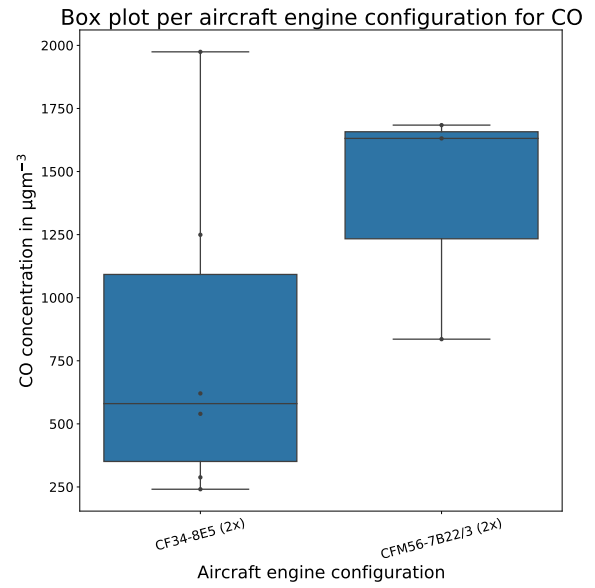
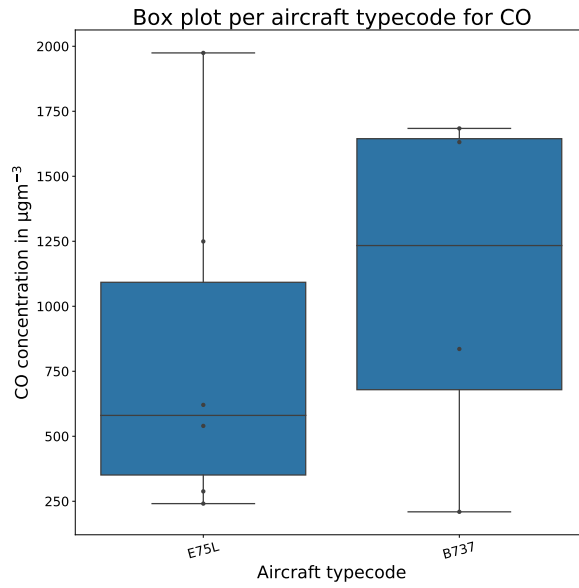


Figure 7.16: Local CO impact per aircraft type for departures during the second and third experiment.

Figure 7.17: Local CO impact per aircraft engine configuration for departures during the second and third experiment.

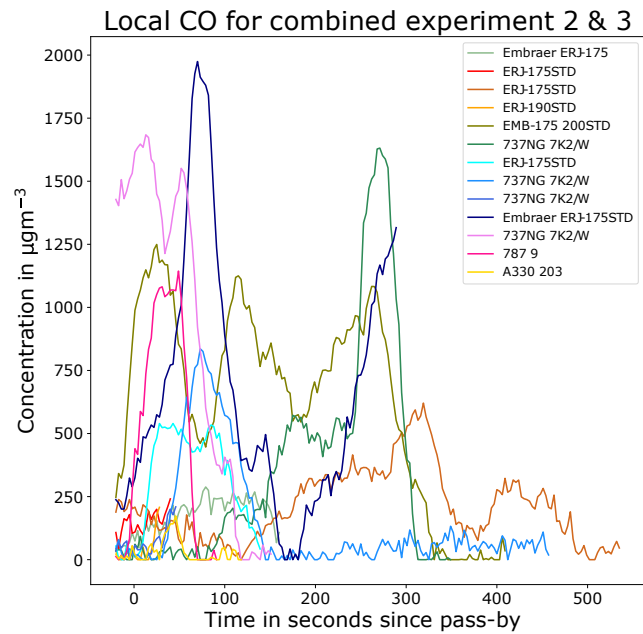


Figure 7.18: Local signals for CO for different aircraft during second and third experiment.

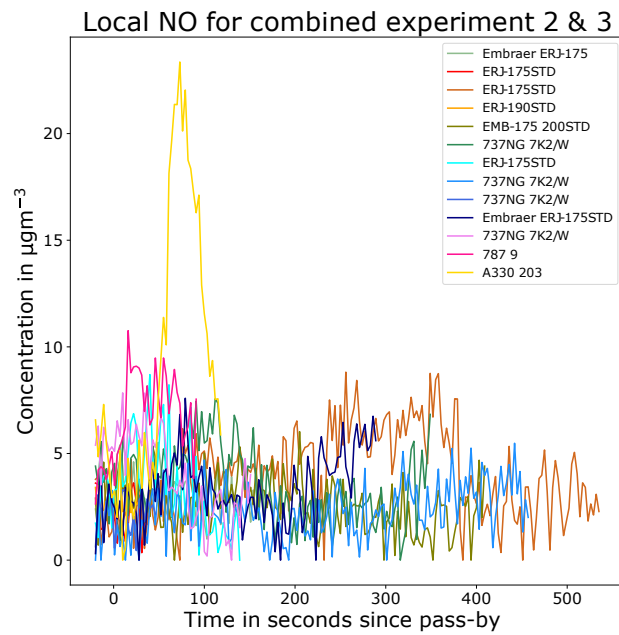
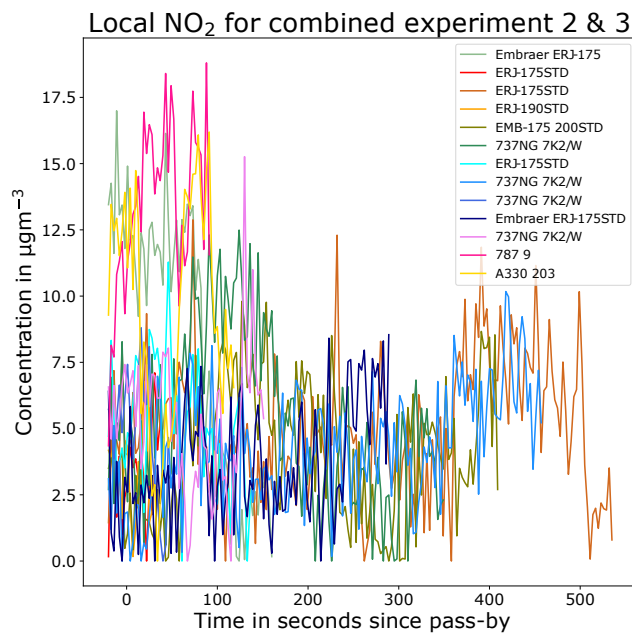


Figure 7.19: Local signals for NO for different aircraft during second and third experiment.

Figure 7.20: Local signals for NO<sub>2</sub> for different aircraft during second and third experiment.

### 7.2.3. Validation Results

The validation results are presented in Figure 7.21 and Figure 7.22. Again, not for every aircraft a value could be calculated due to missing engine information.

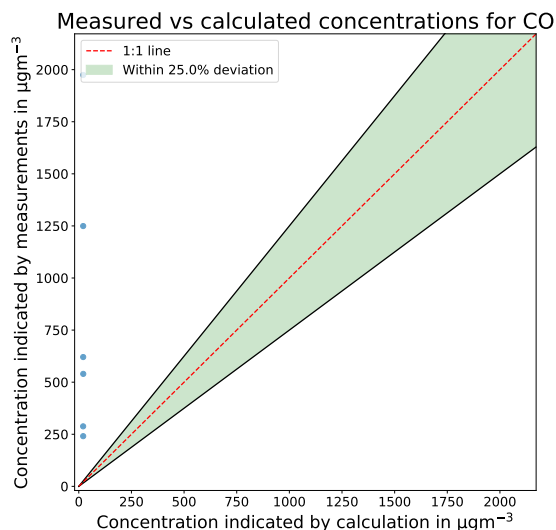


Figure 7.21: Validation results for CO for second and third measurement experiment.

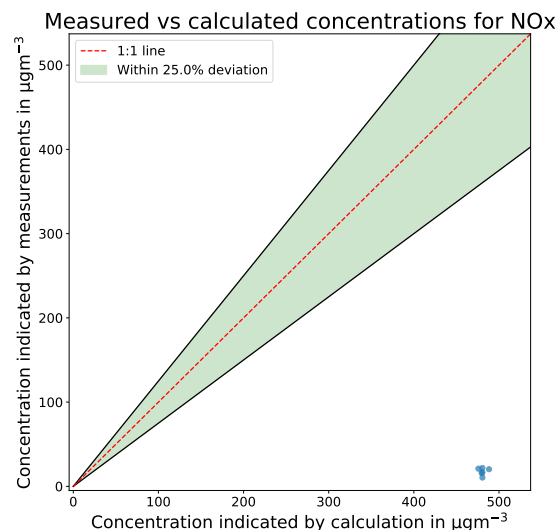


Figure 7.22: Validation results for NO<sub>x</sub> for second and third measurement experiment.

### 7.2.4. Discussion

The track points in Figure 6.7 and Figure 6.10 show departures on the Aalsmeerbaan, Kaagbaan and Oostbaan. All track points are oriented south of the sensor box. The wind roses in Figure 6.6 and Figure 6.9 show wind coming from the south-southwest during the second experiment and wind coming from the south during the third experiment, with maximum speeds of 8.5 m/s and 7.5 m/s, respectively. Conditions for these experiments as well as measurement locations are very similar, which makes aggregating results a logical step.

As can be observed in Figure C.2 in Appendix C, the ADS-B data only allows detection of three departures on the Aalsmeerbaan for this experiment, even though 17 flights were visually observed departing from the Aalsmeerbaan. In Figure C.3 in Appendix C, 17 departures were picked up by the ADS-B during this experiment even though 28 departures from the Aalsmeerbaan were witnessed.

The mixed flight activity plots in Figure G.2 and Figure G.3 in Appendix G show that the number of sound peaks is drastically reduced, thanks to the sound sensor improvements by DEMO, and that the peaks match better with pass-by signals indicated by the ADS-B. Also, it can be seen that there are still many peaks at times when there is no aircraft nearby, according to the ADS-B. Again, this is most likely due to the lack in observed flights by the ADS-B but potentially also due to the noise of a nearby bus lane.

The measured total concentrations during the second experiment, visualised in Figure 7.12 show concentrations up to  $\sim 4000 \mu\text{gm}^{-3}$ . For NO and NO<sub>2</sub> peaks up to  $\sim 150 \mu\text{gm}^{-3}$  and  $\sim 100 \mu\text{gm}^{-3}$  are observed. For the third experiment, total concentrations for CO go up to  $\sim 4000 \mu\text{gm}^{-3}$ . NO and NO<sub>2</sub> concentrations reach maximum levels of  $\sim 150 \mu\text{gm}^{-3}$  and  $\sim 100 \mu\text{gm}^{-3}$ . In addition, it can be seen in Figure 7.13 that measurements from 08:15AM to 09:15AM show aircraft activity without reflecting it in the measurements. This is due to the sensor box being initially positioned  $\sim 20$  m more to the east, thus potentially out of the plume. Due to the wind direction of that day, it was quickly decided to move closer to the runway centre line. Relatively speaking, more NO and NO<sub>2</sub> peaks are present compared to the landing experiment, even though the shortest distance between the sensor box and departing aircraft is 300 m, compared to 200 m during the landing experiment. The peak concentrations during the second experiment line-up with the flights indicated, with some delay. Especially, when looking at the B789 and A332 flights, it looks like these aircraft have largest impact before getting closest to the sensor box. This can be explained due to their lining up with the runway procedure. The B789 and A332 take-off on the Aalsmeerbaan close after each other. They take the same route to the runway and they even start their take-off at the same part of the runway, as visualised in Figure 7.23 and Figure 7.24. The first two CO peaks are present before the closest distance between the sensor box and aircraft is even reached. This is because these aircraft taxi parallel to the runway, towards the start

of it, coming closer and closer to the sensor box. This causes the CO peaks to appear approximately 7 minutes before each take-off. At the start of the runway, each aircraft holds for some time, before departing, but with plumes most likely not reaching the sensor box due to their angle relative to the sensor box. When the aircraft apply thrust and start to roll, the NO and NO<sub>2</sub> peaks arrive at the sensor box. This experiment is complex due to the local wind conditions, which not only transported emissions from Kaagbaan departures, but also from taxi and ground operations.

During the combined results of experiment two and three, there are two similar aircraft and two similar engine configurations that departed three times on the Aalsmeerbaan. Figure 7.16 shows the aggregated statistics for the aircraft type, Figure 7.17 shows such statistics for the engine configuration. It can be observed that the E75L has a larger maximum impact, but that the B737 median impact is above the E75L. Of course, a large factor is the distance to the aircraft, which is not portrayed in these figures.

The local signals for CO, NO and NO<sub>2</sub> indicate clear peaks for CO. For NO and NO<sub>2</sub>, peaks are harder to visually observe and generally below the threshold of  $\sim 25 \mu\text{g m}^{-3}$ .

Finally, the validation results for CO and NO<sub>x</sub> in Figure 7.21 and Figure 7.22 show that the measured CO concentrations are higher than the calculated values. Similarly to the first experiment, the measured NO<sub>x</sub> concentrations are far below the estimated concentrations. The way how the local pollution signal is coupled to a certain flight influences these results. One of the reasons for the high CO measurements is the fact that the aircraft in experiment two and three not only take-off. Aircraft taxi to the runway, hold and then take-off. During the holding or the taxiing, it can be that the CO concentrations are actually higher than during the take-off process due to low thrust settings, as explained in subsection 2.4.3, yet the maximum value is extracted.



Figure 7.23: B789 hold and line-up with runway during second experiment. Figure 7.24: A332 hold and line-up with runway during second experiment.

### 7.3. Experiment 4: Taxi Measurements on Airport Apron

The results of the fourth and final experiment are presented in this section. First, time-series measurements for the total signal are presented along with the decomposed local signal in subsection 7.3.1. Next, subsection 7.3.2 presents the results using the local air quality signal coupled to the flight activity data. Hereafter, the validation results are presented in subsection 7.3.3. Finally, the discussion of these results is presented in subsection 7.3.4. The sound intensity measurements combined with flight activity from the ground radar and ADS-B data are presented in Figure G.4 in Appendix G.

The decomposed baseline pollution signals as well as a timeline of aircraft activity are presented in Figure D.4 and Figure C.4 in Appendix D and Appendix C, respectively. The sound intensity measurements combined with flight activity from the ADS-B and ground radar data are presented in Figure G.4 in Appendix G.

#### 7.3.1. Time-Series Measurements

The total and local pollution signals for the second experiment are visualised in Figure 7.25 and Figure 7.26, respectively. Due to the large variety of aircraft operations on the airport apron, it was decided to colour the aircraft type based on the minimum distance between the aircraft and the sensor box.

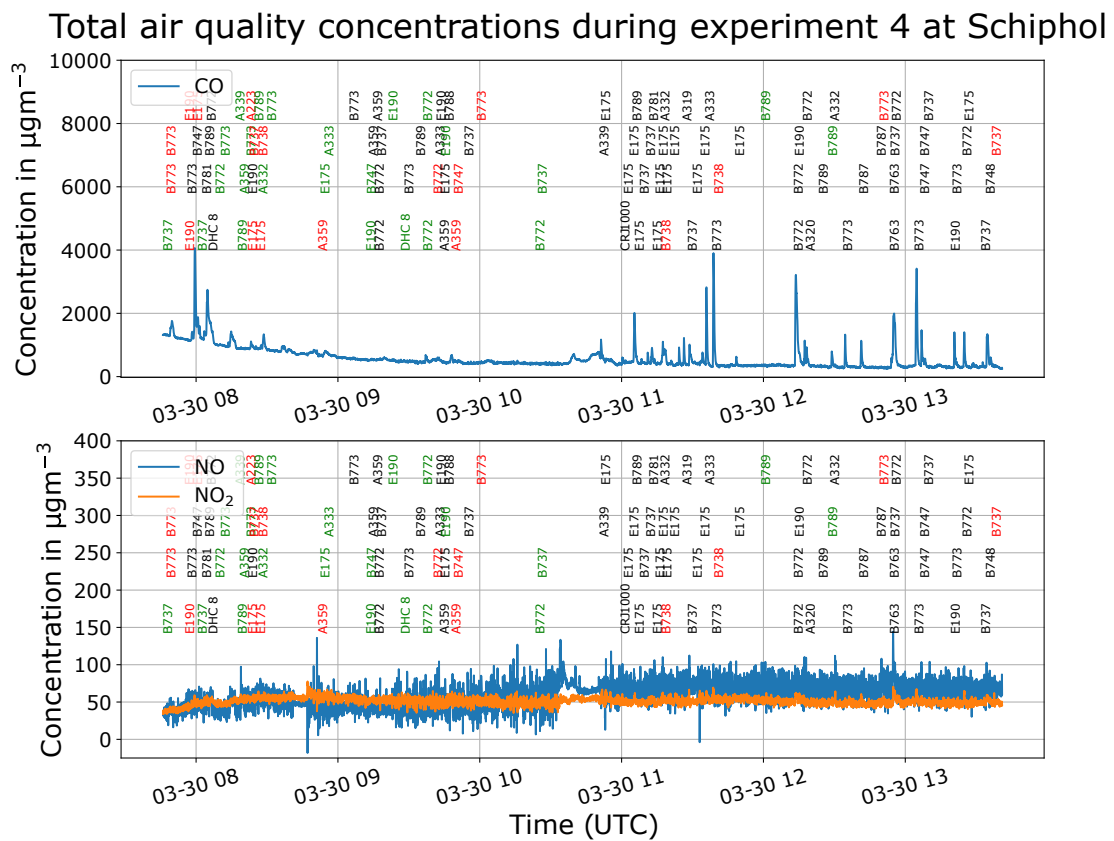


Figure 7.25: Time-series visualisation of total air quality measurements for fourth experiment with aircraft types of nearby aircraft categorised by distance (black: <100 m, red: 100-250 m, green: >250 m).

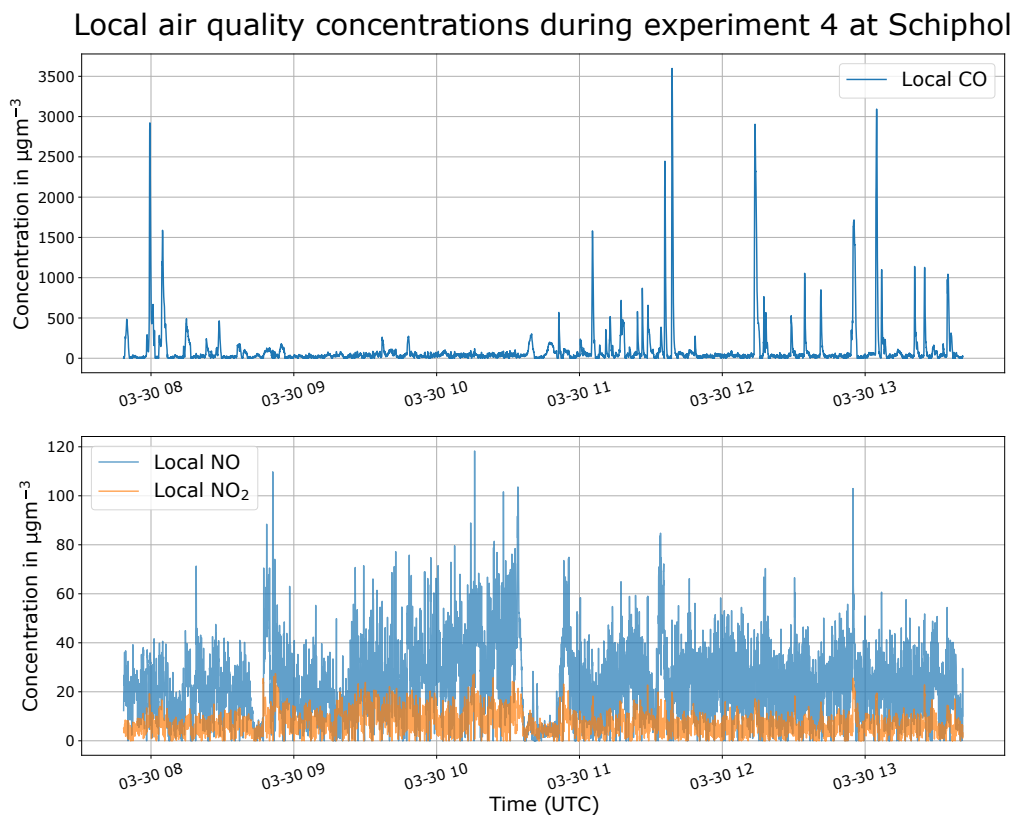


Figure 7.26: Time-series visualisation of decomposed local air quality signal for fourth experiment.

### 7.3.2. Analysis using Flight Activity Coupled to Local Signal

Using the pollutant concentration coupled to each flight, it is possible to analyse specific aircraft and engine configurations in more depth. In addition, it is possible to investigate the pollution signal of specific aircraft. The local air quality impacts per aircraft type and per engine configuration are visualised via box plots. These box plots are constructed per aircraft type and per engine configuration only if three or more data points are available. Swarm plots for the full data set, including the sets where less than three data points are available for a certain aircraft type or engine configuration are presented in Appendix E. For the fourth experiment, these box plots are presented for CO and NO in Figure 7.27, Figure 7.28, Figure 7.29 and Figure 7.30. Individual pollution signals for CO, NO and NO<sub>2</sub> are visualised in Figure 7.31, Figure 7.32 and Figure 7.33.

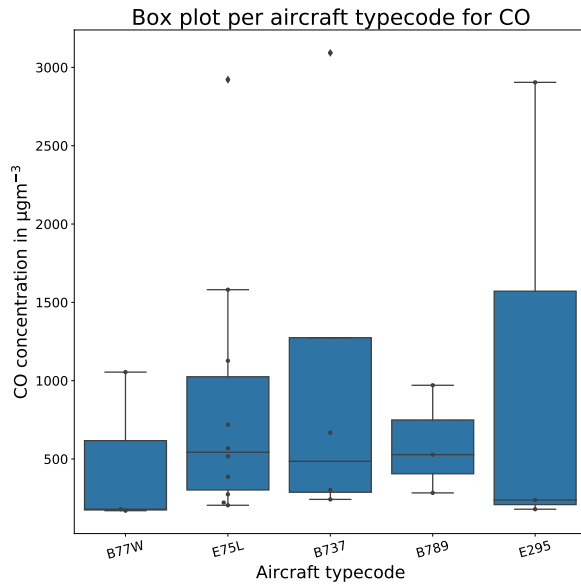


Figure 7.27: Local CO impact per aircraft type for activity during the fourth experiment.

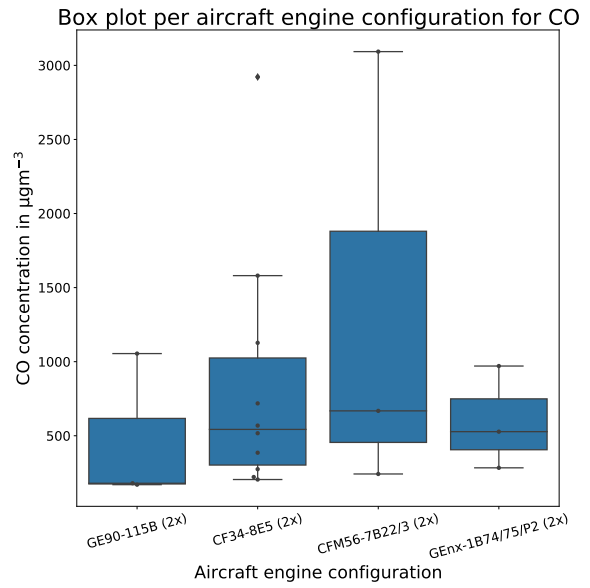


Figure 7.28: Local CO impact per aircraft engine configuration for activity during the fourth experiment.

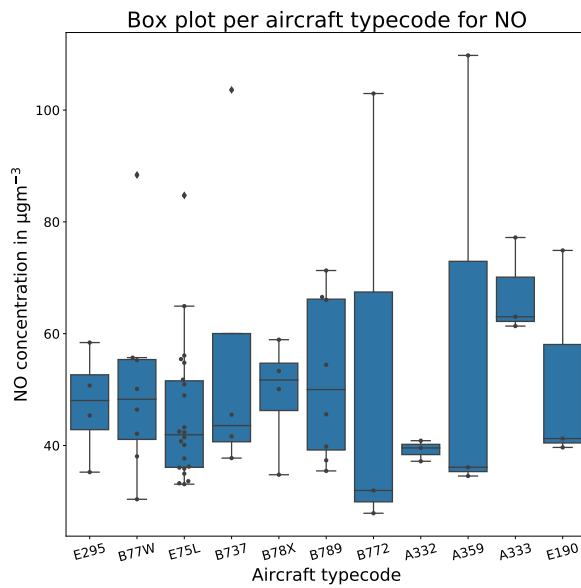


Figure 7.29: Local NO impact per aircraft type for activity during the fourth experiment.

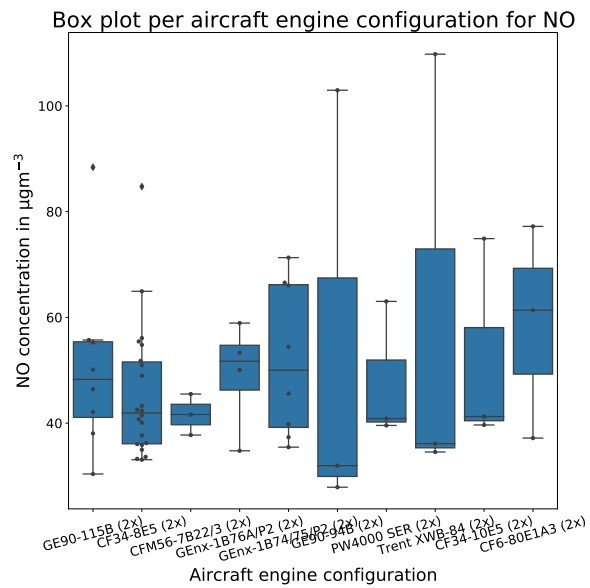


Figure 7.30: Local NO impact per aircraft engine configuration for activity during the fourth experiment.

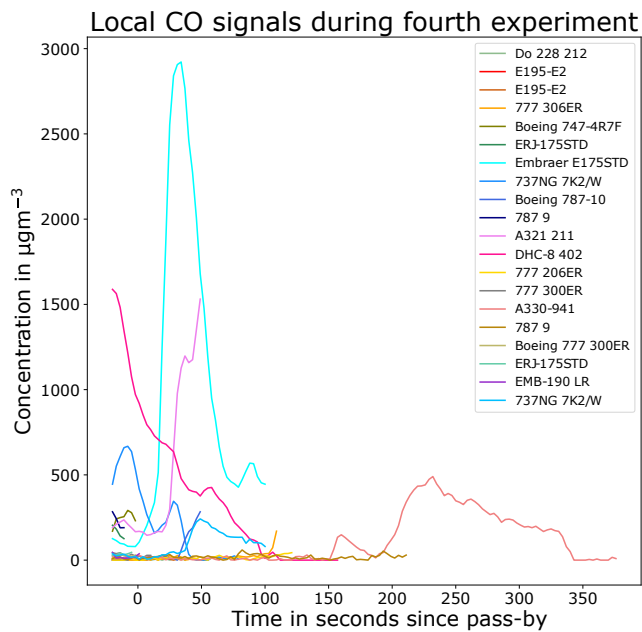


Figure 7.31: Local signals for CO for different aircraft during fourth experiment.

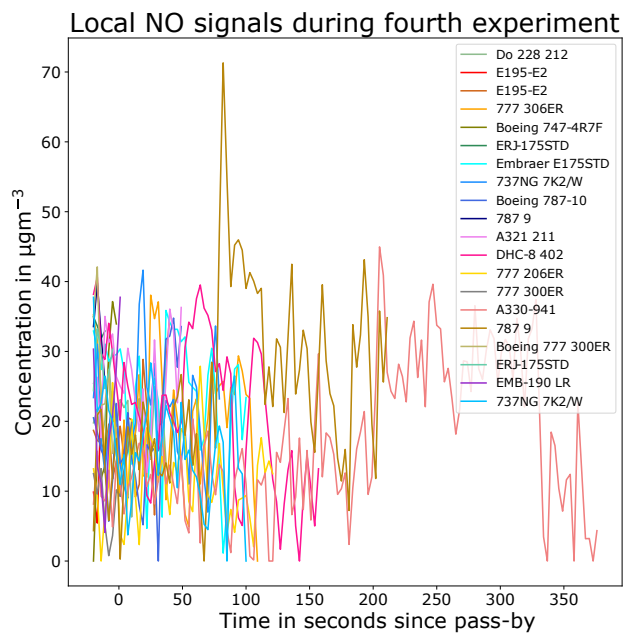


Figure 7.32: Local signals for NO for different aircraft during fourth experiment.

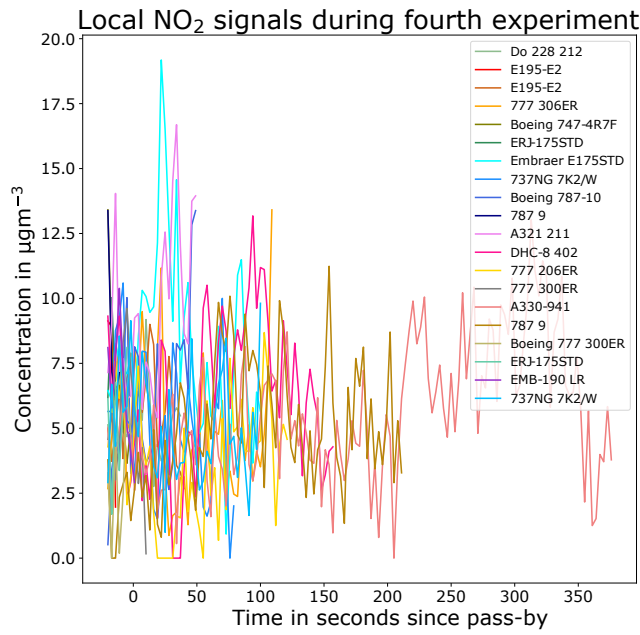


Figure 7.33: Local signals for NO<sub>2</sub> for different aircraft during fourth experiment.

### 7.3.3. Validation Results

The validation results are presented in Figure 7.34 and Figure 7.35. Again, not for every aircraft a value could be calculated due to missing engine information. The exhaust velocities are assumed to be that of the breakaway thrust, which equals 22.22 m/s and is listed in Table 5.3.

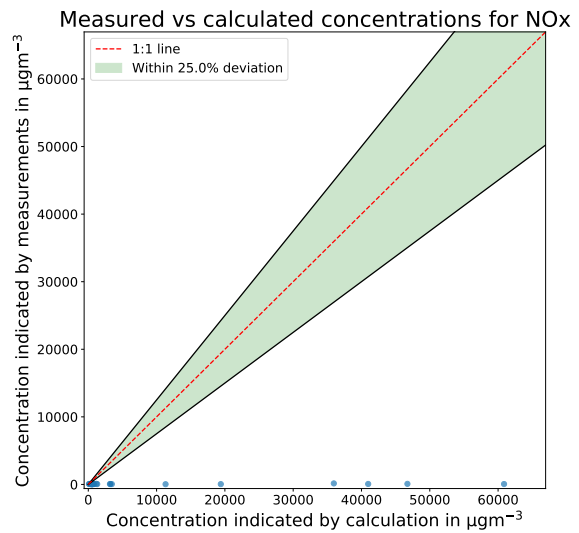
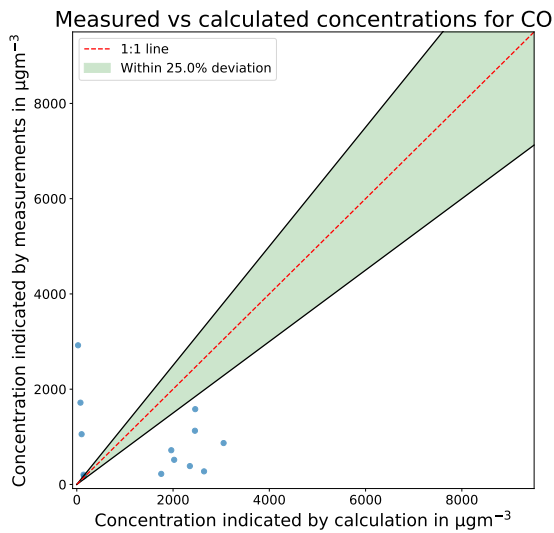


Figure 7.34: Validation results for CO for fourth measurement experiment. Figure 7.35: Validation results for NO<sub>x</sub> for fourth measurement experiment.

### 7.3.4. Discussion

During the fourth experiment, the wind rose in Figure 6.12 shows a wind coming from the south with speeds up to 4.5 m/s. Aircraft tracks are present 360° around the sensor box, as can be seen in Figure 6.14 and Figure 6.15. Sound intensity peaks line-up well with aircraft activity indicated by both

the ADS-B and ground radar data presented in Figure G.4 in Appendix G. It can be seen that sometimes there are sound intensity peaks but no aircraft activity. This can be simply due to vehicular traffic passing by. Also, since aircraft activity is plotted at times when the aircraft is closest to the sensor box, a departure of that aircraft - further away - can cause a second sound intensity peak.

The total measured air quality concentrations in Figure 7.25 show several peaks. Also, it can be seen that the CO signal is not fully stabilised due to its converging tendency. Such behaviour was already observed during earlier experiments when starting up the sensor box for the first time in a while. Moreover, sudden changes in temperature and relative humidity are known to have first-order effects on the destabilisation of the signal, which is a problem when transporting the sensor box to Schiphol airport. However, the interest is not necessarily in the total measured signal but rather the locally extracted pollution signal. Figure 7.26 shows that the problem does not propagate fully to the local signal, which makes it still of use in further analysis.

During this experiment, several times the same aircraft type has passed-by with the same engine configuration. This allows investigating the coherence between the individual aircraft and engines. As can be seen in Figure 7.27 and Figure 7.29, largest impacts are for the B737, E75L and E295 for CO with peaks up to  $\sim 3000 \mu\text{g m}^{-3}$ . For NO, largest impacts are from the A359, B737 and B772, with peaks up to  $\sim 110 \mu\text{g m}^{-3}$ .

The local signals for CO, NO and NO<sub>2</sub> indicate clear peaks for CO. In addition, it shows the weaknesses and strengths of the peak extraction algorithm. It can be seen that there are several CO peaks that are not fully captured. Such peaks are for example in a downward or upward trend, i.e. the first or last point is equal to the global maximum. This means that the peak concentration was potentially higher before, or has the potential to be higher in the future. Yet, the algorithm decides to stop tracking this signal and follow that of a new nearby aircraft activity.

Validation results for this experiment have been obtained by assuming that the aircraft operates in the emission indices for the approach mode. This due to the large uncertainty of the actual thrust setting, and the approach settings seemed most reasonable. The CO validation results in Figure 7.34 show that no validation points lie within the 25% discrepancy area. There are 12 validation points that lie outside of this area, on both sides of the 1-to-1 line. The validation results for NO<sub>x</sub> show similar behaviour as in the previous experiments, which are substantially lower measured concentrations than the calculations indicate.

## 7.4. Discussion of Measurement Results from All Experiments

An aggregation of the results is presented in Figure 7.36a for CO and Figure 7.36b for NO and NO<sub>2</sub>, which shows local air quality impacts per chemical species, per aircraft activity type. A distinction is made between results for CO, and NO and NO<sub>2</sub>, due to the large numeric variations between the species. Largest concentrations are observed for CO, with concentrations up to  $\sim 3500 \mu\text{g m}^{-3}$  for taxi measurements, followed by arrivals with  $\sim 2900 \mu\text{g m}^{-3}$  and departures with  $\sim 2000 \mu\text{g m}^{-3}$ . Even though the taxi measurements were executed generally closest to the aircraft, it can be seen that aviation-attributable CO concentrations are low at times. This is potentially due to the sensor box being out of the plume trajectory due to the local wind conditions and measurement locations of that day.

For the NO and NO<sub>2</sub> measurements, it can be seen that local NO maxima are higher than NO<sub>2</sub> maxima and that the spread of local NO<sub>2</sub> concentrations is lower than that of NO. The largest concentration is that of NO, equal to  $\sim 175 \mu\text{g m}^{-3}$  during the arrivals experiment, which is in fact unexpected as the emission indices for NO are lowest when the engine is in approach or idle thrust setting. The use of thrust reverser can potentially explain this. Finally, it should be noted that a substantial amount of local NO and NO<sub>2</sub> concentrations are not higher than the hourly-averaged concentrations at a reference station, as for example shown in Figure 2.2. This potentially indicates that the NO and NO<sub>2</sub> sensors have difficulties picking up the signal, and which strengthens the necessity of a threshold concentration before attributing.

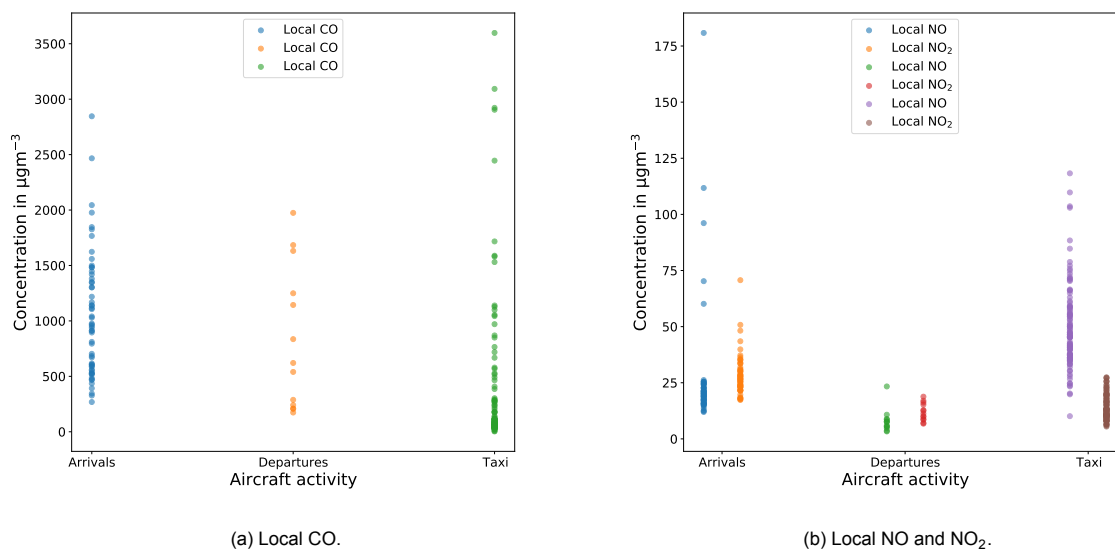


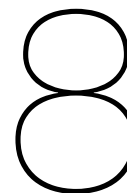
Figure 7.36: Local concentration per aircraft activity type.

When comparing the measurements in this study with the measurements obtained by Popoola et al. [56] at London Heathrow airport, who deploy 17 sensor boxes on the airport apron, it is fair to say that measurement ranges are very similar. They find CO concentrations up to 1500 ppbv ( $1718.19 \mu\text{gm}^{-3}$  at  $T=293 \text{ K}$ ,  $p=101325 \text{ Pa}$ ), NO concentrations up to 300 ppbv ( $368.05 \mu\text{gm}^{-3}$  at  $T=293 \text{ K}$ ,  $p=101325 \text{ Pa}$ ) and  $\text{NO}_2$  concentrations up to 50 ppbv ( $94.06 \mu\text{gm}^{-3}$  at  $T=293 \text{ K}$ ,  $p=101325 \text{ Pa}$ ). These concentrations are the peaks obtained during several weeks of measurements.

In terms of validation, the CO measurements match up to some degree with the validation calculations. The opposite is true for  $\text{NO}_x$ , even though the measurements for NO and  $\text{NO}_2$  are in the same order of magnitude as the measurements obtained by Popoola et al. [56]. The simplicity of the validation model can play a role in this as no chemical transformations are assumed, and the pollutant concentration is assumed to be homogeneously spread across the plume area. Hence, it might be worthwhile to further refine the applied validation methodology for  $\text{NO}_x$ . Several additional assumptions have been made when applying this validation methodology. First, it is assumed that the actual jet engine exhaust velocity of a B787 can represent the actual jet engine exhaust velocities of other aircraft as well. Secondly, when performing the plume impact calculations, the emission indices of the latest jet engine model are considered for each engine type as the engine age is unknown. Finally, the plume's curvilinear distance,  $S$ , from the jet engine exhaust to the sensor box is simply assumed to be a straight line, resulting in calculated impacts that are larger than the truth. The temporal inaccuracy of the OpenSky ADS-B data, which generally indicates aircraft to be further away than they truly are from the sensor box, counters this effect up to some extent.

Furthermore, the WHO limits presented in Appendix A were never exceeded at the measurement locations. The maximum peak for CO is  $\sim 3500 \mu\text{gm}^{-3}$  and the WHO time-weighted average concentration for CO is  $\sim 100000 \mu\text{gm}^{-3}$  in 15 minutes. For  $\text{NO}_2$  the limit specified by the WHO is  $\sim 200 \mu\text{gm}^{-3}$  in 1 hour and the maximum observed concentration is only  $\sim 175 \mu\text{gm}^{-3}$ .

Finally, the coupling of local air quality impacts to flights shows its weaknesses and strengths during these four experiments. In general, the more busy it is at the airport, the more difficult it becomes to account for local air quality impacts. The availability of complete, accurate ADS-B data with good temporal resolution is crucial.



## Conclusion and Recommendations

In this thesis, a low-cost multi-pollutant air quality sensor box has been developed, calibrated and deployed multiple times at Amsterdam Schiphol airport to quantify air quality impacts from arrivals, departures and taxiing aircraft. This chapter concludes the results and provides recommendations for further work.

The final sensor box design is a waterproof casing that contains four low-cost electrochemical gas sensors that respond to CO, NO, NO<sub>2</sub> and O<sub>3</sub> concentrations in ambient air. Additional sensors in the sensor box determine pressure, temperature, relative humidity, sound intensity, UV-light, visible light and IR-light. The pressure, temperature and relative humidity sensors assist in calibrating the measurements obtained by the gas sensors.

Calibration of the sensor box is achieved by collocating it with a regulatory air quality analyser of the Dutch air quality network in Beverwijk, Wijk aan Zee. Regulatory air quality data was provided for CO, NO and NO<sub>2</sub> by the network at 10 s resolution. Multivariate linear regression (MLR) and random forest (RF) models at three different temporal scales, 10 s, 1 min and 60 min, have been constructed per chemical species to transform the raw measurements into meaningful air quality concentrations. It was found that the RF models outperform the MLR models at finest temporal scale (10 s), but the opposite is true at largest temporal scale (60 min). Evaluating and comparing the RMSE on the test and train sets indicated that the RF models suffer from overfitting. Hyperparameter tuning of the RF models resulted in slight improvements for most models but did not reduce the apparent overfit. Regardless of the applied model, the sensor box collocation period in this study is heavily reduced compared to earlier research while not having to sacrifice performance, likely due to the utilisation of 10 s resolution air quality data instead of the standard available hourly resolution. The cross-validated RMSE values for the final CO, NO and NO<sub>2</sub> calibration models are 118.13  $\mu\text{g m}^{-3}$ , 2.38  $\mu\text{g m}^{-3}$  and 3.96  $\mu\text{g m}^{-3}$ , respectively. Corresponding correlation coefficients are 0.94, 0.99 and 0.98, on the test set.

The measurement experiments at Amsterdam Schiphol Airport have been set-up with the intention to quantify aviation-attributable impacts from arrivals, departures and taxiing aircraft. In general, concentration peaks for NO and NO<sub>2</sub> are less apparent compared to CO, with NO generally having larger peaks than NO<sub>2</sub>. Local concentrations during the arrivals experiments do not exceed  $\sim 2600 \mu\text{g m}^{-3}$  for CO,  $\sim 175 \mu\text{g m}^{-3}$  for NO and  $\sim 75 \mu\text{g m}^{-3}$  for NO<sub>2</sub>. Due to the stable wind conditions, it can be observed that plumes reach the sensor box consistently at the same time. Local CO concentrations during the departures experiment are lower compared to the arrivals experiments with maximum peaks for CO around  $\sim 2500 \mu\text{g m}^{-3}$ . This is most likely due to the increased distance (+100 m) between the runway and the sensor box compared to the arrivals experiment. Comparable NO and NO<sub>2</sub> peaks are observed between the arrivals and departures experiment, however more peaks are present in the departures experiment. Local concentrations during the taxi measurements experiment indicate CO peaks up to  $\sim 3500 \mu\text{g m}^{-3}$ , NO peaks up to  $\sim 120 \mu\text{g m}^{-3}$  and NO<sub>2</sub> peaks up to  $\sim 30 \mu\text{g m}^{-3}$ . These lower NO and NO<sub>2</sub> concentrations are explainable via the reduced thrust settings during taxiing and idle modes, at which more CO is to be found. Finally, the WHO air quality exposure limits were never exceeded at the measurement locations.

In terms of validation, measurements obtained using 17 low-cost sensor boxes at London Heathrow airport by Popoola et al. [56] show CO, NO and NO<sub>2</sub> concentrations up to 1718.19  $\mu\text{g m}^{-3}$ , 368.05

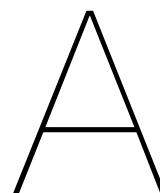
$\mu\text{g m}^{-3}$  and  $94.06 \mu\text{g m}^{-3}$ , respectively (recalculated from parts-per notation at standard conditions), which is in line with the measurements obtained in this study. In addition, the theoretical calculation of the plume travel time for CO during the arrivals experiment matches with the observed travel time in the measurements. The validation calculations indicate that the CO measurements correspond with some discrepancy to the calculations. For the departures experiment, the measured CO concentrations are larger than the calculated values due to the assumption that aircraft operate in the take-off thrust setting, which is in fact only the case for a small part of the captured signal. The CO peaks in this experiment are in fact caused by aircraft holding and taxiing before take-off. Validation calculations for  $\text{NO}_x$  indicate a systematic overestimation or undermeasurement of the concentrations. Further research should investigate the  $\text{NO}_x$  discrepancy between the validation results and the measurements.

Uncertainties remain over several topics. First of all, the use of thrust reversal in the arrivals experiment is unknown, but can potentially explain the presence of NO and  $\text{NO}_2$  peaks in the data. Aircraft thrust setting data can be helpful for resolving such ambiguities. Secondly, the quality of the sound intensity measurements was too low to allow detection of nearby aircraft. Instead, the sound intensity measurements are only presented together with the aircraft activity timelines to observe discrepancies between the two. Thirdly, several assumptions have been made in the validation model. The impact of neglecting chemical transformations should be further investigated, along with the practical assumptions made to implement the validation methodology.

Finally, there are several recommendations to be made for further work. First of all, the discrepancies between the  $\text{NO}_x$  measurements and calculations should be further investigated. A starting point for this could be investigating the validation methodology and the sensor box signal in its purest form for the NO and  $\text{NO}_2$  sensors. Secondly, the aircraft activity data obtained via the OpenSky ADS-B network lacks temporal and spatial resolution. This will enhance the process of coupling aircraft to local air quality peaks as the current implementation of the OpenSky ADS-B network misses flights. Third, there is a trade-off to be made between measuring at peak hours, when there are many aircraft operating at the airport, and measuring during off-peak hours, when it is calm. Measurement during peak traffic hours results in much useful data in a short period of time, but it can become hard to account for individual pollution signals due to the many traffic patterns and intermixing of plumes. Contrarily, measurements during off-peak hours result in less observations over time, but allow easier accountability, which also enhances the confidence of the results. Most likely, the use of multiple low-cost sensor boxes can improve accountability during peak traffic hours. On another note, confidence to the results of a single sensor box can already be added by implementing multiple sensors per chemical species. Fourth, a low-cost gas sensor for  $\text{O}_3$  quantification has been implemented but measurements were never analysed due to its inability to be calibrated during the Wijk aan Zee calibration experiment. Similarly, light sensors have been included in the sensor box to observe any delayed  $\text{O}_3$  formation due to sunlight, but again these were discarded in the air quality analysis as no calibrated  $\text{O}_3$  signal was available. It is recommended to seek ways to calibrate the  $\text{O}_3$  sensor, such that also this signal can be used in future analysis. Finally, knowing that sensor performance changes over time, it is uncertain how well the calibration coefficients hold over time. It is recommended to investigate the performance of the calibration by collocating the sensor box again with an official monitor and quantifying the observed discrepancies.

# Appendices





# WHO and EU Emission Guidelines

Table A.1: WHO guidelines [22, 52].

Species	Time-weighted average concentration	Averaging time
Cadmium	5 ng/m <sup>3</sup>	annual
Carbon disulfide	100 µg/m <sup>3</sup>	24 hours
Carbon monoxide	100 mg/m <sup>3</sup>	15 minutes
	60 mg/m <sup>3</sup>	30 minutes
	30 mg/m <sup>3</sup>	1 hour
	10 mg/m <sup>3</sup>	8 hours
1,2-Dichloroethane	0.7 mg/m <sup>3</sup>	24 hours
Dichloromethane	3 mg/m <sup>3</sup>	24 hours
	0.45 mg/m <sup>3</sup>	1 week
Fluoride	-	-
Formaldehyde	0.1 mg/m <sup>3</sup>	30 minutes
Hydrogren sulfide	150 µg/m <sup>3</sup>	24 hours
Lead	0.5 µg/m <sup>3</sup>	annual
Manganese	0.15 µg/m <sup>3</sup>	annual
Mercury	1 µg/m <sup>3</sup>	annual
Nitrogen dioxide	200 µg/m <sup>3</sup>	1 hour
	40 µg/m <sup>3</sup>	annual
Ozone	100 µg/m <sup>3</sup>	8 hours
PM 2.5	10 µg/m <sup>3</sup>	annual
	25 µg/m <sup>3</sup>	24 hours
PM 10	20 µg/m <sup>3</sup>	annual
	50 µg/m <sup>3</sup>	24 hours
Platinum	-	-
PCBs	-	-
PCDDs/PCDFs	-	-
Styrene	0.26 mg/m <sup>3</sup>	1 week
Sulfur dioxide	20 µg/m <sup>3</sup>	24 hours
	500 µg/m <sup>3</sup>	10 min
Tetrachloroethylene	0.25 mg/m <sup>3</sup>	annual
Toluene	0.26 mg/m <sup>3</sup>	1 week
Vanadium	1 µg/m <sup>3</sup>	24 hours

Table A.2: European Union guidelines [20].

Species	Concentration	Averaging period	Exceedances per year
PM 2.5	25 $\mu\text{g}/\text{m}^3$	1 year	n/a
Sulphur dioxide	350 $\mu\text{g}/\text{m}^3$	1 hour	24
Nitrogen dioxide	200 $\mu\text{g}/\text{m}^3$	24 hours	3
	40 $\mu\text{g}/\text{m}^3$	1 year	n/a
PM 10	50 $\mu\text{g}/\text{m}^3$	24 hours	35
	40 $\mu\text{g}/\text{m}^3$	1 year	n/a
Lead	0.5 $\mu\text{g}/\text{m}^3$	1 year	n/a
Carbon monoxide	10 $\text{mg}/\text{m}^3$	Max daily 8 hour mean	n/a
Benzene	5 $\mu\text{g}/\text{m}^3$	1 year	n/a
Ozone	120 $\mu\text{g}/\text{m}^3$	Max daily 8 hour mean	25 days averaged over 3 years
Arsenic	6 $\text{ng}/\text{m}^3$	1 year	n/a
Cadmium	5 $\text{ng}/\text{m}^3$	1 year	n/a
Nickel	20 $\text{ng}/\text{m}^3$	1 year	n/a
PAHs	1 $\text{ng}/\text{m}^3$	1 year	n/a

# B

## Sensor Box Design

Table B.1: Comparison between Arduino and Raspberry Pi.

Parameter	Arduino Uno	Raspberry Pi Model B
Price	\$30	\$35
Size	7.6cm × 1.9cm × 6.4cm	8.6cm × 5.4cm × 1.7cm
Memory	0.002MB	512MB
Clock Speed	16MHz	700MHz
On Board Network	None	10/100 wired Ethernet RJ45
Multitasking	No	Yes
Input voltage	7 to 12V	5V
Flash	32KB	SD Card (2 to 16 GB)
USB	One, input only	Two, peripherals OK
Operating System	None	Linux distributions
Development Environment	Arduino	Scratch, IDLE, anything with Linux support

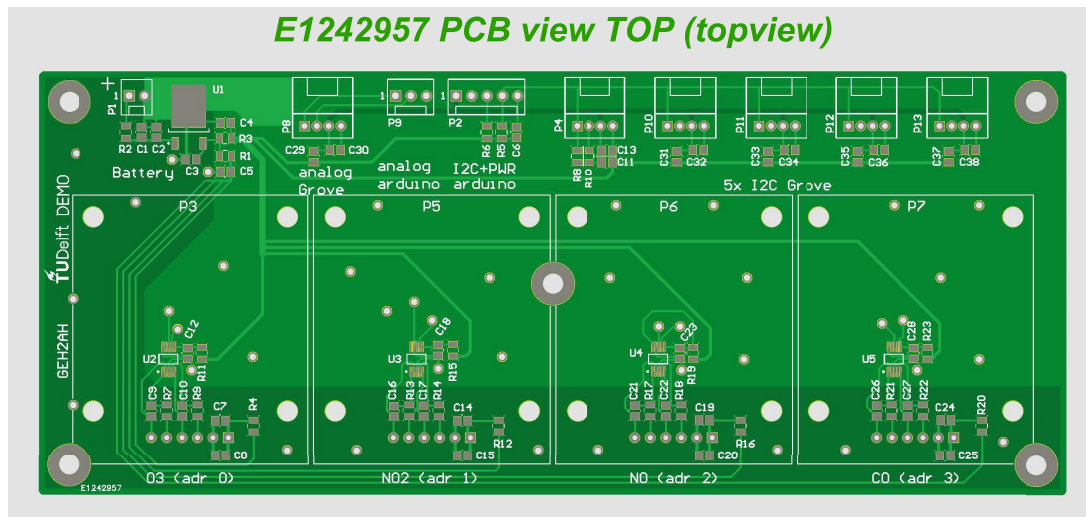
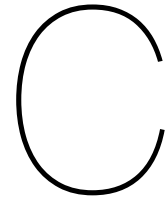


Figure B.1: Customised PCB to host ISBs.





# Flight Schedule via ADS-B Data

## C.1. Experiment 1: Arrivals on the Polderbaan

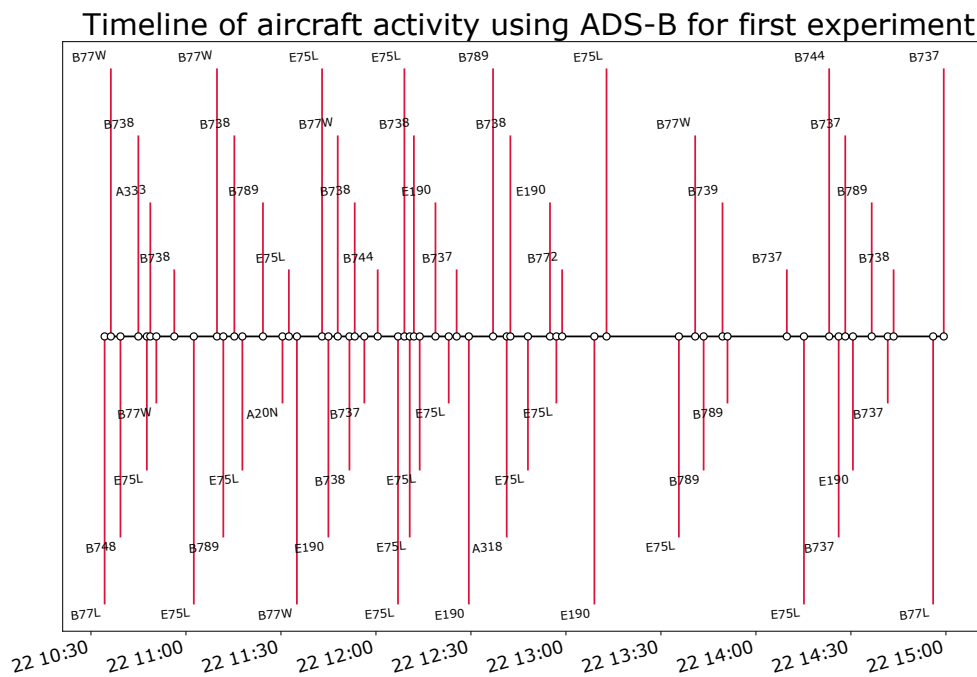


Figure C.1: Timeline of arrivals on the Polderbaan based on OpenSky ADS-B for first experiment.

## C.2. Experiment 2: Departures on the Aalsmeerbaan

Timeline of aircraft activity using ADS-B for second experiment

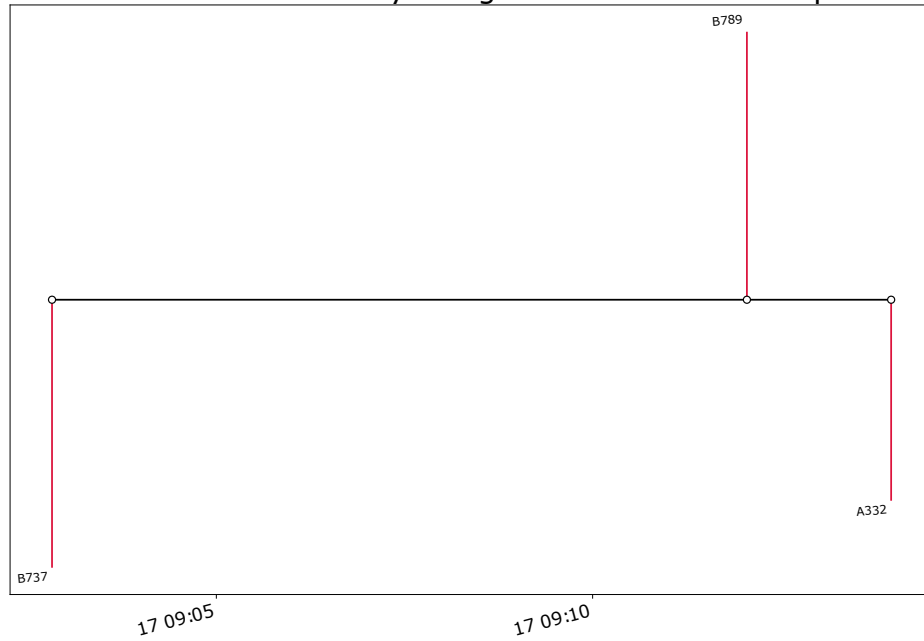


Figure C.2: Timeline of departures on the Aalsmeerbaan based on OpenSky ADS-B for second experiment.

### C.3. Experiment 3: Departures on the Aalsmeerbaan

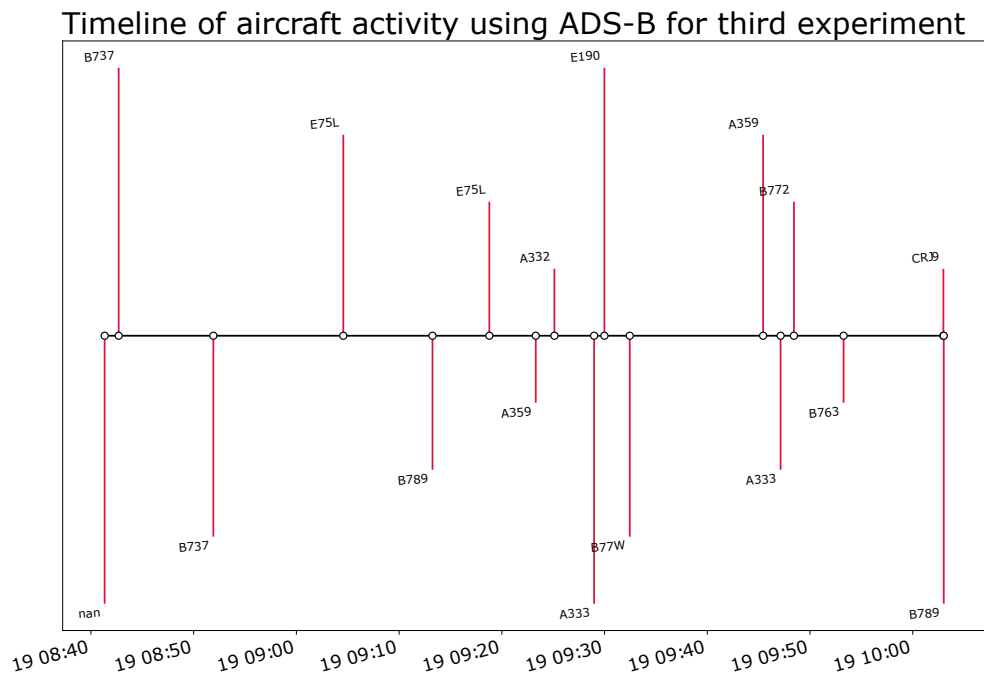


Figure C.3: Timeline of departures on the Aalsmeerbaan based on OpenSky ADS-B for third experiment.

### C.4. Experiment 4: Taxi Measurements on Airport Apron

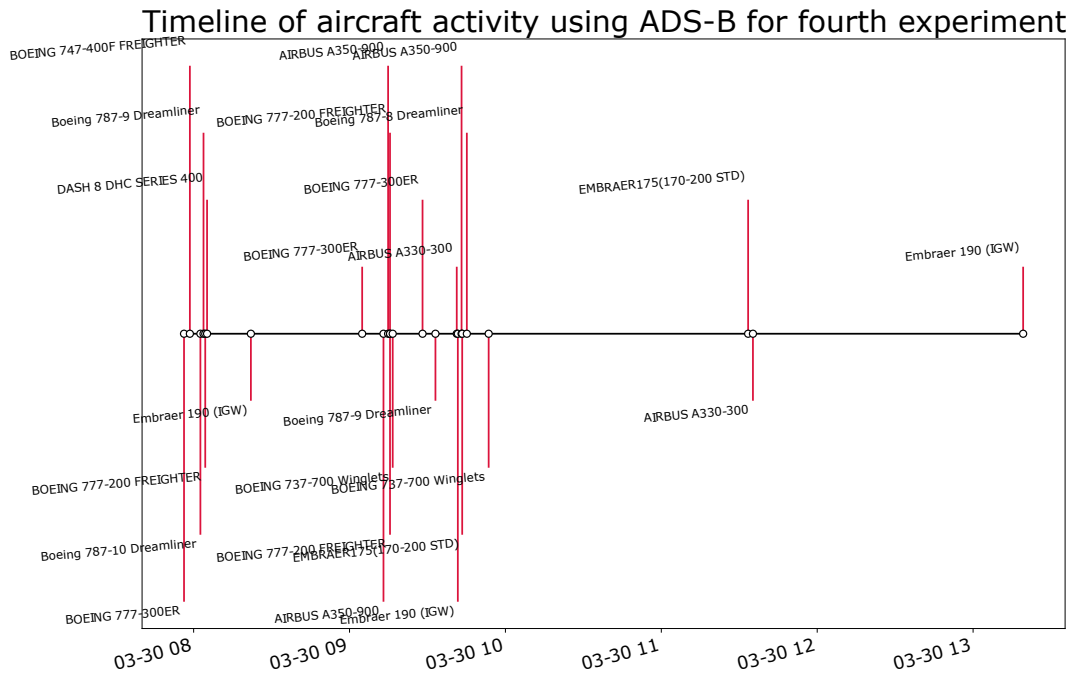
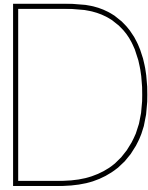


Figure C.4: Timeline of nearby aircraft activity (<50 m) based on ground radar data for fourth experiment.



# Baseline Concentrations

## D.1. Experiment 1: Arrivals on the Polderbaan

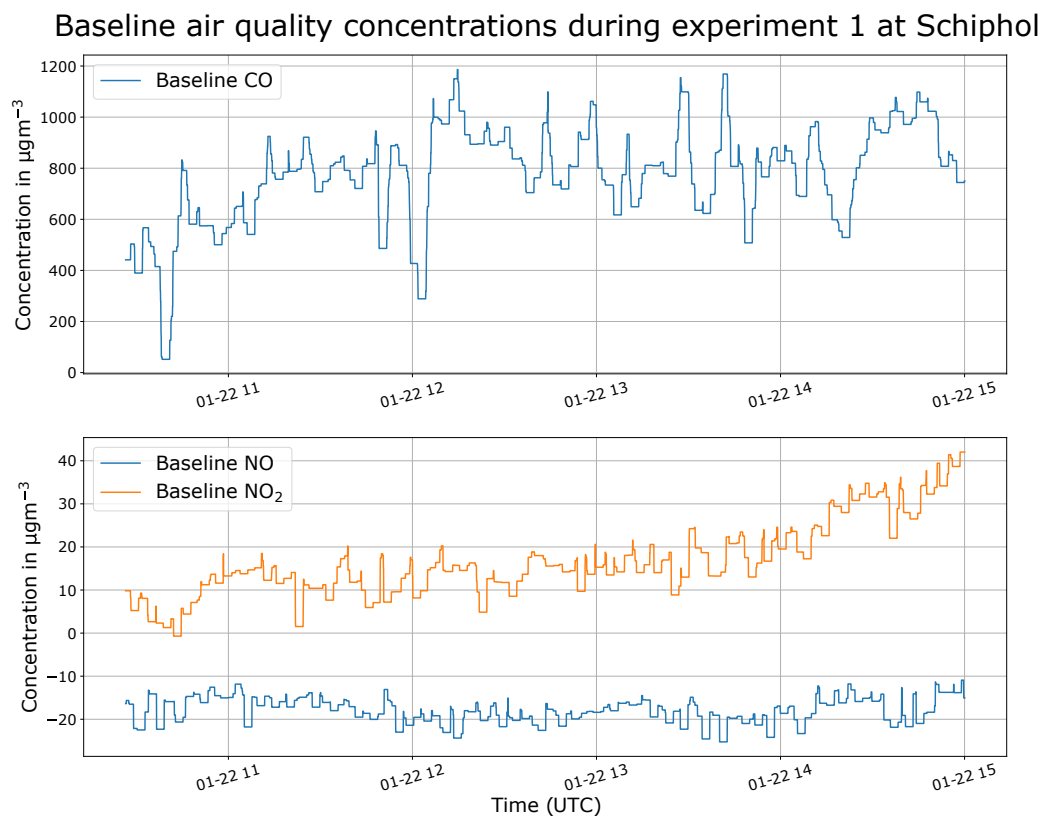


Figure D.1: Time-series visualisation of decomposed baseline air quality signal for first experiment.

## D.2. Experiment 2: Departures on the Aalsmeerbaan and Kaagbaan

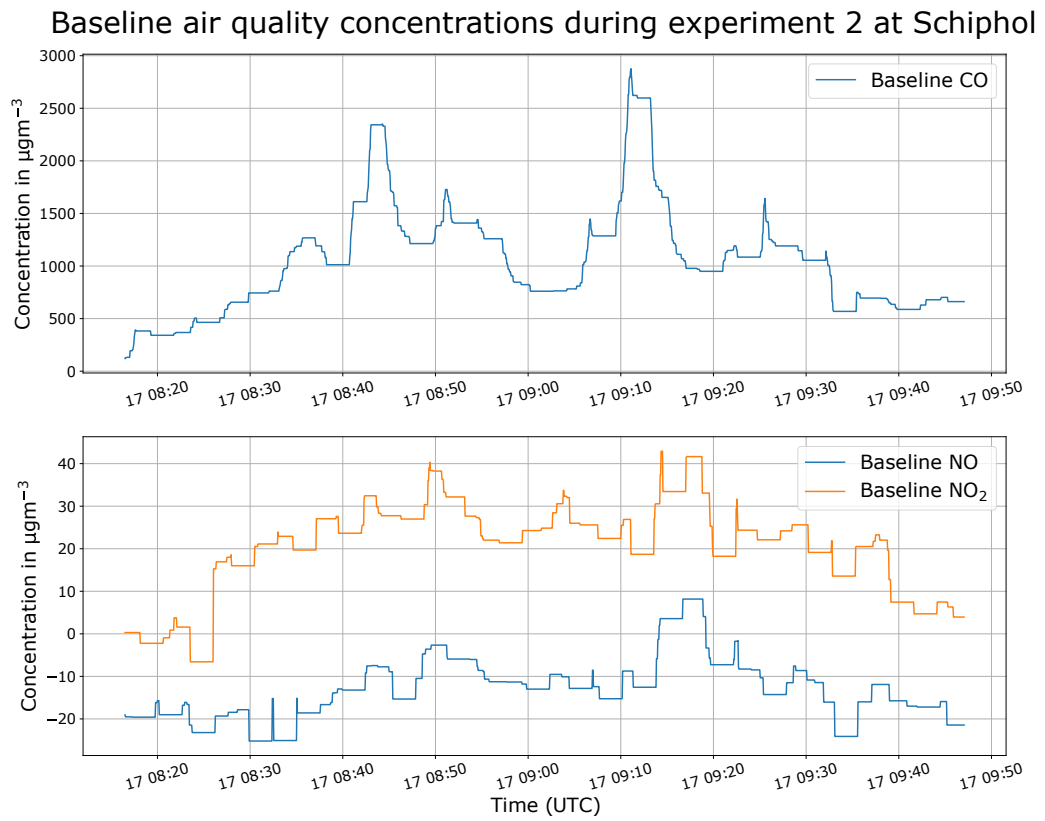


Figure D.2: Time-series visualisation of decomposed baseline air quality signal for second experiment.

### D.3. Experiment 3: Departures on the Aalsmeerbaan and Kaagbaan

Baseline air quality concentrations during experiment 3 at Schiphol

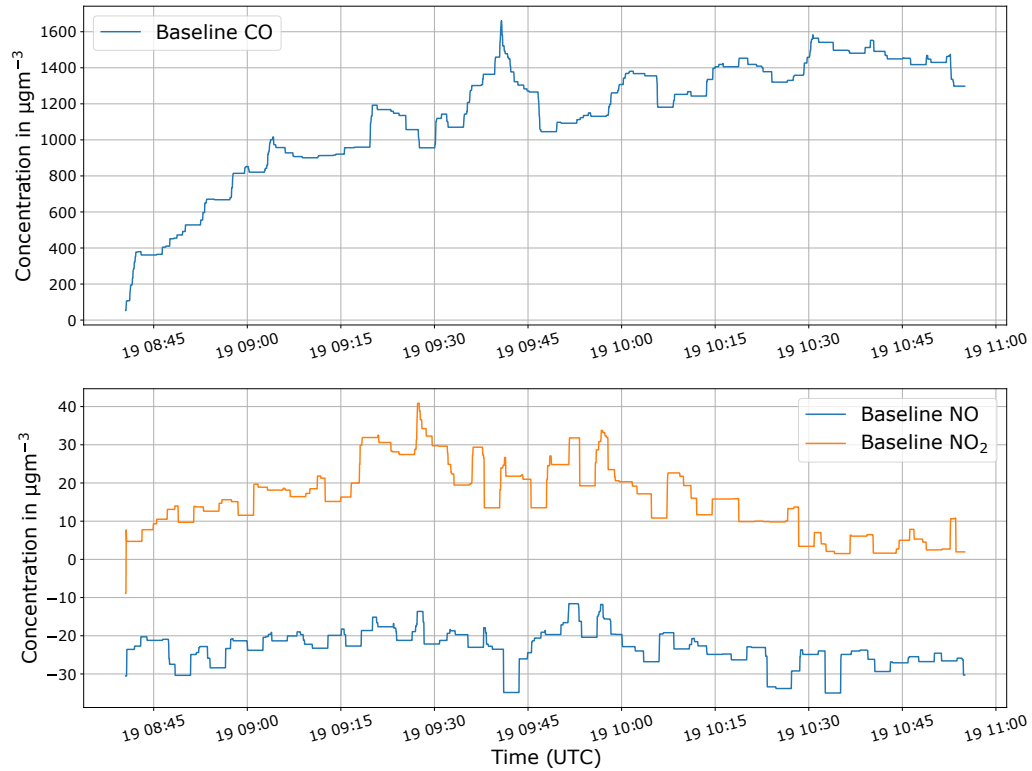


Figure D.3: Time-series visualisation of decomposed baseline air quality signal for third experiment.

## D.4. Experiment 4: Taxi Measurements on Airport Apron

Baseline air quality concentrations during experiment 4 at Schiphol

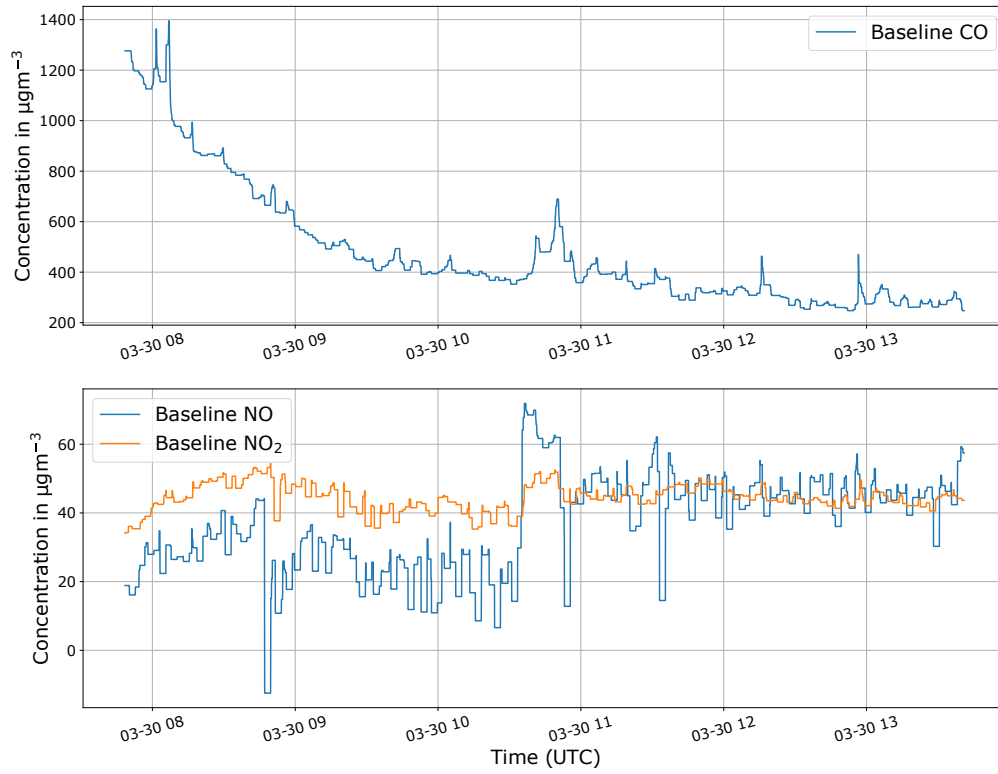
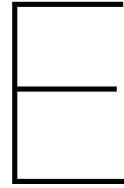


Figure D.4: Time-series visualisation of decomposed baseline air quality signal for fourth experiment.



# Local Air Quality Impacts per Aircraft Type and per Engine Configuration

## E.1. Experiment 1: Arrivals on the Polderbaan

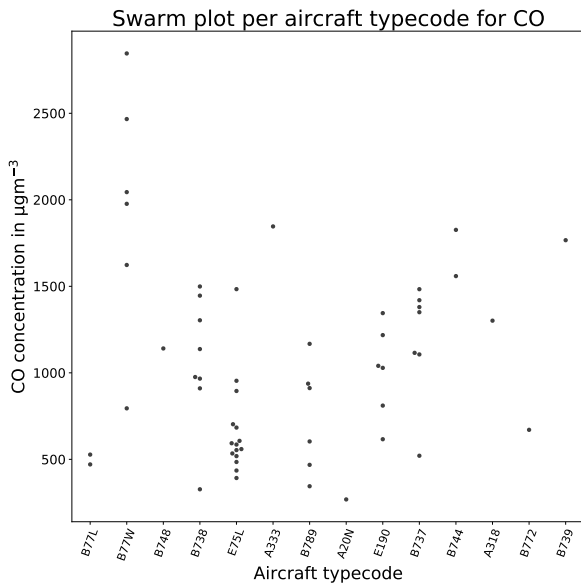


Figure E.1: Local CO impact per aircraft type for landings during the first experiment.

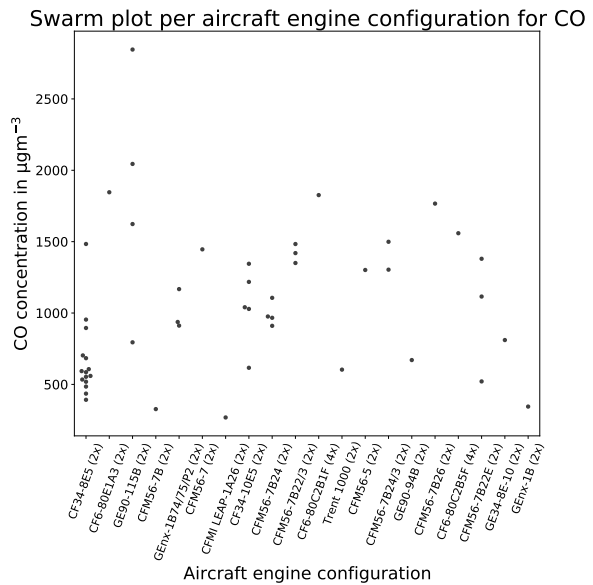


Figure E.2: Local CO impact per aircraft engine configuration for landings during the first experiment.

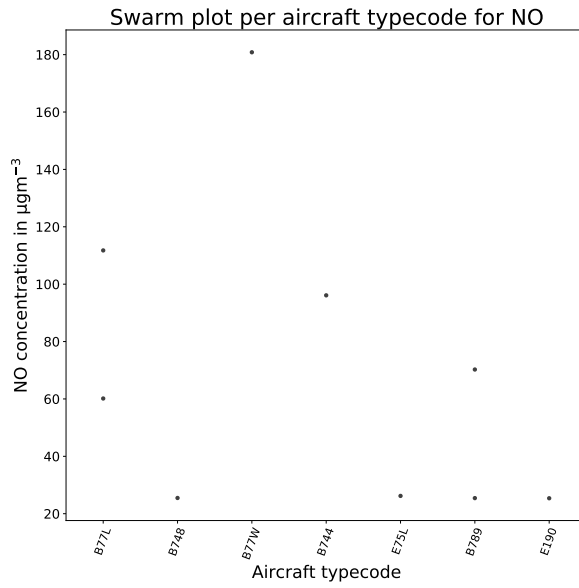


Figure E.3: Local NO impact per aircraft type for landings during the first experiment.

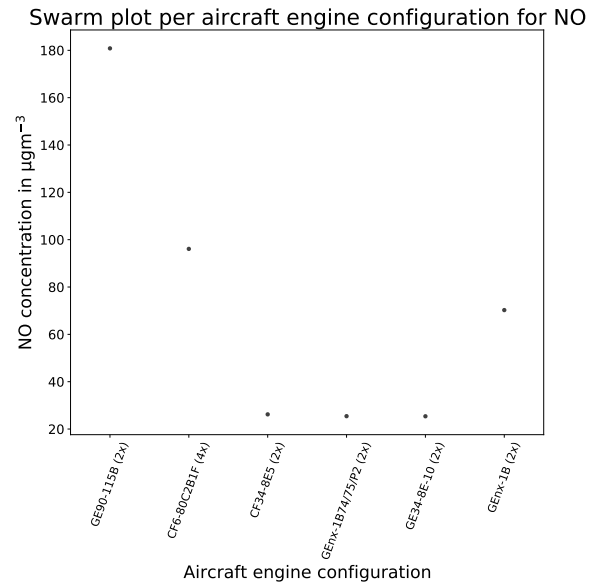


Figure E.4: Local NO impact per aircraft engine configuration for landings during the first experiment.

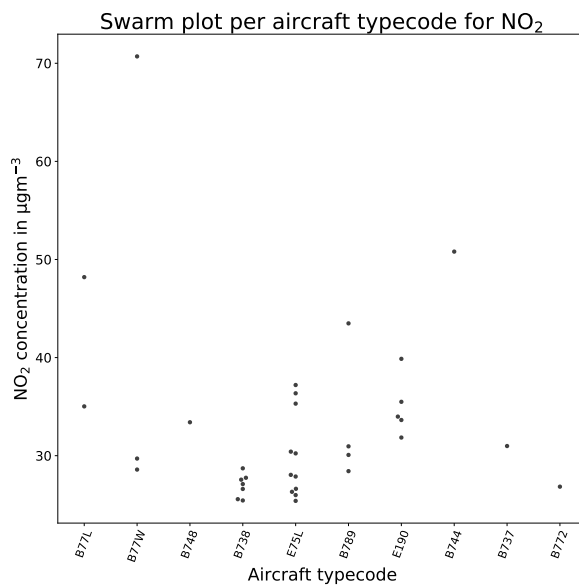


Figure E.5: Local NO<sub>2</sub> impact per aircraft type for landings during the first experiment.

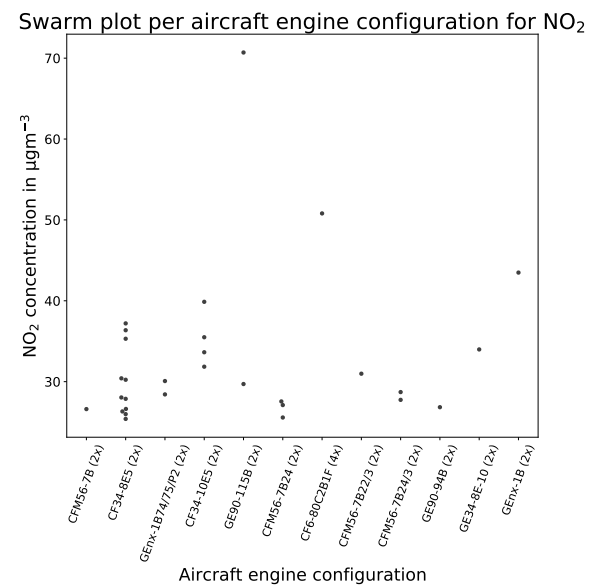


Figure E.6: Local NO<sub>2</sub> impact per aircraft engine configuration for landings during the first experiment.

### E.2. Experiment 2 and 3: Departures on the Aalsmeerbaan

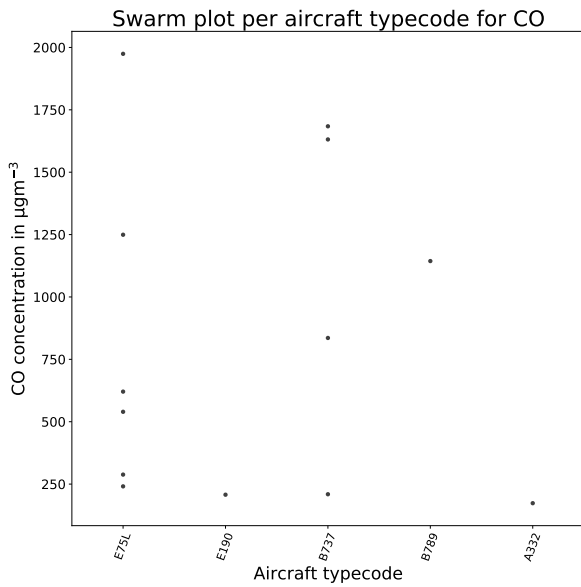


Figure E.7: Local CO impact per aircraft type for departures during the second and third experiment.

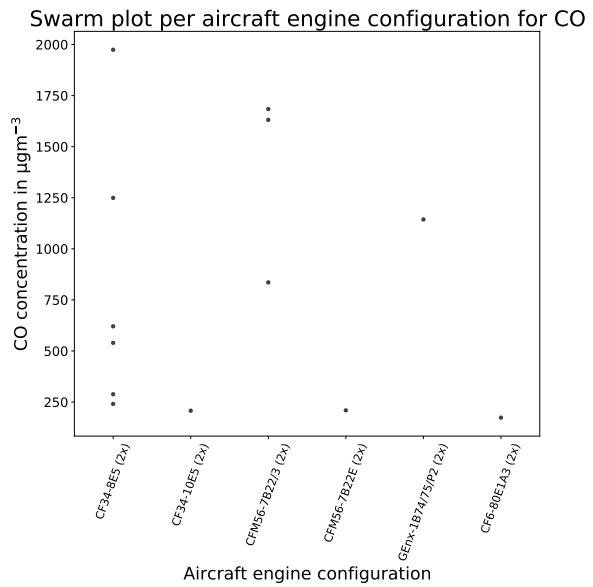


Figure E.8: Local CO impact per aircraft engine configuration for departures during the second and third experiment.

### E.3. Experiment 4: Taxi Measurements on Airport Apron

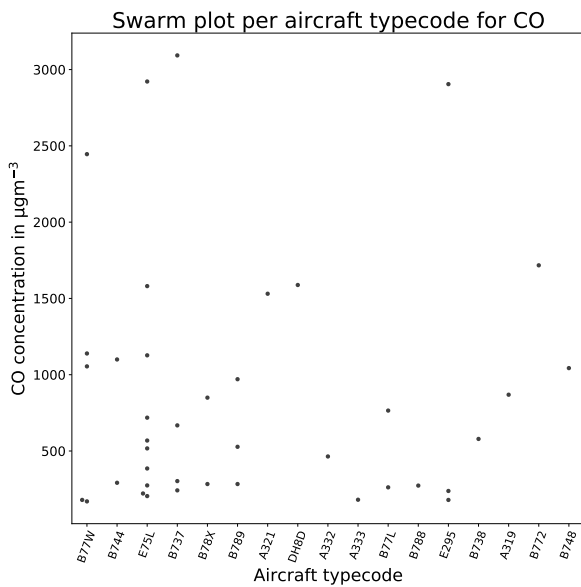


Figure E.9: Local CO impact per aircraft type for activity during the fourth experiment.

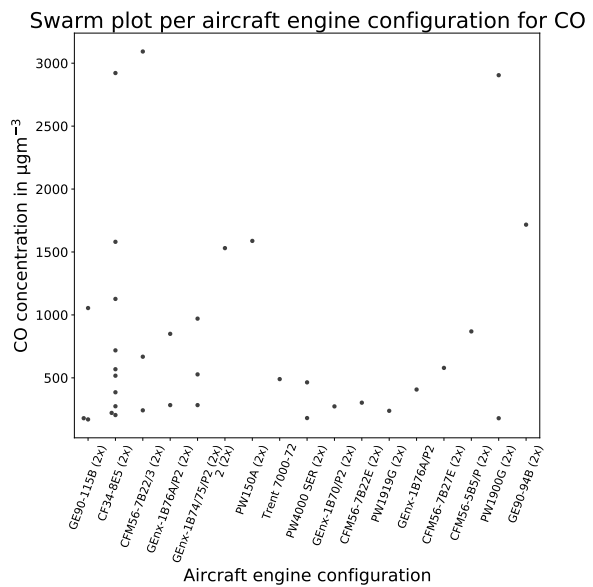


Figure E.10: Local CO impact per aircraft engine configuration for activity during the fourth experiment.

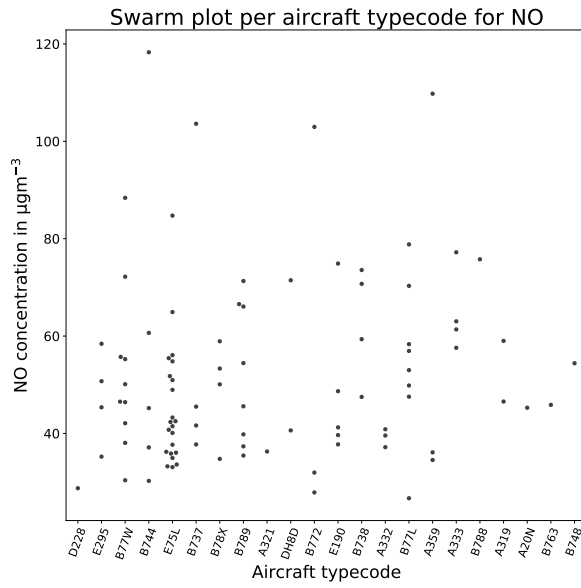


Figure E.11: Local NO impact per aircraft type for activity during the fourth experiment.

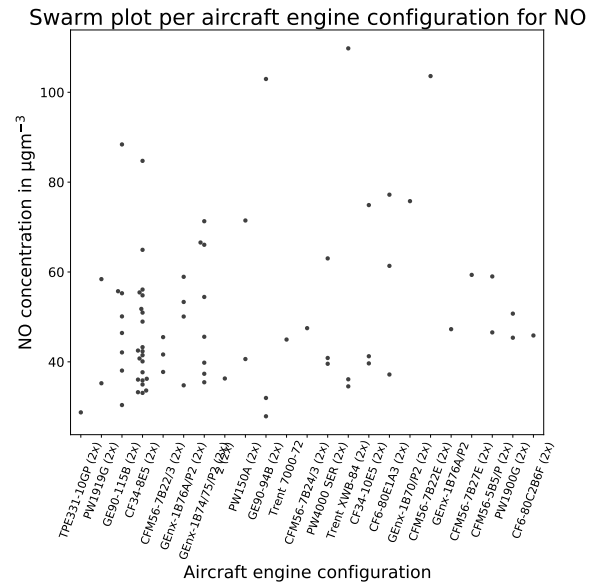


Figure E.12: Local NO impact per aircraft engine configuration for activity during the fourth experiment.

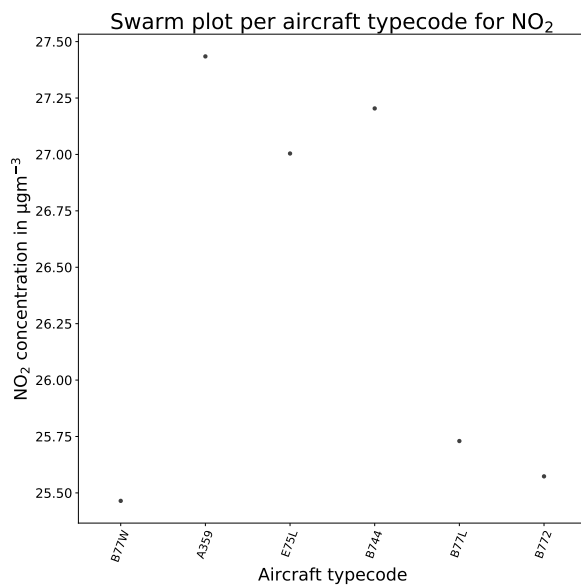


Figure E.13: Local NO<sub>2</sub> impact per aircraft type for activity during the fourth experiment.

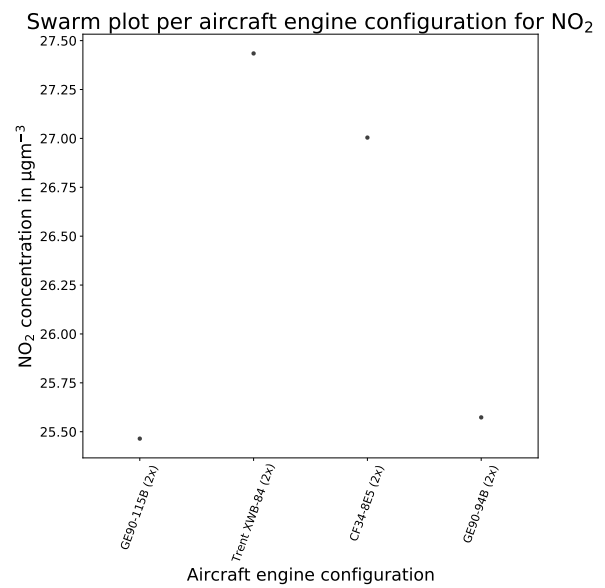
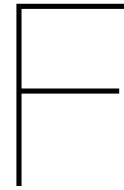


Figure E.14: Local NO<sub>2</sub> impact per aircraft engine configuration for activity during the fourth experiment.



# Flight Schedule via Visual Inspection

## F.1. Experiment 1: Arrivals on the Polderbaan

Table F.1: Visually observed landings on the Polderbaan 22-01-2021.

Local time	Callsign	Local time	Callsign
11:50	KL792	13:36	MS757
11:56	PS101	13:39	AF1740
12:02	KL1856	13:42	KL1010
12:09	EK147	13:49	KL1254
12:11	KL706	13:55	KL1654
12:15	TK7768	13:57	KL1316
12:18	KL1986	13:59	KL719
12:21	EY917	14:09	KL1944
12:24	SV215	14:13	KL1144
12:30	PS1253	14:35	KL1364
12:33	KL954	14:41	KL744
12:36	QR273	14:43	KL862
12:43	KL1766	14:49	KL1602
12:45	KL1780	14:51	KL686
12:48	KV901	14:55	KL1110
12:50	KL1474	14:56	KL1642
12:52	KLM9868	15:09	KL1168
12:53	KL1074	15:16	KL1304
12:56	KL1958	15:23	MP7122
12:59	KL1352	15:25	KL1234
13:11	KL1272	15:28	HV6732
13:12	KL1422	15:30	TP674
13:14	KL1794	15:36	AM25
13:15	KL1414	15:42	KL1374
13:17	KL1440	15:43	KL936
13:20	KL1280	15:46	A3626
13:23	KL1564	15:56	CK205
13:25	KL1128	15:59	KL1386
13:29	KL1994		

## F.2. Experiment 2: Departures on the Aalsmeerbaan and Kaagbaan

Table F.2: Visually observed departures on the Aalsmeerbaan and Kaagbaan 17-02-2021.

Local time	Callsign	Aircraft type	Runway	Local time	Callsign	Aircraft typecode	Runway
9:25	KL1351	E175	Aalsmeerbaan	10:17	KL1669	E190	Kaagbaan
9:27	KL1993	E175	Aalsmeerbaan	10:19	S2323	A350	Kaagbaan
9:30	KL1985	E175	Aalsmeerbaan	10:22	FB462	E190	Kaagbaan
9:32	HV5663	Unknown	Kaagbaan	10:23	KL	EXXX	Kaagbaan
9:37	KL1793	E190	Aalsmeerbaan	10:25	KL591	B777	Kaagbaan
9:39	CZ452	B777	Kaagbaan	10:29	KL661	B787	Kaagbaan
9:40	KL1903	E175	Aalsmeerbaan	10:27	B610	A220	Kaagbaan
9:42	KL935	B737	Kaagbaan	10:30	DL259	A330	Kaagbaan
9:43	KL623	A330	Kaagbaan				
9:45	KL	B737	Aalsmeerbaan				
9:47	KL1601	B737	Aalsmeerbaan				
9:48	KL	EXXX	Aalsmeerbaan				
9:49	KL	EXXX	Aalsmeerbaan				
9:50	FR	A319	Kaagbaan				
9:52	KL1653	E175	Aalsmeerbaan				
9:53	KL1601	B78	Kaagbaan				
9:55	KL1373	B737	Aalsmeerbaan				
9:56	HV6143	B737	Kaagbaan				
10:01	KL1109	B737	B737				
10:03	KL1385	B737	Aalsmeerbaan				
10:04	KL1109	B737	Kaagbaan				
10:04	KL1869	E175	Aalsmeerbaan				
10:05	KL791	B777	Unknown				
10:06	KL1855	E175	Aalsmeerbaan				
10:08	KL605	B787	Kaagbaan				
10:09	KL1975	B737	Aalsmeerbaan				
10:11	Unknown	E175	Kaagbaan				
10:13	KL569	B787	Aalsmeerbaan				
10:14	KL535	A330	Aalsmeerbaan				
10:14	KL755	B777	Kaagbaan				

### F.3. Experiment 3: Departures on the Aalsmeerbaan

Table F.3: Visually observed departures on the Aalsmeerbaan 19-02-2021.

Local time	Callsign	Aircraft type
9:39	KL1555	E175
9:41	U22724	A320
9:42	KL1373	B737
9:46	KL	Unknown
9:48	KL	Unknown
9:52	KL1823	E190
9:54	KL1385	B737
9:57	KL1653	E175
9:59	KL	E175
10:06	KL1765	E175
10:10	OS372	E195
10:12	KL	Unknown
10:15	KL567	B787
10:17	KL	Unknown
10:20	KL13636	E175
10:25	SQ323	A350
10:27	KL535	A330
10:29	DL259	A330
10:30	Unknown	Unknown
10:33	KL591	B777
10:35	BT610	A220
10:37	EI603	A320
10:46	DL135	A350
10:48	DL73	A330
10:50	KL735	B777
10:53	DL161	B767
11:06	UA71	B787
11:04	LH989	CRJ900





## G.2. Experiment 2: Departures on the Aalsmeerbaan

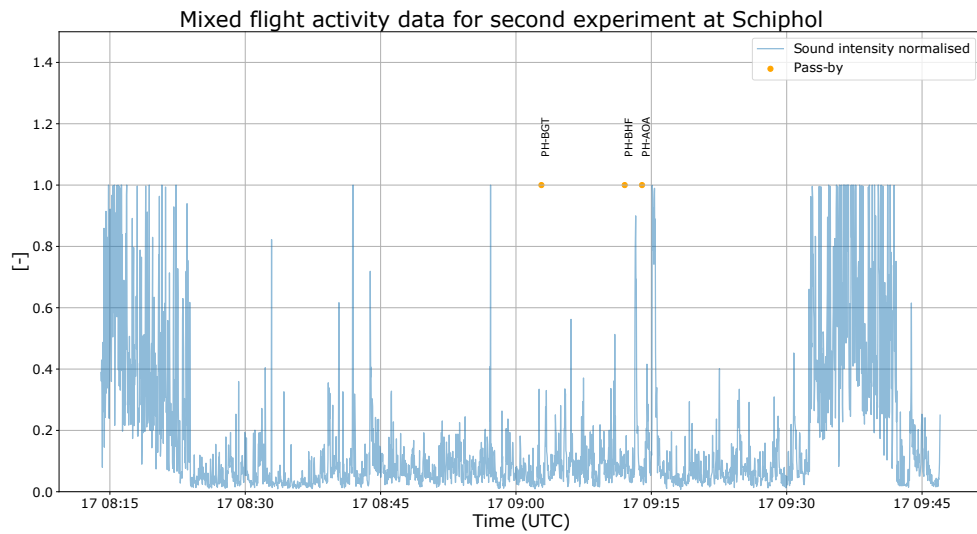


Figure G.2: Mixed flight activity based on ADS-B signal pass-by and normalised sound intensity for second experiment.

## G.3. Experiment 3: Departures on the Aalsmeerbaan

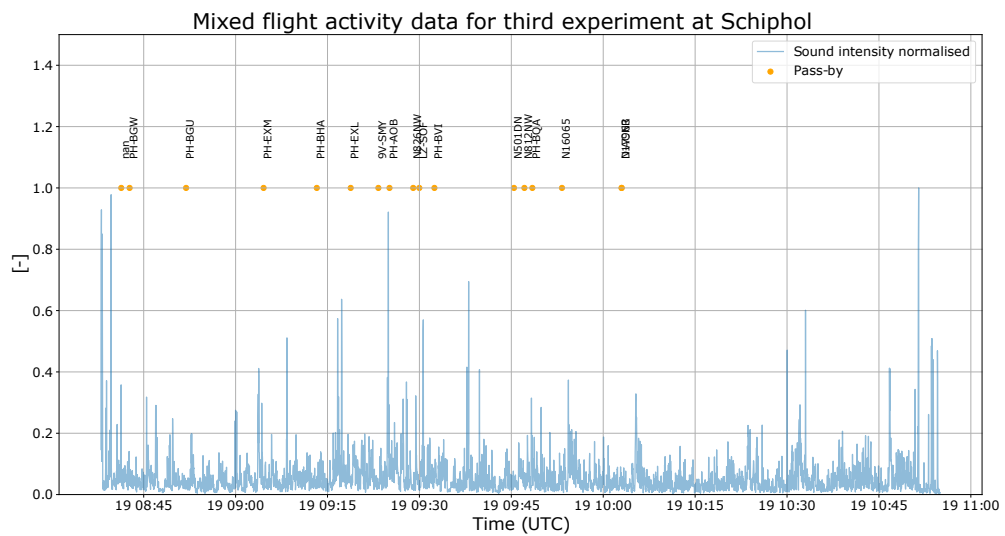


Figure G.3: Mixed flight activity based on ADS-B signal pass-by and normalised sound intensity for third experiment.

### G.4. Experiment 4: Taxi Measurements on Airport Apron

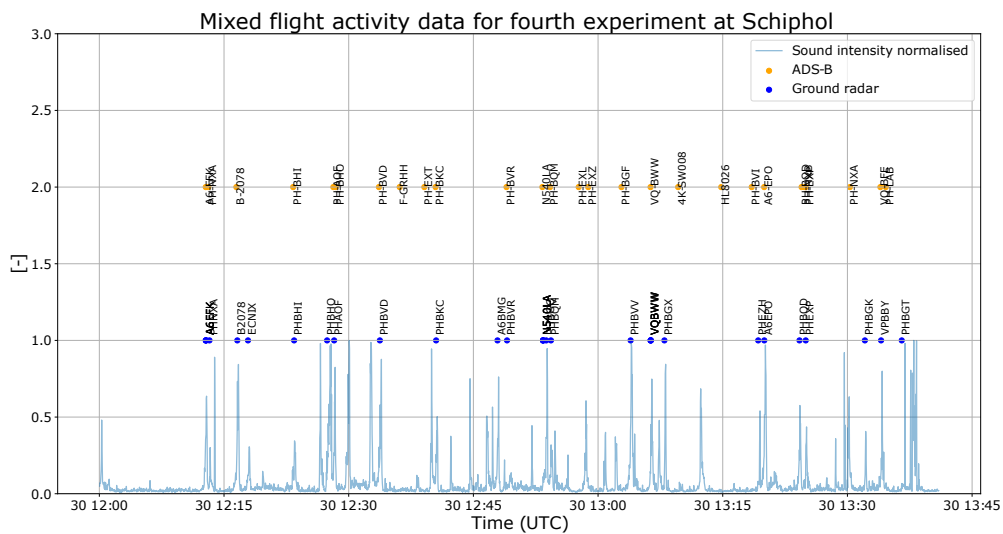
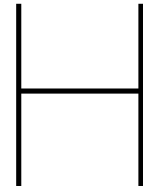


Figure G.4: Mixed flight activity based on ADS-B signal pass-by and normalised sound intensity for subset of fourth experiment.





# Sensor Box Operating Procedures

## H.1. Operating Procedures

Two separate Arduino scripts are responsible for the correct operation of the sensor box. The first script called `x_sensorBox_V2.ino` is the main sensor box operating code and is the code that needs to be uploaded to the Arduino to allow sampling air quality. The second script called `set_time_on_rtc.ino` is responsible for setting the correct time on the real-time clock.

### H.1.1. Air Quality Sampling

The first script, `x_sensorBox_V2.ino`, requires the operating procedures presented in Figure H.1.

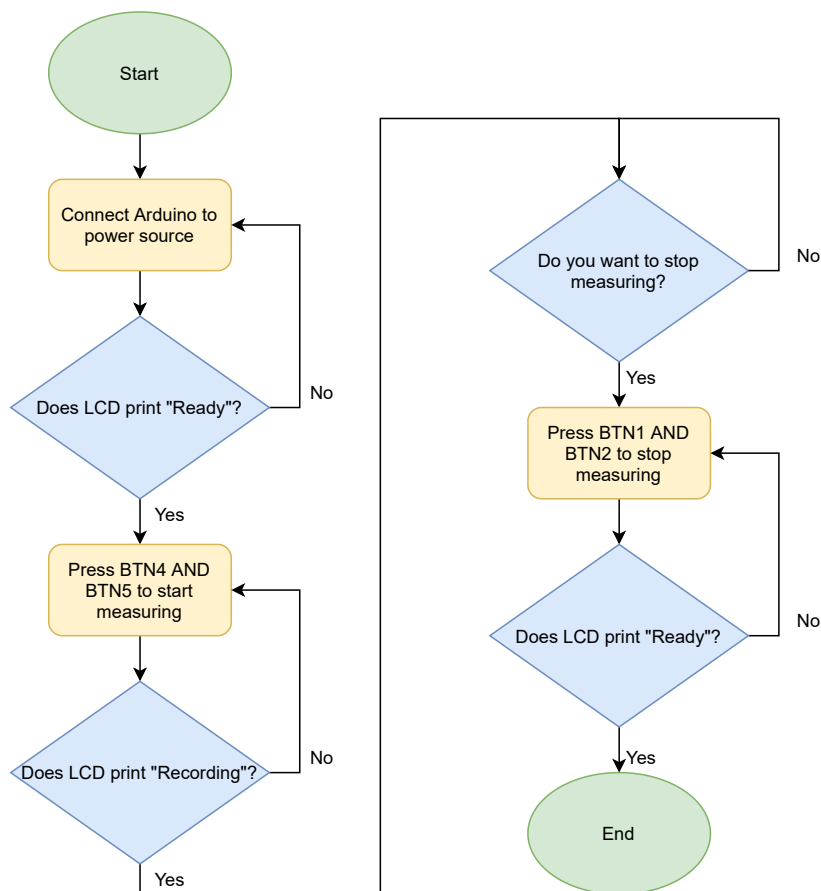


Figure H.1: Sensor box operating procedures for `x_sensorBox_V2.ino`.

In this state, the sensor box samples air quality, temperature, relative humidity, pressure, UV-light, visible light, infrared light and sound intensity. It then immediately writes this information to the SD card, coupled to a timestamp. Two signals are obtained per air quality sensor. The first signal corresponds to the raw working electrode (WE) output, the second signal represents the raw auxiliary electrode (AE) output. For clarity, Figure H.3 presents a diagram of the internal sensor box layout, which assists in identifying the correct buttons.

### H.1.2. Calibrating the Real-Time Clock

The second script, `set_time_on_rtc.ino` is only required when setting the time on the real-time clock, which should be done before every important experiment. Time is set manually via pushing a button when the installed time on the Arduino matches the current time. The installed time however is in the coordinated universal time format. The post-processing code is written under the assumption that the measurements are in UTC time.

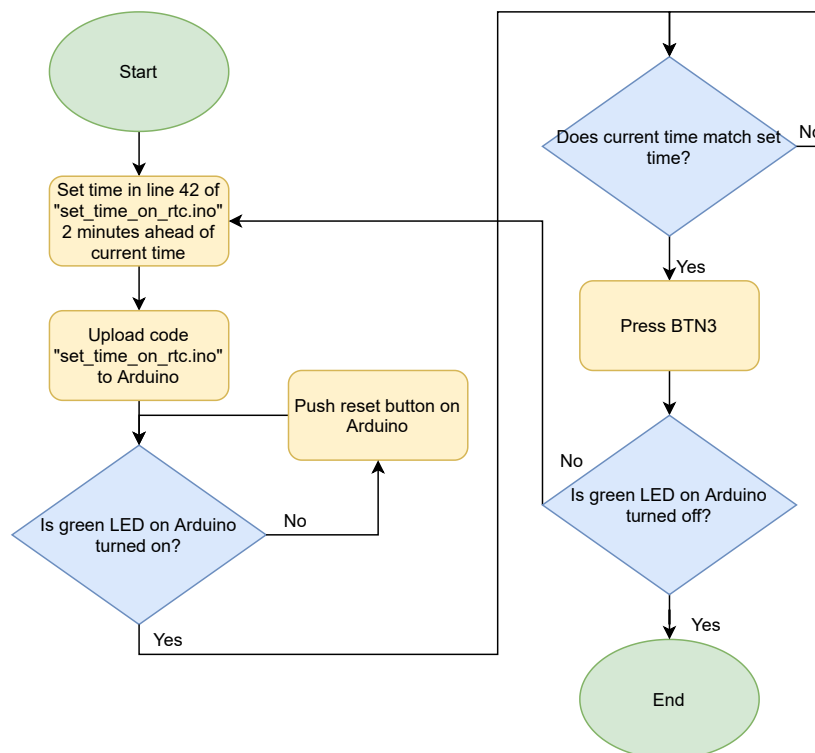


Figure H.2: Sensor box operating procedures for `set_time_on_rtc.ino`.

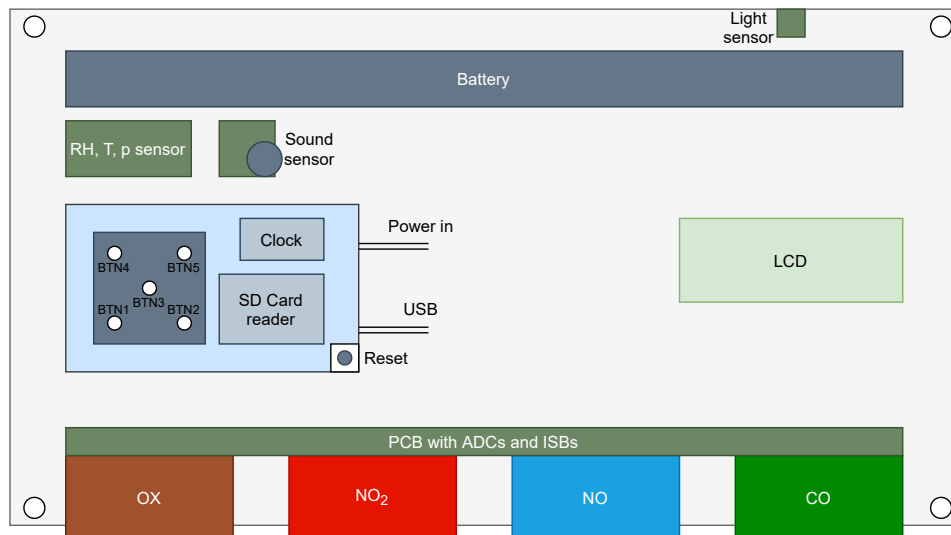


Figure H.3: Graphical internal lay-out of the final sensor box.

## H.2. Code

The code to operate the sensor box is written in the Arduino programming language. The to be discussed post-processing code is written in Python 3.7.6. Both the sensor box code and the to be discussed post-processing code are available via <https://gitlab.tudelft.nl/ance-dedoussi/air-quality-sensor>.



# METAR Data

Table I.1: METAR data for first experiment at Schiphol airport.

datetime_utc	pressure	dewpoint	elevation	flight_category	humidity	icao	temperature	visibility	wind_speed	wind_direction
2021-01-22 08:55:00+00:00	988.92	1	-2	VFR	76	EHAM	5	9999	13	250
2021-01-22 09:25:00+00:00	989.92	2	-2	VFR	76	EHAM	6	9999	13	250
2021-01-22 09:55:00+00:00	989.92	2	-2	VFR	76	EHAM	6	9999	15	250
2021-01-22 10:25:00+00:00	990.92	2	-2	VFR	71	EHAM	7	9999	13	260
2021-01-22 10:55:00+00:00	990.92	2	-2	VFR	76	EHAM	6	9999	18	250
2021-01-22 11:25:00+00:00	990.92	2	-2	VFR	71	EHAM	7	9999	16	260
2021-01-22 11:55:00+00:00	990.92	2	-2	VFR	71	EHAM	7	9999	17	250
2021-01-22 12:25:00+00:00	991.92	2	-2	VFR	71	EHAM	7	9999	18	250
2021-01-22 12:55:00+00:00	991.92	2	-2	VFR	71	EHAM	7	9999	18	250
2021-01-22 13:25:00+00:00	991.92	2	-2	VFR	71	EHAM	7	9999	17	250
2021-01-22 13:55:00+00:00	991.92	2	-2	VFR	71	EHAM	7	9999	15	250
2021-01-22 14:25:00+00:00	992.92	2	-2	VFR	71	EHAM	7	9999	12	240
2021-01-22 14:55:00+00:00	992.92	2	-2	VFR	76	EHAM	6	9999	14	240
2021-01-22 15:25:00+00:00	992.92	2	-2	VFR	76	EHAM	6	9999	13	240
2021-01-22 15:55:00+00:00	992.92	2	-2	VFR	81	EHAM	5	9999	10	230



J

## Final Calibration Equations

$$CO_{corrected} = 85.38 \cdot Pressure + 213.28 \cdot NO\_AUX + 102.03 \cdot CO\_AUX + 164.28 \cdot NO\_WE \\ + 3817.57 \cdot CO\_WE - 228.34 \cdot Temperature - 64.36 \cdot OX\_AUX$$

$$NO_{corrected} = -1.03 \cdot Pressure + 1.74 \cdot NO2\_WE - 42.55 \cdot NO\_AUX + 179.80 \cdot NO\_WE \\ - 3.51 \cdot CO\_AUX + 2.42 \cdot CO\_WE - 3.72 \cdot Temperature - 4.05 \cdot Humidity \\ + 5.60 \cdot OX\_WE + 6.51 \cdot OX\_AUX - 10.71 \cdot NO2\_AUX$$

$$NO_{2corrected} = 12.83 \cdot Pressure + 75.20 \cdot NO2\_WE + 28.61 \cdot NO\_AUX + 23.67 \cdot NO\_WE \\ + 16.41 \cdot CO\_AUX - 5.29 \cdot CO\_WE - 19.63 \cdot Temperature + 6.49 \cdot Humidity \\ - 14.17 \cdot OX\_WE - 38.20 \cdot OX\_AUX + 17.88 \cdot NO2\_AUX$$



# Bibliography

- [1] 59a0e06f75d35.jpg (500×500), . URL <https://www.isweek.com/Uploads/20170826/59a0e06f75d35.jpg>.
- [2] AAN 104 How Electrochemical Gas Sensors Work, .
- [3] Air | Alphasense, . URL <http://www.alphasense.com/index.php/air/>.
- [4] Automatic-Dependent-Surveillance-Broadcast-ADS-B-system-17.png (699×519), . URL <https://www.researchgate.net/profile/Busyairah-Syd-Ali/publication/304782280/figure/fig1/AS:551182794199040@1508423626286/Automatic-Dependent-Surveillance-Broadcast-ADS-B-system-17.png>.
- [5] Automatic Dependent Surveillance Broadcast (ADS-B) - SKYbrary Aviation Safety, . URL [https://www.skybrary.aero/index.php/Automatic\\_Dependent\\_Surveillance\\_Broadcast\\_\(ADS-B\)](https://www.skybrary.aero/index.php/Automatic_Dependent_Surveillance_Broadcast_(ADS-B)).
- [6] BRITISH AIRWAYS TECHNICAL DOCUMENTS RELATING TO AIRCRAFT OPERATIONS SUPPORTING THE PROJECT FOR THE SUSTAINABLE DEVELOPMENT OF HEATHROW, . URL [http://www.britishairways.com/cms/global/pdfs/csr/PSDH\\_Technical\\_Reports.pdf](http://www.britishairways.com/cms/global/pdfs/csr/PSDH_Technical_Reports.pdf).
- [7] Civil Turbojet/Turbofan Specifications, . URL <http://www.jet-engine.net/civtfspec.html>.
- [8] Commercial airlines: worldwide fuel consumption 2005-2021, . URL <https://www.statista.com/statistics/655057/fuel-consumption-of-airlines-worldwide/>.
- [9] Diagram-of-k-fold-cross-validation-with-k-10-Image-from-Karl-Rosaen-Log.ppm (850×468), . URL <https://www.researchgate.net/profile/Johar-Ashfaque/publication/332370436/figure/fig1/AS:746775958806528@1555056671117/Diagram-of-k-fold-cross-validation-with-k-10-Image-from-Karl-Rosaen-Log.ppm>.
- [10] The Environment Cube! Know the Land Beneath You!, . URL <https://www.hackster.io/dhairya-parikh/the-environment-cube-know-the-land-beneath-you-b3c2dd>.
- [11] Grove - Sound Sensor Based on LM358 amplifier - Arduino Compatible, . URL <https://www.seeedstudio.com/Grove-Sound-Sensor-Based-on-LM386-amplifier-Arduino-Compatible.html>.
- [12] ICAO Aircraft Engine Emissions Databank, . URL <https://www.easa.europa.eu/domains/environment/icao-aircraft-engine-emissions-databank>.
- [13] living-room\_good-4715bd2e054802ffb2ec91331be9b99c687aee58-s1200.png (1200×899), . URL [https://media.npr.org/assets/img/2015/05/24/living-room\\_good-4715bd2e054802ffb2ec91331be9b99c687aee58-s1200.png](https://media.npr.org/assets/img/2015/05/24/living-room_good-4715bd2e054802ffb2ec91331be9b99c687aee58-s1200.png).
- [14] Local Air Quality Technology Standards, . URL [https://www.icao.int/environmental-protection/Pages/LAQ\\_TechnologyStandards.aspx](https://www.icao.int/environmental-protection/Pages/LAQ_TechnologyStandards.aspx).
- [15] Luchtmeetnet.nl, . URL <https://www.luchtmeetnet.nl/>. Library Catalog: [www.luchtmeetnet.nl](http://www.luchtmeetnet.nl).
- [16] Microchip\_mcp3423-E-UN\_25951.jpg (640×640), . URL [https://snapeda.s3.amazonaws.com/partpics/Microchip\\_MCP3423-E-UN\\_25951.jpg](https://snapeda.s3.amazonaws.com/partpics/Microchip_MCP3423-E-UN_25951.jpg).

- [17] The OpenSky Network API documentation — The OpenSky Network API 1.4.0 documentation, . URL <https://opensky-network.org/apidoc/#>.
- [18] Restricting Use of Reverse Thrust as an Emissions Reduction Strategy - Colin Rice, 2002, . URL <https://journals.sagepub.com/doi/abs/10.3141/1788-16>.
- [19] Seeed LoRa IoT Solution, . URL <https://www.hackster.io/SeeedStudio/seed-lora-iot-solution-b5ee95>.
- [20] Standards - Air Quality - Environment - European Commission, . URL <https://ec.europa.eu/environment/air/quality/standards.htm>.
- [21] What Is Air Pollution | Environmental Pollution Centers, . URL <https://www.environmentalpollutioncenters.org/air/>.
- [22] WHO | Air quality guidelines – global update 2005, . URL <http://www.who.int/airpollution/publications/aqg2005/en/>. Library Catalog: [www.who.int](http://www.who.int) Publisher: World Health Organization.
- [23] Worldwide air traffic - fatalities 2020, . URL <https://www.statista.com/statistics/263443/worldwide-air-traffic-fatalities/>.
- [24] B. C. Airplanes. 787 Airplane Characteristics for Airport Planning, December 2015. URL <http://www.boeing-suppliers.com/assets/pdf/commercial/airports/acaps/787.pdf>.
- [25] F. Amato, T. Moreno, M. Pandolfi, X. Querol, A. Alastuey, A. Delgado, M. Pedrero, and N. Cots. Concentrations, sources and geochemistry of airborne particulate matter at a major European airport. *Journal of Environmental Monitoring*, 12(4):854–862, April 2010. ISSN 1464-0333. doi: 10.1039/B925439K. URL <https://pubs.rsc.org/en/content/articlelanding/2010/em/b925439k>. Publisher: The Royal Society of Chemistry.
- [26] S. R. H. Barrett, R. E. Britter, and I. A. Waitz. Impact of aircraft plume dynamics on airport local air quality. *Atmospheric Environment*, 74:247–258, August 2013. ISSN 1352-2310. doi: 10.1016/j.atmosenv.2013.03.061. URL <https://www.sciencedirect.com/science/article/pii/S1352231013002458>.
- [27] C. Borrego, A. M. Costa, J. Ginja, M. Amorim, M. Coutinho, K. Karatzas, T. Sioumis, N. Katsifarakis, K. Konstantinidis, S. De Vito, E. Esposito, P. Smith, N. André, P. Gérard, L. A. Francis, N. Castell, P. Schneider, M. Viana, M. C. Minguillón, W. Reimringer, R. P. Otjes, O. von Sicard, R. Pohle, B. Elen, D. Suriano, V. Pfister, M. Prato, S. Dipinto, and M. Penza. Assessment of air quality microsensors versus reference methods: The EuNetAir joint exercise. *Atmospheric Environment*, 147:246–263, December 2016. ISSN 1352-2310. doi: 10.1016/j.atmosenv.2016.09.050. URL <http://www.sciencedirect.com/science/article/pii/S1352231016307610>.
- [28] Y. S. Chati and H. Balakrishnan. Aircraft Engine Performance Study Using Flight Data Recorder Archives. In *2013 Aviation Technology, Integration, and Operations Conference*, AIAA AVIATION Forum. American Institute of Aeronautics and Astronautics, August 2013. doi: 10.2514/6.2013-4414. URL <https://arc.aiaa.org/doi/10.2514/6.2013-4414>.
- [29] D. de Jonge. Datarapport Luchtkwaliteit Haarlemmermeer meetresultaten 2019, June 2020.
- [30] R. E. Dodson, E. Andres Houseman, B. Morin, and J. I. Levy. An analysis of continuous black carbon concentrations in proximity to an airport and major roadways. *Atmospheric Environment*, 43(24):3764–3773, August 2009. ISSN 1352-2310. doi: 10.1016/j.atmosenv.2009.04.014. URL <http://www.sciencedirect.com/science/article/pii/S135223100900329X>.
- [31] EPA. Nitrogen Oxides (NOx), Why and How They are Controlled, 1999. URL <https://www3.epa.gov/ttn/catc/dir1/fnoxdoc.pdf>.

- [32] B. J. Finlayson-Pitts and J. N. P. Jr. *Chemistry of the Upper and Lower Atmosphere: Theory, Experiments, and Applications*. Elsevier, November 1999. ISBN 978-0-08-052907-3. Google-Books-ID: mRoJUB5fxRwC.
- [33] B. D. Garg, S. H. Cadle, P. A. Mulawa, P. J. Groblicki, C. Laroo, and G. A. Parr. Brake Wear Particulate Matter Emissions. *Environmental Science & Technology*, 34(21):4463–4469, November 2000. ISSN 0013-936X. doi: 10.1021/es001108h. URL <https://doi.org/10.1021/es001108h>. Publisher: American Chemical Society.
- [34] A. Géron. *Hands-on Machine Learning with Scikit-Learn, Keras, and TensorFlow: Concepts, Tools, and Techniques to Build Intelligent Systems*. O'Reilly Media, June 2019. ISBN 978-1-4920-3264-9.
- [35] H.-H. Hsu, G. Adamkiewicz, E. Andres Houseman, J. Vallarino, S. J. Melly, R. L. Wayson, J. D. Spengler, and J. I. Levy. The relationship between aviation activities and ultrafine particulate matter concentrations near a mid-sized airport. *Atmospheric Environment*, 50:328–337, April 2012. ISSN 1352-2310. doi: 10.1016/j.atmosenv.2011.12.002. URL <http://www.sciencedirect.com/science/article/pii/S1352231011012544>.
- [36] H.-H. Hsu, G. Adamkiewicz, E. A. Houseman, J. D. Spengler, and J. I. Levy. Using mobile monitoring to characterize roadway and aircraft contributions to ultrafine particle concentrations near a mid-sized airport. *Atmospheric Environment*, 89:688–695, June 2014. ISSN 1352-2310. doi: 10.1016/j.atmosenv.2014.02.023. URL <http://www.sciencedirect.com/science/article/pii/S1352231014001198>.
- [37] D. Hunton, J. Ballenthin, J. Borghetti, G. Federico, T. Miller, W. Thorn, A. Viggiano, B. Anderson, W. Cofer III, D. McDougal, and C. Wey. Chemical ionization mass spectrometric measurements of SO<sub>2</sub> emissions from jet engines in flight and test chamber operations. *Journal of Geophysical Research Atmospheres*, 105(D22):26841–26855, 2000. doi: 10.1029/2000JD900383.
- [38] A. Industries. Adafruit Assembled Data Logging shield for Arduino. URL <https://www.adafruit.com/product/1141>.
- [39] v. B. J.P, V. W.P.J., S. Savad, and M. Francesco. Gas Turbines, February 2011.
- [40] M. P. Keuken, M. Moerman, P. Zandveld, J. S. Henzing, and G. Hoek. Total and size-resolved particle number and black carbon concentrations in urban areas near Schiphol airport (the Netherlands). *Atmospheric Environment*, 104:132–142, March 2015. ISSN 1352-2310. doi: 10.1016/j.atmosenv.2015.01.015. URL <http://www.sciencedirect.com/science/article/pii/S1352231015000175>.
- [41] K. Koutroumbas, S. Theodoridis, and K. Koutroumbas. *Pattern Recognition*. Elsevier Science & Technology, Burlington, UNITED STATES, 2008. ISBN 978-0-08-094912-3. URL <http://ebookcentral.proquest.com/lib/delft/detail.action?docID=534973>.
- [42] M. Lopes, A. Russo, J. Monjardino, C. Gouveia, and F. Ferreira. Monitoring of ultrafine particles in the surrounding urban area of a civilian airport. *Atmospheric Pollution Research*, 10(5):1454–1463, September 2019. ISSN 1309-1042. doi: 10.1016/j.apr.2019.04.002. URL <http://www.sciencedirect.com/science/article/pii/S1309104218307591>.
- [43] M. Masiol and R. M. Harrison. Aircraft engine exhaust emissions and other airport-related contributions to ambient air pollution: A review. *Atmospheric Environment*, 95:409–455, October 2014. ISSN 1352-2310. doi: 10.1016/j.atmosenv.2014.05.070. URL <http://www.sciencedirect.com/science/article/pii/S1352231014004361>.
- [44] M. Masiol and R. M. Harrison. Quantification of air quality impacts of London Heathrow Airport (UK) from 2005 to 2012. *Atmospheric Environment*, 116:308–319, September 2015. ISSN 1352-2310. doi: 10.1016/j.atmosenv.2015.06.048. URL <http://www.sciencedirect.com/science/article/pii/S1352231015301898>.

- [45] M. Masiol, T. V. Vu, D. C. S. Beddows, and R. M. Harrison. Source apportionment of wide range particle size spectra and black carbon collected at the airport of Venice (Italy). *Atmospheric Environment*, 139:56–74, August 2016. ISSN 1352-2310. doi: 10.1016/j.atmosenv.2016.05.018. URL <http://www.sciencedirect.com/science/article/pii/S1352231016303594>.
- [46] M. I. Mead, O. A. M. Popoola, G. B. Stewart, P. Landshoff, M. Calleja, M. Hayes, J. J. Baldovi, M. W. McLeod, T. F. Hodgson, J. Dicks, A. Lewis, J. Cohen, R. Baron, J. R. Saffell, and R. L. Jones. The use of electrochemical sensors for monitoring urban air quality in low-cost, high-density networks. *Atmospheric Environment*, 70:186–203, May 2013. ISSN 1352-2310. doi: 10.1016/j.atmosenv.2012.11.060. URL <http://www.sciencedirect.com/science/article/pii/S1352231012011284>.
- [47] R. Merino-Martinez, M. Snellen, and D. G. Simons. Calculation of the Fan Rotational Speed Based on Flyover Recordings for Improving Aircraft Noise Prediction Models. page 8.
- [48] B. Mijling, Q. Jiang, D. de Jonge, and S. Bocconi. Field calibration of electrochemical NO<sub>2</sub> sensors in a citizen science context. *Atmospheric Measurement Techniques*, 11(3):1297–1312, March 2018. ISSN 1867-8548. doi: 10.5194/amt-11-1297-2018. URL <https://amt.copernicus.org/articles/11/1297/2018/>.
- [49] T. Mokalled, J. Adjizian Gérard, M. Abboud, C. Trocquet, R. Nassreddine, V. Person, and S. le Calvé. VOC tracers from aircraft activities at Beirut Rafic Hariri International Airport. *Atmospheric Pollution Research*, 10(2):537–551, March 2019. ISSN 1309-1042. doi: 10.1016/j.apr.2018.09.009. URL <http://www.sciencedirect.com/science/article/pii/S1309104218302733>.
- [50] S. S. Nambisan, J. Kajkowski, and R. Menon. A Preliminary Survey of Ground Service Equipment Running Times and Its Implications for Air Quality Estimates at Airports. pages 144–152, April 2012. doi: 10.1061/40530(303)11. URL <https://ascelibrary.org/doi/abs/10.1061/40530%28303%2911>. Publisher: American Society of Civil Engineers.
- [51] M. Nič, J. Jiráť, B. Košata, A. Jenkins, and A. McNaught, editors. *IUPAC Compendium of Chemical Terminology: Gold Book*. IUPAC, Research Triangle Park, NC, 2.1.0 edition, June 2009. ISBN 978-0-9678550-9-7. doi: 10.1351/goldbook. URL <http://goldbook.iupac.org>.
- [52] W. H. Organization, editor. *Air quality guidelines for Europe*. Number no. 91 in WHO regional publications. World Health Organization, Regional Office for Europe, Copenhagen, 2nd ed edition, 2000. ISBN 978-92-890-1358-1. OCLC: 18166272.
- [53] D. A. Parker, H. C. Burridge, J. L. Partridge, and P. F. Linden. Vertically distributed wall sources of buoyancy. Part 1. Unconfined. *Journal of Fluid Mechanics*, 907, January 2021. ISSN 0022-1120, 1469-7645. doi: 10.1017/jfm.2020.808. URL <https://www.cambridge.org/core/journals/journal-of-fluid-mechanics/article/vertically-distributed-wall-sources-of-buoyancy-part-1-unconfined/67F089C97A39203DC012DCC08550EAAC>. Publisher: Cambridge University Press.
- [54] S. L. Penn, S. Arunachalam, Y. Tripodis, W. Heiger-Bernays, and J. I. Levy. A comparison between monitoring and dispersion modeling approaches to assess the impact of aviation on concentrations of black carbon and nitrogen oxides at Los Angeles International Airport. *Science of The Total Environment*, 527-528:47–55, September 2015. ISSN 0048-9697. doi: 10.1016/j.scitotenv.2015.03.147. URL <http://www.sciencedirect.com/science/article/pii/S0048969715004696>.
- [55] M. Penza. Chapter 12 - Low-cost sensors for outdoor air quality monitoring. In E. Llobet, editor, *Advanced Nanomaterials for Inexpensive Gas Microsensors*, Micro and Nano Technologies, pages 235–288. Elsevier, January 2020. ISBN 978-0-12-814827-3. doi: 10.1016/B978-0-12-814827-3.00012-8. URL <http://www.sciencedirect.com/science/article/pii/B9780128148273000128>.

- [56] O. A. M. Popoola, D. Carruthers, C. Lad, V. B. Bright, M. I. Mead, M. E. J. Stettler, J. R. Saffell, and R. L. Jones. Use of networks of low cost air quality sensors to quantify air quality in urban settings. *Atmospheric Environment*, 194:58–70, December 2018. ISSN 1352-2310. doi: 10.1016/j.atmosenv.2018.09.030. URL <http://www.sciencedirect.com/science/article/pii/S1352231018306241>.
- [57] C. Psanis, E. Triantafyllou, M. Giamarelou, M. Manousakas, K. Eleftheriadis, and G. Biskos. Particulate matter pollution from aviation-related activity at a small airport of the Aegean Sea Insular Region. *Science of The Total Environment*, 596-597:187–193, October 2017. ISSN 0048-9697. doi: 10.1016/j.scitotenv.2017.04.078. URL <http://www.sciencedirect.com/science/article/pii/S0048969717309154>.
- [58] G. Ratliff, C. Sequeira, I. Waitz, M. Ohsfeldt, T. Thrasher, and T. Thompson. PARTNER Project 15 final report. page 181.
- [59] H. Ritchie and M. Roser. Air Pollution. *Our World in Data*, April 2017. URL <https://ourworldindata.org/air-pollution>.
- [60] A. L. Robinson, A. P. Grieshop, N. M. Donahue, and S. W. Hunt. Updating the Conceptual Model for Fine Particle Mass Emissions from Combustion Systems Allen L. Robinson. *Journal of the Air & Waste Management Association*, 60(10):1204–1222, October 2010. ISSN 1096-2247. doi: 10.3155/1047-3289.60.10.1204. URL <https://doi.org/10.3155/1047-3289.60.10.1204>. Publisher: Taylor & Francis \_eprint: <https://doi.org/10.3155/1047-3289.60.10.1204>.
- [61] K. Schäfer, C. Jahn, P. Sturm, B. Lechner, and M. Bacher. Aircraft emission measurements by remote sensing methodologies at airports. *Atmospheric Environment*, 37(37):5261–5271, December 2003. ISSN 1352-2310. doi: 10.1016/j.atmosenv.2003.09.002. URL <http://www.sciencedirect.com/science/article/pii/S1352231003007362>.
- [62] G. Schürmann, K. Schäfer, C. Jahn, H. Hoffmann, M. Bauerfeind, E. Fleuti, and B. Rappenglück. The impact of NO<sub>x</sub>, CO and VOC emissions on the air quality of Zurich airport. *Atmospheric Environment*, 41(1):103–118, January 2007. ISSN 1352-2310. doi: 10.1016/j.atmosenv.2006.07.030. URL <http://www.sciencedirect.com/science/article/pii/S1352231006007989>.
- [63] M. E. J. Stettler, S. Eastham, and S. R. H. Barrett. Air quality and public health impacts of UK airports. Part I: Emissions. *Atmospheric Environment*, 45(31):5415–5424, October 2011. ISSN 1352-2310. doi: 10.1016/j.atmosenv.2011.07.012. URL <http://www.sciencedirect.com/science/article/pii/S135223101100728X>.
- [64] The Things Network. Joost Wesseling (RIVM) - Air quality measurements using cheap sensors, 2018. URL <https://www.youtube.com/watch?v=FgvghFFSQ6c&t=203s>.
- [65] J. Thongplang. Air pollution modelling: what is it and what can it tell us?, August 2016. URL <https://www.aeroqual.com/air-pollution-modelling>.
- [66] D. B. Topalović, M. D. Davidović, M. Jovanović, A. Bartonova, Z. Ristovski, and M. Jovašević-Stojanović. In search of an optimal in-field calibration method of low-cost gas sensors for ambient air pollutants: Comparison of linear, multilinear and artificial neural network approaches. *Atmospheric Environment*, 213:640–658, September 2019. ISSN 1352-2310. doi: 10.1016/j.atmosenv.2019.06.028. URL <http://www.sciencedirect.com/science/article/pii/S1352231019304194>.
- [67] A. Unal, Y. Hu, M. E. Chang, M. Talat Odman, and A. G. Russell. Airport related emissions and impacts on air quality: Application to the Atlanta International Airport. *Atmospheric Environment*, 39(32):5787–5798, October 2005. ISSN 1352-2310. doi: 10.1016/j.atmosenv.2005.05.051. URL <http://www.sciencedirect.com/science/article/pii/S1352231005004838>.
- [68] O. US EPA. Criteria Air Pollutants, April 2014. URL <https://www.epa.gov/criteria-air-pollutants>.

- [69] O. US EPA. Ground-level Ozone Basics, May 2015. URL <https://www.epa.gov/ground-level-ozone-pollution/ground-level-ozone-basics>.
- [70] Y. Wang, Y. Du, J. Wang, and T. Li. Calibration of a low-cost PM<sub>2.5</sub> monitor using a random forest model. *Environment International*, 133:105161, December 2019. ISSN 0160-4120. doi: 10.1016/j.envint.2019.105161. URL <http://www.sciencedirect.com/science/article/pii/S0160412019322780>.
- [71] J. Wesseling, H. de Ruiter, C. Blokhuis, D. Drukker, E. Weijers, H. Volten, J. Vonk, L. Gast, M. Voogt, P. Zandveld, S. van Ratingen, and E. Tielemans. Development and Implementation of a Platform for Public Information on Air Quality, Sensor Measurements, and Citizen Science. August 2019.
- [72] R. White, I. Paprotny, F. Doering, W. Cascio, P. Solomon, and L. Gundel. Sensors and 'apps' for community-based: Atmospheric monitoring. page 11, May 2012. URL [https://www.researchgate.net/publication/279606358\\_Sensors\\_and\\_'apps'\\_for\\_community-based\\_Atmospheric\\_monitoring](https://www.researchgate.net/publication/279606358_Sensors_and_'apps'_for_community-based_Atmospheric_monitoring).
- [73] X. Yang, S. Cheng, J. Lang, R. Xu, and Z. Lv. Characterization of aircraft emissions and air quality impacts of an international airport. *Journal of Environmental Sciences*, 72:198–207, October 2018. ISSN 1001-0742. doi: 10.1016/j.jes.2018.01.007. URL <http://www.sciencedirect.com/science/article/pii/S100107421732140X>.
- [74] S. H. L. Yim, G. L. Lee, I. H. Lee, F. Allroggen, A. Ashok, F. Caiazzo, S. D. Eastham, R. Malina, and S. R. H. Barrett. Global, regional and local health impacts of civil aviation emissions. *Environmental Research Letters*, 10(3):034001, February 2015. ISSN 1748-9326. doi: 10.1088/1748-9326/10/3/034001. URL <https://doi.org/10.1088%2F1748-9326%2F10%2F3%2F034001>. Publisher: IOP Publishing.
- [75] Z. Yu, D. S. Liscinsky, E. L. Winstead, B. S. True, M. T. Timko, A. Bhargava, S. C. Herndon, R. C. Miake-Lye, and B. E. Anderson. Characterization of Lubrication Oil Emissions from Aircraft Engines. *Environmental Science & Technology*, 44(24):9530–9534, December 2010. ISSN 0013-936X. doi: 10.1021/es102145z. URL <https://doi.org/10.1021/es102145z>. Publisher: American Chemical Society.
- [76] X. Zhang, B. Gao, A. E. Creamer, C. Cao, and Y. Li. Adsorption of VOCs onto engineered carbon materials: A review. *Journal of Hazardous Materials*, 338:102–123, September 2017. ISSN 0304-3894. doi: 10.1016/j.jhazmat.2017.05.013. URL <http://www.sciencedirect.com/science/article/pii/S0304389417303564>.